JUSTUS-LIEBIG-
UNIVERSITÄT
GIESSEN

High-Resolution Experiments with the Multiple-Reflection Time-Of-Flight Mass Spectrometer at the Fragment Separator FRS

INAUGURALDISSERTATION ZUR ERLANGUNG DES
DOKTORGRADES DER NATURWISSENSCHAFTLICHEN FAKULTÄT
DER JUSTUS-LIEBIG-UNIVERSITÄT GIESSEN

vorgelegt von
CHRISTINE HORNUNG
geboren in Gießen

FACHBEREICH 07 - MATHEMATIK UND INFORMATIK, PHYSIK, GEOGRAPHIE
II. PHYSIKALISCHES INSTITUT JUSTUS-LIEBIG-UNIVERSITÄT GIESSEN

MAY 2018

Erstgutachter: Prof. Dr. Dr. h.c. Hans Geissel
Zweitgutachter: Prof. Dr. Christoph Scheidenberger

Contents

1. Introduction

The matter in our universe consists of atoms characterized by their number of electrons, protons and neutrons [Mackintosh et al. (2001)]. Neutral atoms have bound the same number of negatively charged electrons and positively charged protons via the Coulomb force. Protons and neutrons form the nucleus, which represent to more than 99.9 % the total mass of an atom. The number of electrons and protons in an atom determines the chemical properties, whereas the nuclear stability (lifetime) is critically determined by the number of neutrons in an isotope. The isotopes of one element have a fixed number of protons (Z) and a variable number of neutrons (N). Stable nuclei exist only with a sensitive balance of the proton-to-neutron ratio in the so-called valley of stability formed in the Z-N plane.

Exotic nuclei have an unbalanced proton-to-neutron ratio in comparison to nuclei in the valley of stability. This results normally in a short lifetime of the nuclei and the resulting decay tries to reestablish the energetically favoured configuration of the stable species. Exotic nuclei can decay via different modes including the emission of electrons, positrons, alpha particles and protons, often accompanied by photon radiation. The proton and two-proton radioactivity have been recently discovered with short-lived exotic nuclei produced in nuclear reaction experiments at GSI, whereas the other decay modes are known since more than 100 years [Pfützner et al. (2012)]. Similar like the shell structure of the electrons in the atomic elements, also the nuclear properties are influenced by closed shells formed by magic numbers of protons and neutrons. The magic numbers observed in and near the valley of stability can change for exotic nuclei, especially close to the drip-lines [Leistenschneider et al. (2018); Sorlin and Porquet (2008)]. Nuclei characterized by magic proton and neutron numbers are stable or longer-lived compared to neighbouring species in the chart of nuclei and their shape is often spherical. In general, exotic nuclei have different shapes [Gaffney et al. (2013)] and shorter half-lives. The study of exotic nuclei is driven by the discovery of novel nuclear structure and decay properties and their role in the element synthesis during the evolution of stars [Grawe et al. (2007)].

The mass of a nucleus reflects the total binding energy of the nucleons [Aston (1927)] and thus determines many nuclear properties. A measure for the binding energy is the Mass Excess (ME) defined as the difference of the actual mass of a nucleus and the corresponding value of the mass number A ($A = N + Z$). The direct values of ME or the differences of masses for neighbours in the chart of nuclei (e.g., one-neutron separation energy S_n) reveal basic informations of nuclear properties as shown in Figure 1.1 [Scheidenberger (2005)]. The masses of nuclei can be measured directly by high precision mass spectrometry or determined indirectly from their decay properties. By measuring the masses of nuclei, one can study, due to Einsteins energy-mass equivalence, the appearance of excited metastable states, known as nuclear isomers. Their lifetimes are much longer than common excited states [Dracoulis et al. (2016); Walker and Dracoulis (1999)]. Nuclear isomers can have lifetimes longer than the corresponding ground state.

The discovery of nuclear isomerism is assigned to Otto Hahn [Hahn (1921)]. The naming of nuclear isomers goes back to Frederick Soddy who used for the first time the analogy between chemical and nuclear isomers [Soddy (1917)]. The applications of nuclear isomers open up a broad field, ranging from research concerning new possibilities for the storage of energy up to the impact on nuclear astrophysics and the production of the elements in the universe [Aprahamian and Sun (2005)].

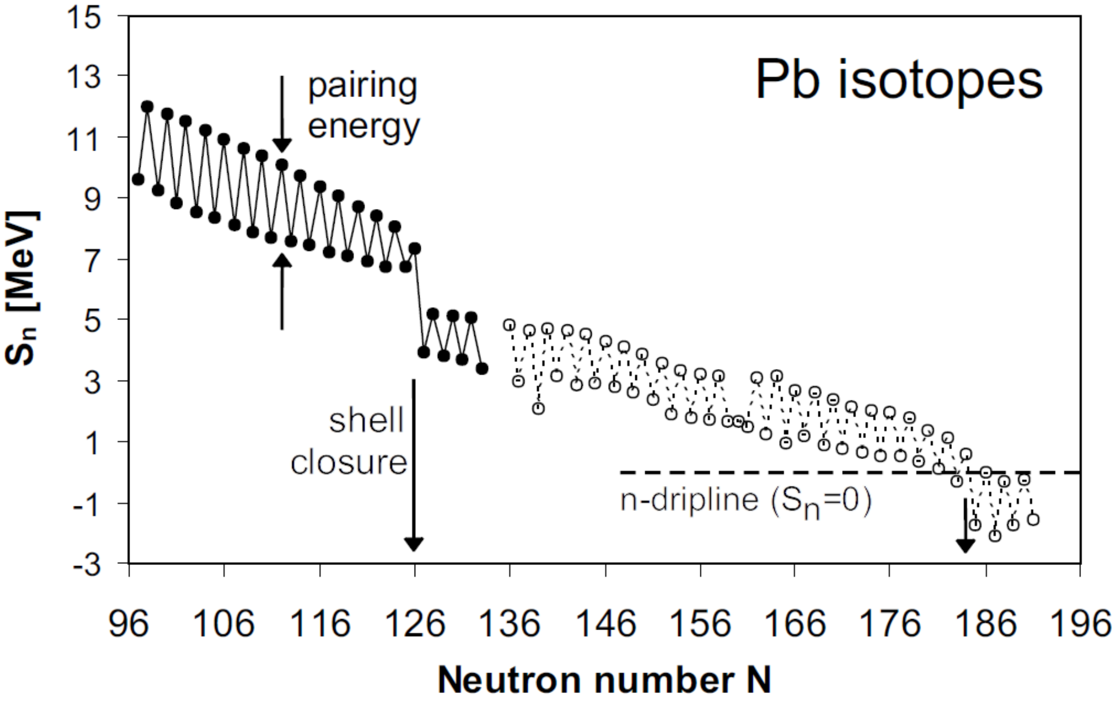

Figure 1.1.: Measured and predicted one-neutron separation energy S_n of different lead isotopes. The full squares correspond to measured values [Audi et al. (2003)], the open ones correspond to FRDM model calculations [Möller et al. (1995)]. The S_n values indicate nuclear shell closures, the energy difference due to the pairing of nucleons, and the limit of nuclear existence due to unbound neutrons, the neutron-dripline [Scheidenberger (2005)].

The properties of nuclear isomers [Dracoulis et al. (2016); Walker (2010)] are also of high importance to the understanding the structure of nuclei:

- The difference in half-life can be used to resolve complex excitation spectra
- The lifetime of high-spin isomers can be longer than the corresponding ground state
- Isomers give access to investigate high excitation level schemes
- Shapes of nuclei can be classified by deformations and shape coexistence
- The underlying structure for their existence gives access to the conservation of the total nuclear angular momentum projected on the deformation axis
- Underlying concepts and properties of isomers can be used as stringent tests for nuclear models

Due to the long half-life of high-spin isomers, they can be investigated by high precision mass spectrometry. During the last two decades, high-resolution direct mass measurements of isomers were mainly performed with storage rings [Franzke et al. (2008)] and Penning traps [Blaum (2006)]. In this work, direct mass measurements of short lived exotic nuclei and their isomers with an MR-TOF-MS [Dickel et al. (2015b); Plaß et al. (2013b)] are presented in Section 6.5. The first measurement of the $(1/2)^-$ isomeric state in ^{97}Ag is presented in Section 6.6. A novel method to provide spatially separated clean isomeric beams was developed and successfully applied [Dickel et al. (2015a)]. This topic is presented in Section 6.5.2.

2. Exotic Nuclei

In this work, short-lived nuclei and their isomeric states were investigated via mass spectrometry. The nuclei were produced in high-energy fragmentation reactions with ^{124}Xe and ^{238}U projectiles. The experiments gave access to exotic nuclei in the region above ^{208}Pb nuclei and neutron-deficient nuclei below the doubly-magic ^{100}Sn nucleus. A short motivation for the focus on these areas in the chart of nuclides is given before the principles of production and separation of the projectile fragments are outlined. Simple models for the population of isomeric states are given in the subsequent chapter, since the study of isomers plays an important role in this thesis.

2.1. Motivation for Studies of Exotic Nuclei in the regions above ^{208}Pb and below ^{100}Sn

Above the doubly-magic nucleus ^{208}Pb a region of very short-lived nuclei opens up in the nuclear chart with half-lives down to nanoseconds. The masses of these nuclei are currently only known via their Q-values. The Q-values relate the masses of the nuclei before and after a reaction. In this case, the Q-values relate the mother and daughter nuclei in the reaction of α-decay. The accurate measurement of the kinetic energies of the emitted α-particles leads to the determination of the absolute mass difference of the mother and daughter nuclei, because the rest mass of the α-particle is well known. In this way, the measured masses in this region are determined via the chains of nuclides linked via α-radioactivity. Therefore, a direct and independent measurement is desirable for the masses of the α-emitters in this region. A fast and accurate experimental technique is required for this goal. These requirements can be fulfilled by a multiple-reflection time-of-flight mass spectrometer [Dickel et al. (2015b); Plaß et al. (2013b)].

Since the experimental discovery of ^{100}Sn nuclei [Schneider et al. (1994)], a lot of progress has been made for the heaviest N = Z nuclei [Faestermann et al. (2013)]. New isotopes were identified and their half-lives and decay properties have been measured.

The ^{100}Sn nucleus is presently the heaviest self-conjugate doubly-magic nucleus experimentally investigated. Due to its uncommon level scheme, dominated by an intruder state, unique structure features arise as high-spin isomers and a super-allowed Gamow-Teller β^+/EC decay [Hinke et al. (2012)]. The Gamow-Teller β^+-decays were systematically investigated also for other N=50 isotones in this region [Batist et al. (2010)].

Precise knowledge of the masses in this region is of special interest. Despite of the experimental efforts, documented by recent Penning trap measurements [Breitenfeldt et al. (2009); Elomaa et al. (2008, 2009a,b); Haettner et al. (2011); Weber et al. (2008)], the mass of the ^{100}Sn is still only known with a large uncertainty ($\Delta m/m = 10^{-5}$) [Chartier et al. (1996)]. In the region below ^{100}Sn, the odd-odd N = Z nuclei decaying with β^--emission from the ground states often have a long-lived isomeric state in addition, which can decay in a super-allowed β-decay. Obviously, direct mass measurement have to ensure which state was measured. A part of the chart of nuclides in this region is shown in Figure 2.1, indicating the long-lived isomeric states with the errors of their excitation energies. In this figure the coloured isotopes are those, where ground and isomeric states have a half-life of more than 1 ms. Red and orange colours indicate all isomers, for which the half-life of the isomer is longer than the corresponding ground state. The mass measurements of these nuclides are particularly difficult to measure with high-resolution methods, because both states cannot be simultaneously measured. In green and red colour all isotopes are highlighted, where the ground and isomeric states can be resolved with a mass resolving power below 500000.

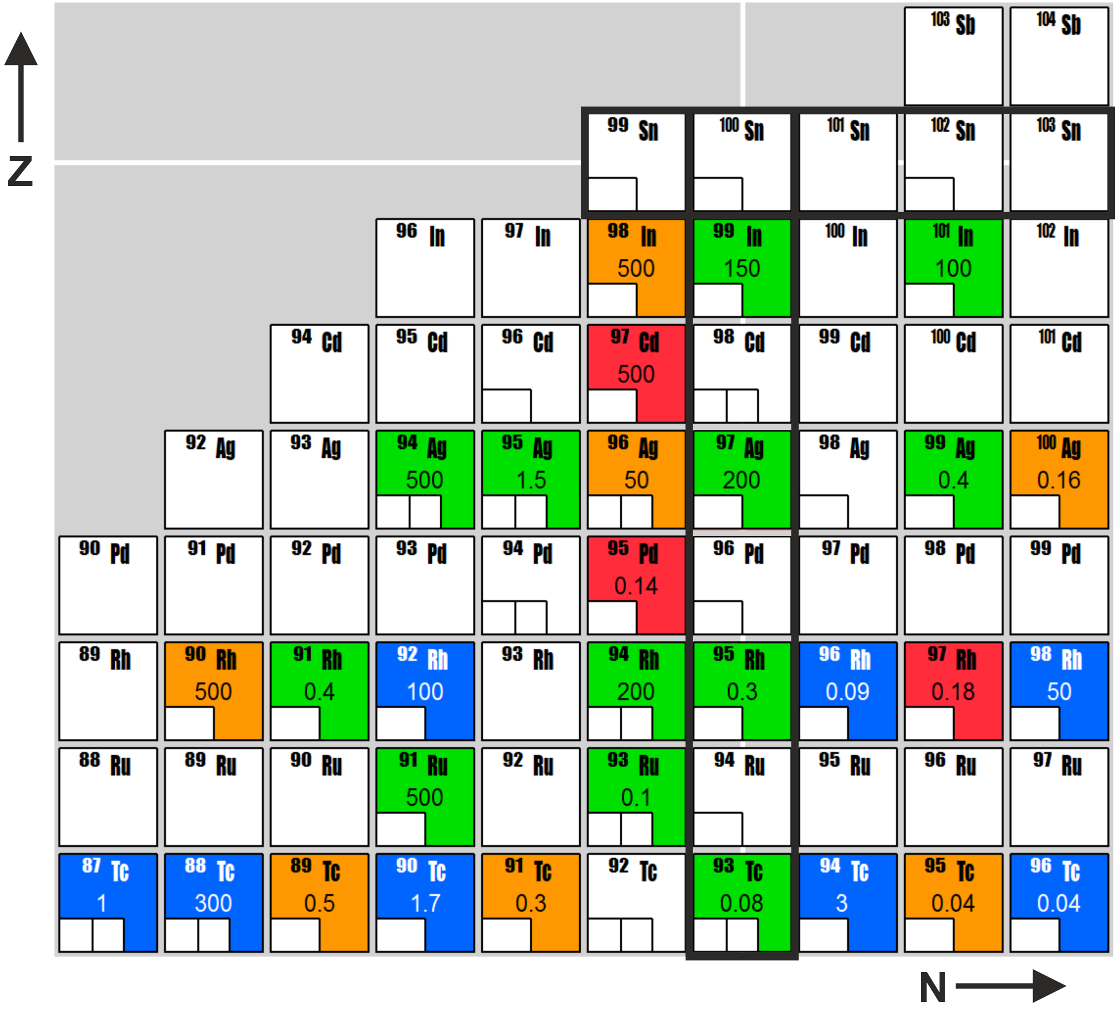

Figure 2.1.: Chart of nuclides zoomed at the region below ^{100}Sn. The focus is on the isomeric states, where ground and isomeric state have both a half-life of more than 1 ms. The errors of the corresponding excitation energies are shown. The colour code indicates the necessary mass resolving power to resolve the ground and the isomeric state and includes the half-life information. The green colour indicates if the half-life of the isomer is shorter than the one of the ground state and the necessary mass resolving power is higher than 500000. In red colour all nuclei are shown, for which the isomer has a longer half-life than the ground state and the necessary resolving power is higher than 500000. In the case that the necessary resolving power is lower than 500000, the nuclei are shown in orange colour if the isomer has a longer half-life than the ground state and the blue colour if the half-life is shorter.

The mass measurements of the ground and isomeric states in this work are a first step to explore the nuclear structure and excitations in this region of the nuclear chart. By measuring ground and isomeric states simultaneously, it is possible to confirm and classify previous measurements.

The nuclei in the neighbourhood of ^{100}Sn, close to the proton drip-line, are also of interest in astrophysical scenarios, since in this region the rapid proton capture process ends. In the astrophysical processes the proton capture rates become fast and compete with the β^+-decays, this leads to so-called waiting points, which have an important influence on the resulting abundance of elements in the universe.

2.2. Projectile Fragmentation and Population of Isomers

In general, in projectile fragmentation a high energetic heavy nuclei impinges on a light target. Nucleon-nucleon reactions dominate the fragmentation process for projectile kinetic energies exceeding the Fermi velocity of the bound nucleons. The fragmentation reaction can be described by a two-step approach, the so-called abrasion-ablation model. In the first step, nucleons are removed from the target or projectile which results in the production of a target-like and a projectile-like excited prefragment, respectively. In the second step, an excited prefragment deexcites by a statistical evaporation cascade of nucleons.

Fragmentation reactions can provide high angular momenta. This leads to a relatively high probability to populate isomeric states [Young et al. (1993)]. The angular-momentum distribution of a fragmentation reaction in the scope of an abrasion-ablation model was investigated in reference [de Jong et al. (1997)]. Further investigations by more sophisticated theoretical approaches were developed [Pal and Palit (2008)] and compared with experimental values from γ-spectroscopy [Gladnishki et al. (2004); Pfützner et al. (2002)].

The population probability of a final fragment depending on the angular momentum J in a basic approach is given by

$$P\left(J,\sigma^2\right) = \frac{2J+1}{2\sigma^2} exp\left(-\frac{J\left(J+1\right)}{2\sigma^2}\right) . \tag{2.1}$$

In this scope, σ^2 is the spin-cutoff parameter, which is correlated with the width of the level density distribution. It can be related to the moment of inertia of a nucleus and its temperature. Goldhaber formulated a statistical model approach to describe the width of a momentum distribution by the mass number of both the fragment and the projectile and the mean square momentum [Goldhaber (1974)]. An approximation of the spin-cutoff parameter depending on the mass number of the projectile A_p and final fragment A_f, on the number of the on average evaporated nucleons per abraded nucleon $\bar{\nu}$ and on the average square value of the angular-momentum projection of a nucleon in the nucleus $\left\langle j_z^2 \right\rangle$ can be written as

$$\sigma_f^2 = \left\langle j_z^2 \right\rangle \frac{\left(A_p - A_f\right)\left(\bar{\nu}A_p + A_f\right)}{\left(\bar{\nu}+1\right)^2\left(A_p - 1\right)} . \tag{2.2}$$

In order to obtain the abundance ratio between the isomer and the ground state, it is assumed that all states with a higher angular momentum than the isomeric state will only decay to the isomer. This extremely simplified approach neglects the possibility that the isomeric state can be skipped in the γ-cascade. In the literature, this approach is known as the sharp cutoff model. Furthermore, it is assumed that all angular momentum population below the first isomer will populate the ground state of the nucleus. This will lead to the following expression for the isomer-to-ground state ratio:

$$R_{isomer-to-ground} = \frac{\int_{J_{iso}}^{\inf} P\left(J\right)dJ}{\int_0^{J_{iso}} P\left(J\right)dJ} = \frac{exp\left(-\frac{J_{iso}\left(J_{iso}+1\right)}{2\sigma_f^2}\right)}{1 - exp\left(-\frac{J_{iso}\left(J_{iso}+1\right)}{2\sigma_f^2}\right)} . \tag{2.3}$$

Besides the sharp cutoff model, there are other approaches, e.g. a model description based on an empirical spin mixing [Gasques et al. (2006)]. In this model, an effective angular momentum cutoff is introduced together with a spreading parameter for the transition between two states. This allows to take into account that a given spread in the momentum distribution is caused by the emission of nucleons and the γ-cascade of the prefragment.

The abrasion-ablation model is a very simplified approach to describe the population of isomeric states. Only single-particle excitations are considered and, more importantly, it does not cover non-yrast isomeric states. The comparison with experimental data showed the deficit of understanding and describing the process [Bowry et al. (2013)].

2.3. In-Flight Separation via the Bρ-ΔE-Bρ Method

Exotic nuclei can be produced via different nuclear reactions and can be experimentally studied after separation from the primary beam and from the abundant background [Geissel et al. (1995)]. In-flight separation is superior for rare short-lived nuclei documented by the highest discovery rates of new isotopes and new elements [Thoennessen (2013)]. The limitation in lifetime is only the flight time through the separator system, which is in the microsecond second range and lower. The Bρ-ΔE-Bρ method is the currently most successful separation method tailored to the efficient separation of projectile fragments.

The combination of the magnetic rigidity ($B\rho$) analysis and the atomic energy loss in a layer of profiled matter (degrader) placed at a dispersive spectrometer stage leads to a spatial separation in-flight. This separation process is known as the Bρ-ΔE-Bρ method [Geissel et al. (1992)]. A first mass-to-charge selection of fully stripped reaction products is performed with the FRagment Separator (*FRS*) by the first two magnetic dipole stages. In the case of fully stripped ions, their charge is equal to their number of protons Z. All ions with the same Bρ are focused on one point of the degrader. This implies that they all have the same momentum-to-charge ratio. However, they can still differ in their number of nucleons A and charge Z. The energy loss is proportional to Z^2. This fact is used as the second separation criterion by the magnetic rigidity analysis with the two magnetic dipole stages behind the energy degrader. In this way, isotopic spatial separation can be achieved. The best spatial separation can be reached, if the degrader at the mid-focal plane is shaped in a way that the achromatic condition of the FRS ion-optics is preserved. It provides a high separation performance for all exotic ions up to the heaviest bare projectile fragments. Ions with half-lives down to roughly 100 ns can be separated, only being limited by the time-of-flight through the ion optical system.

A precise knowledge of the energy loss inside matter and high velocities to provide bare fragments are necessary for the successful application of this method. Only an uncertainty of one percent of the energy loss in the degrader could prevent detecting the ion of interest in the final focal plane. High projectile velocities are needed to ensure that multiple ionic charge states do not disturb the unambiguous Bρ analysis.

3. Mass Measurement of Atomic Nuclei

The mass of a nucleus can be measured with the application of different methods. Recent reviews on this topic are the references [Blaum et al. (2013); Franzke et al. (2008); Lunney et al. (2003)]. In general, one distinguishes between direct and indirect experimental methods. Indirect methods are mainly based on the determination of the Q-values of reactions including radioactive decays. Indirect methods rely on an accurate knowledge of particle properties in the reaction and decay. In direct methods, the mass of an ion is determined via recording of kinematic properties in special ion-optical systems. The accuracy is achieved with reduction of the phase space by applying cooling in special electromagnetic storage devices. In general, cooling requires time, leading to limitation for very short-lived ions. A solution is to apply isochronous systems, which go without the application of cooling [Franzke et al. (2008); Plaß et al. (2015)]. Examples for direct methods are storage ring measurements, measurements with a trap, or via a time-of-flight system. These methods are complementary in their ranges of applicability with respect to accuracy, resolution, sensitivity, time for the measurement cycle, and the required number of exotic nuclei for a high-accuracy result. In the following sections the principles of indirect and direct methods are discussed.

3.1. Indirect Methods of Mass Measurements

The mass of a nucleus can be determined by indirect methods, whereby the mass is measured via the Q-value [Mayer-Kuckuk (1992)] of a selected reaction. Radioactive decays can be used in this category as well, e.g., α- and β-decays, where the kinetic energy spectrum of the emitted particles are measured. The strength of this method is the access to very short-lived nuclei down to species, which are formed in a resonance reaction.

α-radioactivity represents a two-body reaction, a parent nucleus emits an α-particle. Here, the Q-value (Q_α) includes the kinetic energy of the emitted α-particle (E_α) and the mass of the daughter nucleus $m_{Doughter}$ [Mayer-Kuckuk (1992)]:

$$Q_\alpha = E_\alpha \left(1 + \frac{m_\alpha}{m_{Doughter}}\right) , \tag{3.1}$$

where m_α is the rest mass of the α-particle, which is well known. In this way, the Mass Excess (ME) of the daughter nucleus can be measured via E_α and the knowledge of the mass of the parent nucleus:

$$Q_\alpha = ME_{Parent}(Z,N) - ME_{Doughter}(Z-2,N-2) - m_\alpha c^2 . \tag{3.2}$$

The mass assignment is easy if the decay directly connects the ground states of the parent and daughter nuclei. In general, also excited states of both the parent and daughter nuclei can be involved. However, this requires a precise knowledge of the corresponding level schemes and their population. Experimentally high-resolution γ-spectroscopy can be employed to determine the possible excitation energies.

In β-radioactivity, driven by the weak interaction, one distinguishes between β^--, β^+- and Electron Capture (EC) decay. β^-- and β^+-decays are characterized by a three-body-process.

In this decay modes, a neutron is converted to a proton or vice versa and simultaneously, an electron and an antineutrino, or a positron and a neutrino are emitted. As a consequence the kinetic energy is shared between the electron (positron), the antineutrino (neutrino) and the recoil of the daughter nucleus. Therefore, the kinetic energy of the emitted β-particles is not a discrete value, but represents a continuous distribution with an upper limit given by the β-endpoint energy $E_{\beta-endpoint}$. In case of an EC-decay, the binding energy of the electron in the atomic shell $E_{Electron}$ has to be taken into account in addition. Analogous to the discussed α-decay, the excited states of the involved parent and mother nuclei have to be measured via photon spectroscopy (E_γ). The Q-value relations are:

$$\begin{aligned} Q_{\beta^-} &= E_{\beta-endpoint}\left(1+\frac{m_e}{m_{Doughter}}\right)+E_\gamma\,,\\ Q_{\beta^+} &= E_{\beta-endpoint}\left(1+\frac{m_e}{m_{Doughter}}\right)+E_\gamma\,,\\ Q_{EC} &= E_{\beta-endpoint}\left(1+\frac{m_e}{m_{Doughter}}\right)+E_\gamma+E_{Electron}\,. \end{aligned} \tag{3.3}$$

3.2. Direct Methods of Mass Measurements

3.2.1. Storage Ring Mass Spectrometry

The revolution frequency (time) of ions travelling on closed orbits in a storage ring can be used to determine their mass-to-charge ratio. An overview of this technique is given in [Franzke et al. (2008)]. During the stored ions circulate in the ultra-high vacuum of the ring, their revolution frequency f can be measured with sensitive pick-up probes. The revolution frequency is related to their mass-to-charge ratio (m/q) via

$$\frac{\Delta f}{f}=\frac{1}{\gamma_T^2}\frac{\Delta(m/q)}{(m/q)}+\left(1-\frac{\gamma^2}{\gamma_T^2}\right)\frac{\Delta v}{v}\,, \tag{3.4}$$

where v is the ion velocity and its spread Δv. γ_T corresponds to the transition energy and γ is the relativistic Lorentz factor. The mass-to-charge ratio can directly be determined from the revolution frequency, if the second term of Equation 3.4 can be cancelled. This can be achieved by two complementary techniques, either the velocity spread of the stored ions is reduced to $\approx 10^{-7}$, or with an operation of the ion-optical system at its transition point. Under this condition the mean velocity of the stored ions corresponds to a γ-value which is equal to γ_T. The first method is applied in Schottky Mass Spectrometry (*SMS*) [Litvinov et al. (2004); Radon et al. (1997)]. In SMS the stored ions are cooled via electron and stochastic cooling. The cooling process requires a certain time, due to this, only longer-lived exotic nuclei ($T_{1/2} >$ few seconds) can be investigated. Depending on the velocity spread, presently electron cooling in the Experimental Storage Ring (*ESR*) [Franzke (1987)] took a few seconds, whereas stochastic precooling is much faster. The second storage-ring technique is known as Isochronous Mass Spectrometry (*IMS*) [Knöbel et al. (2016)]. It is an extremely fast method limited only by the number of recorded revolutions. The revolution time of the stored ions in the isochronous ESR is about 500 ns, thus in principle, ions characterized by lifetimes down to the μs range can be measured.

3.2.2. Penning Trap Mass Spectrometry

Presently, mass measurements of exotic nuclei with Penning traps reach the highest resolution and precision [Blaum (2006); Bollen et al. (1990)]. In a Penning trap the ions are stored in a small volume by magnetic and electric fields. The ions are confined in radial direction by a homogeneous magnetic field, in axial direction by an electric field. The mass measurement in Penning traps are based on the measurement of the cyclotron frequency ν_c given by

$$\nu_c = \frac{qB}{2\pi m} \ . \tag{3.5}$$

The stored ions are excited by an induced variable frequency close to ν_c. When the ions are resonantly excited, they accumulate additional radial energy, which is a signature of the corresponding actual cyclotron frequency to be determined.

In more detail, the mass of a nucleus can be measured in a Penning trap by two different techniques:

- Fourier Transform Ion-Cyclotron-Resonance Mass Spectrometry (*FT-ICR MS*) [Marshall et al. (1998)]
- Time-Of-Flight Ion-Cyclotron-Resonance technique (*TOF-ICR*) [König et al. (1995)]

In the FT-ICR MS the resonantly excited ion motion is detected as an induced signal by pickup-electrodes. This signal is Fourier analysed and a corresponding mass spectrum is obtained. In the TOF-ICR technique the Time-Of-Flight (*TOF*) of the ions from the trap to the detector is measured as a function of the applied frequency. The TOF is shortest in the case of the resonant excitation. The nowadays widely used TOF-ICR is a scanning technique, therefore, it is less suitable for isotopes with a very low production rate. Due to its non-broadband characteristics only one isotope in one state can be seen at a time. This leads to ambiguous identifications in the case of the existence of isomeric states in the isotope of interest.

Recently, large progress has been achieved with the implementation of the so-called Phase-Imaging method (*PI*) [Eliseev et al. (2013)]. There a 40-fold gain in the resolving power and a five-fold increase for the accuracy has been presented.

3.3. Time-of-Flight Mass Spectrometry

The mass-to-charge ratio of ions with a fixed kinetic energy can be determined with a Time-Of-Flight Mass Spectrometer (*TOF-MS*) by measuring the TOF in comparison with a reference ion [Cameron and Eggers Jr. (1948)]. In the simplest version, a TOF-MS analyser consists of a field free linear drift tube, where lighter ions need a shorter TOF than heavier ones, because they have the same initial kinetic energy. In the case that all ions start at the same time with the same kinetic energy, this leads to a spatial separation of the ions depending on their mass-to-charge ratio. If all ions would have the identical start conditions, with respect to their position, angle, direction and energy, this would result in a delta-shaped peak for each of the different ion species. However, in reality, one has to assume a finite incident phase space which leads to a spread in the measured time distributions. The mass-to-charge ratio (m/q) for an ion with a kinetic Energy $E_{kin,z}$, defined by the electric field $U(z)$ along the axis of the analyser z, can be derived by:

$$\begin{aligned} E_{kin,z} =& \frac{1}{2} m v_z^2 = qU(z) \ , \\ (m/q) =& 2U(z) \frac{(t)^2}{z^2} = a \left(t_{meas} - t_{TFS}\right)^2 \ , \end{aligned} \tag{3.6}$$

with the measured flight time t_{meas} and the calibration constant a. The constant t_{TFS} reflects the delay caused by the signal processing of the electronics. Due to the simultaneous measurement of the calibrant ion and the ion of interest, it is not necessary to know accurately the length of the flight-path.

TOF mass spectrometry has several advantages. It offers both a large mass range and a non-scanning operation, which lead to a high sensitivity. Due to short measurement times ($\approx ms$), also nuclei with short half-lives are accessible with this device. The mass resolving power R_m of a TOF-MS is given by the measured mass-to-charge ratio (m/q) divided by the FWHM of the corresponding distribution $\Delta(m/q)$

$$R_m = \frac{(m/q)}{\Delta(m/q)} = \frac{t}{2\Delta t} \, . \tag{3.7}$$

In order to achieve the highest possible resolving power, the ion-optical properties have to be chosen in such a way that the energy-time focus is placed in the detector plane. Linear TOF-MS are limited in their resolving power by the available length of the drift tube. Ways to overcome this problem are e.g., to reflect the ions in an electrostatic mirror in order to prolong the flight path, or to let the ions travel through the same sector field many times (multiple turns). Both implementations reduce the size of the experimental setup. An overview of typical TOF systems is illustrated in Figure 3.1 [Plaß et al. (2013b)]. In general, one distinguishes between systems with an open and a closed flight path. A system with an open flight path provides, depending on the start conditions of the ions, a fixed resolving power, but its electronic requirements are easier to implement, since no switching of fields is required. In general, systems with a closed flight path can reach an arbitrary long flight path and can be implemented in a smaller construction. However, by using the same flight path several times, lighter ions can overtake heavier ones, which might lead to an ambiguous assignment between TOF and mass, unless the different number of turns are distinguishable.

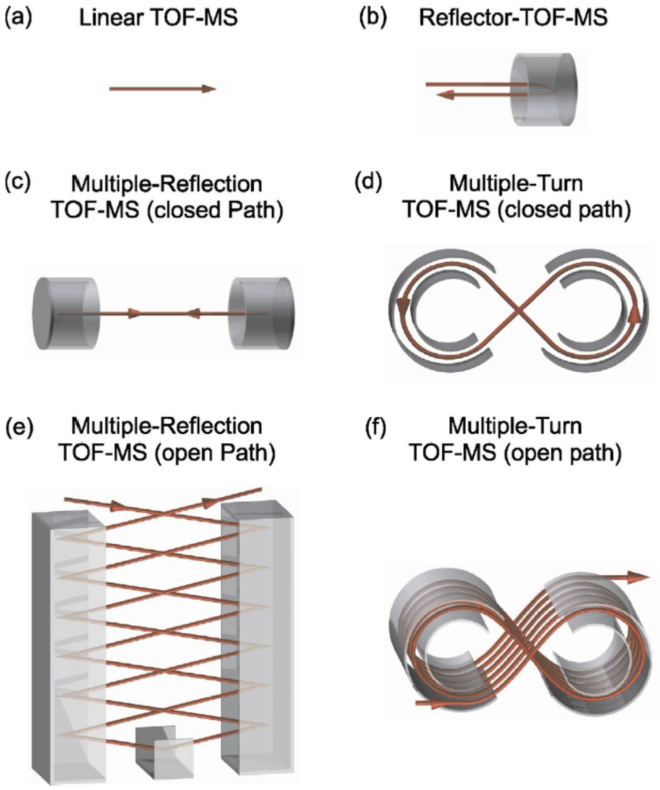

Figure 3.1.: Schematic overview of different analyser types of TOF systems [Plaß et al. (2013b)]: (a) Linear TOF-MS, (b) single reflection TOF-MS, (c) multiple-reflection TOF-MS with closed path, (d) multiple-turn TOF-MS with closed path, (e) multiple-reflection TOF-MS with open path, (f) multiple-turn TOF-MS with open path.

Important for the performance of a TOF-MS are the starting conditions, as it was pointed out already in reference [Cameron and Eggers Jr. (1948)]. A TOF-MS requires a nearly mono-energetic ion pulse with a small spatial and angular spread. Due to this, the choice of the ion source and the injection system is of great importance. A lot of TOF systems work with special injection traps. There, the ions are cooled beforehand in order to decrease the velocity and spatial spread, and are released with a well-known energy in a short time.

Multiple-Reflection Time-of-Flight Mass Spectrometry

In Multiple-Reflection Time-Of-Flight (*MR-TOF*) mass spectrometry [Plaß et al. (2013b); Wollnik and Przewloka (1990)] the flight path of the ions is increased by undergoing several reflections inside of the analyser. The reflections are performed by a pair of electrostatic mirrors. A high-resolution MR-TOF Mass Spectrometer (*MR-TOF-MS*) can also be a very powerful device for particle identification. It is able to identify the particles directly via mass measurements. These spectrometers represent a broadband and non-scanning technique. In the first step, a broad mass-to-charge window can be investigated and afterwards the final results are obtained with a mass resolving power of up to 600000 [Ayet San Andrés (2018); Dickel (2010); Dickel et al. (2015b)].

The flight time for one isochronous turn t_{IT} in the analyser for an ion with a mass-to-charge ratio (m/q) can be described by

$$t_{IT}\left((m/q)\right) = A\sqrt{(m/q)}\,, \tag{3.8}$$

where A is a constant.

In an MR-TOF-MS the analyser is designed to be isochronous. In this case, the time focus is after each isochronous turn at the same position in the analyser. In order to achieve the highest resolving power a time focus has to be in the detector plane, in this case the flight time depends on the mass-to-charge ratio only. This can be achieved by a special geometry of the electrostatic system which takes into account that the ions travel through the non-isochronous injection and ejection section [Yavor et al. (2015)]. This can be done with an electrostatic reflector shifting the time focus towards to detector plane [Dickel et al. (2017)]. In the Time-Focus-Shift (*TFS*) mode, the ions travel from the ejection of the injection trap trough the analyser and the electrostatic reflector to the detector, this flight time t_{TFS} can be described as the fraction λ_{TFS} of the TOF of an isochronous turn. This fraction, which is a mass-to-charge independent parameter, is given by

$$t_{TFS}\left((m/q),\lambda_{TFS}\right) = \lambda_{TFS}t_a = \lambda_{TFS}A\sqrt{(m/q)}\,. \tag{3.9}$$

4. Experimental Setup

The FRS Ion Catcher (*FRS-IC*) [Plaß et al. (2013a)] is a high accuracy and high resolution experimental setup installed at the final focal plane of the fragment separator FRS [Geissel et al. (1992)] at GSI. The FRS-IC is primarily a device for accurate mass measurements of exotic nuclei. However, it can also be employed for isomer, half-life and reaction studies. Furthermore, it can be combined with auxiliary detectors and laser systems for other spectroscopy experiments. The FRS-IC serves as a test facility for the future Low-Energy Branch (*LEB*) of the Super-FRS [Geissel et al. (2003); Winfield et al. (2013)] at FAIR.

4.1. The Fragment Separator FRS

The FRS at GSI [Geissel et al. (1992)] is a versatile magnetic forward separator/spectrometer with four dipole-magnet stages, each including quadrupole and hexapole magnets. The FRS has three ion-optical branches. The symmetric direct branch (75m length) including the FRS-IC is employed in the experiments of this work. The other two ion-optically equivalent branches are used for experiments in combination with the storage-cooler ring ESR [Franzke (1987); Franzke et al. (2008)] and mainly experiments with the complex R^3B setup including a large acceptance dipole magnet [Aumann (2007)]. Relativistic fragments with a maximum magnetic rigidity ($B\rho$) of 18 Tm can be spatially separated in-flight with the FRS via two-fold $B\rho$ analysis in front and behind a thick energy degrader, see Section 2.3.

In the first two magnetic dipole stages of the FRS, the fragments are separated by their mass-over-charge ratio. The kinetic energies of the projectiles, provided by the synchrotron SIS-18 [Blasche and Franczak (1992)], can be selected high enough to have fully ionized fragments emerging from the production target which is installed at the entrance of the FRS. This means, the separation is according to A/Z, because the mean velocity of the different projectile fragments is not very different. At the dispersive central focal plane (*F2*) a thick, specially shaped degrader is placed, wherein the fragments lose energy (ΔE). ΔE is dependent on Z^2 of the fragments. Combined with the two-fold $B\rho$ analysis, the fragments can be isotopically and spatially separated at the final focal plane. This spatial separation in flight is called $B\rho$-ΔE-$B\rho$ method [Geissel et al. (1992)], discussed in Section 2.3. An example for the $B\rho$-ΔE-$B\rho$ method with the FRS is illustrated in Figure 4.1. A simulation illustrates the separation of ^{78}Ni ions produced via fragmentation of 500 MeV/u ^{86}Kr projectiles [Geissel et al. (2013)]. All projectile fragments with the same A/Z ($\approx$78/28) are selected with the first half of the FRS before they penetrate the wedge-shaped degrader. The energy degrader is installed in vacuum at the central dispersive focal plane. The different isotopes are spatially separated at the final focal plane of the FRS (*F4*).

In combination with the FRS-IC, especially with the gas-filled Cryogenic Stopping Cell (*CSC*) [Purushothaman et al. (2013); Ranjan et al. (2011); Reiter (2015)], the FRS has to be operated in an energy-bunching mode with a mono-energetic degrader [Geissel et al. (1989)]. The energy bunching provides a substantial compression of the fragment range distribution. A narrow range straggling is required because of the small material density in the CSC. The goal is to enable an efficient stopping of the selected fragments in the CSC. A variable, homogeneous degrader in

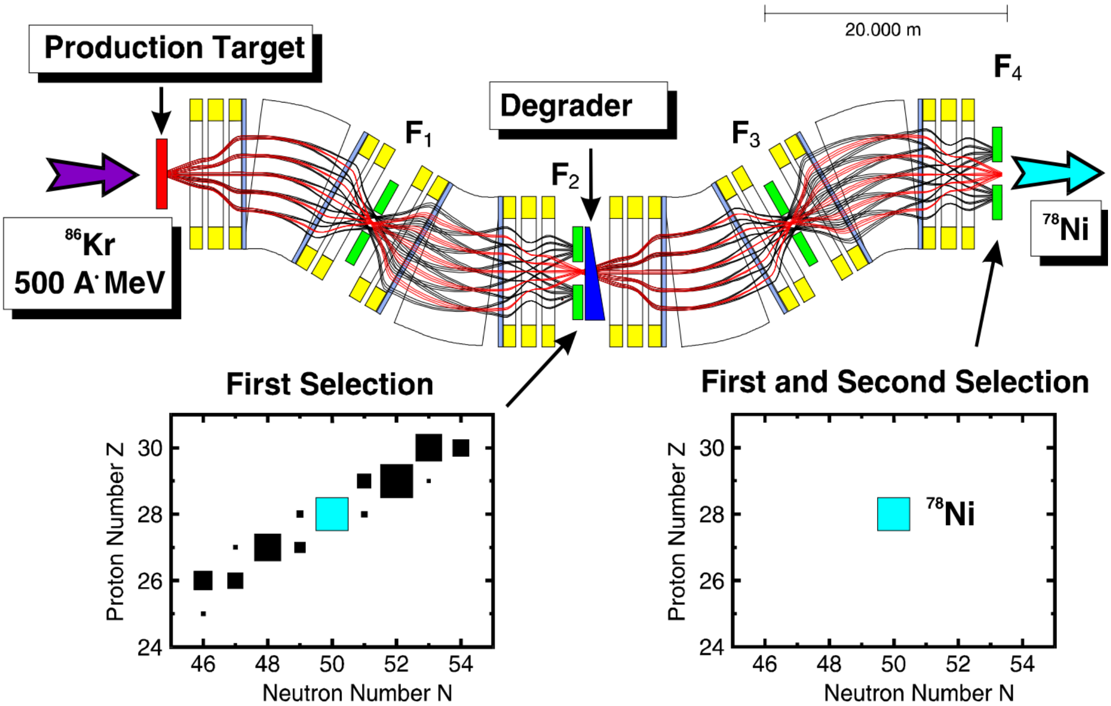

Figure 4.1.: Simulated separation of ^{78}Ni ions in the FRS via the Bρ-ΔE-Bρ method [Geissel et al. (1992, 2013)]. The calculations of the ion-optical elements and the envelopes are shown in the dispersive direction. ^{78}Ni projectile fragments are selected by the position of the slits.

front of the CSC is used to adjust the mean range of the isotope of interest to be placed inside the CSC, in order to stop the maximum number of selected fragments for further analysis. The stopped exotic nuclei are identified and measured with the high-resolution MR-TOF-MS [Dickel (2010); Dickel et al. (2015b); Plaß et al. (2008)].

Detectors, Data Acquisition and Particle Identification

Particle detectors are installed at the different focal planes of the FRS to provide a complete Particle IDentification (*PID*) in flight of the fragments. The detector system includes intensity monitoring and particle tracking, which are needed to measure the production cross sections and the kinematics of the selected fragments in addition to the PID task. The detectors used for the PID in flight are plastic SCIntillators (*SCI*), MUltiple Sampling Ionisation Chambers (*MUSIC*) and Time-Projection Chambers (*TPC*) which record event-by-event the flight time, the energy deposition and the magnetic rigidity, respectively. The determination of the Bρ value requires the knowledge of the field values of the dipole magnets and the applied ion-optical properties, such as the dispersion and magnification. A SEcondary Electron TRAnsmission Monitor (*SEETRAM*) is used to determine the primary-beam intensity at the target.

Both, the spatial separation and the identification in flight with the FRS require an elaborated calibration of the detectors and the magnet fields. The Bρ resolving power of the ion-optical system of the FRS and the internal resolution of the employed particle detectors should provide together an unambiguous identification of the different fragments flying with high velocities through the FRS and its transmission detectors. A major goal is that in an two-dimensional scatter plot, the different nuclides must be well separated. With an absolute identification of one of these resolved distributions, all other fragments are automatically known as well.

The accurate calibration procedure is immense important for most experiments with exotic nuclei, especially for the discovery of new isotopes. Therefore, independent cross checks are employed to verify the achieved particle identification on-line [Farinon (2011)]. A common way is to make use of well-known decay characteristics such as coincident measurements of α-particles or the γ-decay of μs-isomers.

A novel and versatile method has opened up with the MR-TOF-MS at the FRS-IC used for the first time as a mass-tagger [Reiter (2015)]. A detailed discussion of this method and first experimental results are shown in Section 6.1.2.

4.2. FRS Ion Catcher

The FRS-IC consists out of a gas-filled CSC [Ranjan et al. (2011); Reiter (2015)], low energy Radio-Frequency Quadrupole (*RFQ*) based beamline, including the first Diagnostic Unit (*DU1*) [Reiter (2011, 2015)] and its new extension (*DU2*) (Section 4.7), and an MR-TOF-MS [Dickel (2010); Dickel et al. (2015b); Plaß et al. (2008)]. A schematic view is shown in Figure 4.2. It illustrates all important features of the FRS-IC. The FRS-IC is placed at the final focal plane of the FRS. Together with the CSC, the MR-TOF-MS has the ability to perform particle identification and high accuracy mass measurements of short-lived exotic nuclei. The strength of the combination of an MR-TOF-MS together with a CSC has been demonstrated in several commissioning experiments at the FRS. It has been shown that efficient stopping and thermalisation of ions produced in high-energy fission and projectile fragmentation reactions is possible.

4.2.1. Gas-Filled Cryogenic Stopping Cell

In the gas-filled CSC, ions are thermalised and extracted towards an RFQ based beamline. The CSC consists out of two chambers. The inner one contains the stopping gas (helium, neon or argon), the outer one provides the thermal isolation vacuum for the cryogenic operation. In the CSC the ions are stopped due to atomic collisions with the stopping gas and undergo charge-exchange reactions. Depending on their ionization potential they remain as singly-, doubly- or triply-charged ions [Reiter (2015); Wense et al. (2016)].

The ions are guided by a DC ring structure (*DC cage*) towards the back side of the CSC. The DC cage covers with a diameter of 25 cm and a length of 104.5 cm a stopping volume of about 50000 cm^3 [Ranjan et al. (2011)]. In order to prevent the ions form hitting the back side of the CSC, a repelling RF structure combined with a DC gradient towards the exit nozzle is used, called *RF carpet*. The ions are extracted from the CSC by the gas flow through the exit nozzle. A survival and extraction efficiency of about 80 % was measured independent of the element. The areal density of the helium gas in the CSC was up to 5.6 mg/cm^2. Depending on the range distribution of the stopped fragments, a total efficiency for stopping, survival and extraction of about 20 % was achieved. Additionally, a mean extraction time from the CSC with helium gas was measured for ^{221}Ac to be 23.9 ms [Purushothaman et al. (2013)]. This short extraction time makes short-lived ions in the ms region available for mass measurements at the FRS-IC. An α-source of ^{223}Ra ions is mounted inside of the CSC. The recoiling daughter ions can be used for commissioning, calibrating and monitoring of the ion extraction and transport efficiency. After the experiments in 2014 the ^{223}Ra ions source was replaced by the longer-lived α-emitter ^{228}Th [Rink (2017)].

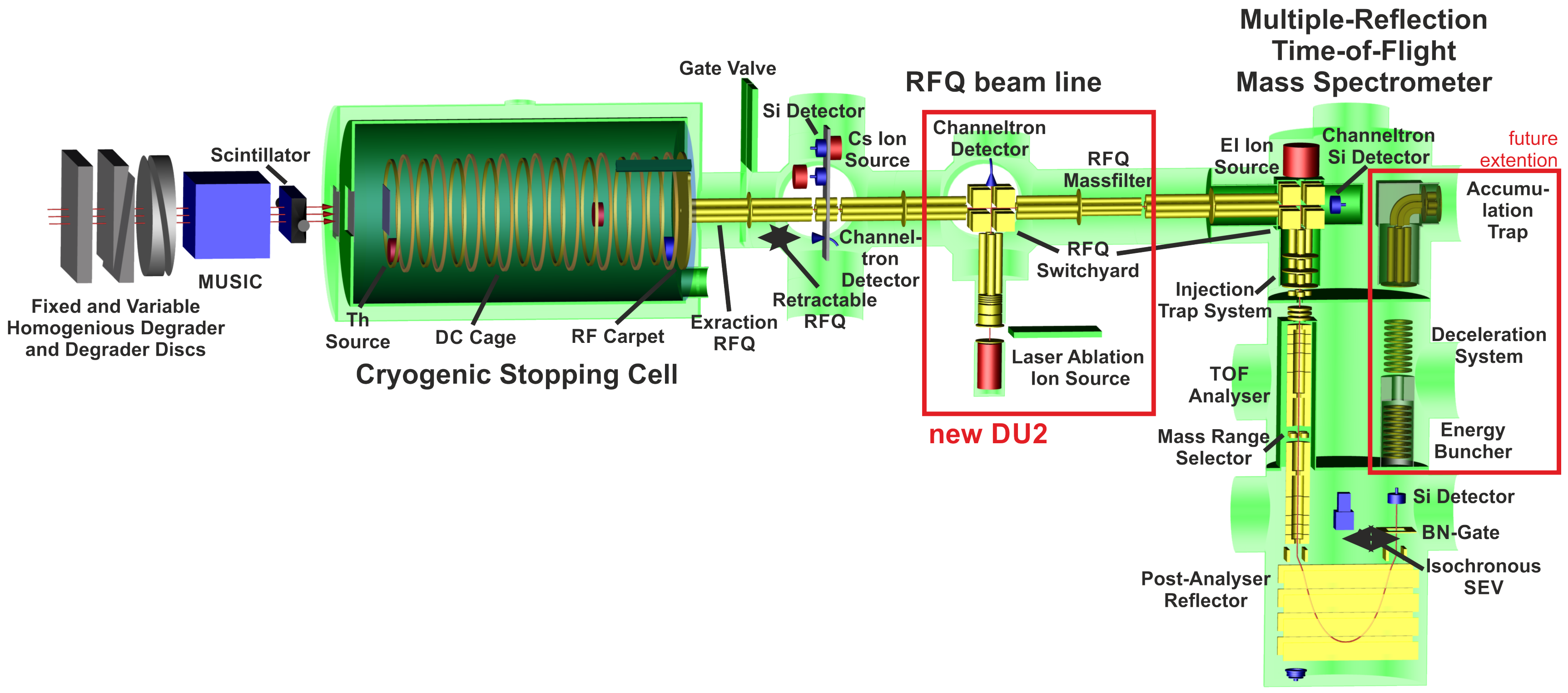

Figure 4.2.: Schematic view of the FRS Ion Catcher with the CSC, the upgraded RFQ based beamline (*DU2*), including diagnostics tools, laser ablation ion source, a dedicated RFQ mass filter, and the MR-TOF-MS (from the left to the right)

4.2.2. RFQ Based Beamline

The CSC and the MR-TOF-MS are connected via an RFQ based beamline through the first Diagnostics Unit (*DU1*) and an RFQ based Switch Yard (*SY*). DU1 is an important diagnostics tool for the CSC because it identifies and quantifies the ions extracted. DU1 supports and verifies the effective operation of the CSC. The first RFQ after the CSC was used as a mass filter in order to restrict the transported mass range [Miskun (2015)].

The DU1 consists of three segments. The first and the last are resistive RFQs which guide and transport the ions by a linear drag field. The middle segment consists of two movable sleds which include two identical silicon surface barrier detectors (Ortec Ultra BU-016-150-100 bakeable). In front of surface barrier detectors a negatively biased aluminium foil is mounted. Furthermore a channeltron detector (Photonis 5901 Magnum Electron Multiplier), a thermal caesium ion source and a transport RFQ are installed. The detectors and one RFQ segment are mounted on a sled which is movable perpendicular to the beamline axis. This allows to guide the ions either towards the MR-TOF-MS or to one of the detectors. The sleds also allow to open up space for closing a gate valve in order to separate the vacuum systems of the CSC and the MR-TOF-MS. The thermal caesium ion source is used to optimize the transport of the down-stream beamline towards the MR-TOF-MS. This enables to commission the MR-TOF-MS independently of the operation of the CSC. The multiple RFQ system opens the possibility to use the transition from one to another RFQ for Collision-Induced Dissociation (*CID*). This can be used in order to break up molecules and strongly improve the cleanliness of the beams delivered to the MR-TOF-MS [Greiner (2017)].

Differential pumping is an important task of the beamline between the high pressure CSC and the MR-TOF-MS, which requires high-vacuum conditions in the analyser. The vacuum chamber of the DU1 is designed in a way to provide space for three turbo-molecular pumps, with a total pumping speed up to 4000 l/s, which are used to pump the extraction region behind the CSC.

The last part of the RFQ beamline, on the top part of the MR-TOF-MS, includes an RFQ based SY. The gas-filled SY is a novel design and was developed and implemented at the II. Physical Institute in Gießen [Greiner (2013); Plaß et al. (2015)]. The RFQ SY can be thought of six gas-filled RFQs deflecting from the central point of the SY along three perpendicular axes. The rectangular tripod electrodes with a cubic cross section are produced from a resistive carbon-filled plastic. An RF voltage is applied in a way that opposite lying electrodes have always the same phase. Additionally, DC voltages are applied to the electrodes in order to guide the ions through the SY. Depending on the applied DC voltages the SY allows to merge and split up beams to different directions. It can also be used as an RFQ-based 90° bender. It is possible to change the applied DC voltages to operate the SY in a pulsed fashion and to change the mode of ion transport within one millisecond.

A combination of a thermal earth-alkaline ion source and an electron impact ion source is mounted on the top of the SY. This allows to have calibrants available over a broad mass range [Ebert (2016)], using different gases such as SF_6, Xe or C_3F_8. The calibrant ions and the ions stopped in the CSC can be merged in the SY. However, due to their different directions they have a slightly different phase space afterwards. Ions produced in the electron impact source were used in the experiments described below, to determine the calibration parameters.

4.2.3. MR-TOF-MS

The ions enter the MR-TOF-MS [Dickel (2010); Dickel et al. (2015b); Plaß et al. (2008)] from top via the RFQ beamline. Afterwards, they are guided through a multiple trap-system towards the analyser. The analyser is followed by the post-analyser reflector and the detector sled. As shown in Figure 4.3, the MR-TOF-MS can be operated in three different modi:

- Time-Focus Shift (*TFS*) mode
- Mass measurement mode
- Isobar/isomer separation mode

In the trap system the ions are accumulated, cooled and bunched before they reach the analyser. The analyser is a planar four electrode design, published in [Yavor et al. (2015)], with the main drift tube on ground potential. Each side acts as an electro-statical mirror. The endcaps of both mirrors of the analyser are pulsed for injection and ejection.

The TOF-spectrum can represent ions with different number of turns, depending on the mass-to-charge ratio difference. This can be controlled by selecting only a certain mass window. Ions outside of this window will be deflected. This is done by the Mass Range Selector (*MRS*). The MRS is a pulsed electrical quadrupolar deflector in the centre of the analyser. During a measurement this can be used to suppress contamination from different mass regions.

After the ions are released from the analyse, they pass through the Post-Analyser Reflector (*PAR*) [Dickel et al. (2017); Yavor et al. (2015)]. In the PAR the intermediate energy-time focus inside of the analyser is shifted to the position of the detector plane and a final tuning of the focus can be done.

4.2.4. Detector and Data Acquisition System

The detectors are mounted on a one-dimensional movable detector sled. It gives the possibility to change between different detectors and MR-TOF-MS modes (see above) in a few minutes. At the detector sled three slots for detectors are available, see Figure 4.4.

For the TFS mode and the mass measurement mode an isochronous Secondary Electron Multiplier (*SEV*) (ETP MagneTOF DM 167 from SGE Analytical Science Pty Ltd.) is used on the right-hand side of the detector sled. This is a secondary electron multiplier with an isochronous electron transport from the conversion plate to the first dynode. The isochronous condition is provided by crossed electric and magnetic fields. This detector offers a signal width of less than 0.5 ns and a detection efficiency of nominally 80%.

For the mass separator mode, the middle slot is equipped with a Bradbury-Nielson ion Gate (*BNG*) [Bradbury and Nielsen (1936)], which is a fast switching electrical ion gate. The BNG is followed by a silicon surface barrier detector (Ortec Ultra BU-016-150-100 bake-able). The silicon detector was mounted on top of a mounting structure which provided space for two Micro-Channel Plate (*MCP*) detectors. When the ions pass through the BNG, it can be pulsed in a way that only the ion of interest can pass whereas the other species are deflected and removed from the selected beam.

In addition, a silicon detector of the same kind as the one mounted on top of the BNG is mounted on the left slot of the detector sled. This one allows to determine the efficiency with ions from the α-source.

The signal from the isochronous SEV detector were amplified by a factor of ten and digitalised with a Time-to-Digital Converter (*TDC*). Two different TDCs were used in the experiments: the Ortec Model 9353 and the Fast ComTec MC6SA. The data evaluated in this work were taken with the TDC from Ortec. The data were handled by the MAc software [Bergmann (2015, 2019); Pikhtelev (2014)]. Additionally, the data acquisition with the Fast ComTec has been included in the standard FRS DAQ.

The data in MAc are taken in histogram-mode with a TOF binning of 1.6 ns with a resolution in measurement time of 1 to 10 s. The software MAc provides several advantages, because it is specifically developed for the data acquisition of MR-TOF-MS data. In the software MAc,

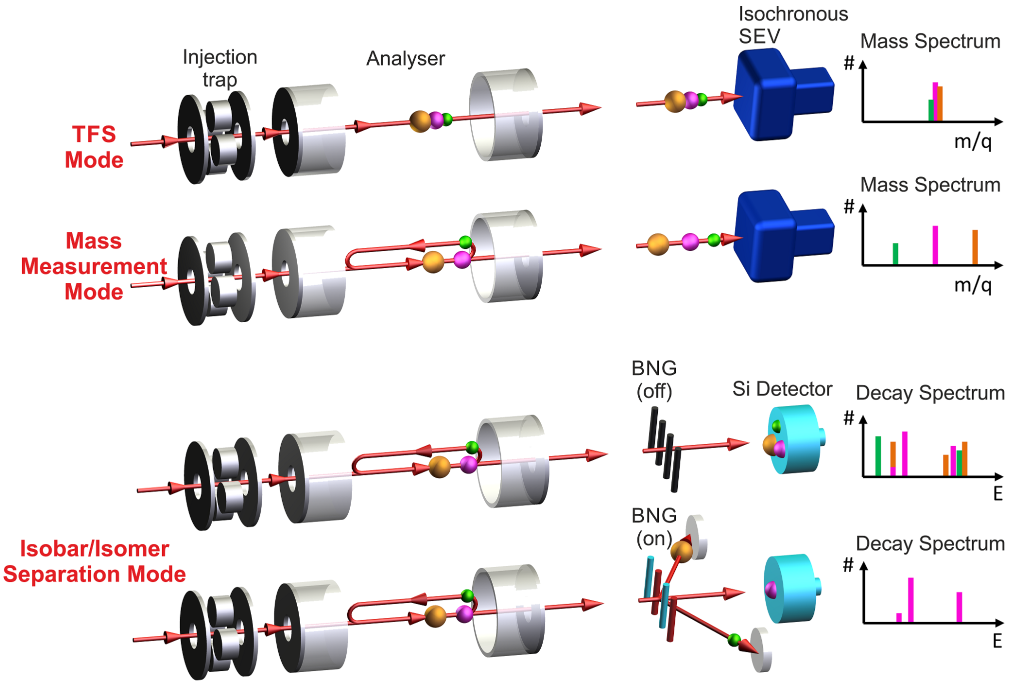

Figure 4.3.: The different operation modes of the MR-TOF-MS are the Time-Focus Shift (*TFS*) mode, the mass measurement mode and the isobar/isomer separation mode with the Bradbury-Nielson ion Gate (*BNG*) on and off. In the TFS mode the ions pass the analyser only once, the intermediate energy-time focus inside of the analyser is transformed to the position of the detector plane. A broad-band mass-to-charge spectrum can be detected in this mode. In the mass measurement mode, the ions are travelling an arbitrary number of isochronous turns in the analyser. This results in an extended difference in TOF of the stored ion species and is the base for high resolution mass spectrometry. In the isobar/isomer separation mode with a BNG the difference in TOF of the different ion species is converted to a spatial separation. Currently, the ions are detected behind the BNG by a silicon detector.

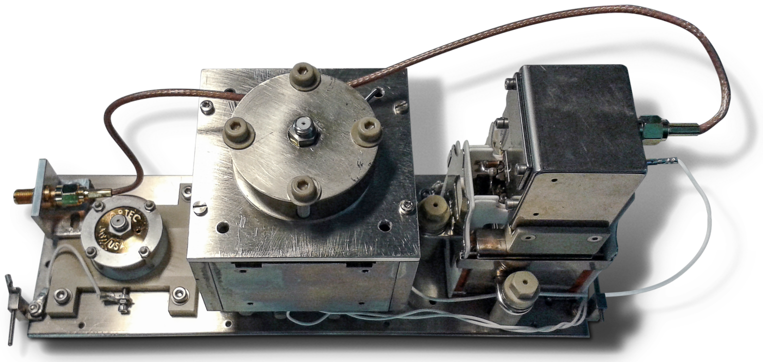

Figure 4.4.: Different detectors required for the different MR-TOF-MS operating modes are mounted on a "sled". The left slot is used for a Si-detector. On the central position the Bradbury-Nielson ion Gate (*BNG*) is mounted with a Si-detector on top. The right-hand side detector slot is used for an isochronous secondary electron multiplier (ETP MagneTOF DM 167 from SGE Analytical Science Pty Ltd.).

major parts of the mass analysis are implemented. It provides e.g. a control of the trigger system and features for calibration, data displaying and export. The data are exported in units of mass-to-charge ratio in form of list mode files [Bergmann (2019)].

4.3. Isobar Separation

An MR-TOF-MS can not only be used as a mass spectrometer but also as a mass separator. In order to use an MR-TOF-MS as a mass separator the separation in time at the time-focus has to be converted in a spatial separation. This can be achieved with a fast switching ion gate such as the BNG at the FRS-IC. The basic principle with and without a deflecting voltage at the BNG is shown in Figure 4.3. Isobar separation has been demonstrated by separating carbon monoxide or nitrogen ions by [Dickel (2010); Plaß et al. (2008)], showing the capability of the combination of an MR-TOF-MS and a BNG.

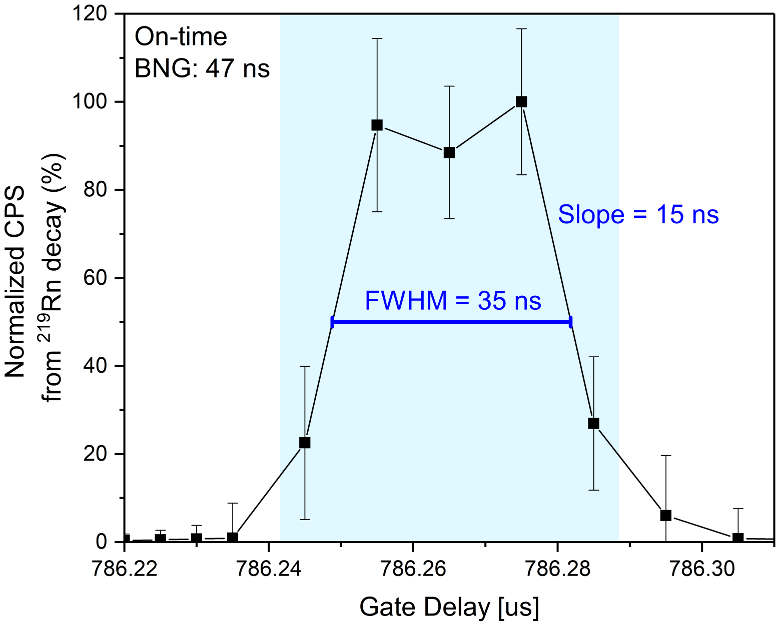

Figure 4.5.: Transmission of spatially separated ^{219}Rn ions from the ^{223}Ra-source in the CSC using the BNG. The delay of the BNG was scanned, in this way the opening time of the gate was moved over the ^{219}Rn peak. From this measurement the FWHM and the slope of the BNG were determined. For the standard operation of the MR-TOF-MS of 50 Hz corresponding to a time-of-flight of 20 ms this implies a resolving power of 285000 if one has to cut on both sides of the ion of interest, and of 650000 if one considers cutting with the slope.

In this work the performance of the MR-TOF-MS as a high-resolution mass separator has been investigated and characterized with α-emitting ions from a ^{223}Ra-source detected behind the BNG. Special electronics for the BNG has been developed to provide the fast switching of the BMG [Ayet San Andrés (2018)]. The transmission of the α-decaying ^{219}Rn was measured while scanning the gate delay of the BNG and with this moving the gate over the ^{219}Rn peak, which has by itself a FWHM of about 10 ns. The opening time of the BNG was set to its minimum of 47 ns. This resulted in a measured FWHM of 35 ns and a slope of 15 ns. For the standard operation of the MR-TOF-MS of 50 Hz corresponding to a time-of-flight of 20 ms this implies a resolving power of 285000 if one has to cut on both sides of the ion of interest, and of 650000 if one considers cutting with the slope. This means that peaks, which are resolved in the mass spectrum can also be separated by the BNG. The result of the measurement with ^{219}Rn is shown in Figure 4.5. With the BNG a suppression of at least four orders of magnitude can be achieved.

This method was applied to exotic nuclei for separation of the ground and the isomeric state, in order to produce a pure isomeric beam (Section 6.5.2). From the mass separation with high resolving power of short lived exotic nuclei new possibilities arise, e.g. to perform mass selective decay spectroscopy. A first mass-selected half-life measurement of ^{215}Po (half-life 1.78 ms) was performed at the FRS-IC [Rink (2017)].

4.4. Experiment with 1 GeV/u Uranium Fragments

In the experiment S411 at GSI in 2014 a 1 GeV/u ^{238}U beam was provided from the heavy-ion synchrotron SIS-18 with an intensity of up to $7 \cdot 10^8$ ions per spill (measured with a SEETRAM) with a set spill length of 2 s. The primary beam was focused on two beryllium targets with an area density of 1.629 g/cm^2 and 6.333 g/cm^2 for projectile fragmentation and fission, respectively. Both targets had a niobium backing of 0.233 g/cm^2 providing better ionisation of the fragments. The fully ionised fragments were separated in-flight in the FRS. Together with a wedge shaped mono energetic aluminium degrader (degrader discs set to 10 mrad) with an areal density of 4.063 g/cm^2 at the central focal plane of the FRS the ions were energy-bunched.

A event-by-event PID in-flight was performed in the second half of the FRS. At the mid focal plane the degrader system was mounted behind a set of slits in x and y direction. The degrader system was surrounded by two SCIs. The last SCI was followed by two TPCs. After the fourth dipole magnet of the FRS a TPC was placed and followed by two MUSICs and again a TPC. With a slit in x direction the isotope of interest could be selected after the second TPC. Afterwards a SCI provided the number of selected ions. After passing the SCI the ions were slowed down in a homogeneous degrader with variable thickness at the final focus of the ion optics of the FRS. As last detector in front of the CSC the ions passed a third MUSIC, which is used to measure the amount of fragmentation in the homogeneous degrader, this MUSIC is also used to measure the stopping range of the fragments before injecting them into the CSC.

The ions were injected in the CSC with an areal density of 3.5 mg/cm^2, corresponding to a temperature of 88° K and pressure of 64 mbar of the helium gas, where they are thermalised. For the measurement of ^{211}Po the areal density was increased to 5.6 mg/cm^2, corresponding to a temperature of 86° K and a pressure of 95 mbar of the helium gas. The ions were ejected into the RFQ beamline and passed on towards the MR-TOF-MS. A photo of the area around the final focus of the FRS during this beam time, with the CSC and the MR-TOF-MS, is shown in Figure 4.6.

4.5. Experiment with 300 MeV/u Uranium Fragments

In the experiment S411 at GSI in 2016 a 300 MeV/u ^{238}U beam was provided from the heavy-ion synchrotron SIS-18 with an intensity of up to $2.5 \cdot 10^8$ ions per spill (measured with a SEETRAM) with a set spill length of 1 s. The primary beam was focused on a beryllium target with an area density of 0.270 g/cm^2 for projectile fragmentation. The primary beam energy was limited, caused by constraints from the UNILAC and the SIS-18. Due to this, beam conditions as expected at the LEB of FAIR could be used for experiments. The experiments under these conditions were a test run, performed especially considering the aspect of the possibilities of PID at the LEB. This is discussed in detail in Section 6.1.2.

At low primary beam energies the ions with $Z \gtrsim 65$ depart the target with different charge

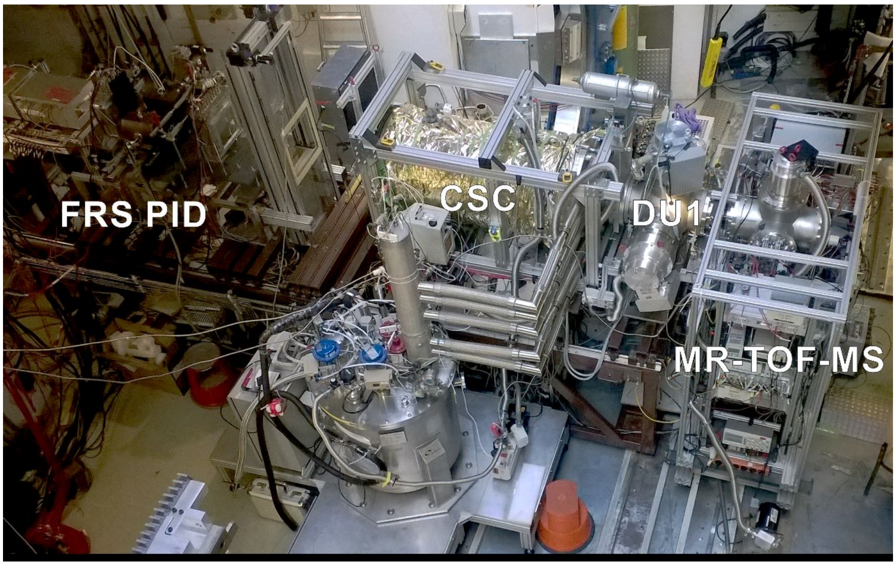

Figure 4.6.: Photo of the FRS Ion Catcher setup during the experiment S411 at GSI in 2014. From the left side to the right side: last part of the FRS PID (not all are mounted), CSC, RFQ beamline (*DU1*) and MR-TOF-MS. In-front of the CSC is the cryostat, providing the cryogenic cooling for the CSC.

states. This makes an unambiguous PID difficult to impossible for the highest Z. The particle identification under this challenging conditions was done using the FRS-IC, see Section 6.1.2.

Due to the low primary beam energy the beamline components where chosen in such a way, that the beam had to pass a minimum amount of matter. At the mid focal plane a set of slits providing a cutting in x and y direction was followed by a SCI and the degrader system. From the degrader system only the discs were used and were set to 2 mrad. The pair of discs corresponds for the centred beam to an area density of 737.1 mg/cm^2. No further detectors apart from the SCI were mounted due to the low energy of the beam. After the fourth dipol of the FRS a TPC was placed the same way as in the experiment from 2014. In 2016 for the experiments with uranium fragments the TPC was followed by a gas degrader [Purushothaman et al. (2017)] and again by a TPC. After the second TPC a slit in x direction and a SCI was mounted. After the SCI the ions were slowed down by a homogeneous degrader with variable thickness at the final focus of the ion optics of the FRS. As the last detector in front of the CSC the ions passed a MUSIC.

Afterwards the ions were injected in the CSC with an areal density of 3.8 mg/cm^2, corresponding to a temperature of 99° K and a pressure of 75 mbar of the helium gas, where they were thermalised, ejected in the RFQ based beamline and passed on towards the MR-TOF-MS.

4.6. Experiment with 600 MeV/u Xenon Fragments

In the experiment S411 in 2016 a 600 MeV/u ^{124}Xe beam was provided from the SIS-18 with an intensity of up to $1 \cdot 10^9$ ions per spill (measured with a SEETRAM) with a set spill length of 500 ms. The primary beam was focused on a pure beryllium target with an area density of 1.622 g/cm^2 for projectile fragmentation.

As for the uranium fragments with low primary beam energies the ions emerged out of the target with different charge states and an unambiguous PID was difficult. Still an event-by-event particle identification was done in the second half of the FRS using the standard detectors.

The setup at the mid focal plane was identical with the one used in the experiment S411 with the 300 MeV/u ^{238}U fragments. For the xenon fragments the degrader discs had an angle of 9 mrad. After the fourth dipole magnet of the FRS a TPC was placed. For the experiments with ^{124}Xe the TPC was followed by two test detector setups, one for tests with a GEM-TPC [Garcia et al. (2017)] and one with a MUSIC. Afterwards a TPC, a MUSIC and a slit in x direction were mounted. The silt was followed again by a SCI providing the number of selected ions. After the SCI the ions were slowed down in a homogeneous degrader with variable thickness at the final focus of the ion optics of the FRS. As the last detector in front of the CSC the ions again passed a MUSIC. Afterwards the ions were injected in the CSC with an areal density of 3.8 mg/cm^2, corresponding to a temperature of 99° K and a pressure of 75 mbar of the helium gas, where they were thermalised, ejected in the RFQ beamline and passed on towards the MR-TOF-MS.

4.7. New Diagnostics Unit 2

4.7.1. Motivation

In an MR-TOF-MS with a closed path lighter ions overtake heavier species, after a certain number of turns. This results in a more complex mass spectrum, caused by an overlay of several mass spectra of different turn numbers. The relative mass-to-charge window $\frac{\Delta(m/q)}{(m/q)}$ depending on the turn number N_{IT} [Yavor et al. (2015)] must be for two ion species with the same N_{IT} smaller than

$$\frac{\Delta(m/q)}{(m/q)} = \left(\frac{N_{IT} + \lambda_{inj}}{N_a + \lambda_{inj} - (1 - \lambda_{mir})}\right)^2 - 1 \,, \tag{4.1}$$

with λ_{inj}, which is the fraction of TOF from the ejection from the injection trap until the exit reflector, and λ_{mir}, which is the TOF inside the pulsed region of one mirror over the TOF of an isochronous turn. A more detailed derivation is given in Section A.2.

In Figure 4.7 the mass-to-charge window $\Delta(m/q)$ for different masses of singly-charged ions is shown depending on the turn number with $\lambda_{inj} = 1$ and $(1 - \lambda_{mir}) = 0.83$, the parameter values are taken from [Yavor et al. (2015)]. The mass-to-charge window decreases with higher turn number, which results in a higher resolving power. In the case that the mass-to-charge window is smaller than one and it is required that the ion of interest and the calibrant have the same turn number, it is necessary to have an isobar for calibration. For a mass of about 100 u, this limit is reached, for singly-charged ions, at about 200 turns. This corresponds to a mass resolving power of about 300000. Carbon clusters, enriched with ^{13}C, are suited well for the calibration of MR-TOF-MS, as well given the above described restrictions, since this kind of molecule can cover all potential mass lines over a broad mass range [Hornung (2013a); Wang (2006)]. They can be produced in laser ablation.

In order to provide those carbon clusters for the use as calibrants in an MR-TOF-MS, certain requirements have to be fulfilled

- The production cycle and with this the laser frequency should suite the needs of the MR-TOF-MS (cycle frequency ~100 Hz).
- A long term stable operation (~weeks) has to be ensured at the highest repetition rate, considering target requirements, laser spot size and ion optics.
- An option to select only the mass unit considered for the calibration, in front of the MR-TOF-MS, has to be available (mass filter).

These requirements on a new calibration source for the MR-TOF-MS at the FRS-IC can be fulfilled by a Laser Ablation Carbon Cluster Ion source (*LACCI*), which will be part of the extension of the RFQ beamline (*DU2*). A particular design was developed for this purpose, allowing easy maintenance and reliable operation.

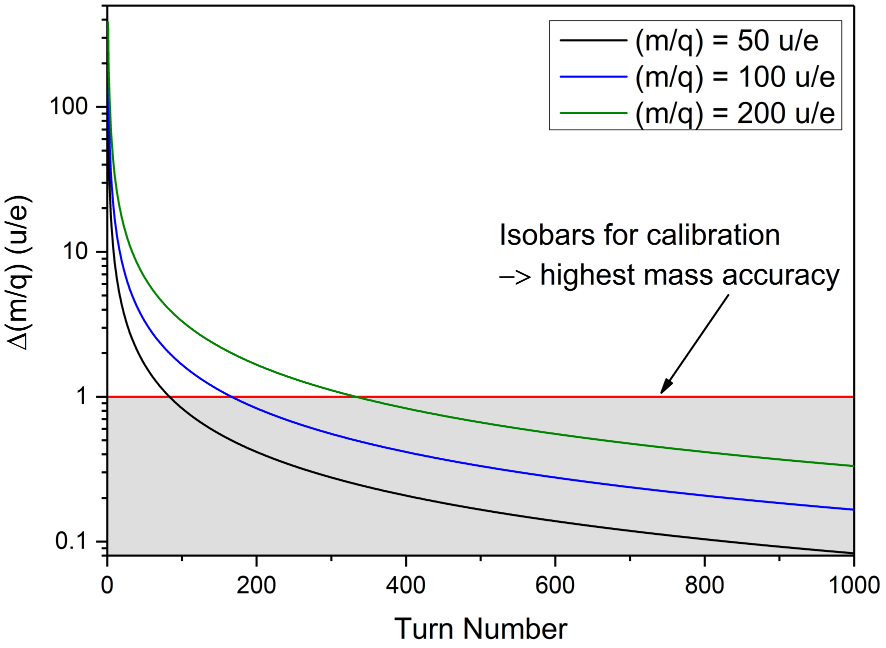

Figure 4.7.: Mass-to-charge window $\Delta(m/q)$ in units of u for different singly-charged masses (50 u, 100 u and 200 u) depending on the turn number N_{IT} with $\lambda_{inj} = 1$ and $(1 - \lambda_{mir}) = 0.83$. The maximum mass-to-charge window decreases with higher turn number, which results in a higher resolving power. In the case that the mass-to-charge window is smaller than one and it is required that the ion of interest and the calibrant have the same turn number, it is necessary to have an isobar for calibration.

The DU2 should fulfil further tasks as an improved differential pumping between the CSC and the MR-TOF-MS. In addition the new parts of the RFQ beamline should provide an improved CID, by providing several dissociation steps.

4.7.2. Production of Ions in Laser Ablation

During the last 20 years laser ablation carbon cluster ion sources have been installed in several nuclear physics laboratories. Laser ablation is a very complex mechanism and varies in its process strongly, depending on the given conditions. The literature considering this topic was collected and discussed emphasising the conditions in LACCI in [Gröf (2017); Hornung (2013a)].

The first laser ablation carbon cluster ion source, explicitly used for the calibration of mass measurements of nuclei, was developed and commissioned at ISOLDE/CERN [Blaum et al. (2002); Scheidenberger et al. (2002)]. It had a simple setup with a fixed target where the ionised clusters were directly extracted into the first Penning trap. Due to this the source suffered from transmission losses and could not provide long term stable extraction of calibration ions.

In the following years the development focused on the long term stability and lead to one dimensional movable solutions. A laser ablation carbon cluster ion source with fulleren targets and a one dimensional movement in forward and backward directions was developed at the II. Physical Institute in Gießen [Wang (2006)]. Here the ions were directly guided into an RFQ. Due to the constant motion it was already possible to achieve, at a repetition rate of 10 Hz, a decrease in count rate by only a factor of two.

At SHIPTRAP the one dimensional motion was implemented in form of a rotating target [Chaudhuri et al. (2007)]. Ion sources based on eccentrical rotation with glassy carbon targets are nowadays widely spread for calibration purposes of Penning traps [Elomaa et al. (2008); Izzo et al. (2016); Lommen (2011); Smorra et al. (2009)]. They are used in different laser and ion optical configurations. As calibration source for a Penning trap they are normally operated at a repetition rate of about 1 Hz, synchronised to the repetition rate of the trap.

Carbon clusters produced in laser ablation were used for systematic investigations of the mass accuracy of Penning traps [Elomaa et al. (2008); Smorra et al. (2009)]. Mass values of heavy nuclei calibrated with carbon clusters can be used as reliable anchor points due to their direct link to the mass standard ^{12}C [Eibach et al. (2016); Ketelaer et al. (2011)]. At SHIPTRAP carbon clusters were used in parallel to rubidium as calibrants in an online mass measurement [Chaudhuri et al. (2007)]. Even after years of operation of the systems, they are not often used as calibrant ion sources, because a stable operation over long times (≈ days/weeks) is not trivial. Several conceptual improvements have been implemented in the design of the system shown here, which will allow a stable operation of the system over days and weeks even at orders of magnitude higher repetition rates.

In addition laser ablation ion sources are used to produce stable ions of scientific interest, e.g. indium, cadmium and palladium isotopes from thin foils for TRIGA-TRAP and LEBIT [Gamage et al. (2016); Smorra et al. (2012)].

4.7.3. Experimental Setup

The extension of the RFQ beamline DU2 consists of LACCI, a dedicated electrostatic ion optics, a Recapturing Unit (*RU*), an RFQ based SY and a mass filter. It will extend the current RFQ beamline between the (*DU1*) and the MR-TOF-MS. A schematic overview, including the main features of the DU2, is shown in Figure 4.8. The entire system is designed in a way to fit together with all required electronics in one frame. This allows to mount the new part of the beamline with a minimal invasion in one piece to the current FRS-IC.

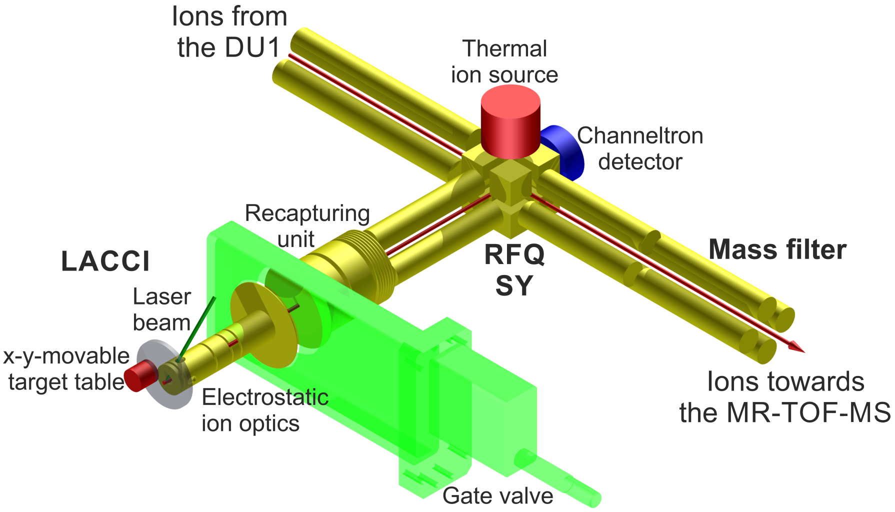

Figure 4.8.: Schematic overview of the extension of the RFQ beamline (*DU2*) consisting of LACCI, a dedicated electrostatic ion optics, a Recapturing Unit (*RU*), an RFQ based Switch Yard (*SY*) and a mass filter. It will extend the current RFQ beamline between the DU1 and the MR-TOF-MS.

LACCI

LACCI consists of a laser setup with a frequency-doubled Nd:YAG laser (TITAN AC 15 MM from IB LASER) and an x-y-movable target table. The Nd:YAG laser provides a polarized light with a wavelength λ of 532 nm and a pulse width of 5 to 10 ns, depending on the electrical current at the diode. The system can be operated at repetition rates that are up to two orders of magnitude higher (up to 100 Hz) compared to existing systems and is thus ideally suited for the needs of the MR-TOF-MS (cycle frequency ∼100 Hz). The laser system with a single target and a first version of the x-y-movable target table was commissioned and characterised in a test setup using an additional MCP based detector placed after the first part of the electrostatic ion optics. A detailed description can be found in [Hornung (2013a)]. The x-y-movable target table was reworked completely after the first commissioning.

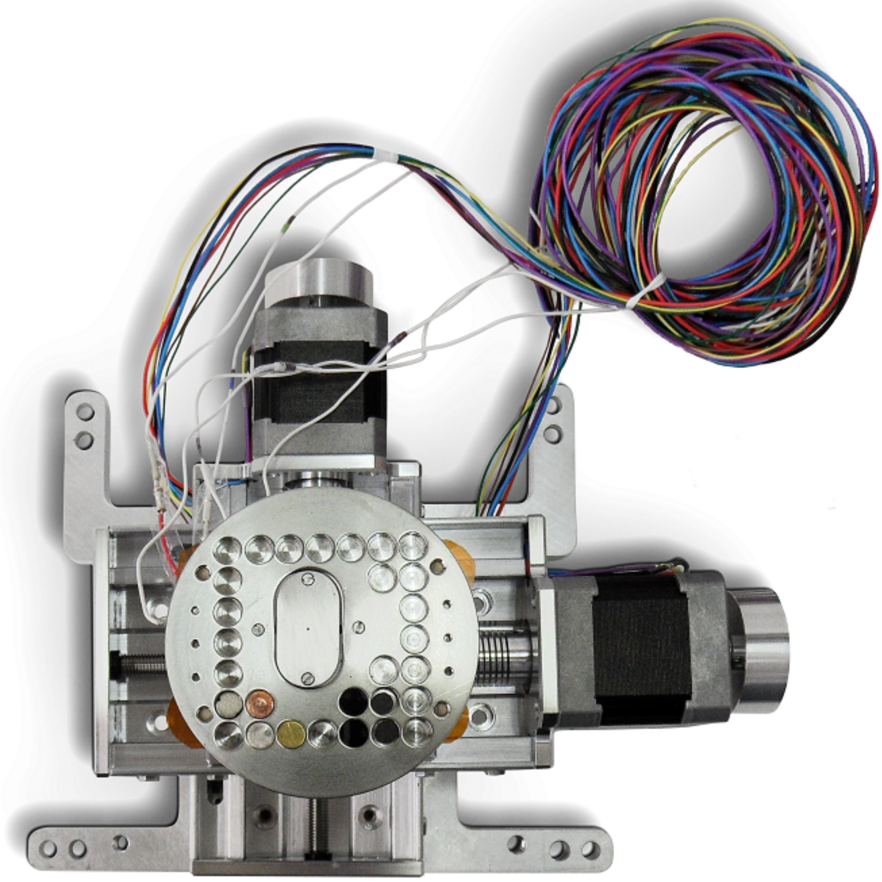

Figure 4.9.: X-y-movable target table at LACCI. Two linear translation states allow to access an area of 25 cm^2 with the laser. The target plate houses 29 target slots and a thermal caesium ion source.

In the future setup the x-y-movable table will be one of the main features of LACCI, since it provides different targets and long-term stable operation. A picture of the x-y-movable target table is shown in Figure 4.9. The target plate of the table has slots for 29 targets of a size up to 6.5 mm in diameter. It is possible to use the whole target surface and to switch fast (∼ s) between different targets due to the x-y-movement. This is a great advantage compared to other laser ablation ion sources, where only a one dimensional movement is implemented.

The table is designed with two commercial linear translation stages (VT-80 from Physik Instrumente (PI)). Each one has a travel range of 50 mm. Due to this an area of 25 cm^2 can be used for the target plate. Inside a backlash free re-circulating ball bearing with a backlash compensated lead screw provide a smooth movement with a uni-directional repeatability of 0.4 μm and a bi-directional repeatability of ± 10 μm. The linear translation states are rated for a usage at a pressure of 10^{-6} mbar. The two step motors of the linear translation stages are controlled via a TMCM-310/SG board from TRINAMIC Motion Control with a dedicated developed software, written by Christian Lotze. The software allows to chose the grid type between a horizontal meander, a vertical meander or a raster in x and y direction with adjustable raster size and speed. A detailed description of the first commissioning of the reworked x-y-movable table and its remote control can be found in [Gröf (2017)].

In order to keep maintenance as easy as possible a dedicated vacuum chamber was designed. It provides the possibility to mount the stack of two linear stages including the target plate in one piece. Its position is defined with alignment pins, due to this a removing and precise repositioning is possible. The vacuum chamber houses the electrostatic ion optics as well which ensures that the relative position of the ion optics and the target plate are aligned to each other. The chamber is designed in a way that there are no cables connected to the opening side. Therefore the x-y-movable target table and the ions optics stay in the same state during opening.

A thermal ion source, which provides caesium ions, is mounted additionally on the target plate. It allows tests of the ion optics and optimization of the beam transport independent of the laser.

Electrostatic Ion Optics

After cluster ions are produced at the target, they pass through an electrostatic ion optical system. With the electrostatic ion optics the ions are extracted from the laser plume and transported, at an energy of about 1 keV, towards the RFQ beamline. Inside the electrostatic part a Pierce electrode, lenses and steeres (four-fold segmented electrodes) are included. The electrostatic beamline ends with a retarding field, followed by a double aperture. The steerer can be operated in a pulsed fashion as an ion gate. In this operation mode it is possible to cut high rate contaminants or unwanted cluster sizes. This reduces the number of ions in the following RFQs and the SY drastically and can prevent problems due to space charge, and thereby make also the weakest produced clusters available with good quality in the downstream beamline.

The electrostatic ion optics from the Pierce electrode until the double aperture was investigated in simulations in SIMION [Hornung (2013b)].

LACCI and the first part of the electrostatic ion optic can be separated vacuum wise from the other parts of the beamline. In addition, these parts of the ion optics are designed in a way to be vented, removed and reassembled in an easy and efficient way. This is important since a higher amount of contaminations of neutral particles from the carbon-clusters is expected from LACCI and therefore cleaning of the ion optics will be an usual maintenance procedure. A bigger spacing between electrodes is part of the design, it increases the robustness. In addition, the targets of LACCI can be easily accessed for changes.

In the RU the ions are slowed down from about 1 keV to a few electron volts before they enter the following RFQ beamline. For this a retarding field is applied. The RU consists out of an einzellens followed by eight equidistant electrodes with a linear potential applied. It can be adjusted to provide the best start conditions for the transport thought the upcoming RFQ beamline.

RFQ Beamline and Switch Yard

In the DU2 the SY, further explained in Section 4.2.2, connects three transport RFQs. The length of the RFQ, which connects the RU with the SY, was investigated in simulations in order to achieve the necessary amount of cooling to support an efficient transport through the 90° bend in the SY [Hornung (2013b)]. The SY is equipped with a channeltron detector and a thermal ion-source for commissioning of the system.

In all RFQs trap segments are implemented at the downstream end, where ions can be accumulated. In combination with a pulsed operation of the SY, this allows to send, pulse-per-pulse, either an bunch of exotic ions (from the CSC) or a calibration ion bunch towards the MR-TOF-MS, while the respective other bunch is accumulated.

Mass Filter

A dedicated mass filter will be added in the context of the extension of the RFQ beamline between the new SY and the SY on top of the MR-TOF-MS. This will open up the possibility to select a certain mass window of interests in-front of the MR-TOF-MS. The advantages of being able to have a mass filter between the CSC and the MR-TOF-MS were shown in previous experiments at the FRS-IC [Miskun (2015)]. There a transport RFQ was used as mass filter. A mass resolving power of about 10 u was reached.

The new dedicated mass filter will follow the design in [Haettner (2011)]. The design includes Brubaker lenses [Brubaker (1968)] and follows earlier investigations considering the rod radius r and the spacing between rods $2 \cdot r_0$. In order to have a perfect quadrupole field all multipole terms in the potential except the quadrupole one are 0. A value for the ratio r/r_0 was estimated to be 1.14511 by optimizing the expansion in such a way that the 12-pole term equals to 0 [Lee-Whiting and Yamazaki (1971)]. This is in agreement with an earlier empirically estimated value of 1.1148 by [Dayton et al. (1954)]. The influence of round rods to the stability diagram was investigated by [Reuben et al. (1996)]. The r/r_0 ratio especially for a mass filter was investigated numerically by [Gibson and Taylor (2001)]. It has been shown that the best performance for a mass filter can be reached with a ratio between 1.12 and 1.13. This ratio will lead to the maximum resolving power of a mass filter. In addition it was shown that a better peak shape with reduced tails can be achieved.

The rod radius r is going to be 8 mm and the field radius r_0 is going to be 7 mm. The chosen values lead to a r/r_0 ratio of 1.143. In general the mass resolving power ΔM of an RFQ mass filter is given in [Austin et al. (1976)] by

$$\Delta M = \frac{4 \cdot 10^9 E_{kin,z}}{f^2 L^2}\,, \tag{4.2}$$

with $E_{kin,z}$ being the kinetic energy of the ions in z-direction in eV, f being the RF frequency and L being the length of the RF mass filter in z-direction. The goal of the design for the mass filter was a mass resolving power of 1 u. In [Haettner (2011)] it was seen that the calculated mass resolving power is about a factor 3 lower than the measured one. Considering a kinetic energy of the ions of 5 eV, a RF frequency of 1.5 MHz and the additional factor, which takes into account the difference between theory and experiment, lead to a length of the mass filter of 20 cm and a final mass resolution of 2/3 u.

The mass filter is surrounded by a shielding grid in order to not disturb the electrical field inside. The effect of fringing fields was estimated from simulation. Here 1 V was applied on the shielding and the field on the quadrupolar axis was calculated. For the chosen ratio $r/r_0 = 1.143$, a value of $1.6E-4$ resulted.

4.7.4. Experimental Results

The setup of the DU2 was commissioned up to the SY [Gröf (2017)], first with ions from the thermal caesium ion source at the x-y-table and in the following with ions produced in laser ablation. For the first part of the commissioning the caesium ion source was used in a pulsed fashion. This allowed to get a first estimate on the TOF of the ions from the x-y-movable target table through the electrostatic ion optics, the RU and the following RFQ until the SY. A TOF of about 45 μs was measured without helium gas in the RFQ system for a mass of 133 u. The TOF path between the target table and the channeltron detector was used during the commissioning to measure the ion content and the size of the carbon clusters produced in the laser ablation.

The setup was further commissioned with carbon clusters produced by laser ablation by LACCI on a glassy carbon target. A TOF and mass spectrum is shown in Figure 4.10. The spectrum shows the expected cluster structure and relative cluster size abundances. For the calibration of the glassy carbon mass spectrum the $^{12}C_5^+$ and $^{12}C_7^+$ cluster were used. This resulted in the following calibration

$$(m/q) = 0.065355 \frac{u}{(\mu s)^2} \cdot (t_{meas} - 1.919 \mu s)^2 \ . \tag{4.3}$$

The x-y-movable target table was recommissioned and characterised. The thermal caesium ion source, which is mounted at the table was used to monitor the movement of the table. The efficiency depending on the source position was measured and its reliability after initialisation of the target table was investigated. The target table showed a high reliability and the expected bi-directional repeatability. A further description of this part of the commissioning can be found in [Gröf (2017)]. The target plate was equipped for the recommissioning with different metals (gold, silver, copper and erbium) and different carbon targets (glassy carbon and fulleren). It is shown that the different targets can be reached and scanned without any interruptions. A run of scanning gold, silver, copper and erbium directly one after another with a repetition rate of 100 Hz is shown in Figure 4.11.

All targets were scanned with the same laser energy of 585 μJ. Due to their different reflectivity and chemical properties, such as melting temperature and ionisation potentials, the count rate differs from target element to target element. In addition the surface of the target and how often it has been scanned before play a roll. In the run in Figure 4.11 all target were scanned first with a horizontal meander and afterwards with a vertical meander. The change can be always seen after half of the measurement time per target by a change in the count rate.

The permanent movement of the target allows to produce a stable count rate over several hours in laser ablation. The long-term stability of LACCI is shown in Figure 4.12 for erbium ions at a laser repetition rate of 100 Hz.

The 2D motion of the movable target is compared to a stationary target and a 1D motion, shown in Figure 4.12. This shows how superior the 2D meander motion is compared to a stationary target and 1D motion. The latter is the established state-of-the-art technique for similar laser ion sources. During the 2D meander motion $4.42 \cdot 10^6$ laser pulses hit the target. If one compares this pulse duration on the target with the usual 1 Hz repetition frequency used in state-of-the-art laser sources for Penning traps, this would lead to a measurement time of about 50 days. In the measurement it was seen that the first layer of the target has different properties compared to the following ones, since it was exposed to its surrounding for a longer time, leading to e.g. oxidation. In order to compare the deterioration of the main target structure in the measurement, the first cycle of motion was not considered and the count rate in Figure 4.12 was normalised afterwards.

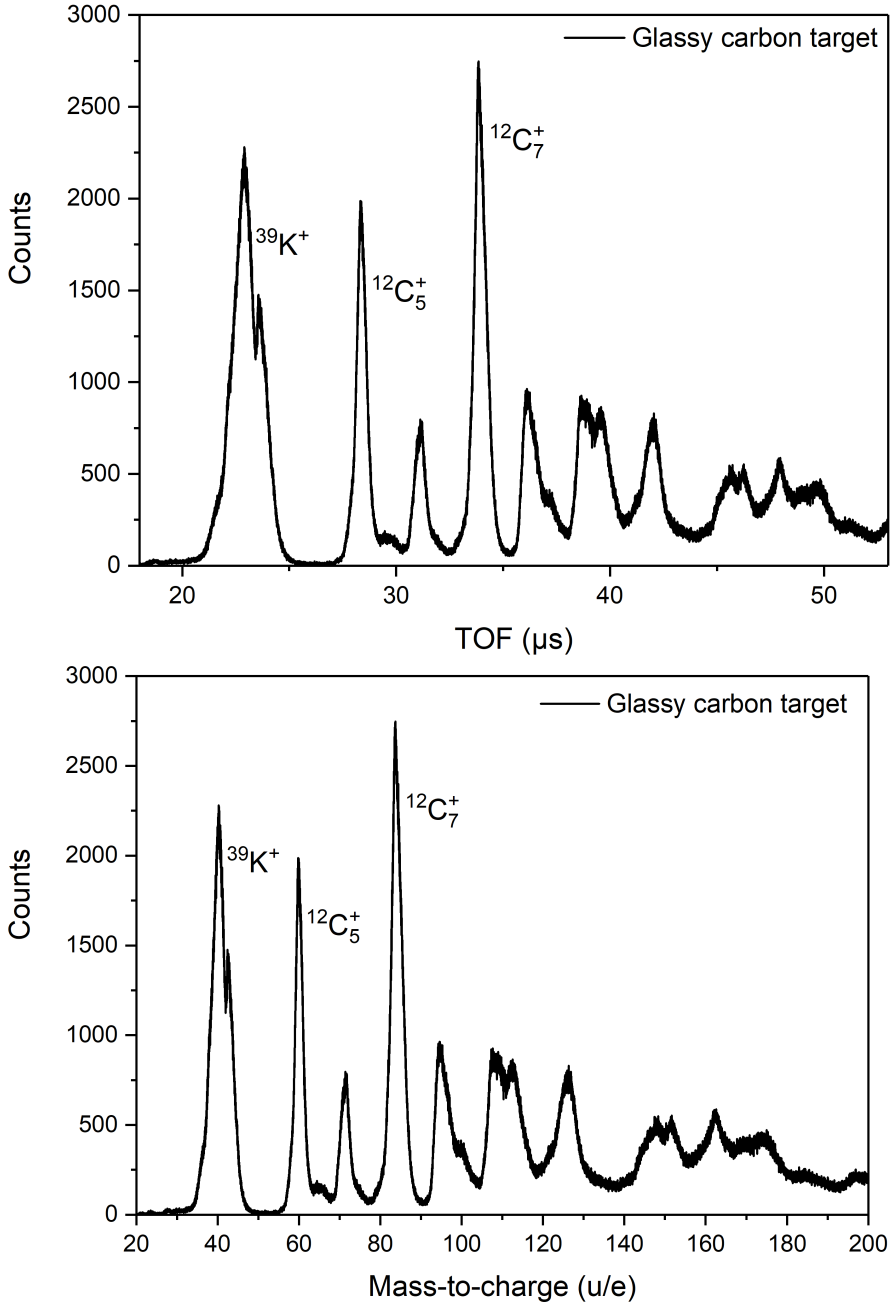

Figure 4.10.: TOF (top) and mass spectrum (bottom) of carbon clusters produced by laser ablation by LACCI on a glassy carbon target, measured with the channeltron detector at the SY. The data acquisition was triggered by the laser signal. The laser was operated at a repetition rate of 100 Hz, supplying an energy on the target of 770 μJ.

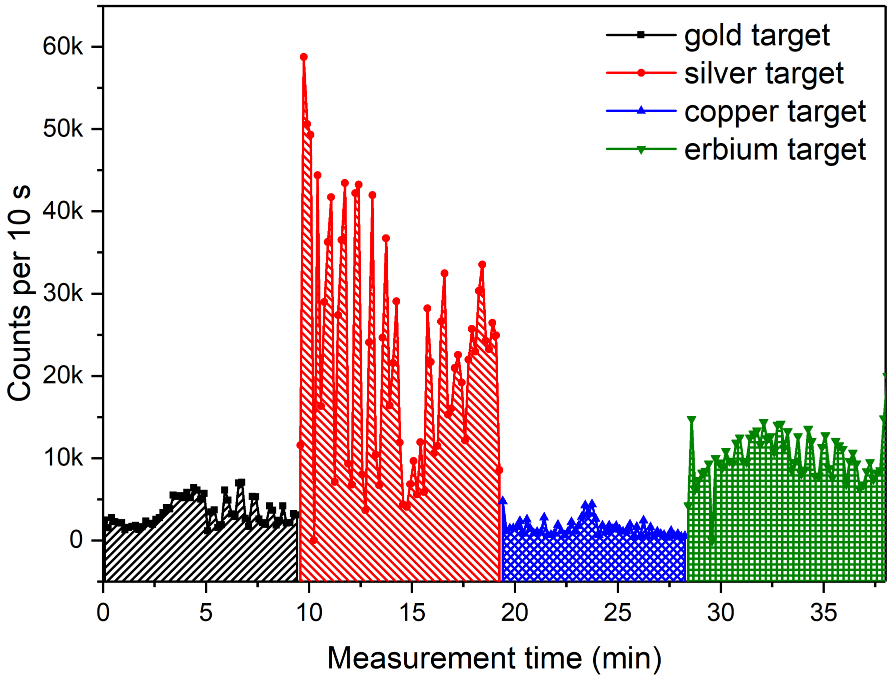

Figure 4.11.: Count rate per 10 s of a run of scanning gold, silver, copper and erbium directly one after another in a meander with a repetition rate of 100 Hz and a laser energy on the target of 585 μJ. The ions were detected with the channeltron detector at the SY.

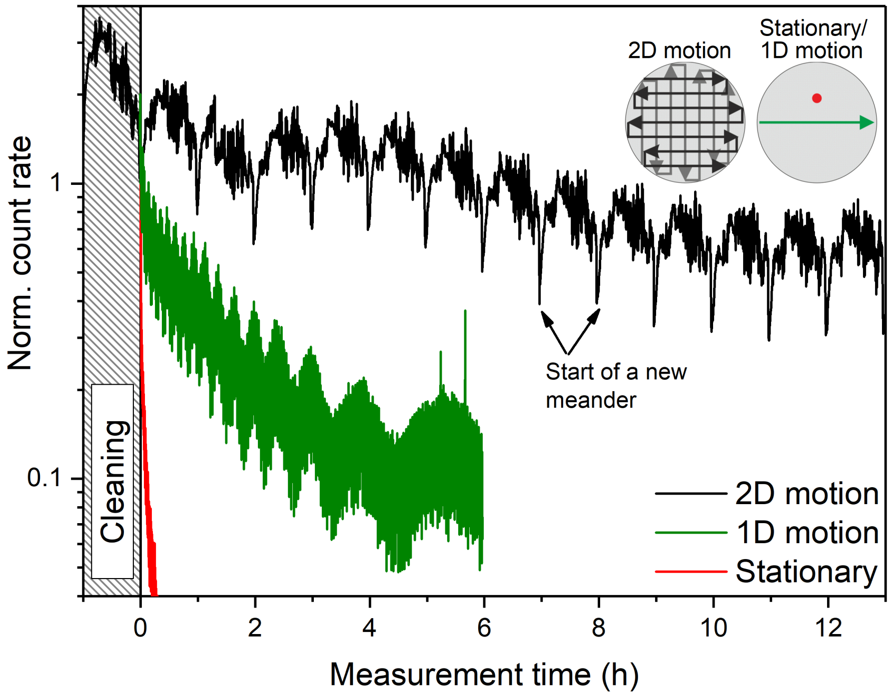

Figure 4.12.: Measurement of the long-term stability of the count rate for erbium ions produced in laser ablation by LACCI with a repetition rate of 100 Hz. The count rate versus time with a 2D motion of the movable target is compared to a stationary target and 1D motion. The latter is the established state-of-the-art technique for similar laser ion sources. The data are normalised to the count rate after cleaning of the target surface, since it was seen that the first target layer has different properties compared to the following layers.

4.7.5. Outlook

In the experiments in 2018 the extension of the RFQ beamline will be an important new part of the FRS-IC. It will lead to an improved performance of the overall system.

The extension of the RFQ beamline will improve differential pumping between the CSC and the MR-TOF-MS. This will enable a higher helium gas pressure in the CSC, while keeping the pressure in the MR-TOF-MS low, to avoid collisional losses during the TOF measurement. A decoupling of the pressure in the CSC and the MR-TOF-MS enables to operate the MR-TOF-MS with optimum performance, even with the highest pressure in the CSC. A higher areal density in the CSC will lead to a higher stopping efficiency, especially for high mass ions. Currently the extraction efficiency for high mass ions is not limited by the repelling force of the RF-carpet but by the pressure in the CSC, limited by the differential pumping between the CSC and the MR-TOF-MS.

Systematic mass dependent studies of the MR-TOF-MS become possible with the carbon cluster ions from LACCI. In addition the system can be prepared and optimized for more regions of different mass, where no other calibrant was previously available. The calibrants produced in LACCI in the DU2 have the advantage, compared to the ions produced in the ion source on top of the MR-TOF-MS SY, that they enter the MR-TOF-MS with the same phase space as ions stopped in the CSC. This will allow to optimize the transport more specific for different mass regions of the ions of interests.

The dedicated mass filter will lead to a higher possible number of ions of interest in the MR-TOF-MS, since unwanted species and molecules will not be transported into the MR-TOF-MS any more. This will result in cleaner mass spectra with less background and therefore to measurements of even more exotic isotopes. The availability of close lying calibrant ions (isobaric in most cases) allows to further increase the mass accuracy of the MR-TOF-MS.

5. Analysis of MR-TOF-MS Data

The mass value and the number of ions are determined from the measured distributions. The data analysis used in this work is based on the developments described in references [Ebert (2016); Jesch (2016)]. Further developments are implemented in this work based on the analysis of a larger data set. Complementary subsets of the data are presented here and in [Ayet San Andrés (2018)].

The data analysis of the present MR-TOF-MS data has specific requirements. It has to be able to cope with very rare nuclei produced with low count rates. The masses of the nuclei and their abundance have to be determined from the measurements. This goal has to be realized even for overlapping distributions with quite different abundances. A schematic mass spectrum is shown in Figure 5.1. It consists of separated peaks with different counts, overlapping peaks with different intensities and distances of their mean values and finally randomly distributed background.

Therefore, the data treatment must include theses different conditions and handle a detailed error analysis.

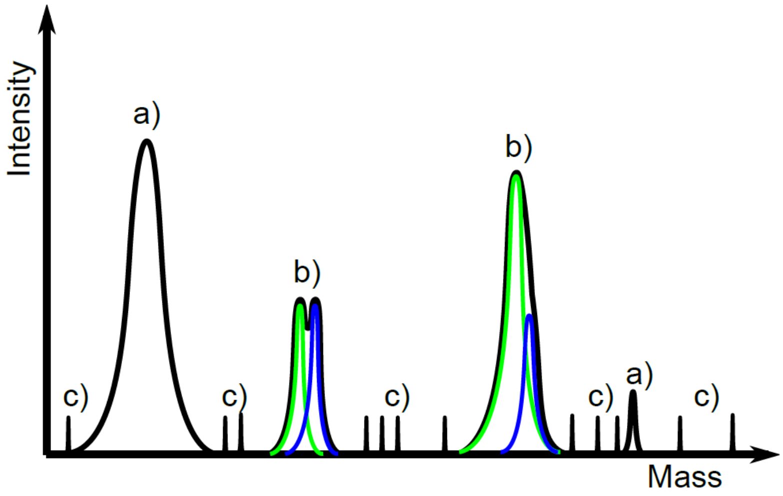

Figure 5.1.: Schematic mass spectrum, taken from [Ebert (2016)]: It consists of separated peaks with different areas (a), overlapping peaks with different intensities and distances between the mean values (b) and randomly distributed background (c).

5.1. Calibration

The conversion from a TOF spectrum to a mass spectrum is in general given via Equation 3.6. In case of an MR-TOF-MS with a closed path the ions can overtake each other depending on their mass-to-charge ratios, see Section 4.7.1. Therefore, one has to consider the different flight paths depending on the number of isochronous turns in the analyser. The flight path s, depending on the number of turns N_{IT} is given by

$$s\left(N_{IT}\right) = s_{TFS} + N_{IT} s_{IT} \, , \tag{5.1}$$

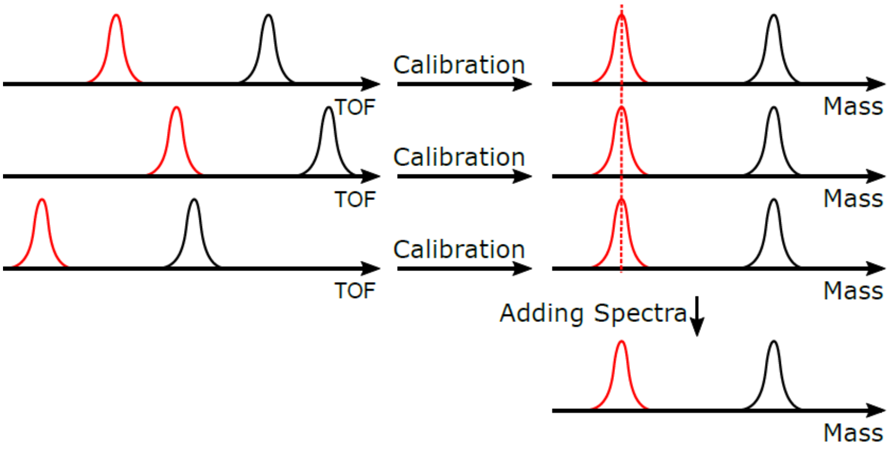

Figure 5.2.: Scheme of the Time Resolved Calibration (*TRC*) taken from [Ebert (2016)]: The distribution of the reference ion in the time and mass spectra is drawn in red color, the ion of interest in black. In the scheme, the TOF spectrum is divided into three duration blocks of the experiment. After the calibration in b the position of the calibrant in all three mass spectra is the same and they are finally added in order to obtain the final mass spectrum.

where s_{TFS} is the flight path in the TFS mode and s_{IT} is the flight path of one isochronous turn. By using Equation 3.6 and replacing the path z with $s\left(N_{IT}\right)$ given in Equation 5.1, the mass-to-charge ratio can be rewritten as

$$\begin{aligned}(m/q)\left(t_{meas}, N_{IT}; c, t_{TFS}, b\right) &= \frac{2U\left(s\right)\left(t_{meas}-t_{TFS}\right)^2}{s_{TFS}^2\left(1+N_{IT}s_a/s_{TFS}\right)^2} \ , \\ &= \frac{c\left(t_{meas}-t_{TFS}\right)^2}{\left(1+N_{IT}b\right)^2} \ ,\end{aligned} \tag{5.2}$$

with the number of turns N_{IT}, the measured TOF t_{meas} and the three calibration parameters c, t_{TFS} and b. t_{TFS} represents a delay given by the electronics, such as cables. It can be considered to be constant as long as the experimental setup is not changed. It should be determined in the TFS mode, in order to get the most accurate estimate of t_{TFS}. The calibration constant c represents the ion path in the TFS mode. The calibration constant b represents the ratio of the path length of one isochronous turn and the TFS path. Equation 5.2 becomes again Equation 3.6 in the case that all ions, including the calibrant ion, undergo the same number of turns, with the single free parameter

$$a = c/\left(1+N_{IT}b\right)^2 \ . \tag{5.3}$$

Therefore, c and b are dependent and one of them can be fixed to an arbitrary value. This allows to use only one calibrant ion in a spectrum, where all ions undergo the same number of turns.

The flight path of one isochronous turn can change over time, depending on the stability of the voltages applied to the analyser and depending on the thermal expansion of the analyser. This causes a change of the ratio between the path length of one isochronous turn and the TFS path and leads to a change in the calibration parameter b. In order to correct the mass spectrum for this, the parameter b is used as a time-dependent variable during the experiment duration t_{exp}. Therefore, the calibration is given by

$$(m/q)\left(t_{meas}, N_{IT}, t_{exp}\right) = \frac{c\left(t_{meas}-t_{TFS}\right)^2}{\left(1+N_{IT}b\left(t_{exp}\right)\right)^2} \ . \tag{5.4}$$

If no corrections for the voltage stabilities or thermal effects over the experiment duration are applied, the time distribution is a broader peak and causes a lower resolving power. In order to

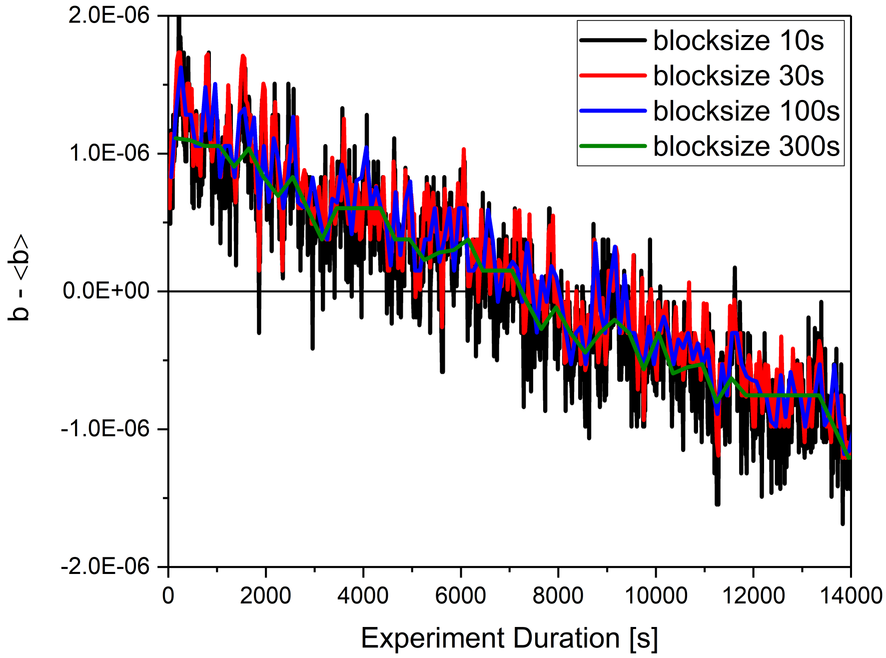

Figure 5.3.: The time dependence of b normalised to the mean value of b is shown over a few hours of experiment duration. The calibrant ion was ^{211}Pb and different block sizes were chosen in the mass measurement of ^{213}Rn ions.

apply the correction, the measurement is divided in blocks of experiment duration, where each block contains its corresponding TOF spectrum. For each of these blocks a separate calibration in b is done which results in one mass spectrum per time block. Afterwards, the mass spectra of all blocks are added up. This technique was already applied to MR-TOF-MS data in references [Ebert (2016); Jesch (2016)] and has presented a large increase in resolving power. The technique is shown schematically in Figure 5.2. In this example, the TOF spectrum is divided in three blocks of experiment duration. The calibrant ion is drawn in red color, the Ion Of Interest (*IOI*) in black. After the calibration of b the position of the calibrant in all three mass spectra is the same and they are finally added in order to obtain the final mass spectrum. This procedure is called in the following Time Resolved Calibration (*TRC*) and is included in the Mass Acquisition software *MAc* [Bergmann (2019)]. The time dependency of the parameter b over a few hours is shown in Figure 5.3. In this measurement the calibrant ion was ^{211}Pb and the reference fragment ^{213}Rn. In this case, the calibrant was continuously provided over the full experiment duration with a stable and sufficient rate.

The size of blocks of experiment duration used in the TRC has to be optimized. If the block size is chosen to small, the number of ions per block is low and the position of the calibrant peak cannot be precisely determined. This would lead to a peak broadening. On the other hand, if the block size is to big not the complete drift scenario is described, which would again cause a broadening of the peak. In the data evaluation the block size is typically chosen such that one block contains about 100 calibrant ions. This corresponds to a block size of 30 s, for the calibrant ^{211}Pb in Figure 5.3. The corresponding mass distribution with a block size of 30 s is shown in Figure 5.6. In this case, the ^{211}Pb peak has a FWHM of 0.99 mu, which corresponds to a mass resolving power of 215000. It was obtained with 128 isochronous turns in the analyser.

It is necessary to determine the peak position of the calibrant ion in the TOF spectrum for each block, in order to calculate b in each block. An interpolated median was chosen to describe the peak position.

An example of a complete calibration with different turn numbers and a mass window of about 10 u is shown in Figure 5.4. The deviation in Mass Excess (*ME*) to the literature value for different molecular ions is shown in dependence of the number of turns. t_{TFS} was determined beforehand in a TFS spectrum and kept fixed. In order to determine c and a time averaged b the molecules (^{12}C ^{13}C ^{19}F$_4$), (^{12}C$_2$ ^{19}F$_4$), (^{12}C$_2$ ^{16}O ^{19}F$_4$) and (^{12}C$_3$ ^{19}F$_3$) were used. They have a maximum turn difference of 25 isochronous turns and cover about 10 u. The TRC was done using the molecule (^{12}C ^{13}C ^{19}F$_3$) in order to determine the time dependence of b. In the latter part of the data analysis, discussed in detail in Section 5.3, a precision calibration is done, which corrects for the change of ME values for different fit algorithms and functions. The molecule (^{12}C$_2$ ^{16}O ^{19}F$_4$) was used for the precise calibration.

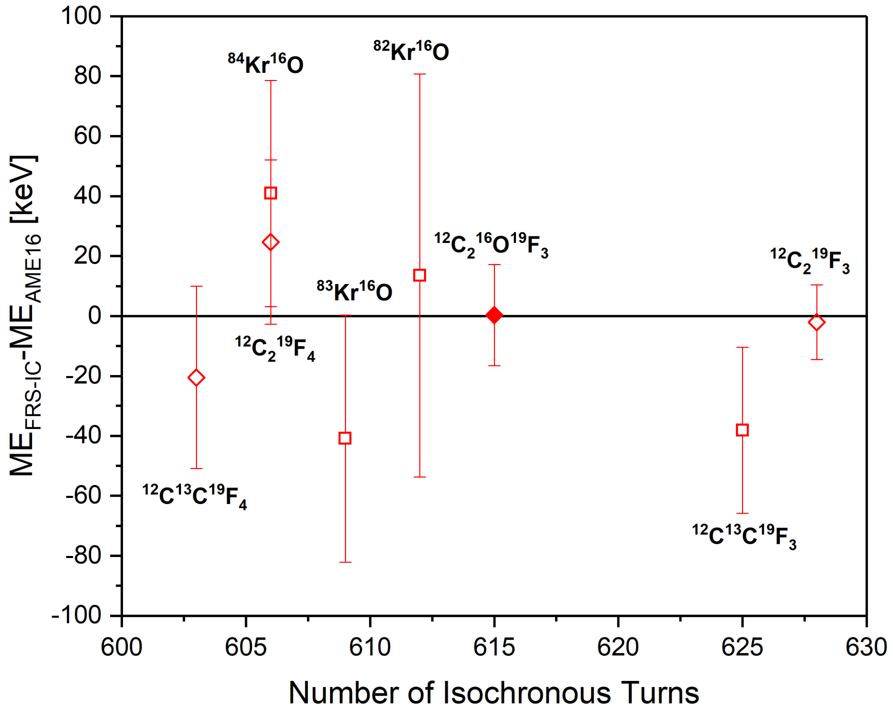

Figure 5.4.: Measured Mass Excess (*ME*) values of molecules compared to the literature values for different numbers of isochronous turns. The molecules (^{12}C ^{13}C ^{19}F$_4$), (^{12}C$_2$ ^{19}F$_4$), (^{12}C$_2$ ^{16}O ^{19}F$_4$) and (^{12}C$_3$ ^{19}F$_3$) (diamond symbols) were used for the calibration with multiple turn numbers. The TRC was done using the molecule (^{12}C ^{13}C ^{19}F$_3$). The molecule (^{12}C$_2$ ^{16}O ^{19}F$_4$) (filled diamond symbols) was used for the precise calibration of these measurements.

5.2. Determination of the Peak Shape

The peak shape of a mass distribution is determined after the calibration. In an MR-TOF-MS experiment, the peak shape of the time distributions and thus of the mass distribution is a result of several processes, which cannot be disentangled. One of the processes is related to collisions with the residual gas atoms, the ions can lose energy and change their direction. Both events will vary the flight path and thus the flight time. Small changes can be compensated by the ion mirror. However, larger changes in energy and angle will lead to tails in the peak shape to longer flight times [Dickel (2010); Schury et al. (2014)]. However, tails can also have their origin from higher-order optical aberrations as demonstrated in computer simulations [Schury et al. (2014); Yavor et al. (2015)].

In order to describe the measured peak shape, it is necessary that the fitting function has enough flexibility to model the influences of the different collision processes and experimental imperfections. These requirements can be fulfilled by the new Probability Distribution Function (*PDF*) called hyper-Exponentially Modified Gaussian (*hyper-EMG*) [Purushothaman et al. (2017)]. This function has been applied in the analysis of the measured spectra in this work.

A hyper-EMG PDF $h_{emg}(x;\, \sigma_G,\, \mu_G,\, \tau_{+i},\, \tau_{-i},\, \eta_{+i},\, \eta_{-i},\, \Theta)$ is given by a convex combination of PDFs of a Positive Skewed EMG (*PS-EMG*) $f_{+emg}(x)$ distribution and a Negative Skewed EMG (*NS-EMG*) distribution $f_{-emg}(x)$ with their weighting constants η_{+i} and η_{-i} and with the mixing weight Θ. It is expressed as

$$\begin{aligned} h_{emg}(x) =& \Theta\sum_{i=1}^{m}\eta_{-i}\, f_{-emg}(x) + (1-\Theta)\sum_{i=1}^{n}\eta_{+i}\, f_{+emg}(x)\ , \\ =& \Theta\sum_{i=1}^{m}\frac{\eta_{-i}}{2\tau_{-i}}\exp\left[\left(\frac{\sigma_G}{\sqrt{2}\tau_{-i}}\right)^2+\frac{(x-\mu_G)}{\tau_{-i}}\right]\mathrm{erfc}\left[\frac{\sigma_G}{\sqrt{2}\tau_{-i}}+\frac{(x-\mu_G)}{\sqrt{2}\sigma_G}\right] \\ &+(1-\Theta)\sum_{i=1}^{n}\frac{\eta_{+i}}{2\tau_{+i}}\exp\left[\left(\frac{\sigma_G}{\sqrt{2}\tau_{+i}}\right)^2-\frac{(x-\mu_G)}{\tau_{+i}}\right]\mathrm{erfc}\left[\frac{\sigma_G}{\sqrt{2}\tau_{+i}}-\frac{(x-\mu_G)}{\sqrt{2}\sigma_G}\right] . \end{aligned} \tag{5.5}$$

Examples on the derived peak shapes are shown in Figure 5.5. The calculated peak shapes of a NS-hyper-EMG, a PS-hyper-EMG and the new hyper-EMG distributions are shown with their underlying structure. The new hyper-EMG distribution, shown in the bottom panel is constructed from the NS-hyper-EMG and PS-hyper-EMG distributions depicted in the top panels.

In an MR-TOF-MS spectrum one assumes that the peak shape is independent of the considered ions, apart from a scaling factor. This holds as long as the ion motion is not disturbed by the influence of different electric fields or a different incident phase space. This can happen if the mass-to-charge ratio of two ions differs a lot or one ion is effected by the pulsed electric fields during the change periods. This is possible at the MRS or the analyser endcaps. In these cases the influenced ions are discarded from the evaluation. In the normal case all ions start with the same phase space and see the same fields, i.e., the peak shape can be determined from a high abundant peak in the spectrum (calibrant).

In order to determine the peak shape, the distribution is fitted by a hyper-EMG function (Equation 5.5) with a Least-Square (*LS*) fit. In the data evaluation, up to three tails on each side were implemented in the fitting algorithms. Additionally, a Gaussian function with an independent mean μ_{side}, sigma σ_{side} and fraction H of the area of the total peak are considered, resulting in the fitting function

$$\begin{aligned} & f_{emg+side}(x;A,\sigma_G,\mu_G,\tau_{+i},\tau_{-i},\eta_{+i},\eta_{-i},\Theta,\mu_{side},\sigma_{side},H) \\ &= AH\left\{\Theta\sum_{i=1}^{m}\frac{\eta_{-i}}{2\tau_{-i}}\exp\left[\left(\frac{\sigma_G}{\sqrt{2}\tau_{-i}}\right)^2+\frac{(x-\mu_G)}{\tau_{-i}}\right]\mathrm{erfc}\left[\frac{\sigma_G}{\sqrt{2}\tau_{-i}}+\frac{(x-\mu_G)}{\sqrt{2}\sigma_G}\right]\right. \\ &\quad\left.+(1-\Theta)\sum_{i=1}^{n}\frac{\eta_{+i}}{2\tau_{+i}}\exp\left[\left(\frac{\sigma_G}{\sqrt{2}\tau_{+i}}\right)^2-\frac{(x-\mu_G)}{\tau_{+i}}\right]\mathrm{erfc}\left[\frac{\sigma_G}{\sqrt{2}\tau_{+i}}-\frac{(x-\mu_G)}{\sqrt{2}\sigma_G}\right]\right\} \\ &\quad +A(1-H)\frac{1}{\sqrt{2\pi\sigma_{side}^2}}\exp\left[-\frac{(x-\mu_{side})^2}{2\sigma_{side}^2}\right] . \end{aligned} \tag{5.6}$$

The additional Gaussian function takes into account that some aberrations appear in the form of side peaks, which can not be described by the pure hyper-EMG function.

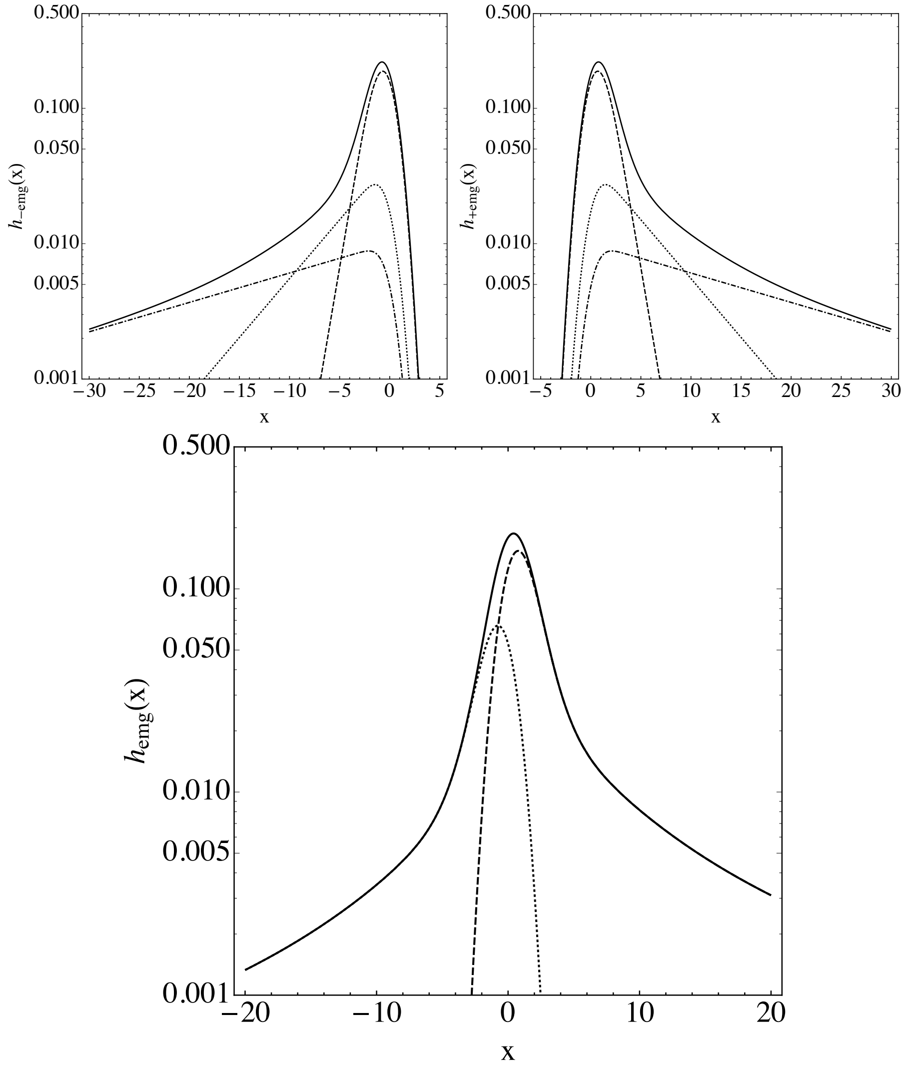

Figure 5.5.: Calculated Negative Skewed hyper-EMG (*NS-hyper-EMG*) (upper panel left), Positive Skewed hyper-EMG (*PS-hyper-EMG*) (upper panel right) and the new hyper-EMG (lower panel) distributions [Purushothaman et al. (2017)]. The solid lines represent the NS-hyper-EMG distribution in the top left panel and the PS-hyper-EMG distribution in the top right panel with the same shape parameters and their corresponding weighted NS-EMG and PS-EMG components. The dashed line corresponds to $\eta_1 = 0.6$, $\tau_1 = 1$, the dotted line to $\eta_2 = 0.2$, $\tau_2 = 5$ and the dash-dotted line to $\eta_3 = 0.2$, $\tau_3 = 20$. The solid line in the bottom panel shows the hyper-EMG distribution constructed from the NS-hyper-EMG (dotted line) and PS-hyper-EMG (dashed line) distributions depicted in the top panels with a mixing weight of $\Theta = 0.3$. All the distributions have the same $\sigma_g = 1$ and $\mu_g = 0$ values.

For the LS-fitting the data has to be binned. The Freedmann-Diaconis rule [Freedman and Diaconis (1981)] is used to determine the bin width w_{bin}. This is defined as

$$w_{bin} = \frac{2 * IQR(x)}{\sqrt[3]{n}} , \tag{5.7}$$

with n being the number of events and IQR is the interquartile range (± 25 % of the counts around μ_G) of a single non-overlapping peak. The LS-minimization is done in the software environment for statistical computing and graphics called "R" [R Core Team (2018)]. It provides with “nlsLM” a non-linear weighted LS-minimizer based on the Levenberg-Marquardt algorithm [Moré (1978)]. In this form the peak shape parameters ($\sigma_G, \tau_{+i}, \tau_{-i}, \eta_{+i}, \eta_{-i}, \Theta, \sigma_{side}, H$ and the relative position of μ_{side}) can be determined from the high abundant ion. This allows to fit the peaks with lower abundance with a known peak shape and only determine μ_G and A in a subsequent fit. An example of a calibrant mass distribution of the calibrant ion ^{211}Pb is shown in Figure 5.6. The selected fragment in this measurement was ^{213}Rn. The corresponding mass distribution is fitted with a hyper-EMG with a different number of exponential tails as well as with and without a Gaussian side peak. The reduced chi-squared χ^2_{Red}, as defined in [Purushothaman et al. (2017)], for the different fits are listed in Table 5.1. Based on the visual impression and the residual standard error, the final fit was chosen to have one exponential tail on each side and a Gaussian side peak.

In order to obtain the peak shape parameters for the IOIs in the spectrum the parameters $\sigma_G, \tau_{+i}, \tau_{-i}, \sigma_{side}$ and the relative position of μ_{side} have to be scaled. $\eta_{+i}, \eta_{-i}, \Theta, H$ can be considered as constants. The mass resolving power R_m (see Section A.1) can be used as a scaling factor for the peak-shape parameters. The scaling factor γ_σ for σ is given by

$$\gamma_\sigma = \frac{\Delta(m/q)_{IOI}}{\Delta(m/q)_{Cal}} \; with \, \Delta(m/q) = (m/q)\,\frac{1}{R_m} . \tag{5.8}$$

The tails on both sides and the peak parameter τ are caused by the aberrations in the analyser. They are independent of the turn-around time Δt_{ta} and therefore the scaling is also independent of Δt_{ta}. This introduces a scaling factor γ_τ of

$$\gamma_\tau = \frac{\Delta(m/q)_{ab,IOI}}{\Delta(m/q)_{ab,Cal}} \; with \, \Delta(m/q)_{ab} = (m/q)\,\frac{1}{R_m|_{\Delta t_{ta}\to 0}} . \tag{5.9}$$

The peak-shape parameters, determined by this scaling procedure, are used for the fit of the mass distribution for the IOI.

exp. tails (left)	exp. tails (right)	side peak	χ^2_{Red}
0	0	without	3.13
1	0	without	2.72
1	0	with	1.74
1	1	without	1.03
1	1	with	0.93

Table 5.1.: Reduced chi-squared χ^2_{Red} for the LS-fit of the measured mass distribution of the calibrant ion ^{211}Pb for different number of tails and side peaks. The corresponding fits are shown in Figure 5.6.

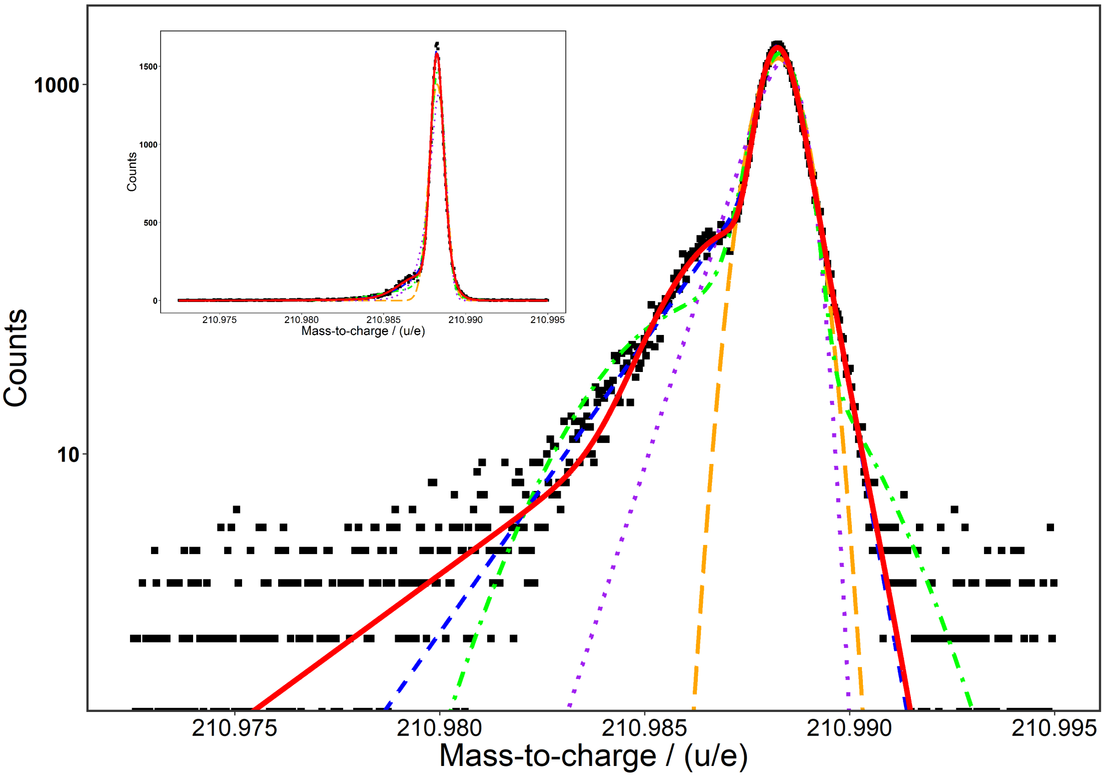

Figure 5.6.: Measured mass distribution of the calibrant ion ^{211}Pb. ^{211}Pb ions were used to determine the peak-shape parameters of the hyper-EMG (red solid line), which then were used for the determination of the mass of ^{213}Rn ions. The peak shape requires one exponential tail on each side and additionally a Gaussian side peak. The side peak results from ion optical effects and is not an additional peak. In addition, a Gaussian function (orange long-dashed line) and a hyper-EMG with a different number of tails with and without a side peak are shown. The fits with one exponential tail to the left side (purple dotted line), with one exponential tail to the left side plus a side peak (green dashed line) and one exponential tail on both sides (blue dash-dotted line) are shown. The reduced chi-squared χ^2_{Red} for the different fits are listed in Table 5.1. The mass distribution in linear scale is shown in the insert.

5.3. Determination of the Final Mass Value

The fit of the mass distribution for the IOI is done with the hyper-EMG function applying the Weighted Maximum Likelihood Estimation (*WMLE*) [Ebert (2016)]. The WMLE has the advantage that it can be applied also to unbinned data. For binned data, the choice of the bin width and the position of the first bin could lead to a shift of the data which would cause an error. The WMLE is a well established method for fitting of unbinned data. The highest accuracy can be reached because the precision of the final mass value is not limited to the bin size. In addition, this method is well suited for data with low count rates. In the WMLE fit only the μ_G and the area of the IOI are fitted. The peak shape parameters are considered to be fixed after scaling. The WMLE fit is done in the software environment for statistical computing and graphics R, like the LS-fit. For the WMLE fit the numerical minimizer “nlm” is used. This minimizer provides a high precision value of the μ_G of the hyper-EMG fit.

In the case of a double-peak fit, it is necessary to determine first the areas of the two peaks with the robust minimizer “constrOptim”. The “constrOptim” minimizer is less precise in the determination of μ_G in the hyper-EMG fit than the “nlm” minimizer. However, the advantages with regard to its robustness dominate. In a second step the data of the double peak are fitted with the precise “nlm” minimizer by using the areal ratio from the “constrOptim” minimizer as a fixed input. For strongly overlapping peaks the fit results are slightly shifted compared to their true value. This can be corrected by the so-called bias correction for overlapping peaks. This bias correction has been described in detail in [Ayet San Andrés (2018); Ebert (2016)]. The basic concept is to first determine the distance of the two overlapping peaks and then to keep this distance fixed in the final fit.

In the fit a weighting by the natural logarithms of the function is applied. The influence of this weighting and different weighting functions was investigated and discussed in reference [Ebert (2016)].

Another factor for the precise calibration is determined from the mass distribution of the calibrant ion. It takes into account that in the TRC the characteristic point of the mass distribution is given by the interpolated median which differs from the one in the hyper-EMG Fit. The corresponding mass value of the calibrant ion is used to calculate a recalibration factor $\gamma_{precise}$:

$$\gamma_{precise} = \frac{(m/q)_{Calib,Lit}}{(m/q)_{Calib,Fit}} . \tag{5.10}$$

The determined mass value for the IOI is then in a final step recalibrated by the corresponding calibration factor $\gamma_{presise}$, which is determined for each data set separately.

Several IOIs are measured multiple times. If several independent measurements are done, the final mass value is calculated by the weighted average of the individual mass values. The weighted average mass value m_{final} and the corresponding error Δm_{final} of n measurements of the same isotope are calculated by

$$m_{final} = \left(\sum_{i=1}^{n} \frac{m_i}{\Delta m_i} \right) / \left(\sum_{i=1}^{n} \frac{1}{\Delta m_i} \right) , \tag{5.11}$$

$$\Delta m_{final} = \left(\sqrt{\sum_{i=1}^{n} \frac{1}{\Delta m_i^2}} \right)^{-1} . \tag{5.12}$$

The error contributions of the same measurement conditions in several individual runs are not independent and thus are added after averaging the other errors.

The final mass value of the neutral atom in the atomic mass unit u is also converted to a Mass Excess (*ME*) value. The ME value is defined as the difference between the mass value in u and the mass number of the isotope.

5.4. Errors

The final error of the measured mass value consists of several independent contributions which are taken into account by the quadratic sum. The different error contributions are shown in the following equation

$$\begin{aligned}\Delta m = \big(&\Delta m^2_{Stat-IOI} + \Delta m^2_{Peakshape} + \Delta m^2_{Bias} + \Delta m^2_{Stat-Calib} + \Delta m^2_{Lit-Calib} + \cdots \\ &\cdots \Delta m^2_{t_{TFS}} + \Delta m^2_{c} + \Delta m^2_{TRC} + \Delta m^2_{NIE} + \Delta m^2_{MRS} + \Delta m^2_{Contamination} + \Delta m^2_{Iso}\big)^{(1/2)} \ .\end{aligned} \tag{5.13}$$

The considered errors include

- Fit errors
- Calibration errors
- Errors due to pulsed electrical fields
- Unknown contamination error
- Unresolved known isobar and isomer error

and are separately discussed in the following.

Fit Errors

Errors originating from the fitting process of the data are considered. These are the statistical error of the IOI $\Delta m_{Stat-IOI}$ and the calibrant $\Delta m_{Stat-Calib}$, the error due to the peak shape $\Delta m_{Peakshape}$ and the error of the bias correction for overlapping peaks Δm_{Bias}. In case of fitting a hyper-EMG, the statistical error can not be determined analytically. In the error calculation its value is determined by fitting of generated data multiple times. The generated data were adapted from the parameters of the IOI. The determined statistical errors for the example of ^{213}Fr for different counts is shown in Figure 5.7. For this case the dependency between the number of ions and the statistical error was determined. The mean value for the FWHM of ^{213}Fr was 1.029 mu. It results in

$$\Delta m_{Stat-^{213}Fr} = \frac{a_{Stat} \cdot FWHM}{\sqrt{Counts}} \text{ with } a_{Stat} = 0.53\,(2) \ . \tag{5.14}$$

The dependence of the statistical error on the number of ^{213}Fr ions is in good agreement with the results of reference [Ebert (2016)]. The statistical error of this hyper-EMG is about 25 % larger then the corresponding one of a pure Gaussian fit. For a pure Gaussian fit a_{Stat} is equal to $\frac{1}{2\sqrt{2\ln 2}} \approx 0.42$.

The peak-shape error corresponds to the non-ideal description of the real shape of the mass distribution by the fitting function. It is determined by changing consecutively one parameter, as obtained by the LS-fit, of the hyper-EMG function by plus/minus its error and performing the WMLE fit with this value for the parameter. The maximum deviation in μ_G from the original WMLE fit of both is determined. This is done for all peak shape parameters. The resulting deviations are summed up quadratically, assuming all parameters are independent from each other. This error depends on the previously discussed choice for the tails and side peak in the LS-fit of the calibrant ion.

The last error considered as part of the fitting procedure is the error in the bias correction for overlapping peaks. This bias correction and its influence on the final mass value in a double

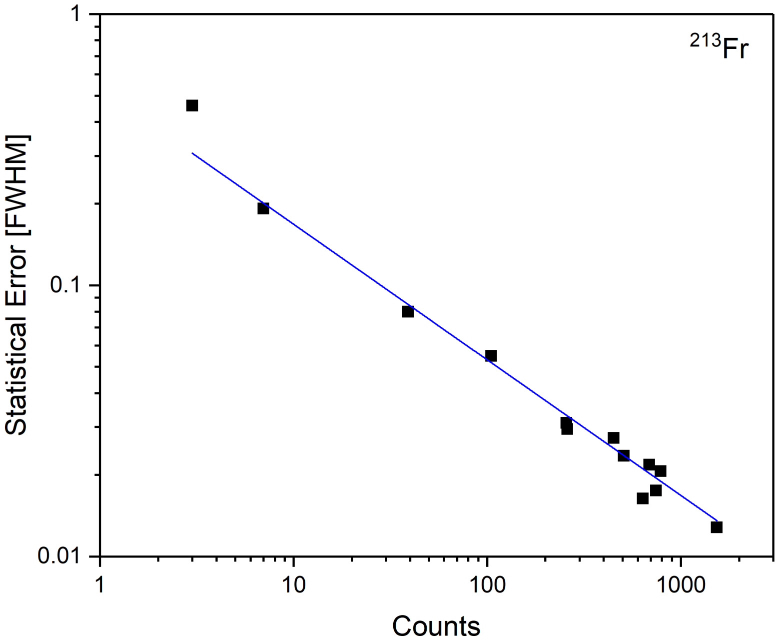

Figure 5.7.: Statistical error Δm_{Stat} depending on the number of measured ^{213}Fr ions.

peak fit is discussed in detail in reference [Ayet San Andrés (2018)]. Based on this discussion, an error of 25 % of the shift in the bias correction for overlapping peaks is taken into account.

Calibration Errors

The individual errors of the calibration parameters t_{TFS} and c, Δt_{TFS} and Δc, are determined within the calibration step. In order to determine them, the peak positions of the calibration ions in the TOF spectrum used for the calibration are shifted separately by plus/minus their error and the calibration parameters are recalculated in both cases. The maximum deviation of the calibration parameters for each calibrant ion to the overall mean value is calculated and summed quadratically for each calibration parameter separately. The resulting values are used as the individual errors Δt_{TFS} and Δc. The error in the determination of t_{TFS}, Δt_{TFS}, results in an error component of the final mass value in units of u, which is given in [Rink (2017)] by

$$\Delta m_{t_{TFS}} = \frac{2\sqrt{c}\,(m/q)_{IOI}}{1+N_{IT}b}\left(\frac{1}{\sqrt{(m/q)_{Cal}}} - \frac{1}{\sqrt{\left|(m/q)_{Cal}-(m/q)_{IOI}\right| + (m/q)_{Cal}}}\right)\Delta t_{TFS}\,. \tag{5.15}$$

The error in the determination of c, Δc, results in an error component of the final mass value in units of u, which is given by

$$\begin{aligned}\Delta m_c &= \left|(m/q)_{IOI}(c) - (m/q)_{IOI}(c\pm\Delta c)\right| \\ &= \left|\frac{c\,(t_{IOI}-t_{TFS})^2}{(1+bN_{a,IOI})^2} - \frac{(c\pm\Delta c)\,(t_{IOI}-t_{TFS})^2}{\left(1+\frac{N_{a,IOI}}{N_{cal,IOI}}\left(\sqrt{\frac{(c\pm\Delta c)(t_{cal}-t_{TFS})^2}{(m/q)_{cal}}}-1\right)\right)^2}\right|\,,\end{aligned} \tag{5.16}$$

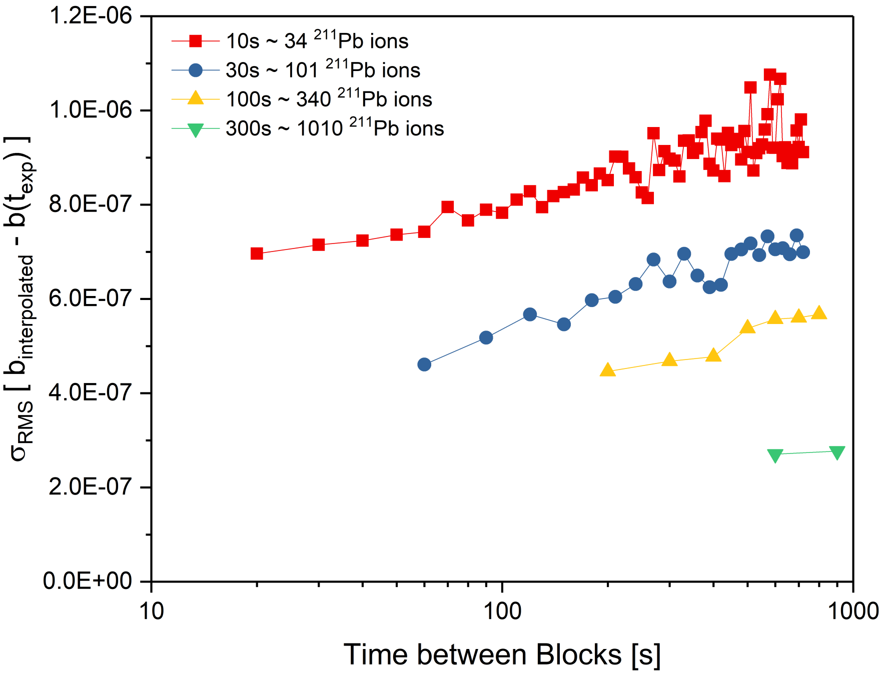

Figure 5.8.: Root mean square value σ_{RMS} of the deviation between the interpolated b and the $b\left(t_{exp}\right)$ in the TRC depending on the time between a pair of $b\left(t_{exp}\right)$ used for the interpolation. The σ_{RMS} is a measure for the expected peak broadening. The investigation of the TRC has been done for different block sizes, corresponding to different numbers of ions inside of one TRC block.

using the calibrant relation

$$b\left(t_{cal},(m/q)_{cal},c\pm\Delta c\right)=\frac{1}{N_{cal,IOI}}\left(\sqrt{\frac{(c\pm\Delta c)\left(t_{cal}-t_{TFS}\right)^2}{(m/q)_{cal}}}-1\right).$$

In the case that the calibrant ion and the IOI have the same number of isochronous turns in the analyser, the error component Δm_c is zero. This is the case, because then the calibration parameters c and b are not independent and the error is described by the error of b.

The error of the TRC appears when the calibrant is not present during the complete measurement time. This has been investigated in an ideal case (TRC calibrant ion always present) and by comparing the expected drift from the TRC with the measured ones. A linear interpolated value, calculated from a pair of $b\left(t_{exp}\right)$ values, was compared to the $b\left(t_{exp}\right)$ inside of the interpolation window. This has been done for different time distances between the pair of $b\left(t_{exp}\right)$ values (time between blocks) and for different block sizes in the TRC. The resulting Root Mean Square (RMS) σ_{RMS} of the deviations between all interpolated b and the $b\left(t_{exp}\right)$ determined, is shown in Figure 5.8 for data of the calibrant ion ^{211}Pb. The reference fragment in this measurement was ^{213}Rn. The σ_{RMS} value is a measure for the resulting peak broadening since the calibrant ion and IOI do not experience the same fields, because they are not passing the system together. In the case of the calibrant ion ^{211}Pb, it was continuously provided over the full experiment duration.

The σ_{RMS} for the time between blocks of the IOI is added quadratically to the peak width of the IOI. For each measurement the effective time between blocks t_{Block}^{eff} is calculated. It is given by

$$t_{Block}^{eff}=\frac{2*\left(t_1-t_{begin}\right)^2+2*\left(t_{end}-t_n\right)^2+\sum_{i=2}^{n}\left(t_i-t_{i-1}\right)^2}{t_{end}-t_{begin}}, \tag{5.17}$$

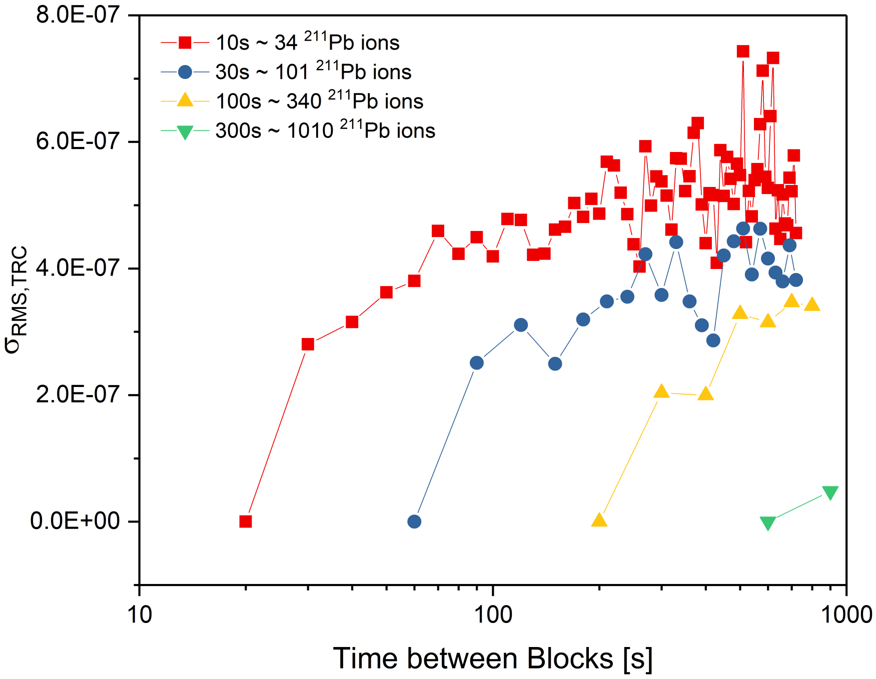

Figure 5.9.: The $\sigma_{RMS,\,TRC}$ value according to Equation 5.18 is considered as an additional error contribution of the measured mass values from the TRC (Equation 5.19). The investigation of the TRC has been done for different block sizes, corresponding to different numbers of ions inside of one TRC block.

with n being the number of blocks used for the TRC and t_n being the measurement time corresponding to the centroid of the n-th TRC block. The magnitude of the changes in TOF due to the electronics and temperature changes is considered as constant over a beamtime.

A second effect of the TRC has to be taken into account besides the peak broadening, which is described by the calculated σ_{RMS}. The mean value of b and therefore the mass scale can have an error, since the IOI and the calibrant can fly through different fields. This effect is most prominent with a small number of TRC blocks. In order to quantify this effect, the RMS value of the mean of each time between the blocks was calculated separately inside of each margin ($\sigma_{RMS,\,Margin}$). This value corresponds to the TRC error including a component based on the statistics in the investigation. The statistical part can be estimated to be the RMS of the deviation between all interpolated b and $b\,(t_{exp})$ divided by the number of steps per margin N_{Steps}. This part can be subtracted quadratically resulting in $\sigma_{RMS,\,TRC}$:

$$\sigma_{RMS,\,TRC} = \sqrt{\left(\sigma_{RMS,\,Margin}\right)^2 - \left(\frac{\sigma_{RMS}}{\sqrt{N_{Steps}}}\right)^2}\,, \tag{5.18}$$

which is shown in Figure 5.9. The $\sigma_{RMS,\,TRC}$ is 0 in the case of a continuous calibration, since in this case the σ_{RMS} and the $\sigma_{RMS,\,Margin}$ are equal and N_{Steps} corresponds to 1.

The value of the $\sigma_{RMS,\,TRC}$ divided by the square-root of the average number of blocks in the TRC O_{IOI} is considered as the additional mass error contribution of the TRC.

$$\Delta m_{TRC} = \frac{\sigma_{RMS,\,TRC}}{\sqrt{O_{IOI}}}\,(m/q)_{IOI}\,. \tag{5.19}$$

Errors due to pulsed electrical fields

The measured mass value of an ion can be shifted due to the exposed pulsed electrical fields. In the analyser of the MR-TOF-MS, two sets of electrodes are pulsed, the endcaps of the analyser and the MRS. This can cause two error components in the mass determination, the Non-Ideal Ejection (*NIE*) Δm_{NIE} for the analyser and the pulsing of the MRS Δm_{MRS}.

The NIE error was investigated with ^{133}Cs ions, by scanning the opening time of the analyser and comparing the TOF. The investigation is discussed in detail in [Ayet San Andrés (2018)]. From this discussion, an average uncertainty in the TOF δt_{NIE} was estimated for both experiments separately. For the experiments with a 1 GeV/u uranium beam, an uncertainty δt_{NIE} of 0.1 ns was estimated. In the experiments with a 600 MeV/u xenon beam, the uncertainty δt_{NIE} was estimated to be 0.5 ns. The measured TOF uncertainties for ^{133}Cs can be converted to an error in the mass-to-charge ratio and are scaled to the IOI:

$$\Delta m_{NIE} = \frac{2\delta t_{NIE}}{t_{IOI}} \sqrt{\frac{(m/q)_{IOI}}{(m/q)_{^{133}Cs^{1+}}}} (m/q)_{IOI} \ . \tag{5.20}$$

The pulsed MRS may lead to a shift in the TOF. This was investigated with ^{133}Cs ions and is discussed in detail in [Ayet San Andrés (2018)]. Depending on the desired mass range in a certain part of the measurement the MRS can be used with a different number of Isolation Cycles (*IC*). The shift from the pulsed field depends on the difference in isolation cycles ΔIC between the IOI and the calibrant. The shift of the calibrant $t_{Shift,\ MRS}$ can be estimated by

$$t_{Shift,\ MRS} = \frac{2 \cdot 0.011 \Delta IC}{t_{cal}} \ . \tag{5.21}$$

Calibrant and IOI can experience different states of the MRS for different time intervals (different duty cycles) $duty_{MRS,Cal}$ and $duty_{IOI,Cal}$, respectively. Different states of the MRS correspond to a different number of IC. The shift in TOF by the MRS is scaled to the duty cycle accordingly. The error due to the pulsed MRS is assumed to be 50 % of the relative mass correction due to the MRS pulsing of the calibrant and the IOI. It can be calculated by:

$$\Delta m_{MRS} = 0.5\,(m/q)_{IOI}\, t_{Shift,\ MRS} \sqrt{\frac{(m/q)_{IOI} + (m/q)_{Cal}}{2}} \left(duty_{MRS,IOI} - duty_{MRS,Cal}\right) \ . \tag{5.22}$$

Unresolved Contamination Error

The error component $\Delta m_{Contamination}$ takes into account the possibility that the measured mass-to-charge distribution is contaminated from an unknown source. This error component was investigated in reference [Rink (2017)] and is estimated by simulations. The number of ions of a non-identified peak around the mass of the IOI is used in order to estimate the number of contamination ions. In these simulations an additional peak with an estimated number of contaminant ions is moved stepwise through the peak of the IOI and the maximum deviation from the original mass-to-charge ratio is derived and corresponds to the considered error for unknown contamination.

Unresolved Known Isobars and Isomers

It is assumed that the mean value $\overline{(m/q)}$ of two or more masses is measured, in the case that it is known that these mass lines are overlapping with a known distance and can not be resolved. Therefore, the individual masses can be calculated by correcting for the known distance between them and assuming that all are populated equally. An additional error contribution Δm_{Iso} has to be taken into account, due to the unresolved mass lines. This error component can be calculated based on probability theory. The standard method for the handling of unresolved mass lines is recommended in the AME 2016 [Wang et al. (2017)] and is shown in more detail in Section A.3. In the case of two overlapping isobars or nuclear states $(m/q)_0$ and $(m/q)_1$ with an unknown distribution the approach leads to

$$\overline{(m/q)} = \frac{1}{2}\left((m/q)_0 + (m/q)_1\right) , \tag{5.23}$$

and to an additional error component of:

$$\Delta m_{Iso} = \frac{\sqrt{3}}{6}\left((m/q)_1 - (m/q)_0\right) . \tag{5.24}$$

6. Experimental Results

Different exotic nuclei were produced in three experiments via projectile fragmentation with a 300 MeV/u ^{238}U beam, with a 1 GeV/u ^{238}U beam, and with a 600 MeV/u ^{124}Xe beam. Details of the experimental conditions and the setups are discussed in Sections 4.4, 4.5 and 4.6. Unique features of the combination of the FRS with the MR-TOF-MS has been shown in the mass measurements of $^{154-155}$Tm and ^{155}Yb ions, which were produced with a 300 MeV/u ^{238}U beam. The measurements are discussed in Section 6.1.

In the experiment with a 1 GeV/u uranium beam, we focused on isotopes above ^{208}Pb with half-lives in the ms region. The masses of $^{211-213}$Fr, $^{212-213,218}$Rn, ^{212g,m,217}At and ^{211g,m}Po ions were determined and the results are discussed in Section 6.2. It was shown with ^{211}Po ions that a clean isomeric beam can be achieved via spatial separation with the MR-TOF-MS [Dickel et al. (2015a)]. The measurements are discussed in Section 6.5.2. The novel results open up new possibilities for mass-selective decay spectroscopy as demonstrated in [Rink (2017)].

In the xenon experiment, the measurements included isotopes in the region below ^{100}Sn. In this region, long-lived isomeric states are abundant. The masses of ^{96,97}Pd, ^{93,94g,m}Rh and ^{93g,94}Ru ions were determined. The results are discussed in Section 6.3.

A new isomeric state was discovered and investigated for ^{97}Ag ions, see Section 6.6. The discovered isomeric state was predicted by systematics applied to isotopes in the neighbourhood.

6.1. Particle Identification

6.1.1. Particle Identification in Flight with the FRS

The verification of the Particle IDentification (*PID*) by proton number (Z) and mass number (A) can be performed with the FRS and its particle detectors applying the Bρ-ΔE*-TOF method. Note, ΔE* represents the energy deposition of the fragments in the ionization chamber (MUSIC) placed at the final focal plane of the FRS. The focal-plane detectors were employed to determine event-by-event the magnetic rigidity, the flight time and the energy deposition for each ion transported through the FRS, see also Section 4.1.

An example of a measured PID spectrum is given in Figure 6.1. The magnetic field values of the FRS were selected for the reference fragment ^{213}Fr which was produced with an 1 GeV/u uranium primary beam. The isotopes ^{212}Fr and ^{213}Fr have been identified by the application of the Bρ-ΔE*-TOF method.

The fragment identification in flight by A and Z in the FRS can be verified by high-resolution mass measurements with the MR-TOF-MS. Only ions with the same atomic range will be simultaneously stopped in the CSC. This range selection provides additional separation and identification criteria. In practice, the range distribution of the fragments was shifted into the CSC by changing the thickness of the homogeneous degrader at the final focal plane of the FRS, see Figure 6.2. The two isobars ^{212}Rn and ^{212}Fr were both simultaneously stopped in the CSC with a suitable thickness selection of the homogeneous degrader F4. One can observe that both range distributions are much wider than the thickness of the gas layer in the CSC and that the mean ranges differ by more than 30 mg/cm^2 Al material. Thus it follows that the optimum rate for

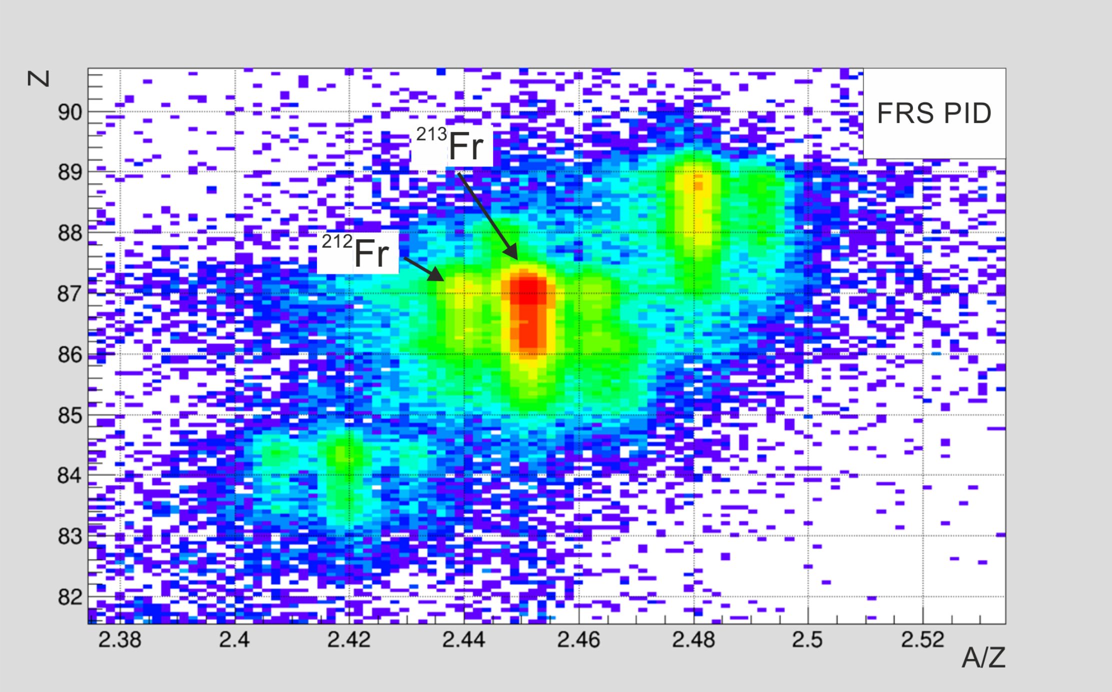

Figure 6.1.: In flight particle identification of ^{212}Fr and ^{213}Fr ions produced in projectile fragmentation of a 1 GeV/u ^{238}U beam. The number of protons (Z) of the ions is determined via the energy deposition in the MUSIC detector. The mass-to-charge ratio (A/Z) is determined from coincident TOF and Bρ measurements (Bρ-ΔE*-TOF method).

the MR-TOF-MS measurements can be achieved by shifting the maximum of the range distribution into the middle of CSC. The measured spectra for the two isobars ^{212}Rn and ^{212}Fr were verified by LISE [Tarasov and Bazin (2008)] and MOCADI [Iwasa et al. (1997)] simulations. Both programs use for the slowing-down down of relativistic ions the ATIMA [Weick et al. (2018)] prediction. The intensities of the different isobars in the measured mass spectrum of the MR-TOF-MS is in excellent agreement with the range calculations and independent range measurements. The latter measurements are based on recording a number-distance curve, which represents a good approximation for the ranges at the energies of these experiments.

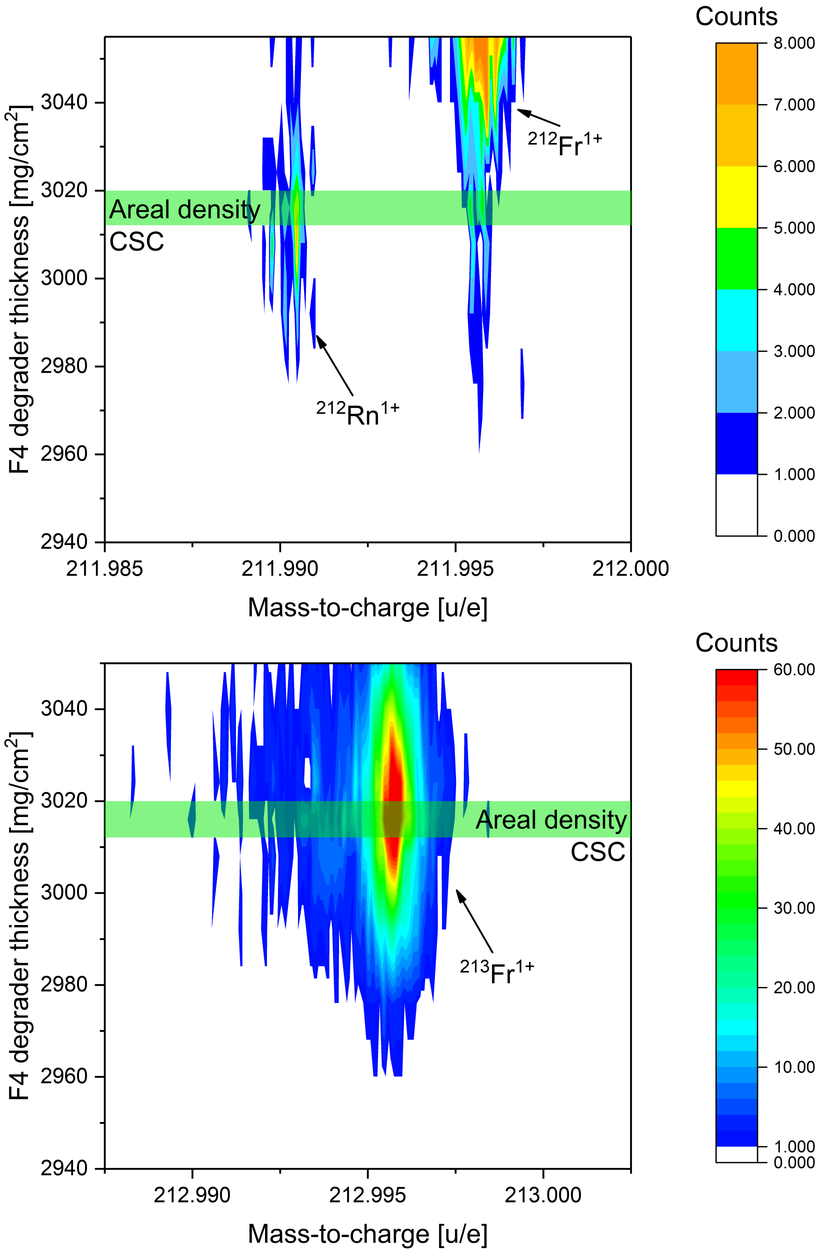

Figure 6.2.: Mass spectra of ^{212,213}Fr and ^{212}Rn ions measured with the MR-TOF-MS for different thicknesses of the degrader at the final focal plane F4 of the FRS. The areal density of the gas in the CSC is also depicted in the figures. The ions were produced via projectile fragmentation of a 1 GeV/u ^{238}U beam.

6.1.2. Novel Particle Identification via Range and Mass Measurements (*R-m* Method) with the FRS Ion Catcher

The MR-TOF-MS combined with the range information of the CSC has the capability to perform a complete PID of exotic nuclei provided by the FRS. This PID deduced from high-resolution mass spectra and atomic range selection is fast, sensitive and universal. This identification method via range (R) and mass (m) measurements (*R-m* method) can also be favourably applied for exotic nuclei at low energies when multiple ionic charges states make an unambiguous application of the $B\rho - \Delta E^{*}$-TOF method difficult, see also Section 4.1.

In a pilot experiment in preparation for the research at the LEB of the Super-FRS [Geissel et al. (2003); Winfield et al. (2013)], see Section 4.5, uranium fragments were produced at 300 MeV/u in the FRS and studied with the MR-TOF-MS. The unambiguous PID is very difficult at this relatively low kinetic energy for the $B\rho$-ΔE^{*}-TOF method, in particular for heavy fragments due to the occurance of multiple charge states in all sections of the FRS. However, the produced isotopes can be unambiguously identified with the MR-TOF-MS applying the R-m method. Medium-mass fragments Have already been identified with a mass resolving power of 75000, see Figure 6.3. ^{154,155}Tm and ^{155}Yb ions were unambiguously identified as demonstrated with the measured mass-to-charge spectrum. The doubly charged ^{154,155}Tm and ^{155}Yb ions were measured with 90 isochronous turns in the analyser of the MR-TOF-MS. The spectrum has been calibrated with the singly charged ^{78}Kr and ^{80}Kr ions recorded after 90 and 89 isochronous turns, respectively. Slowing-down calculations with ATIMA [Weick et al. (2018)] implemented in LISE++ [Tarasov and Bazin (2008)] and MOCADI [Iwasa et al. (1997)] show that at this low energies, isotones emerging from the FRS, have the same atomic range in matter.

Therefore, one expects to measure the isotopes ^{154}Tm and ^{155}Yb together in one mass spectrum of the MR-TOF-MS. This is in excellent agreement with the MR-TOF-MS measurement including the observed abundances and the range straggling. According to Lise++ simulations, the intensity of ^{154}Tm is about one order of magnitude higher than ^{155}Yb, and the mean range of ^{155}Tm ions is larger than for the 154 u isotones. In summary, the calculations and the measurements fully agree.

This pioneering measurement is a clear and impressive demonstration for the fragment identification at low kinetic energies with the novel R-m method applying the FRS-Ion-Catcher with the high-resolution MR-TOF-MS. This novel, universal experimental method has a unique potential for the discovery and study of exotic nuclei produced at low kinetic energies. This statement holds of course not only for fragmentation products, but is valid for fusion and nucleon-transfer reactions as well. It is obvious that the R-m method is ideal for a combination with in-flight separators.

Calculated examples for the application of the R-m method for future measurements in different regions of the chart of nuclides are presented in Figure 6.4. The nuclides of interest are produced via fragmentation of ^{124}Xe, ^{208}Pb and ^{238}U projectiles with the selected reference fragments of ^{94}Ag and ^{202}Os. In the calculations, all isotopes and their isomers with a half-life of more than 1 ms and with a production rate of more than 3.6E-6 pps were considered. The conditions were adapted to the present characteristics of the MR-TOF-MS at the FRS-IC. The number of possibly implanted isotopes in the CSC is relatively large due to the applied mono-energetic degrader and the selected kinetic energy domain of 300 MeV/u. Note, this energy condition exists presently at the in-flight facility Big-RIPS at RIKEN [Kubo (2003)] and will prevail at the LEB of the Super-FRS. The expected isotopes, produced and separated under the selected experimental conditions, are indicated with color in Figure 6.4. In addition, the color code represents the required different mass resolving powers for unambiguous PID. For the required mass resolving power, a value of twice the mass difference between adjacent isobars was implemented

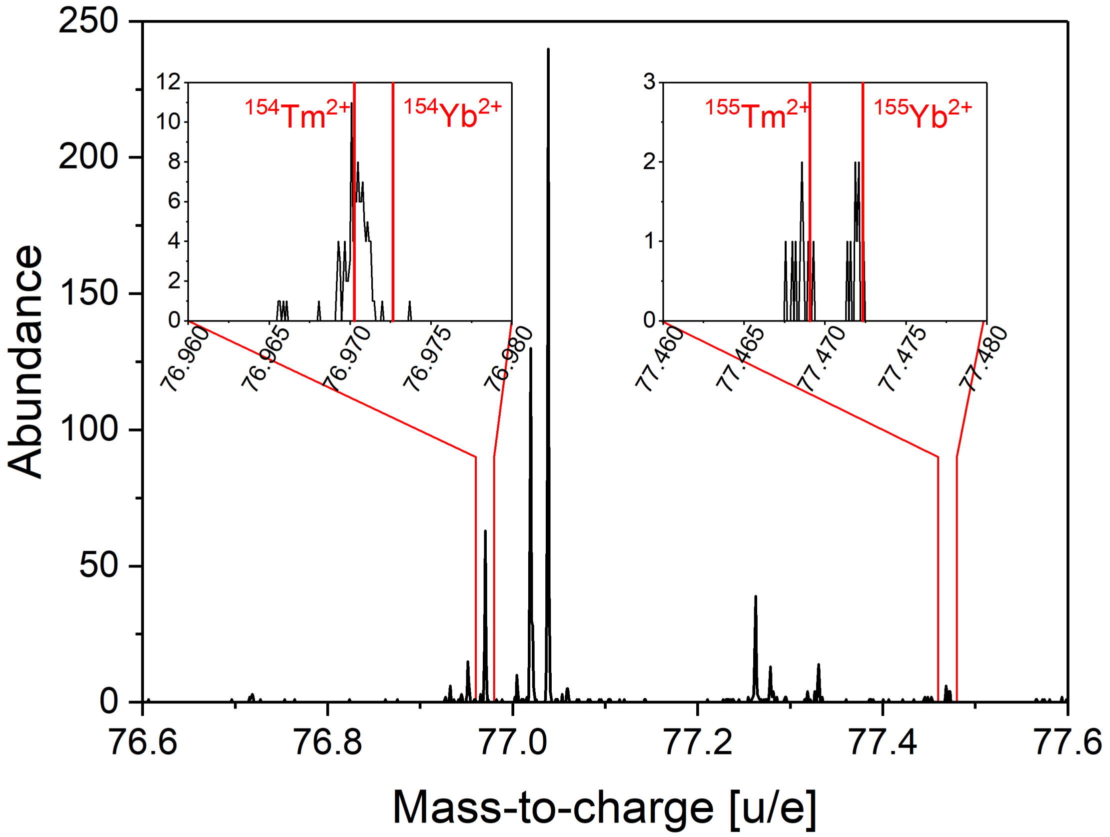

Figure 6.3.: Measured mass-to-charge-spectrum of the doubly charged uranium fragments ^{154,155}Tm and ^{155}Yb. All nuclides are already unambiguously identified by measurements with 90 isochronous turns in the MR-TOF-MS with a modest mass resolving power of 75000.

in the calculation. The required mass resolving power can be provided by the MR-TOF-MS, as proven in recent FRS experiments. The calculated examples clearly demonstrates the scientific potential with the FRS-IC for the research with exotic nuclei over a wide element range.

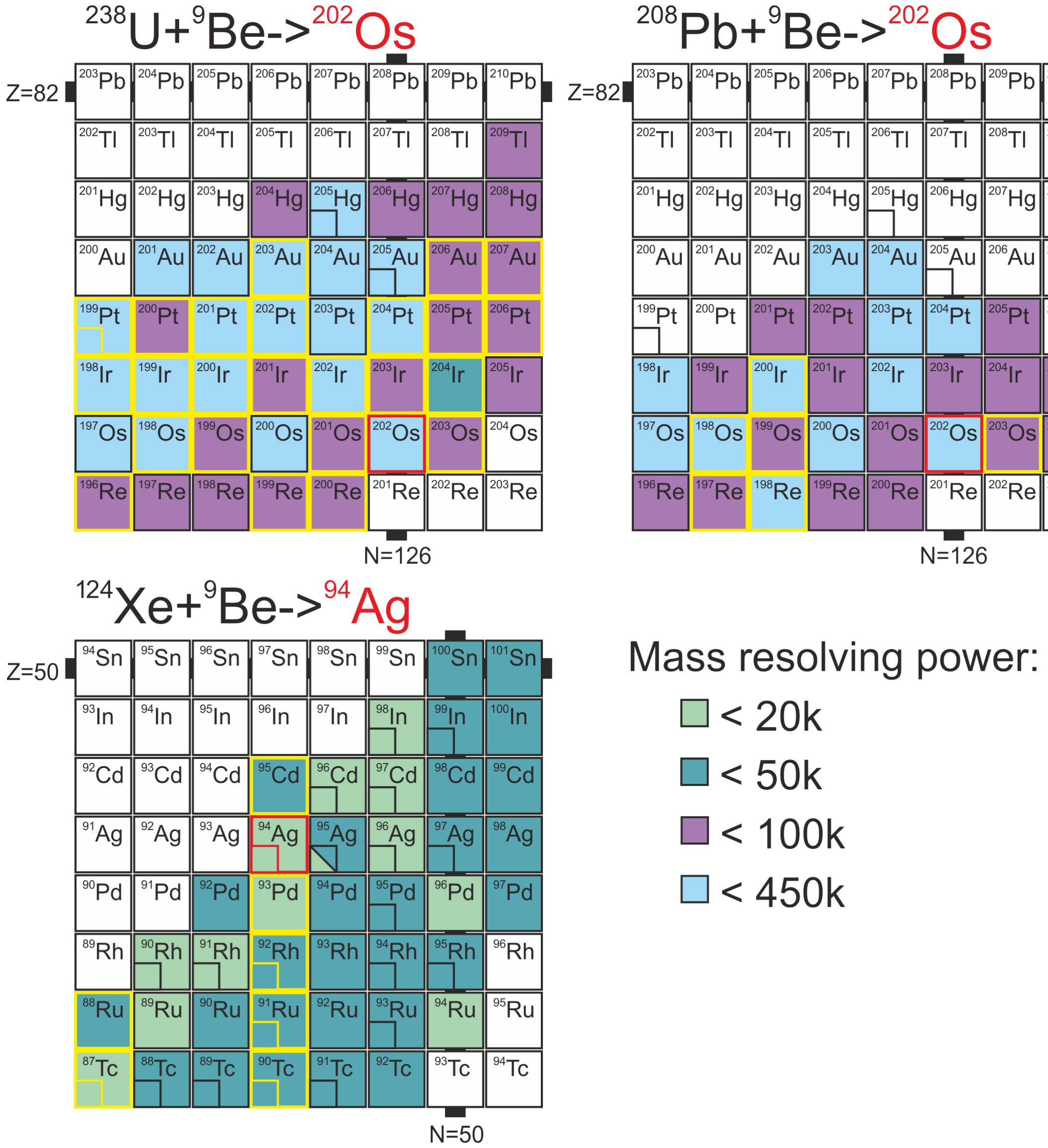

Figure 6.4.: Required mass resolving powers to achieve unambiguous particle identification in two typical isotope domains (^{94}Ag and ^{202}Os). A mass resolving power of twice the mass difference between adjacent isobars has been assumed in the calculation. The fragments were produced and separated at 300 MeV/u. All fragments which are stopped together with the reference fragment (indicated by a red frame) in the CSC are highlighted with a yellow frame. The closed nuclear shells are indicated by black marks.

6.2. Results of Mass Measurements of 1 GeV/u Uranium Fragments

In the following the measured mass values for the 1 GeV/u uranium fragments are presented. The experimental conditions and the setup haven been discussed in Section 4.4.

6.2.1. Calibration

The calibration of the mass spectra is one of the first steps in a mass measurement. A Time-Focus-Shift (*TFS*) spectrum was used to determine the calibration constants c and t_{TFS} according to Equation 5.2. The selected mass region was around 130 u. The TOF and corresponding mass spectra are shown in Figure 6.5. The spectrum contains ^{133}Cs ions, $^{128-134,136}$Xe ions and the SF$_6$-gas breakup fragments $^{32-34}$S^{19}F$_5$. Xenon and SF$_6$ were ionized in the electron impact ion source, which was mounted at the SY on top of the MR-TOF-MS. The caesium ions were produced in a thermal ion source placed at the same position as the electron impact ion source. The TFS-spectrum has a mass resolving power of about 1700, therefore, it is not possible to resolve the isobars at 128 u and 129 u. For this reason these two mass lines were discarded in the calibration. For the determination of c and t_{TFS} in the TFS mode ($N_{IT} = 0$) Equation 5.2 was used with b fixed to 0. This resulted in

$$\begin{aligned} c =& 0.068811 \pm 1.1 \cdot 10^{-5}\ u/\mu s^2\ , \\ t_{TFS} =& 0.252 \pm 0.003\ \mu s\ . \end{aligned} \tag{6.1}$$

In the following, for the Time-Resolved Calibration (*TRC*) of the individual spectra with multiple turns included, c and t_{TFS} were kept fixed to the determined values and the time-dependent calibration parameter b was the only free parameter. This was possible because in all spectra the calibrant and the IOI have performed the same number of turns. For this case, the parameters c and b are correlated, see Equation 5.3.

6.2.2. Measured Masses of $^{211-213}$Fr Ions

The francium isotopes $^{211-213}$Fr were transported together through the FRS with the selected magnetic fields for the reference ion ^{213}Fr^{87+}. The fragments were identified in the FRS with the B$\rho - \Delta$E*-TOF method. The fragments were simultaneously stopped in the CSC and extracted and transported to the MR-TOF-MS. The measurements with $^{211-213}$Fr ions were performed with 128 isochronous turns in the analyser of the MR-TOF-MS. This condition resulted in a mass resolving power of about 200000.

Due to the selected mass window of 3 u, the lighter francium isotopes at 211 u and 212 u could be simultaneously accessed in the measurement of ^{213}Fr. For the mass of 211 u, the abundant ^{211}Pb peak, originated from the ^{223}Ra α source in the CSC, was used as a calibrant to determine the parameter b in the TRC.

The three masses of the francium isotopic chain were measured several times with the MR-TOF-MS. The peak shape in the mass measurements was redetermined for each run from the abundant ^{211}Pb mass distribution. The fits were done with one exponential tail on each side, as well as with and without a Gaussian side peak, depending on the requirements of the peak shape of ^{211}Pb.

The mass-to-charge ratios of the singly-charged francium isotopes were always redetermined in the different measurements. The measurements can be considered as independent, because they were performed with different conditions or on different days. The masses of ^{211}Fr and ^{212}Fr

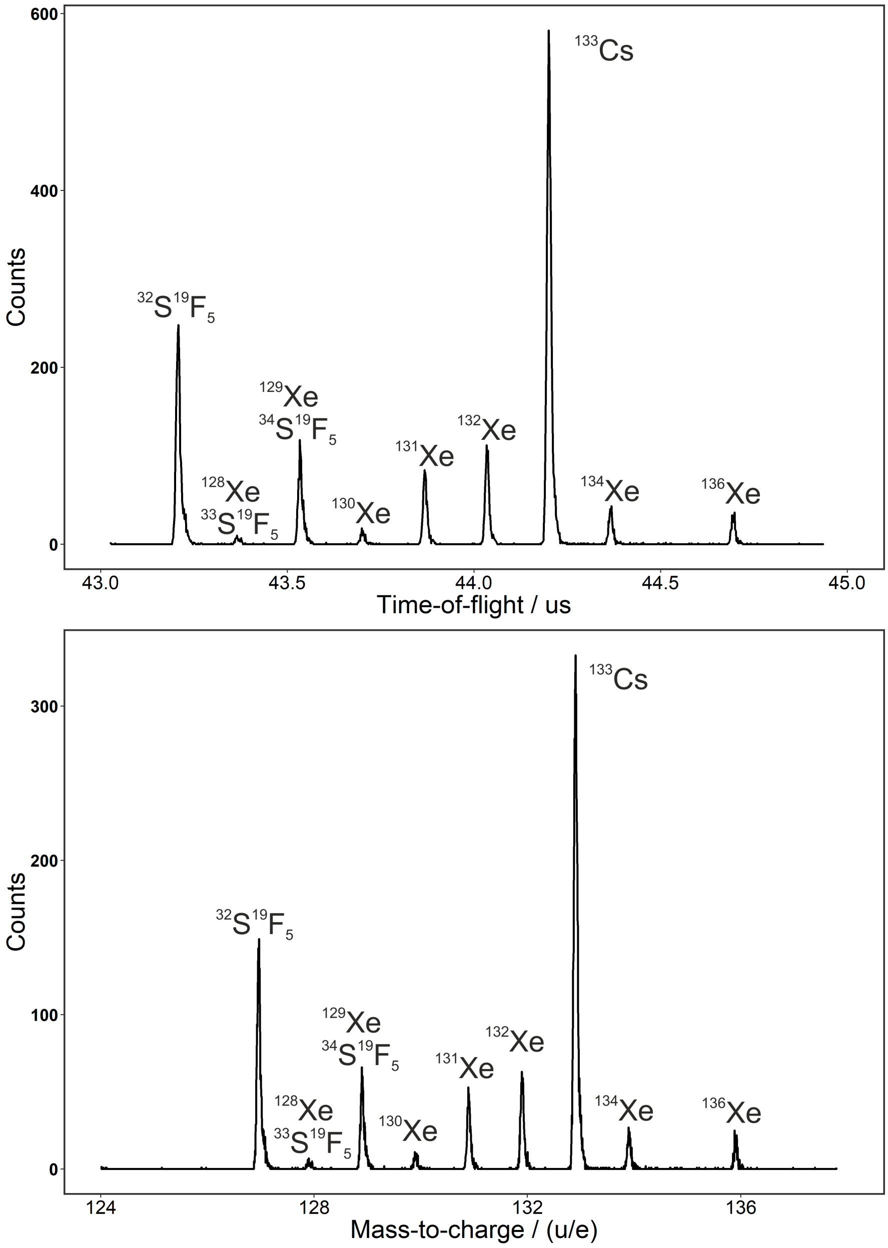

Figure 6.5.: Time-of-flight (top panel) and mass spectrum (bottom panel) recorded in the time-focus-shift mode ($N_{IT} = 0$). The distributions in time and mass corresponds to ^{133}Cs, $^{128-134,136}$Xe and $^{32-34}$S^{19}F$_5$ ions. The spectrum was used to determine the calibration parameters c and t_{TFS} for the experiment with 1 GeV/u uranium fragments.

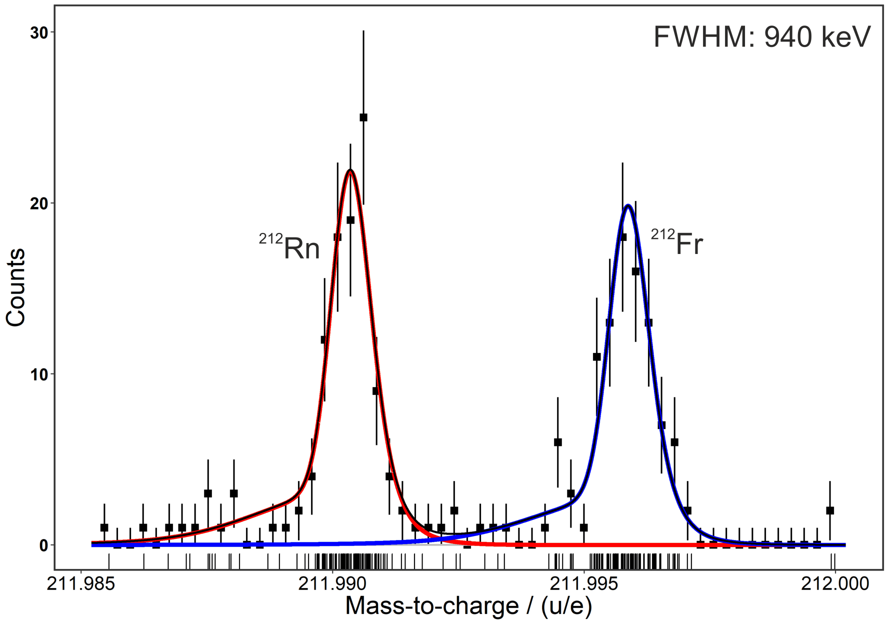

Figure 6.6.: Measured mass distribution of ^{212}Rn and ^{212}Fr ions. The distributions are fitted by a double hyper-EMG (red line for ^{212}Rn and blue line for ^{212}Fr) with one exponential tail at each side plus a Gaussian side peak. The peak-shape parameters were determined by the high intense ^{211}Pb distribution and scaled to the masses of ^{212}Rn and ^{212}Fr. The histogram of the measured spectrum is only drawn to guide the eye. The evaluation was based on measured unbinned data (rug graph) with the WMLE procedure.

were determined in double-peak fits together with the masses of ^{211}Pb and ^{212}Rn, respectively. ^{213}Fr appeared mostly as a single-peak, only in a few measurements the neighbouring ^{213}Rn mass distribution had to be considered and a double-peak fit was required.

The measured mass distributions of ^{212}Rn and ^{212}Fr ions, fitted with double peaks, are shown in Figure 6.6.

The mass and ME values of $^{211-213}$Fr for the different measurements are listed with their total errors in Table B.1, B.2 and B.3. The results of the single measurements are combined and weighted by their errors (Equation 5.11) and the resulting mean value for each isotope is given in Table 6.1.

Isotope	ME [keV]	Total Error [keV]	Mass [u]	Total Error [u]
^{211}Fr	-4061	40	210.9956399	4.25E-05
^{212}Fr	-3530	28	211.9962099	3.01E-05
^{213}Fr	-3562	12.3	212.9961756	1.35E-05

Table 6.1.: Measured mass and ME values for $^{211-213}$Fr atoms. (The values correspond to neutral atoms.) The given mass and ME values are mean values determined from single measurements weighted by their errors (Equation 5.11).

^{213}Fr is with a total error of 12.3 keV (1.35E-05 u), corresponding to an accuracy of $6 \cdot 10^{-8}$, the exotic nuclei with the highest accuracy measured with the MR-TOF-MS at the FRS-IC. This accuracy is better by a factor of two compared to what was reached before with other MR-TOF-MS systems in the same mass region [Rosenbusch et al. (2018)]. The achieved accuracy has the same order of magnitude as the highest ever reached accuracy with an MR-TOF-MS of $3.5 \cdot 10^{-8}$

[Kimura et al. (2018)].

The masses of the chain of francium isotopes was measured since the 1950s several times in different laboratories. In particular, it was investigated systematically at the ISOL facility ISOLDE, where it can be produced with high production rates. Besides direct mass measurements, the francium chain was studied intensively via Q_α-values. The isotopes $^{211-213}$Fr have been measured and discussed by [Kuusiniemi et al. (2005); Valli et al. (1967)], [Bowman et al. (1982); Hornshoj et al. (1974); Kuusiniemi et al. (2005); Momyer et al. (1955)] and [Bowman et al. (1982); Devaraja et al. (2015); Hornshoj et al. (1974); Kuusiniemi et al. (2005); Valli et al. (1967)], respectively.

The half-life of the francium isotopes near the closed neutron shell N=126 are relatively long (3.1 min for ^{211}Fr, 20.0 min for ^{212}Fr and 34.14 s for ^{213}Fr). For this reason, they are perfect test cases for our experiments to compare with Penning trap mass measurements. The ground-state masses of ^{211,212}Fr were measured with the Penning trap mass spectrometer ISOLTRAP with a resolving power of 500000 [Bollen et al. (1992)]. In the measurement ME values of -4177(24) keV for ^{211}Fr and -3553(26) keV for ^{212}Fr were determined. 15 years later the isotope chain was investigated again by the ISOLDE Penning trap mass spectrometer [Kowalska et al. (2009)]. In these measurements ME values of -4140.1(11.7) keV, -3516.0(8.8) keV and -3553.0(5.1) keV were determined for the isotopes $^{211-213}$Fr, respectively.

The ground-state masses of ^{211}Fr and ^{213}Fr were investigated in earlier experiments at the FRS-IC as well [Ebert (2016); Jesch (2016)]. The masses were measured with the MR-TOF-MS, resulting in 210.995389(154) u and 212.996016(207) u respectively. However, the previous experiments were limited in resolving power. Recently, significant improvements were obtained by technical changes described in reference [Ayet San Andrés (2018)]. In addition, the data evaluation was further developed.

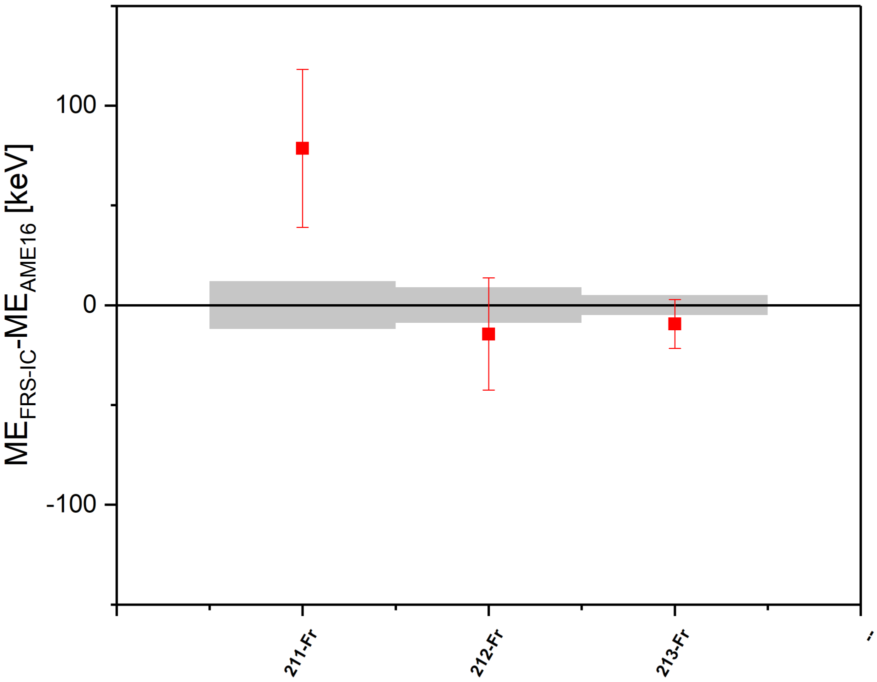

Figure 6.7.: Difference of measured MR-TOF-MS Mass Excess (*ME*) values (full red squares) of $^{211-213}$Fr atoms and the corresponding AME 2016 [Wang et al. (2017)] values, both data sets corresponds to neutral atoms. The AME 2016 errors are indicated by the grey bars, whereas the total errors of the MR-TOF-MS results are given by the red bars.

The weighted averaged ME values determined in MR-TOF-MS measurements are compared with the AME 2016 [Wang et al. (2017)] values in Figure 6.7. The determined ME values of ^{212,213}Fr are in good agreement with the AME values based on Penning trap results. The measured MR-TOF-MS ME value of ^{211}Fr is about two sigma larger than the one determined with the Penning trap. A possible reason for this difference can be the influence of the high intensity ^{211}Pb peak close to ^{211}Fr mass distribution formed by less than 10 counts.

6.2.3. Measured Masses of ^{212,213}Rn Ions

The ^{212}Rn nucleus has a closed shell with 126 neutrons and a half-life of 23.9 min whereas the neighboring isotope ^{213}Rn has only a half-life of 19.5 ms. Previously, the ground-state masses of ^{212,213}Rn nuclei were only determined via their Q_α values. Both mass values are directly measured with the MR-TOF-MS at the FRS-IC for the first time.

In the mass measurement, ^{212}Rn fragments were transported through the FRS together with ^{212}Fr and ^{213}Fr ions and also in the field setting for ^{213}Rn ions. The actual mass measurements of ^{212}Rn ions were performed under different FRS settings and by scanning the range distribution via variation of the homogeneous degrader thickness.

Due to the high sensitivity of the MR-TOF-MS, low abundant exotic nuclei can be identified and their masses can be measured. ^{212,213}Rn has been measured in the MR-TOF-MS with 128 isochronous turns in the analyser. This selection corresponds to a total flight time of about 5.8 ms and a mass resolving power of about 200000. ^{213}Rn was independently identified by the appearance of its α-decay daughter ^{209}Po, which was observed in the mass spectrum with 129 isochronous turns in the analyser.

The peak shape parameters of the fit function were determined by the measured mass distribution for the intense ^{211}Pb peak. The same procedure was done for the time-resolved calibration. A typical hyper-EMG WMLE-fit is shown in Figure 5.6. The fit of the ^{211}Pb distribution requires one exponential tail at each side plus an additional Gaussian side peak. This side peak results from instrumental imperfections and ion-optical aberrations. ^{212}Rn and ^{212}Fr are close to each other in their mass-to-charge ratio. Therefore, the mass distributions have to be fitted by two distributions with a partial overlap (double-peak fit). The peak shape parameters were scaled to the average of the isobars ^{212}Rn and ^{212}Fr and to the ^{213}Rn peak. An example of the measured double-peak structure of the isobars ^{212}Rn and ^{212}Fr is shown with the corresponding fit-results in Figure 6.6.

Isotope	ME [keV]	Total Error [keV]	Mass [u]	Total Error [u]
^{212}Rn	-8600	30	211.9907673	3.21E-5
^{213}Rn	-5723	66	212.9938561	7.03E-05

Table 6.2.: Results of the experimental mass and Mass Excess (*ME*) values of $^{212-213}$Rn.

The individual mass-to-charge ratios were evaluated and the mass and ME values of the different measurements are listed in Table B.4. The final mass value for the singly-charged ^{212}Rn ions was determined by averaging the single measurements weighted by their individual errors (Equation 5.11). ^{213}Rn was only measured once. The final mass and ME values are listed in Table 6.2.

As described in Section 5.4 each total error of the mass value for each individual isotope is separately calculated in each measurement. The quadratic sum of the different error components determines the total error (Equation 5.13). In Table 6.3 the different error contributions for the ^{213}Rn mass value are presented. It is observed that the error of the ^{213}Rn mass value is dominated by the statistical error and the error due to an unknown unresolved contamination. The statistical error corresponds to 165 ions in the mass measurement. For the estimation of the error component caused by an unknown contamination of 32 ions, a contamination of about 20 % was assumed in the simulation. Since the calibrant ion for the TRC was continuously produced and was travelling the same number of turns as the IOI, the TRC error and the c error are 0. No bias correction for overlapping peaks was done and the MRS was operated during the entire measurement with the same number of isolation cycles. No known isobaric contamination had to be considered.

The different error contributions for the measured mass values of each isotope were separately evaluated in each measurement. The dominant error contribution is always dependent on the conditions of the mass measurement. The total error represents the weighted sum of the individual contributions with the assumption that the different measurements were independent.

Statistical error $\left[10^{-7}\right]$	2.01
Peak shape error $\left[10^{-7}\right]$	0.07
Bias correction error $\left[10^{-7}\right]$	0
TRC error $\left[10^{-7}\right]$	0
Calibrant error $\left[10^{-7}\right]$	0.21
c error $\left[10^{-7}\right]$	0
t_{TFS} error $\left[10^{-7}\right]$	0.05
NIE error $\left[10^{-7}\right]$	0.44
MRS error $\left[10^{-7}\right]$	0
Contamination error $\left[10^{-7}\right]$	2.58
Iso error $\left[10^{-7}\right]$	0
Total error $\left[10^{-7}\right]$	3.30
Total error [keV]	66

Table 6.3.: Errors listed for the individual contributions for the measured ^{213}Rn mass value. The square root of the quadratic sum of the different components represents the total error (Equation 5.13).

The ^{212}Rn mass value is known from its α-decay (^{212}Rn(α)^{208}Po), but not directly measured. In the mid of the 1950s the kinetic energy of the emitted α-particle was measured with a magnetic spectrograph [Momyer et al. (1955)]. An α-energy of 6264(5) keV was measured, from this a Q_α value of 6392.3(5) keV can be determined (Equation 3.1). In the α-spectrum the peak corresponding to ^{212}Rn was well separated. Therefore is was possible to verify the identification of the α-line by measuring the half-life of ^{212}Rn. ^{211}At and ^{211}Rn were evaluated from the same α-spectrum and are in agreement with other literature values. The α-energy was investigated again by [Golovkov et al. (1971)] resulting in 6262(3) keV, corresponding to a Q_α value of 6382.5(3) keV. The ME value of ^{212}Rn was directly determined for the first time in this work. The measured weighted mean value of the ME of ^{212}Rn is compared to the primary literature values and the AME-2016 evaluation [Wang et al. (2017)], see Figure 6.8. Our measured ME value for the neutral ^{212}Rn atom is about 2 σ larger than the one determined by [Momyer et al. (1955)] and [Golovkov et al. (1971)]. This observation is most likely not due to a population of any excited state, since the known excited states have a half-life of a few hundred ns only and thus would not been observed with the MR-TOF-MS. From the peak shape in the measurements no hint arises for any underlying additional structure, since the measured FWHM of the

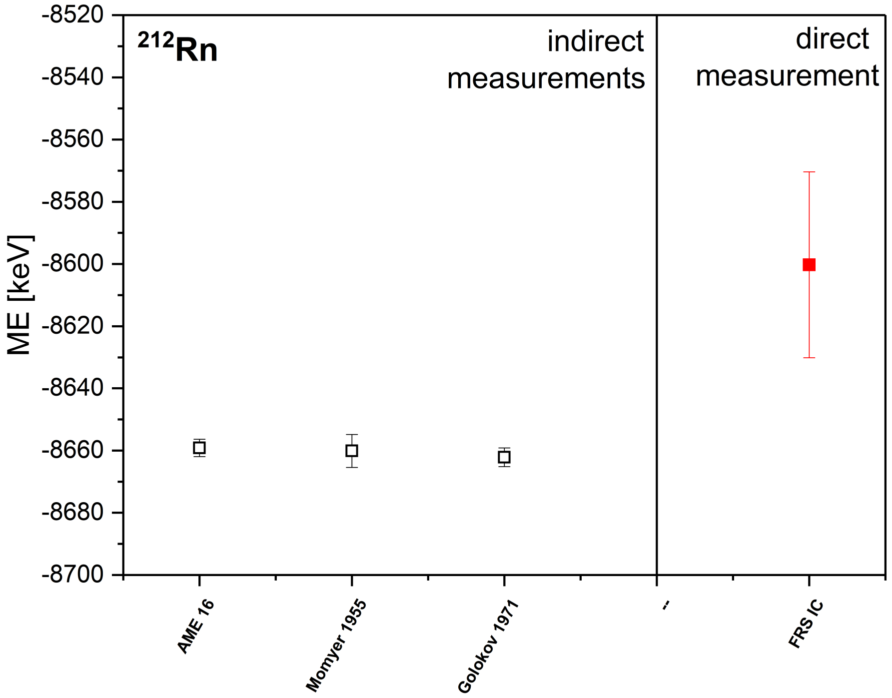

Figure 6.8.: The weighed mean value of the Mass Excess (*ME*) of ^{212}Rn atoms (full red square), measured with the MR-TOF-MS, is compared to the literature values from α-decay measurements [Golovkov et al. (1971); Momyer et al. (1955)] and to the AME 2016 value [Wang et al. (2017)] (both open black squares). The ME value of ^{212}Rn atoms was directly determined for the first time in this work.

^{212}Rn peak is as expected from scaling from ^{211}Pb. However, the possibility of a contamination with ^{212}At can not be fully excluded. The difference in the ME values of these two isobars is 32 keV and their expected range distributions are overlapping. Nonetheless, in the FRS PID ^{212}Rn appears as the second most abundant peak besides ^{213}Rn. ^{212}At cannot be clearly distinguished from potential background signals, therefore, it could appear in small amounts which. This could explain the observed shift in ME value.

For a long time the mass of ^{213}Rn was only known via its α-decay. The α-decay energy of ^{213}Rn was determined for the first time in studies at the Lawrence Radiation Laboratory in Berkeley [Valli et al. (1967, 1970)]. Neutron deficient isotopes were produced in reaction with light beams impinging on bismuth, lead, thallium and gold targets. In these experiments α-spectroscopy was performed Si semiconductor detectors. The kinetic energies of the emitted α-particles were measured for the decays of ^{213}Rn(α)^{209}Po and the Q_α value determined. In more recent α-spectroscopy experiments using different production reactions [Heßberger et al. (2000); Kuusiniemi et al. (2001); Liu et al. (2005)] the first results were confirmed. The ground state mass of ^{213}Rn has been measured directly with the MR-TOF-MS at the FRS-IC for the first time [Jesch (2016)]. However, only 27 ions were recorded in this pilot experiment. Therefore, the mass ^{213}Rn was remeasured with higher statistics and an improved MR-TOF-MS. The new ME value was compared to the literature values and the AME 2016 result [Wang et al. (2017)] in Figure 6.9. The measured ME value of this experiment is in excellent agreement with the ME values determined via α-decay spectroscopy. The comparison to the value determined in reference [Jesch (2016)] clearly shows the improvement of the performance of the MR-TOF-MS at the FRS-IC. The weighted average of the two direct ME values was calculated to be -5765(63) keV and is also given in Figure 6.9.

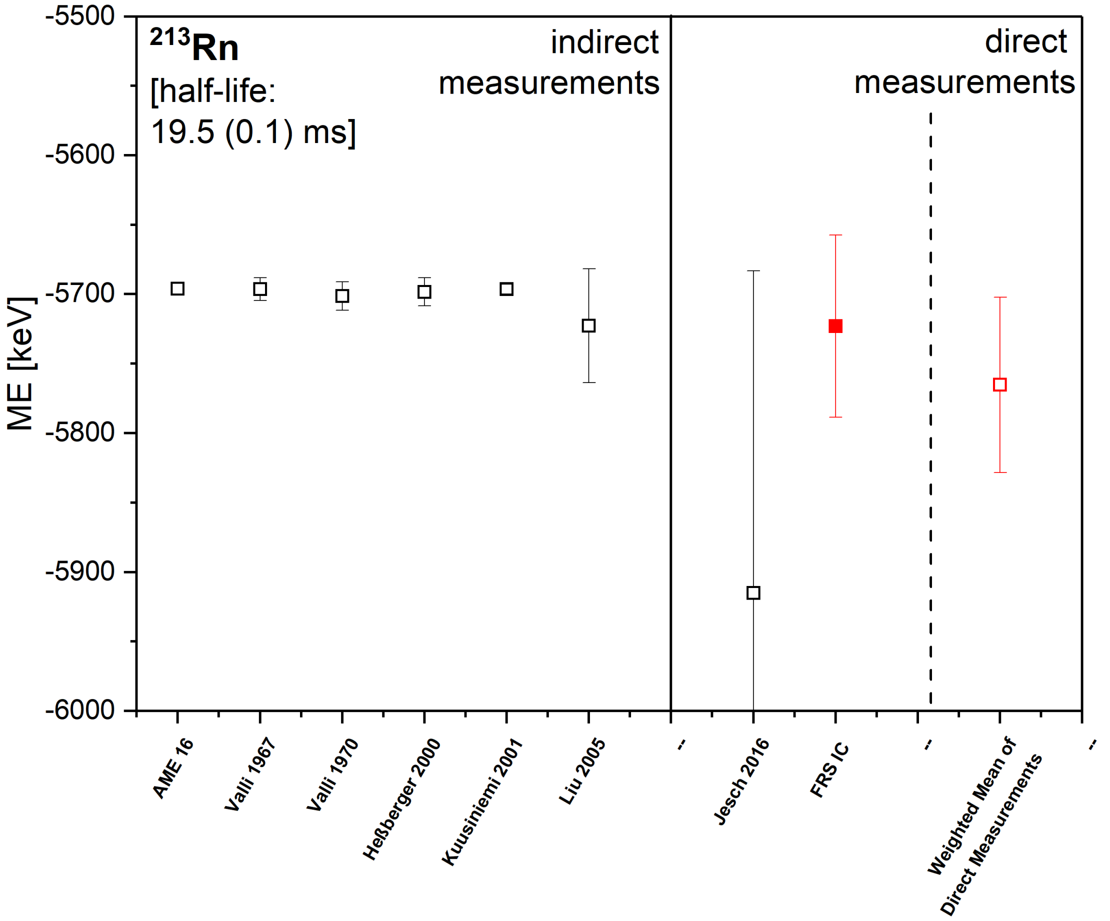

Figure 6.9.: Comparison of measured Mass Excess (*ME*) of ^{213}Rn atoms. The present experiment (full red square) agrees well with the literature values from α-spectroscopy [Heßberger et al. (2000); Kuusiniemi et al. (2001); Liu et al. (2005); Valli et al. (1967, 1970)] and the AME 2016 value [Wang et al. (2017)] (open black squares). The weighted average of the two directly measured ME values from MR-TOF-MS (open red square) is given in the rightmost panel.

6.2.4. Measured Masses of ^{218}Rn Ions

The short-lived ^{218}Rn nucleus, with a half-life of only 33.75(15) ms [Suliman et al. (2012)], is part of the α-decay chain of ^{230}U. ^{230}U is under discussion to be used for radio-nuclear applications in medicine [Alfassi et al. (2006)].

The mass-to-charge ratio of ^{218}Rn was measured with the MR-TOF-MS with 128 isochronous turns. A mass resolving power of about 170000 was achieved in this measurement. In the measurement a mass window of 3 u was covered. The high abundant ^{219}Rn, the α-decay daughter of the ^{223}Ra source in the CSC, was used for calibration to determine b in the TRC and the peak shape parameters. The peak shape of the ^{219}Rn mass distribution requires one exponential tail on both sides. The peak shape parameters were scaled to ^{218}Rn.

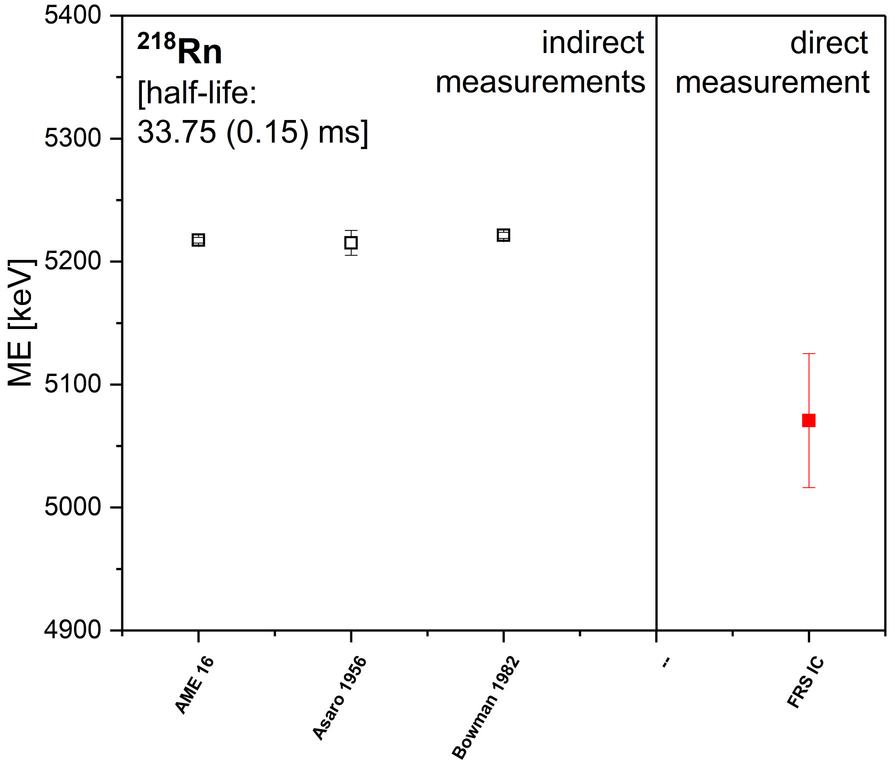

Figure 6.10.: Comparison of measured Mass Excess (*ME*) of ^{218}Rn atoms. The ME value of the present experiment (full red square) is systematically lower by more than 2 sigma values from α-decay measurements [Asaro and Perlman (1956); Bowman et al. (1982)] and the AME 2016 value [Wang et al. (2017)] (open black squares).

The mass-to-charge ratio of ^{218}Rn was determined multiple times with different thicknesses of the homogeneous degrader placed at the final focal plane of the FRS. This experimental procedure may lead to changes of the ion-to-background ratio. The measurements were done with different statistics from 90 down to only four ions. The individual mass-to-charge ratios were evaluated and the ME values were determined. The mass and ME values of the different measurements are listed in Table B.5. The final mass for the singly charged ^{218}Rn was determined by averaging the single measurements weighted by their individual errors (Equation 5.11). The final value is given in Table 6.4. The ME of ^{218}Rn was directly determined for the first time in this work.

In the past the mass of ^{218}Rn was determined in α-spectroscopy experiments [Asaro and Perlman (1956); Bowman et al. (1982)]. In Figure 6.10 our directly determined ME value is

Isotope	ME [keV]	Total Error [keV]	Mass [u]	Total Error [u]
^{218}Rn	5071	54	218.0054436	5.85E-5

Table 6.4.: Measured mass and ME values of ^{218}Rn atoms with the MR-TOF-MS. The given ME value is the mean value determined from the results of the single measurements and weighted by their errors (Equation 5.11).

compared to the values from α-decay spectroscopy. The present result is about 2.7 σ lower. A contamination of other exotic nuclei is not possible in this case, since all neighbouring isobars would be well separated in mass. However, ^{218}Rn has a positive ME value, in principle the influence of molecular contaminants could be possible. This possibility was investigated with a combinatorial search and all reasonable molecules were discarded as contaminants.

6.2.5. Measured Masses of ^{212g,m}At Ions

The ^{212}At nucleus has a half-life of 314 ms for the $(1)^-$ ground state and a $(9)^-$ isomeric state with a half-life of 119 ms. Both states decay via α-decay. The branch of internal conversion via γ emission is less than 1 % [Browne (2005)].

In the measurement the magnetic fields of the FRS were set to centre the reference fragment ^{216}Fr. The goal was to produce ^{212}At ions via the α-decay of ^{216}Fr. Both nuclei, ^{216}Fr and ^{212}At, have a $(9)^-$ isomeric state. The $(9)^-$ isomer of ^{216}Fr decays like its ground state $(1)^-$ via α-decay [Kurcewicz et al. (2007)]. A decay scheme is shown in Figure 6.11. Both, the ground state and the $(9)^-$ isomer have a similar half-life of 700 ns and 850 ns, respectively. Therefore both states decay in the CSC, where the recoil energy can be absorbed by the helium gas. In this way, the ground and isomeric state of ^{212}At is populated and can be measured in the MR-TOF-MS.

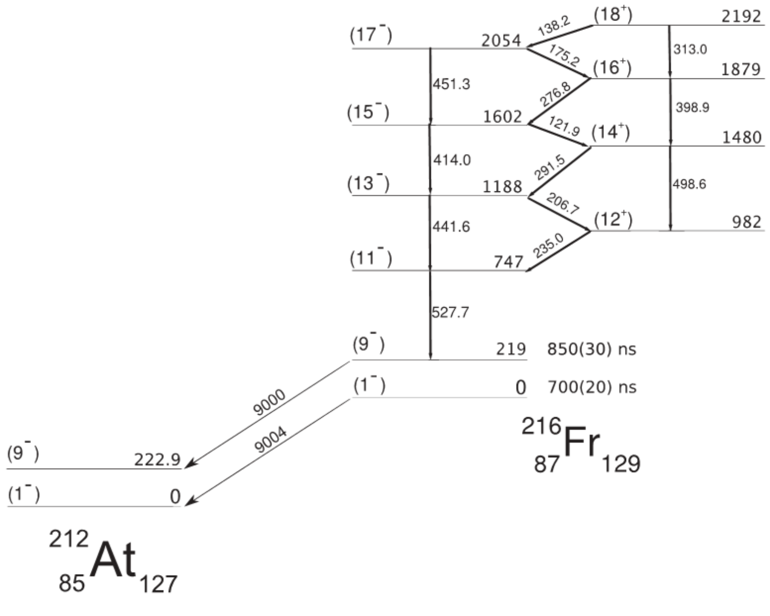

Figure 6.11.: α-decay scheme of ^{216}Fr taken from [Kurcewicz et al. (2007)].

Kurcewicz et al. [Kurcewicz et al. (2007)] reported an isomeric ratio for the $(9)^-$ state of 0.28(1) for ^{212}At and 0.31(2) for ^{216}Fr. The latter nucleus was populated via α-decay of ^{220}Ac. Since mainly the ground state of ^{216}Fr decays (95(1) %), this suggests a significant population of

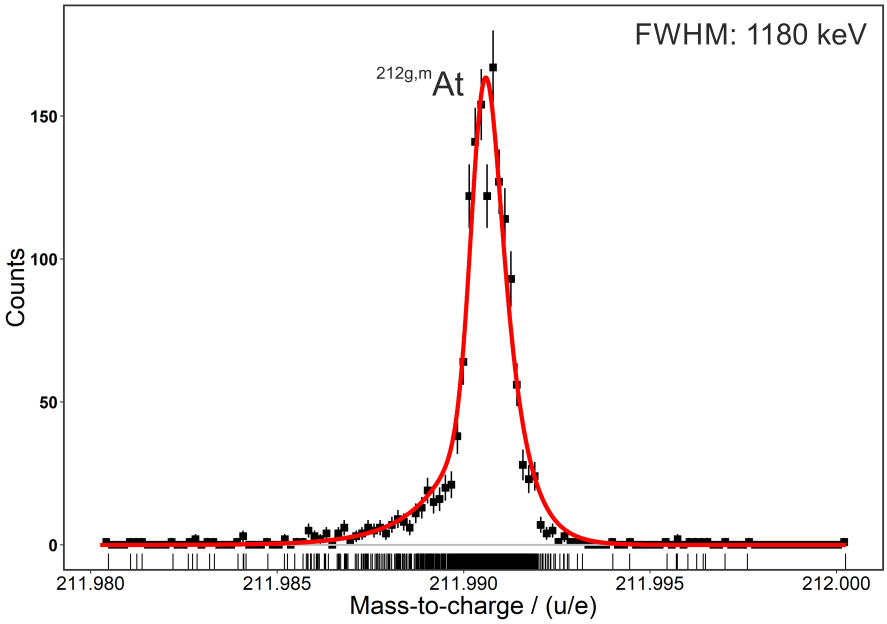

Figure 6.12.: Measured mass distribution of ^{212g,m}At fitted by a hyper-EMG (red line) with one exponential tail to each side. The peak shape parameters were determined by the high statistic ^{211}Pb peak and scaled for the mass of ^{212}At. The histogram of the measured spectrum is only drawn to guide the eye. The evaluation was based on measured unbinned data (rug graph) with the WMLE procedure.

the isomeric state. In a later investigations [Wojtasiewicz et al. (2009)] the isomeric ratio for the $(9)^-$ state in ^{212}At was again determined. The obtained value was 0.09(2) which differs strongly from the reported value of reference [Kurcewicz et al. (2007)].

^{212g,m}At ions were measured in the MR-TOF-MS with the selection of 128 isochronous turns. This condition yielded a mass resolving power of about 180000. With the selected 128 isochronous turns a mass window of 3 u can be covered. The ions within this mass window have the same number of turns. The peak shape parameters in this measurement were determined from the mass distribution of ^{211}Pb which was obtained from the ^{223}Ra α-source in the CSC. The ^{211}Pb shape parameters were scaled to the ^{212}At mass. The hyper-EMG fit required one exponential tail on each side. Since it was not possible to resolve the ground and the isomeric state in ^{212}At with achieved resolving power, the mass value was determined with a single-peak fit (Figure 6.12), a broadening of the peak was not observed. The published excitation energy of the $(9)^-$ state in ^{212}At is 223(7) keV [Jain et al. (2015)].

The mass value determined from the WMLE-fit of 211.9908859(922) u was converted into the ME value of -8490(86) keV. With the known excitation energy of 223(7) keV [Jain et al. (2015)] following the procedure in Section 5.4 (subtracting and adding half of the known excitation energy, respectively) the ME values of the ground and the isomeric state were estimated and are shown in Figure 6.13. The resulting ME values are given in Table 6.5.

The ground state and isomer masses of ^{212g,m}At had not yet been directly measured. Their mass values are determined in α-spectroscopy [Fransson et al. (1976); K. and Hyde (1968); Liang et al. (1996); Reeder (1970)].

The present mass values for ^{212g,m}At atoms, deduced by subtracting and adding half of the known excitation energy, agree well with the previous indirectly measured values. Therefore, it can be concluded, that both states are equally populated.

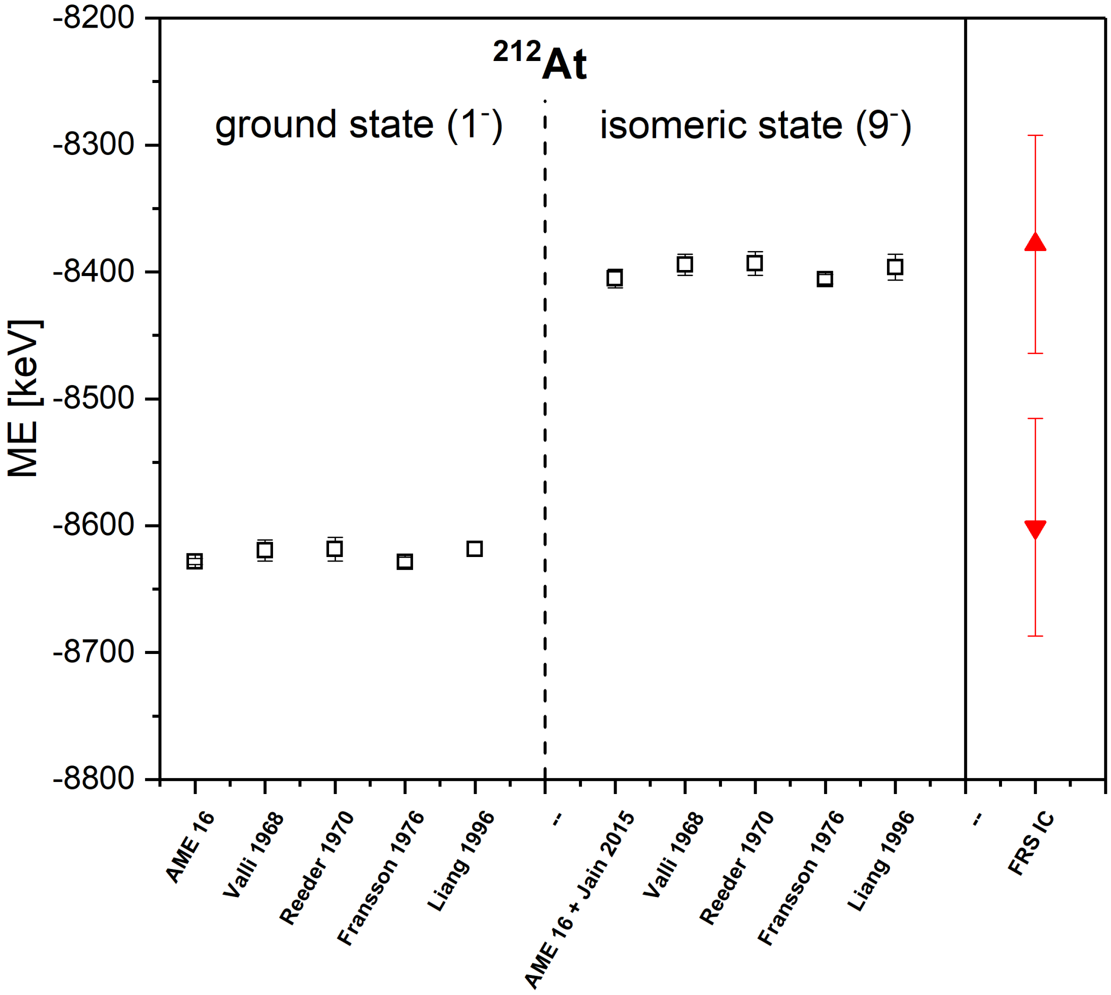

Figure 6.13.: Measured ME values for the ^{212g,m}At nucleus which was populated via the α-decay of ^{216}Fr. In the present measurement ground and isomeric state could not be resolved. Therefore, the ME values of the ground and the isomeric state were estimated by subtracting and adding half of the known excitation energy, respectively. The resulting ME values are compared to literature values (open black squares) for the ground and the isomeric states. The literature values were determined from α-decay measurements [Fransson et al. (1976); K. and Hyde (1968); Liang et al. (1996); Reeder (1970)]. In addition the AME 2016 value [Wang et al. (2017)] for the ground state is given. The ME value of the isomeric state was obtained via the combination of the ME value for the ground state from the AME 2016 and the value of the excitation energy of the isomeric state from reference [Jain et al. (2015)].

Isotope	ME [keV]	Total Error [keV]	Mass [u]	Total Error [u]
^{212g}At	-8601	86	211.9907662	9.22E-5
^{212m}At	-8378	86	211.9910056	9.22E-5

Table 6.5.: Results of the ME values of ^{212g,m}At. The ground and the isomeric state could not be resolved in the measurement. Therefore, ME value of the ground and the isomeric state were estimated by subtracting and adding half of the known excitation energy, respectively.

6.2.6. Measured Masses of ^{217}At Ions

The mass of ^{217}At ions has been measured with the MR-TOF-MS. It has a half-life of 32.3 ms. In the mass measurements were performed with 128 isochronous turns in the MR-TOF-MS. This condition determined the achieved mass resolving power of about 170000. In the measurement a mass window of 3 u was covered. This allowed to measure ^{219}Rn ions simultaneously with the ^{217}At ions. The isotope ^{219}Rn appears in the spectrum with high abundance and was therefore used to calculate b in the TRC and to determine the peak-shape parameters. The LS-fit with a hyper-EMG required one exponential tail on both sides. The peak-shape parameters were scaled from the mass ^{219}Rn distribution to ^{217}At. The measured mass and ME values are given in Table 6.6. As described in Section 5.4 the total error is square root of the quadratic sum of all individual error components (Equation 5.13). All error components were separately calculated for each measurement and isotope. In Table 6.7 the error budget of ^{217}At is shown. The error of ^{217}At is dominated by the statistical error, which corresponds to only 19 ions in the measurement. Since the calibrant ion for the TRC was continuously produced and undergoing the same number of turns as the IOI, the TRC error and the c error are 0. No bias correction for overlapping peaks was done and the MRS was operated during the entire measurement with the same number of isolation cycles. No unknown or known isobaric contamination had to be considered.

Isotope	ME [keV]	Total Error [keV]	Mass [u]	Total Error [u]
^{217}At	4433	135	217.004759	1.45E-4

Table 6.6.: Measured mass and ME values for ^{217}At atoms.

Statistical error $[10^{-7}]$	6.66
Peak shape error $[10^{-7}]$	0.33
Bias correction error $[10^{-7}]$	0
TRC error $[10^{-7}]$	0
Calibrant error $[10^{-7}]$	0.39
c error $[10^{-7}]$	0
t_{TFS} error $[10^{-7}]$	0.05
NIE error $[10^{-7}]$	0.44
MRS error $[10^{-7}]$	0
Contamination error $[10^{-7}]$	0
Iso error $[10^{-7}]$	0
Total error $[10^{-7}]$	6.69
Total error [keV]	135

Table 6.7.: The errors are listed for the individual, independent error components for the ^{217}At mass measurement. The quadratic sum of the different components results in the total error (Equation 5.13).

The mass of ^{217}At was previously only known from α-spectroscopy experiments [Bowman et al. (1982); Valli (1964); Vorob'ev et al. (1960); Vylov et al. (1977); Walen (1962)] The values from literature and the ME value from the MR-TOF-MS measurement are compared in Figure 6.14. The directly determined ME value with the MR-TOF-MS agrees with the values from the indirect method.

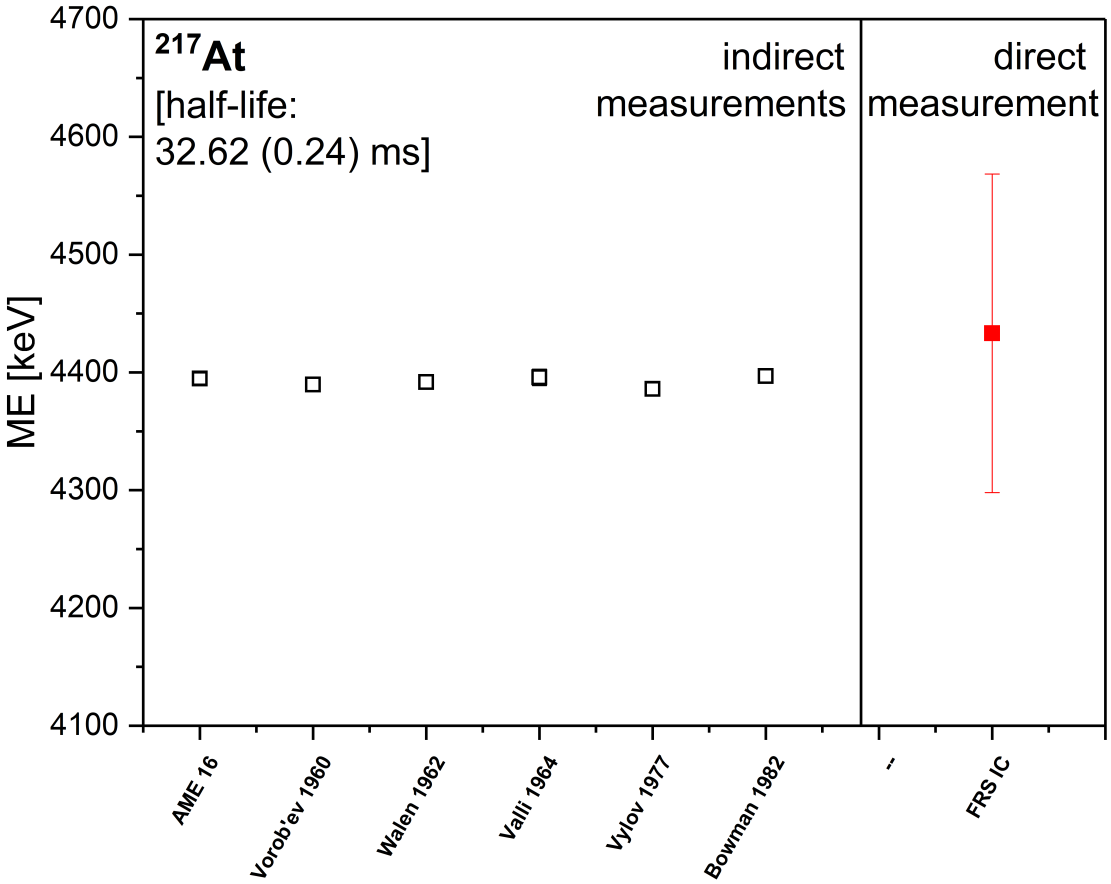

Figure 6.14.: The measured mass and ME values for ^{217}At are compared to literature values (open black squares) from α-decay measurements [Bowman et al. (1982); Valli (1964); Vorob'ev et al. (1960); Vylov et al. (1977); Walen (1962)] and to the AME 2016 value [Wang et al. (2017)].

6.2.7. Measured Masses of ^{211g,m}Po Ions

The ^{211g,m}Po is an interesting nucleus, since it has a long half-life of 516 ms and has an $(25/2)^+$-isomeric state, with a half-life of 25.2 s. The ground state and the isomeric-state decay with close to 100 % via α-decay. The population of the isomeric state has been studied in different production reactions, such as ^{208}Pb(α,n) [Cottle et al. (2017)], ^{210}Po(d,p) [Bhatia et al. (1979)] or incomplete fusion of ^{6,7}Li+^{209}Bi and ^{9}Be+^{208}Pb along with the following breakup reactions [Gasques et al. (2006)].

In the present experiment, the ground and isomeric state of ^{211}Po were produced via fragmentation of 1 GeV/u ^{238}U projectiles in a beryllium target, separated with the FRS and finally stopped in the CSC for mass measurement with the MR-TOF-MS. In the mass measurement, the ^{211}Po ions travelled 192 isochronous turns in the analyser of the MR-TOF-MS. This condition determined the achieved mass resolving power of about 300000. This is not enough to resolve the ground state of ^{211}Pb and isomeric state of ^{211}Po which are separated by 500 keV.

^{211}Pb ions were used for calibration although the mass distributions have overlap in their spectra. Therefore, the source was blocked by an electric field (220 V, DC) during the measurement of ^{211g,m}Po ions. Despite of this confinement a small amount of ^{211}Pb ions were still in ^{211g,m}Po mass spectrum (2 cts./min).

Therefore the measurement was calibrated at the beginning and at the end of the measurement, when no beam was impinging in the CSC. The peak shape was taken from the high statistics ^{211}Pb peak without ^{211}Po being present, it required one exponential tail on each side. ^{211g,m}Po was fitted with a triple hyper-EMG, considering the underlying ^{211}Pb peak. In the WMLE-fit the rate and the mass of ^{211}Pb were used as fixed values, estimated as described above. The fit is shown in Figure 6.15. The mass-to-charge ratio of the ground and the isomeric state of ^{211}Po were determined and converted in ME values. The final values are listed in Table 6.8.

Isotope	ME [keV]	Total Error [keV]	Mass [u]	Total Error [u]
^{211g}Po	-12692	117	210.9863751	1.26E-4
^{211m}Po	-11047	111	210.9881408	1.19E-4

Table 6.8.: Results of the Mass Excess (*ME*) of ^{211g,m}Po in keV produced in projectile fragmentation with a 1 GeV/u ^{238}U beam impinging on a beryllium target.

The investigations of ^{211}Po nuclei started already in the 1930s with first measurements of the α-decay chain of thorium [Lewis and B.V. (1934)], which was evaluated about 10 years later [Seaborg and Perlman (1948)]. From this point on, ^{211}Po was used already as a standard for other measurements [Meinke et al. (1952)]. The α-decay measurements were continued in several studies and α-decay energies of 7430(50) keV [Jentschke et al. (1954)], 7440(10) keV [Perlman et al. (1962)], 7448.3(2) [Walen et al. (1962)], 7460(20) keV [Hahn et al. (1969)], 7450(3) keV [Golovkov et al. (1969)], 7448(10) keV [Valli et al. (1970)], 7448(2) keV [Bowman et al. (1982)] and 7450(3) keV [Lambrecht and Mirzadeh (1985)] were determined for the ground state in different energies. These lead to Q_α values of 7570(50) keV, 7594.3(3.0) keV, 7594.5(0.5) keV, 7604(20) keV, 7594.3(3.0) keV, 7592(10) keV, 7592(2) keV and 7600.6(2.0) keV, respectively. In addition, the α-decay of the $(25/2)^+$-isomer was investigated and the kinetic energy of the α-particles measured. decay and α-decay energies of 8700(50) keV [Jentschke et al. (1954)], 8870(10) keV [Perlman et al. (1962)], 8885(5) keV [Bowman et al. (1982)] and 8885(15) keV [Kudo et al. (1989)], corresponding to Q_α values of 8870(50) keV, 9047(10) keV, 9057.1(5.1) keV and 9049(15) keV, respectively, were determined. Besides the measured Q_α value for the isomeric state given in [Jentschke et al. (1954)], all

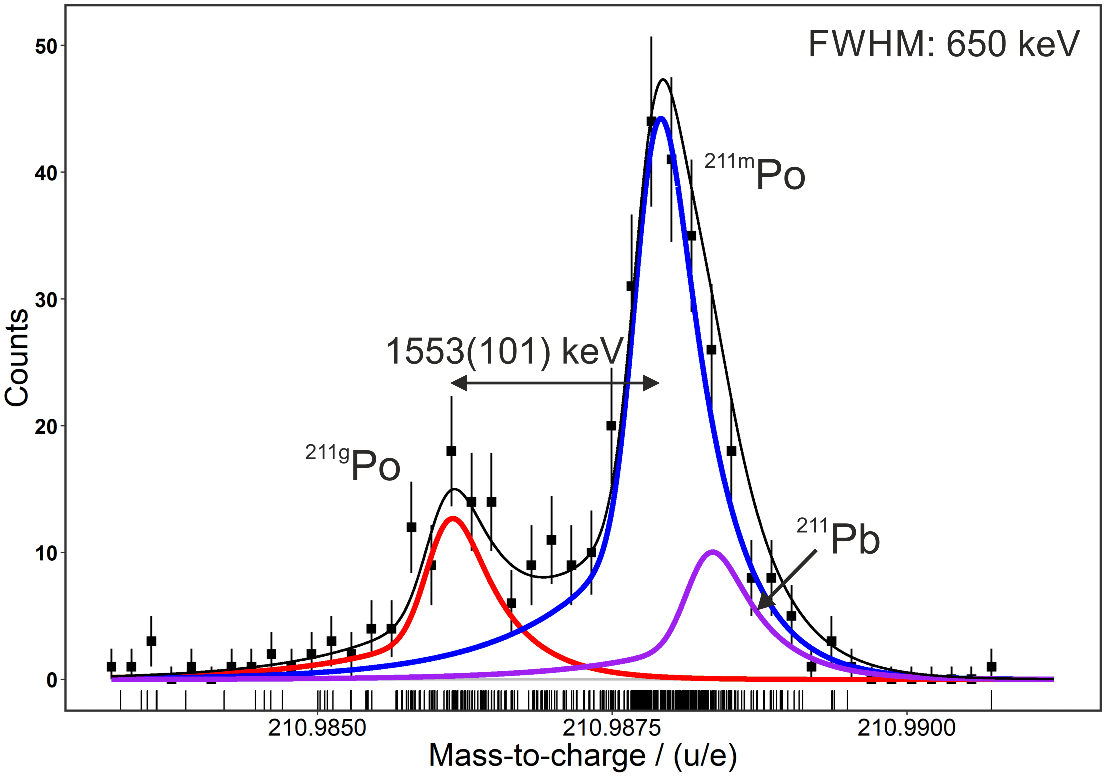

Figure 6.15.: Measured mass distribution of the ground and the isomeric state of ^{211}Po fitted by a triple hyper-EMG (red line for ^{211g}Po, blue line for ^{211m}Po and purple line for ^{211}Pb) with one exponential tail on both sides. During the measurement the ^{223}Ra source was blocked. The peak shape parameters were determined by the high statistic ^{211}Pb peak without ^{211}Po impinging in the CSC and scaled for the mass of ^{211}Po. In the fit, the ^{211}Pb peak was used with fixed parameters. Its intensity was estimated from a measurement without beam and with the ^{223}Ra source blocked. To guide the eye, the histogram of the measured ions is drawn. The data were recorded unbinned and treated with WMLE method. The measured data are shown in the rug graph.

measurements are in agreement with each other.

The isotope ^{211}Po was measured with the MR-TOF-MS already in an earlier experiment [Ebert (2016)]. In this measurement a mass value of 210.986720(207) u was determined. In the measurement the isometric state was not considered, since ^{211}Po was not produced directly in the FRS. The reference fragment in the FRS was the α-decaying ^{215}Rn isotope. It has a half-life of 2.3(1) μs and therefore decays in the CSC. The isotope ^{215}Rn has no isomeric state and the α-decay is a pure decay between the ground states of ^{215}Rn and ^{211}Po. Hence, it was assumed that only the ground state in ^{211}Po was populated. In the measurement of Ebert the ^{211}Po peak was overlapping with the calibrant ^{211}Pb. The mass was determined in two spectra with a different ratio between the ^{211}Po and the ^{211}Pb.

In Figure 6.16 the final ME value of the ground state of ^{211}Po is compared to the values derived in α-decay measurements and to the previous MR-TOF-MS measurement. In both cases the ME value is lighter than the one obtained from the α-decay measurement. Both states are about three σ lighter.

With the direct measurement of the ground and the isomeric state it is possible to determine the excitation energy of the isomeric state. For the $(25/2)^+$-isomer an excitation energy of 1553(101) keV was calculated. In the Atlas of Nuclear Isomers [Jain et al. (2015)] an excitation energy of 1462(5) keV is stated. Within their error bars they are in agreement. In Figure 6.16, the excitation energy as determined from the measured ME values of the ground and the isomeric state is compared to the excitation energies derived in α-decay measurements.

The isomer-to-ground state ratio of the $(25/2)^+$-isomer was determined. It reflects the population of the ground and first isomeric state in the fragmentation reaction of 1 GeV/u ^{238}U beam impinging on a beryllium target at relativistic energies. There is only a minimal feeding via an internal transition from the $(25/2)^+$-isomer to the $(9/2)^+$ ground state of 0.016(4) % [Singh et al. (2013)]. A ratio of 3.26(0.30) was determined in the mass evaluation, without a correction for the difference in half-life. The isomer-to-ground state ratio for this reaction was determined in the same experiment via α-decay spectroscopy [Reiter (2015)]. There an isomer-to-ground state ratio of 3.67(0.12) for the $(25/2)^+$-isomer was determined. The results from the two measurement techniques are compared to ground-to-isomer ratios calculated by the approach given in Section 2.2 and calculations done using the ABRABLA code [Gaimard and Schmidt (1991)] in Table 6.9. The comparison shows that the analytical approach and the calculation with the ABRABLA code both underestimate the population of the isomeric states. This was already seen in earlier investigations, e.g. for the high-spin $(43/2)^+$-isomer of ^{211}Po [Bowry et al. (2013)] and for other high-spin isomers in the region above ^{208}Pb [Podolyák et al. (2006)].

	MR-TOF-MS	α-Spectroscopy	Analytical Approach	ABRABLA Code
$R_{isomer-to-ground}$	3.26(0.30)	3.67(0.12)	0.10	0.25

Table 6.9.: Isomer-to-ground state ratio of the $(25/2)^+$-isomer in ^{211}Po populated in projectile fragmentation with a 1 GeV/u ^{238}U beam impinging on a beryllium target.

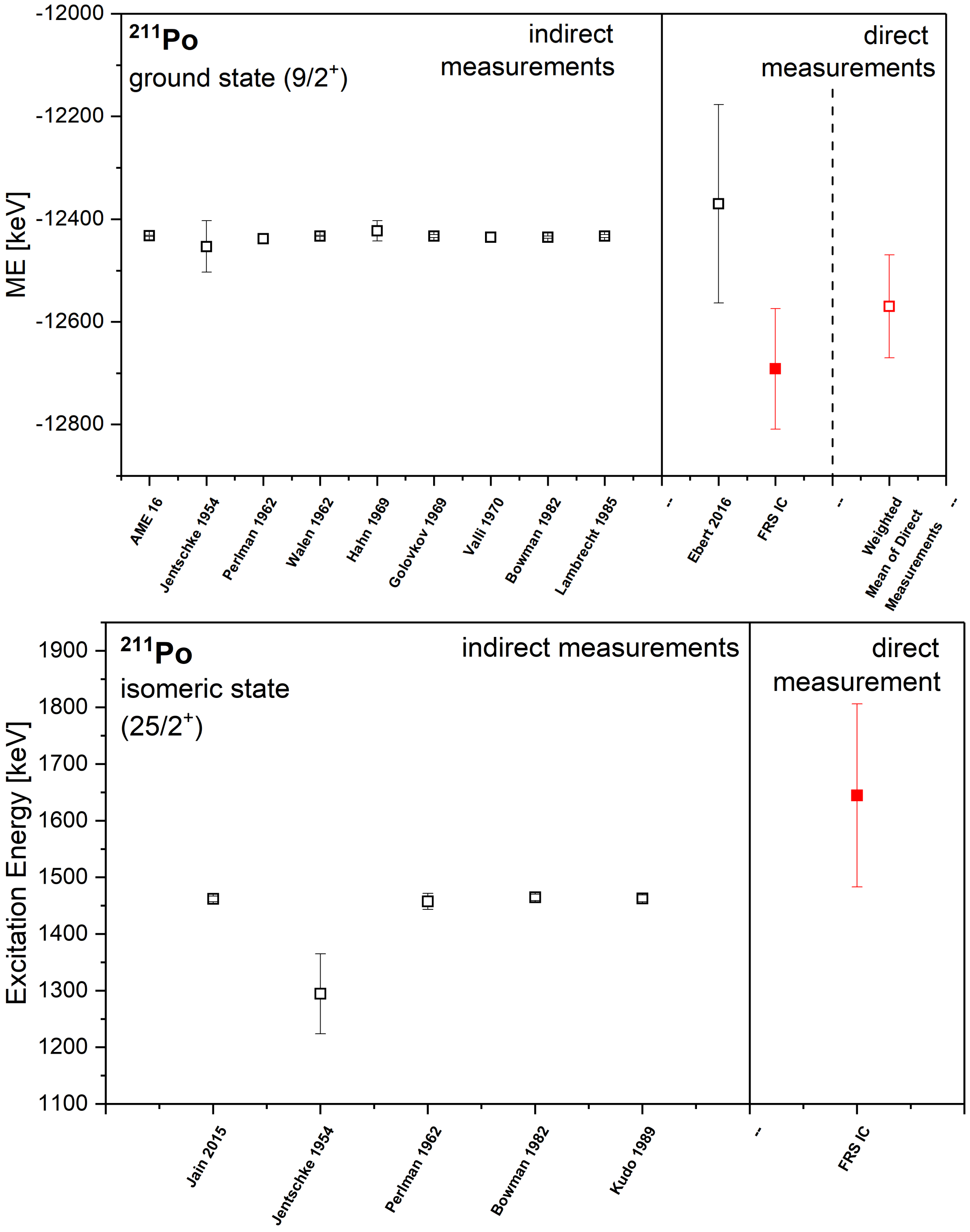

Figure 6.16.: The value of the Mass Excess (*ME*) of the ground state and the value of the excitation energy of the isomeric state of ^{211}Po (full red squares) in keV are compared to literature values (open black squares). The literature values of the ground state are determined from α-decay measurements [Bowman et al. (1982); Golovkov et al. (1969); Hahn et al. (1969); Jentschke et al. (1954); Lambrecht and Mirzadeh (1985); Perlman et al. (1962); Valli et al. (1970); Walen et al. (1962)] and by measuring the mass-to-charge ratio directly with an MR-TOF-MS [Ebert (2016)]. In addition the AME 2016 value [Wang et al. (2017)] is given. Additionally the value for the excitation energy of the isomeric state from [Bowman et al. (1982); Jentschke et al. (1954); Kudo et al. (1989); Perlman et al. (1962)] and from the Atlas of Nuclear Isomers [Jain et al. (2015)] are given.

6.3. Results of Mass Measurements of 600 MeV/u Xenon Fragments

In the following, the results of the 600 MeV/u xenon fragments experiment are presented. The experimental conditions and setup have been discussed in Section 4.6.

6.3.1. Mass Calibration of Xenon Fragments

In the experiment with xenon fragments, a TFS spectrum of the mass region of 130 u was used to determine the calibration constants c and t_{TFS}, see Equation 5.2. The calibration spectrum consists of ^{133}Cs and $^{128-134,136}$Xe ions. The xenon isotopes were ionized in the electron impact ion source filled xenon gas. The electron-impact ion source is mounted on top of the MR-TOF-MS. As a second gas for calibration, ($^{12,13}C_3\ ^{19}F_8$) was used in the electron impact ion source. However, this gas has only a very weak mass line at 131 u inside of the selected mass window and was therefore not applied for the calibration. The caesium ions were produced in a thermal ion source, placed at the same position as the electron impact ion source. The TFS spectrum had a mass resolving power of about 2000. For the determination of c and t_{TFS} in the TFS mode ($N_{IT} = 0$) Equation 5.2 was used with b fixed to 0. We obtained:

$$\begin{aligned} c =& 0.06621 \ \pm \ 3 \cdot 10^{-5} \ u/\mu s^2 \ , \\ t_{TFS} =& 0.201 \ \pm \ 0.011 \ \mu s \ . \end{aligned} \tag{6.2}$$

The error bars in the calibration for the xenon fragments are larger than the ones for the uranium fragments, caused by the smaller TOF window covered in the calibration.

In order to achieve a high resolving power in the experiment with xenon fragments, the number of isochronous turns was in the order of 600. This caused a small mass window and forced that all ions travelled the same number of turns. In order to cover a bigger mass window, many spectra showed a variety of isotopes which might belong to different turn numbers. In this case, only t_{TFS} was used as a fixed parameter in the data evaluation. The calibration constant c was determined using a time-averaged b in each measurement. Calibrants with different turn numbers were included. This took into account that the electric fields for the TFS turn and the isochronous turns are different. TRC provided the time-dependent b parameter, whereas c and t_{TFS} were determined from the multiple turn spectrum.

6.3.2. Measured Masses of ^{96,97}Pd Ions

The ^{96,97}Pd isotopes were transported together with the isotope ^{97}Ag to final focal plane of the FRS. ^{96}Pd and ^{97}Ag ions overlap in their range distribution and therefore, were stopped simultaneously in the CSC. To stop the ^{97}Pd ions in the CSC, 90 mg/cm^2 and 50 mg/cm^2 less matter was needed. Several mass measurements were taken with different degrader thicknesses at the final focal plane of the FRS. In the measurements with the MR-TOF-MS, the ^{96}Pd ions had 615 and the ^{97}Pd ions 612 isochronous turns in the analyser. This condition yielded a mass resolving power up to 450000.

The measurements allowed different turn numbers in same TOF-spectrum. The identification of the same isotope at a different number of isochronous turns confirms identification. Therefore, measurements were performed with ^{96}Pd and ^{97}Ag ions, where the analyser was tuned on an additional turn.

The spectra were also calibrated with different numbers of isochronous turns. The MRS was switched between different mass ranges several times, in order to provide the necessary broadband measurement for the calibration and to have a small amount of background. With this technique, it was possible to achieve an accurate calibration with the necessary mass range and on the other hand, to perform a low background mass measurement of the IOI.

The peak shape in the measurements of the isotopes ^{96,97}Pd was determined from ($^{12}C_2$ ^{16}O $^{19}F_3$) for 612 isochronous turns or from ($^{12}C_2$ $^{19}F_4$) for 603 isochronous turns. The individual mass-to-charge ratios were independently evaluated. The mass and ME values of the different measurements are listed in Table B.6 and Table B.7. The results of the single measurements are averaged weighted by their errors (Equation 5.11). The mean value for each isotope is given in Table 6.10.

Isotope	ME [keV]	Total Error [keV]	Mass [u]	Total Error [u]
^{96}Pd	-76240	38	95.9181533	4.12E-5
^{97}Pd	-77798	37	96.9164801	3.94E-5

Table 6.10.: Measured Mass Excess (*ME*) values of ^{96,97}Pd ions produced in the experiment with a 600 MeV/u ^{124}Xe beam. The given ME values represent the mean values. (Equation 5.11).

The isotope ^{96}Pd has been investigated in the mid 1980s by β-γ coincidence spectroscopy [Rykaczewski et al. (1985)] and in shell model calculations [Blomqvist and Rydström (1985)]. A β-endpoint energy of 1149(50) keV for the γ-line at 1275 keV was determined in spectroscopy, which corresponds to a Q_{EC}-value of 3446(50) keV. Due to systematic errors the Q_{EC}-value was adapted to 3450(150) keV. With the ME of ^{96}Rh known at this time, a ME value for ^{96}Pd of -76230(150) keV was determined. With the ME of ^{96}Rh from the AME 2016 [Wang et al. (2017)], the measured β-endpoint energy corresponds to a ME of -76238(150) keV. In a multi-step shell model a ME of -76270 keV was calculated in [Blomqvist and Rydström (1985)]. Their calculations considered the binding energies as free parameters and performed a corresponding least square minimization. The mass of ^{96}Pd was directly remeasured by JYFLTRAP [Weber et al. (2008)]. They measured a ME value of -76179.0(4.7) keV, which was about 50 keV heavier than the one determined from the Q_{EC}-value.

The measured ME value of ^{96}Pd given in Table 6.10 deviates from the ME value in the AME 2016 [Wang et al. (2017)] by 1.5 σ, corresponding to about 60 keV. The value measured with the MR-TOF-MS is closer to the one determined from the Q_{EC}-value, deviating by 10 keV only.

The isotope ^{97}Pd has been investigated by β-γ coincidence spectroscopy [Göktürk et al. (1980)] and in a Penning trap measurement [Elomaa et al. (2009a)]. In spectroscopy the Q_{EC}-value was determined from the β-endpoint measurement in coincidence with the 265 keV γ-window. They determined a β-endpoint energy of 3500(300) keV, which corresponds to a Q_{EC}-value of 4800(300) keV. The mass value of ^{97}Pd from the β-endpoint measurement was confirmed by a high precision Penning trap measurement by JYFLTRAP. They measured a ME value of -77805.9(4.9) keV.

The measured ME value of ^{97}Pd presented in Table 6.10 is in agreement with the AME 2016 and the Penning-trap measurement by JYFLTRAP. The deviation is about 6 keV, corresponding 0.2 σ.

6.3.3. Measured Masses of ^{93,94}Ru Ions

The isotopes ^{93,94}Ru were produced together at the FRS besides the goal fragment ^{94}Rh. Several measurements with different degrader settings at the final focal plane around the stopping range of ^{94}Rh were performed. The isotopes ^{93}Ru and ^{94}Ru have a similar stopping range as

^{94}Rh. Compared to ^{94}Rh, ^{93}Ru requires about 40 mg/cm^2 less and ^{94}Ru about 50 mg/cm^2 more material to be stopped. The ions were measured in the MR-TOF-MS undergoing 628 and 625 isochronous turns in the analyser, respectively. This corresponds to a mass resolving power of about up to 330000. Each TOF-spectrum was calibrated independently in a multiple turn calibration in order to determine the calibration parameter c. The multiple turn calibration of the measurement of the isotope ^{93}Ru is shown in Figure 5.4. The TRC was done in the different measurements with the molecules ($^{12}C_3$ $^{19}F_3$) (628 isochronous turns) and ($^{12}C_2$ ^{13}C $^{19}F_3$) (625 isochronous turns) respectively. The peak shape was determined in the different measurements depending on the molecular abundance of the molecules ($^{12}C_3$ $^{19}F_3$), ($^{12}C_2$ ^{13}C $^{19}F_3$) and ($^{12}C_3$ ^{16}O $^{19}F_3$) (615 isochronous turns) requiring up to one exponential tail on both sides of the hyper-EMG. Depending on the distance between the molecules used for the determination of the peak shape and the corresponding IOI, the peak shape parameters were scaled respectively and the mass-to-charge ratios of the IOIs were determined individually for each measurement. The mass and ME values of the different measurements of ^{94}Ru are listed in Table B.8. The results of the single measurements of ^{94}Ru are combined weighted by their errors (Equation 5.11). The mean value for each isotope is given in Table 6.11.

Isotope	ME [keV]	Total Error [keV]	Mass [u]	Total Error [u]
^{93}Ru	-77177	44	92.9171471	4.75E-5
^{94}Ru	-82546	26	93.9113833	2.81E-5

Table 6.11.: Results of the Mass Excess (*ME*) of ^{93,94}Ru in keV produced in projectile fragmentation with a 600 MeV/u ^{124}Xe beam impinging on a beryllium target. The given ME value of ^{94}Ru corresponds to the mean value determined from the results of the single measurements weighted by their errors (Equation 5.11). ^{93}Ru was only measured once.

As described in Section 5.4, the total error is the quadratic sum of all individual error components (Equation 5.13). All error components are calculated separately for each measurement and isotope. In Table 6.12 the error budget of ^{93}Ru is presented. The error of ^{93}Ru is not dominated by only one error component. The errors considering the statistics, the unresolved unknown contamination and the MRS pulsing have all the same order of magnitude and contribute significantly to the total error. Known isobaric contamination had not to be considered in the measurement.

The ^{93}Ru nucleus has a $(1/2)^-$ isomeric state with an excitation energy of 734.40(0.10) keV and a half-life of 10.8(0.3) s [Audi et al. (2017)]. In the measurements with the MR-TOF-MS, only one state of ^{93}Ru was observed. We assumed that the measured state corresponds to the $(9/2)^+$ ground state. In other experiments investigating isotopes with similar level schemes, it was observed that the $(1/2)^-$ was only rarely populated. For example, for the isotope ^{109}In, which also has a $(9/2)^+$ ground state and a $(1/2)^-$ isomeric state, the isomer-to-ground-state ratio was measured with the MR-TOF-MS at the FRS-IC [Miskun (2019); Spataru (2017)]. An isomer-to-ground-state ratio of 0.05 was observed for the $(1/2)^-$ isomer. The ground state of ^{93}Ru was measured with 20 counts only. If one assumes a similar population ratio one would expect to measure one count of the $(1/2)^-$ isomeric state. However, a single count cannot give a decisive result in this measurements.

The ME value of ^{93}Ru was determined for the first time in a β-endpoint measurement in coincidence in Jyväskylä [Äystö et al. (1983); Trzaska et al. (1983)]. A β-endpoint energy of 5315(85) keV was determined in two independent measurements, corresponding to a Q_{EC}-value of 6337(85) keV for the $(9/2)^+$ ground state. Together with the Q_{EC}-value of the ground state, the Q_{EC}-value of the $(1/2)^-$ isomeric state was derived to be 7070(85) keV. The ME

Statistical error $[10^{-7}]$	2.89
Peak shape error $[10^{-7}]$	1.11
Bias correction error $[10^{-7}]$	0
TRC error $[10^{-7}]$	0.83
Calibrant error $[10^{-7}]$	0.96
c error $[10^{-7}]$	0.37
t_{TFS} error $[10^{-7}]$	0.005
NIE error $[10^{-7}]$	0.45
MRS error $[10^{-7}]$	1.65
Contamination error $[10^{-7}]$	2.12
Iso error $[10^{-7}]$	0
Total error $[10^{-7}]$	5.12
Total error [keV]	44

Table 6.12.: The errors are listed for the individual error components of ^{93}Ru. The quadratic sum of the different components results in the total error (Equation 5.13).

values of ^{93}Ru and ^{94}Ru isotopes were directly measured by JYFLTRAP and SHIPTRAP [Weber et al. (2008)] in Penning trap measurements, improving the ME value determined from the Q_{EC}. For ^{93}Ru at JYFLTRAP a ME value of -77214.0(4.0) keV was measured. ^{94}Ru was measured twice in different reactions, once at JYFLTRAP and once at SHIPTRAP, together resulting in an average ME value of -82580.6(4.1) keV. Afterwards, the masses of ^{93}Ru and ^{94}Ru isotopes were investigated by the Canadian Penning trap (*CPT*) mass spectrometer [Clark et al. (2005); Fallis et al. (2011)] as well. They determined a ME value of -77217.6(2.9) keV and -82588.0(4.7) keV respectively. This result is in agreement with the previous Penning trap measurements. The two measured ME values determined with the MR-TOF-MS are in agreement with the AME-2016 values, see Figure 6.20.

6.3.4. Measured Masses of ^{94g,m}Rh Ions

For the ^{94}Rh nucleus, two states with half-lives of the order of seconds are reported. The relative order of the two states and their assigned spins is currently under discussion. In the NUBASE 2016 [Audi et al. (2017)] the ground state is assigned to the $(4)^+$ state with a half-life of 70.6 s. For the isomeric state, a spin of $(8)^+$ and a half-life of 25.8 s have been reported.

Isotope	ME [keV]	Total Error [keV]	Mass [u]	Total Error [u]
^{94g}Rh	-72862	24	93.9217794	2.54E-5
^{94m}Rh	-72533	35	93.9221331	3.7E-5

Table 6.13.: Measured mass and Mass Excess (*ME*) values of ^{94}Ru atoms. The ground and isomeric states are produced in projectile fragmentation with a 600 MeV/u ^{124}Xe beam in a beryllium target. The given ME values correspond to the mean value determined from the results of the single measurements weighted by their errors (Equation 5.11).

In the MR-TOF-MS measurements the ground and the isomeric state of ^{94}Rh nuclei were measured with 625 isochronous turns in the analyser. Both states were measured twice with different degrader settings in the final focal plane of the FRS. The isotopes ^{93}Ru and ^{94}Ru were

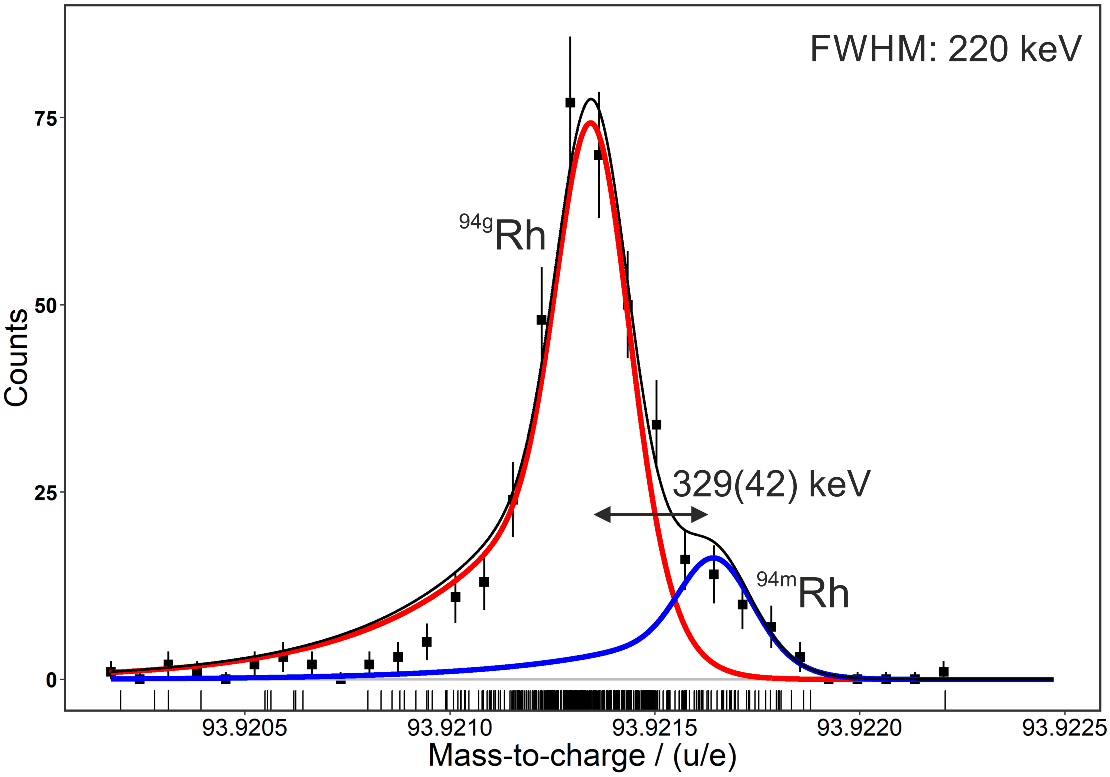

Figure 6.17.: Measured mass distribution of ^{94}Rh ions. The ground and isomeric states are fitted by a double hyper-EMG (red line for ^{94g}Rh and blue line for ^{94m}Rh) with one exponential tail on both sides. The peak-shape parameters were determined from the ($^{12}C_3$ ^{16}O $^{19}F_3$) calibration measurements and scaled to the mass of ^{94}Rh. The histogram of the measured spectrum is only drawn to guide the eye. The evaluation was based on measured unbinned data (rug graph) with the WMLE procedure.

in the same TOF-spectra. The relative abundance of the isotopes in the spectra for the different degrader thicknesses were compared with the expected ratios from simulations and were in agreement. The calibration and peak-shape determination is discussed above in the subsection of ^{93,94}Ru nuclei. The mass-to-charge ratios in the individual mass-spectra were determined by applying a double-peak fit with a hyper-EMG. The measured mass distribution of ^{94g,m}Rh ions and the corresponding fitted curves are shown in Figure 6.17. The mass distributions of the ground and the isomeric state have a large overlap with a difference in their μ_G-values of 329(42) keV. The ME values from the two measurements are combined and weighted by their errors (Equation 5.11). The mass and ME values of the different measurements of the ground and the isomeric state are listed in Table B.9 and Table B.10, respectively. The mean values for the ground and the isomeric state are given in Table 6.13.

In the NUBASE 2016, the assignment of the ground state is based on a β-endpoint measurement of the $(4)^+$ state, which was reported originally as $(3)^+$ state, with a half-life of 70.7 s [Oxorn et al. (1980)]. In this reference, a Q_{EC}-value of 10.0(0.4) MeV for ^{94}Rh decaying to ^{94}Ru was reported. It was assigned to the isomeric state. Shell model calculations [Herndl and Brown (1997)] predicted that the 70.6 s state is the isomeric state with a spin of $(4)^+$. They assigned the $(8)^+$ with 25.8 s to the ground state and expected an excitation energy of 145 keV for the $(4)^+$ state.

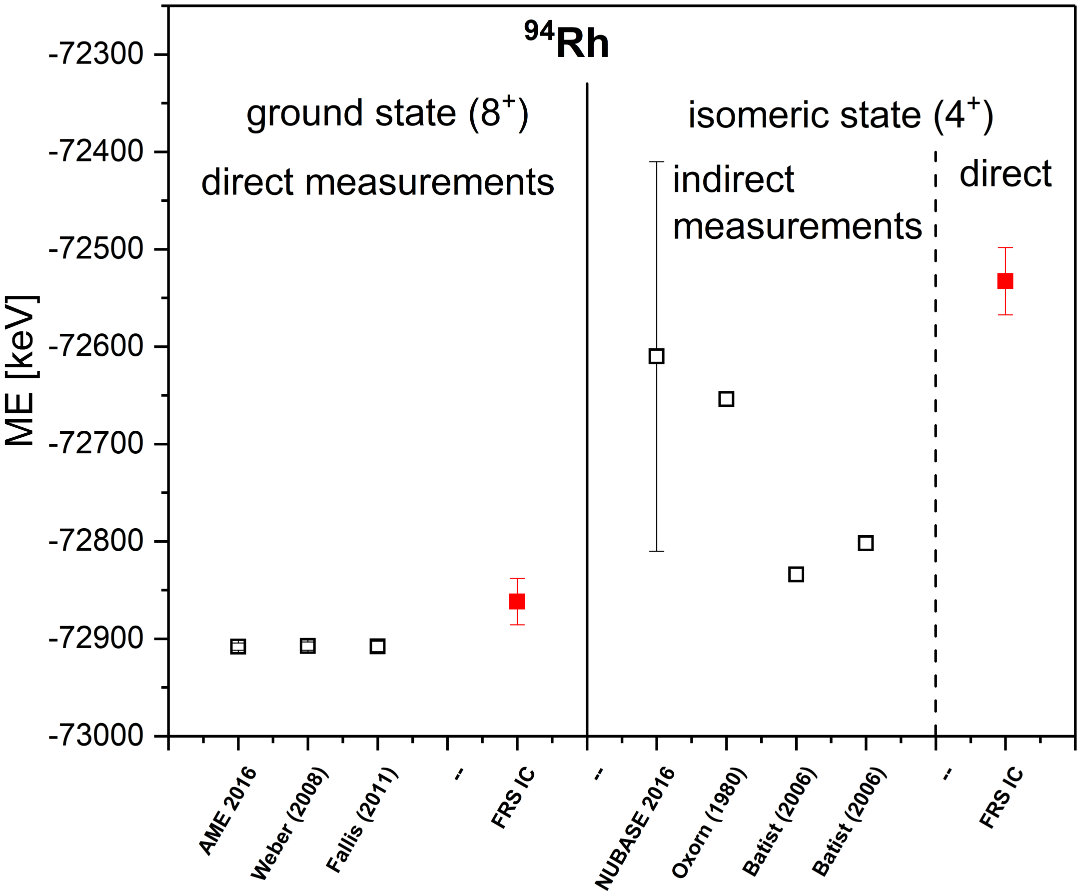

Figure 6.18.: Measured ME values of ^{94}Rh $(8)^+$ ground and $(4)^+$ isomeric states (full red square). The mean value of the present experiment is compared to the literature values (open black squares) from β-endpoint measurement [Oxorn et al. (1980)], total γ-ray absorption techniques [Batist et al. (2006)], Penning trap measurements [Fallis et al. (2011); Weber et al. (2008)] and to the AME 2016 [Wang et al. (2017)] and NUBASE 2016 [Audi et al. (2017)] values.

From our mass measurement, it was possible to determine the excitation energy of 329(42) keV for the isomeric state. In the NUBASE 2016, [Audi et al. (2017)] an excitation energy of 300(200) keV is estimated. A level scheme similar to ^{94}Rh is found for its neighbouring isotope ^{92}Tc. A spin of $(8)^{+}$ is assigned to the ground state of ^{92}Tc and its 1 μs isomer is considered to be a $(4)^{+}$ state [Audi et al. (2017)]. The $(4)^{+}$ isomer in ^{92}Tc has an excitation energy of 270.09(0.08) keV. Form other isotonic chains in this region of the chart of nuclei, e.g. the N=50 isotones shown in Figure 6.27, one would expect an increase in excitation energy with increasing number of protons. This expected effect is in agreement with the excitation energy of ^{94}Rh measured with the MR-TOF-MS compared to the excitation energy in ^{92}Tc.

^{94}Rh was investigated in Penning trap measurements at JYFLTRAP [Weber et al. (2008)]. There only one state was measured in the fusion reaction ^{40}Ca+^{58}Ni. This reaction has been investigated earlier at SHIP at GSI [Kurcewicz et al. (1982)]. In this measurement the grow-in behaviour of the 25.8 s and the 70.7 s state were compared. The 25.8 s state is produced directly in the reaction, while 70.6 s state (lower spin) showed a feeding from the β decay of ^{94}Pd.

Based on the results from Kurcewicz et al. and on an additional study of the states in ^{94}Ru, Weber et al. assigned the mass measured at JYFLTRAP to the $(8)^{+}$ state, following the argumentation that fusion-evaporation reactions generally tend to produce higher spin states. Additionally, to the ME value of the $(8)^{+}$ state in ^{94}Rh the ground state masses of ^{94}Pd and ^{94}Ru were measured at JYFLTRAP and SHIPTRAP [Weber et al. (2008)]. With the subsequent measurement of these three isotopes it was possible to determine Q_{EC}-values of the β-decays of ^{94}Pd and of the $(8)^{+}$ state of ^{94}Rh. This has yielded Q_{EC}-values of 6809.6(6.3) keV and 9673.1(5.9) keV, respectively. The Q_{EC}-values of the β decays of ^{94}Pd and of the 70.7 s state of ^{94}Rh, which was assigned to a spin of $(4)^{+}$, were studies by total γ ray absorption techniques [Batist et al. (2006)]. They measured Q_{EC}-values of 6700(320) keV and 9750(320) keV. The ME value of ^{94}Rh was investigated by the CPT mass spectrometer [Clark et al. (2005); Fallis et al. (2011)] as well. In this measurement, only one state was observed and they followed the same arguments as Weber et al. to assign the measured value to the $(8)^{+}$ in ^{94}Rh. A graphical overview of all measurements of both long living states of ^{94}Rh in comparison with the ME value determined at the FRS-IC is given in Figure 6.18.

The ME value of the present experiment for the ground state of ^{94}Rh is about 50 keV higher (1.5σ) than the AME-2016 value. For the isomeric state the literature data are very controvers. The directly measured excitation energy with the MR-TOF-MS in combination with the spin assignment above disentangles the level scheme of ^{94}Rh and fixes all levels on an absolute scale, which are only measured relative to the isomeric state. The resulting level scheme is shown in Figure 6.19. The additional informations on the level scheme are taken from the Evaluated Nuclear Structure Data File (*ENSDF*), published in [Abriola and Sonzogni (2006)].

From the measured mass distribution of ^{94g,m}Rh a ground-to-isomeric state ratio of 0.29(7) was determined. A theoretical prediction with the approach discussed in Section 2.2 is not possible.

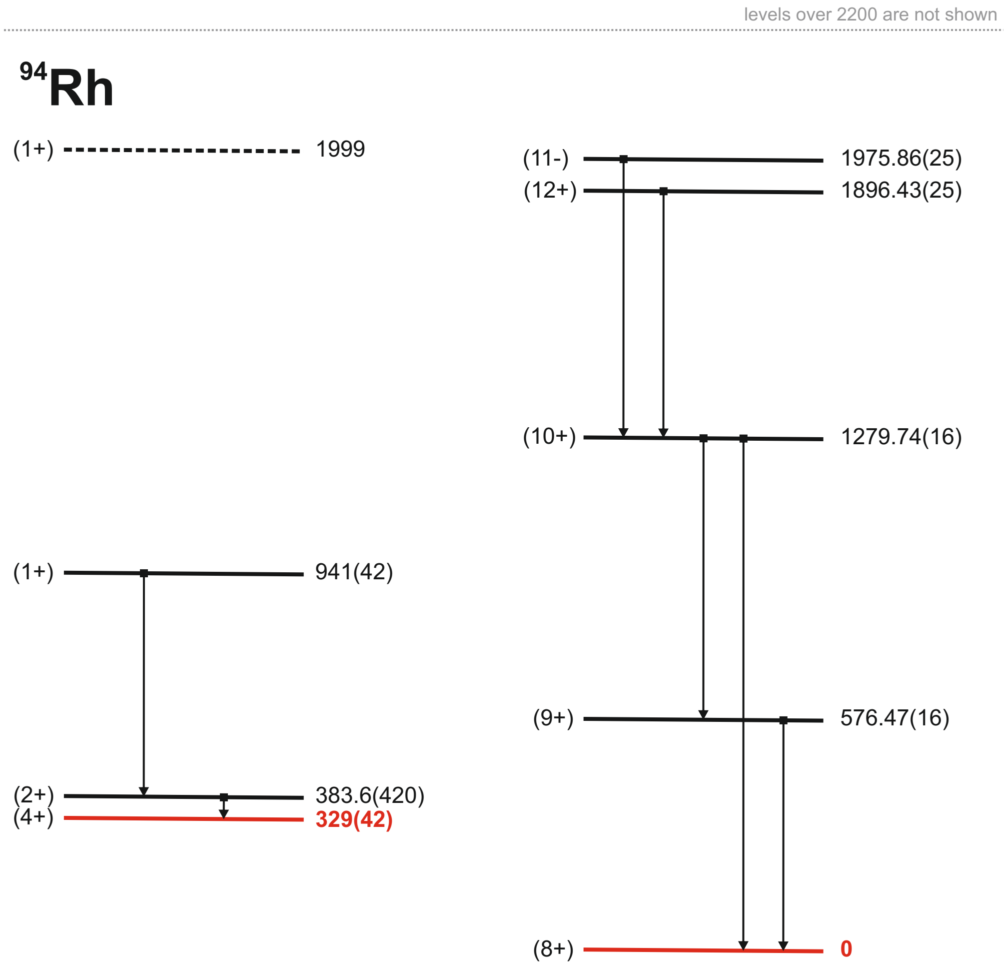

Figure 6.19.: Level scheme of ^{94}Rh. The directly measured ground and isomeric states separated by 329(42) keV are in red color. The suggested assignment of the spins of the ground and isomeric states is based on the agreement with the Penning trap measurements and their spin assignment. The further level informations are taken from the ENSDF, published in [Abriola and Sonzogni (2006)].

6.4. Experimental Mass Values compared with with Mass Models

The experimental mass values of this work, measured with the MR-TOF-MS at FRS-IC, are summarized and compared to the compilation AME in this chapter. The comparison is done with ME values of the ground states and is presented in Table 6.14 and 6.15. A comparison with the AME-2016 ME values is given together with the measured ME values and is shown in Figure 6.20.

The measured ME values from this work and 25 additional ones, determined in the thesis of S. Ayet [Ayet San Andrés (2018)], were used to investigate the systematic errors of the MR-TOF-MS measurements. This goal is motivated by two reasons: a) Most of the remeasured masses have for the literature values smaller errors than the present MR-TOF-MS results b) The mass values of this work have substantial smaller error bars compared to the pilot experiments with the MR-TOF-MS at FRS-IC

A histogram with the differences of ME values, measured in this work and the corresponding AME-2016 [Wang et al. (2017)] values, are shown in Figure 6.21. A fit with a Gaussian function was performed, leading to a mean value μ of 1.7(4.4) keV and a standard deviation σ of 34.9(8.9) keV. This comparison represents an important results because it clearly demonstrates that no hidden systematic errors, exceeding the given distribution, can mask the mass values presented in this work. This is really a great success for a new experimental method which was achieved in the first pilot experiments. An additional check with the so-called Birge ratio [Birge (1932)] of 0.914 confirms the latter statement.

The measured ME values of this work are compared to calculations with mass models. An overview on mass models can be found e.g. in [Erler et al. (2012)]. For the theoretical values of the microscopic-macroscopic finite-range droplet model (*FRDM 2012*) [Möller et al. (2016)], the Hartree-Fock-Bogoliubov model (*HFB-24*) [Goriely et al. (2013)] and the Duflo-Zuker model (*DZ-28*) [Duflo and Zuker (1995)] are selected as shown in Figure 6.22.

Isotope	$\mathrm{ME}_{FRS\ IC}$ [keV]	$\mathrm{ME}_{FRS\ IC}$ error [keV]	$\mathrm{ME}_{AME\ 16}$ [keV]	$\mathrm{ME}_{AME\ 16}$ error [keV]	Deviation [keV]
^{211}Fr	-4061	40	-4140	12	79
^{212}Fr	-3530	28	-3516	9	-14
^{213}Fr	-3562	12.3	-3553	5	-9.4
^{211}Po	-12692	82	-12433	1.3	-259
^{212}Rn	-8600	30	-8660	3	60
^{212}At	-8601	86	-8628	2.4	27
^{213}Rn	-5723	41	-5696	3	-27
^{217}At	4433	135	4395	5	38
^{218}Rn	5071	54	5217	3.2	-147

Table 6.14.: Mass Excess (*ME*) values for the heavier ions of this work are compared with the corresponding ME values from the AME-2016 [Wang et al. (2017)] The differences are listed in the rightmost column.

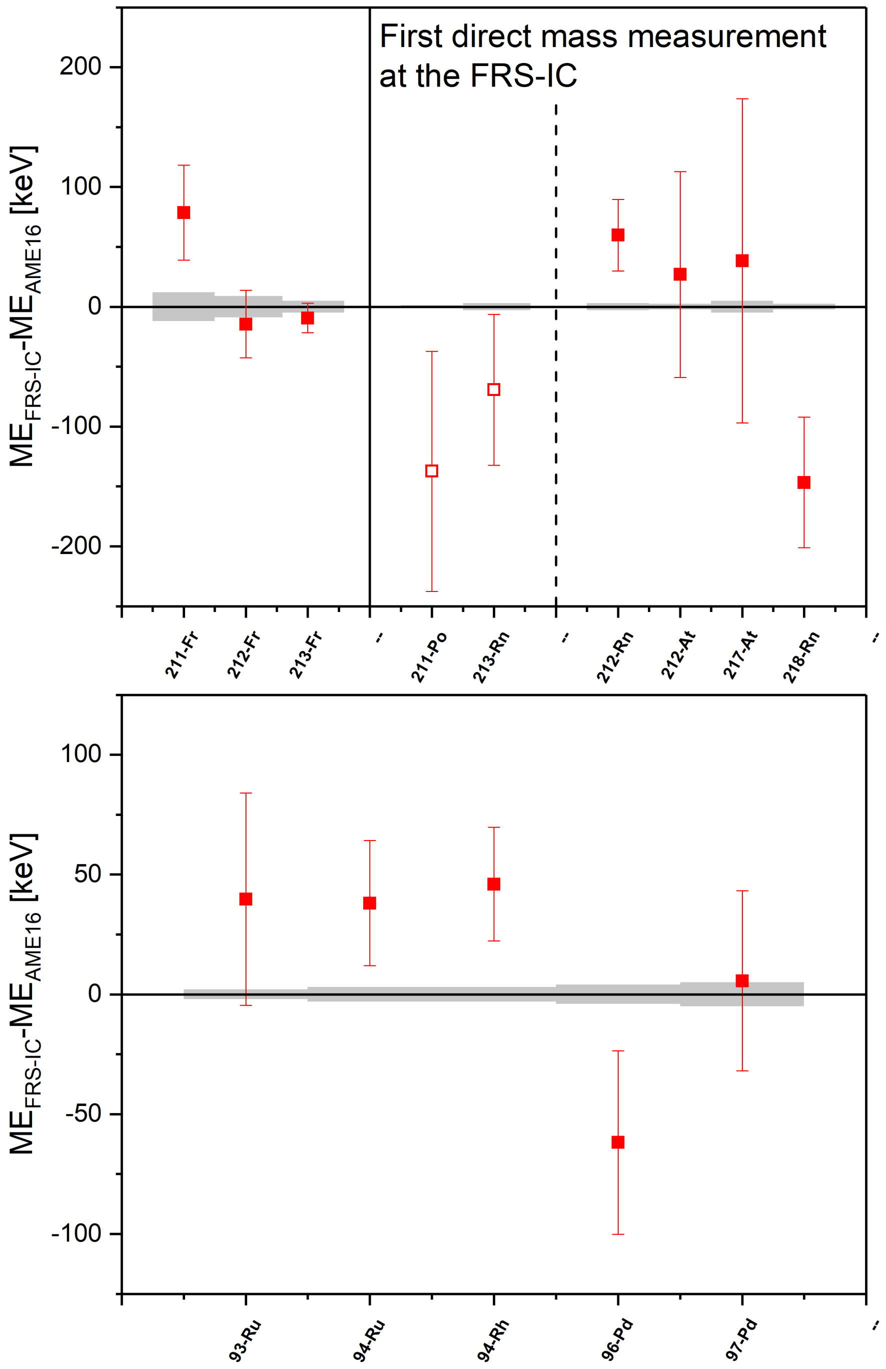

Figure 6.20.: Measured Mass Excess (*ME*) values of this work compared with the compilation of AME-2016 [Wang et al. (2017)]. The red-colored error bars indicate the FRS-IC measurement, whereas the error bars from AME 2016 are given by the grey band. In the upper panel, the results of the uranium experiment are depicted; in the lower panel the results came from the xenon experiment

Isotope	$ME_{FRS\ IC}$ [keV]	$ME_{FRS\ IC}$ error [keV]	$ME_{AME\ 16}$ [keV]	$ME_{AME\ 16}$ error [keV]	Deviation [keV]
^{93}Ru	-77177	44	-77217	2	40
^{94}Ru	-82546	26	-82584	3	38
^{94}Rh	-72862	24	-72908	3	46
^{96}Pd	-76240	38	-76183	4	-57
^{97}Pd	-77798	37	-77806	5	8

Table 6.15.: Mass Excess (*ME*) values for medium-mass ions of this work are compared with the corresponding ME values from the AME-2016 [Wang et al. (2017)] The differences are listed in the rightmost column.

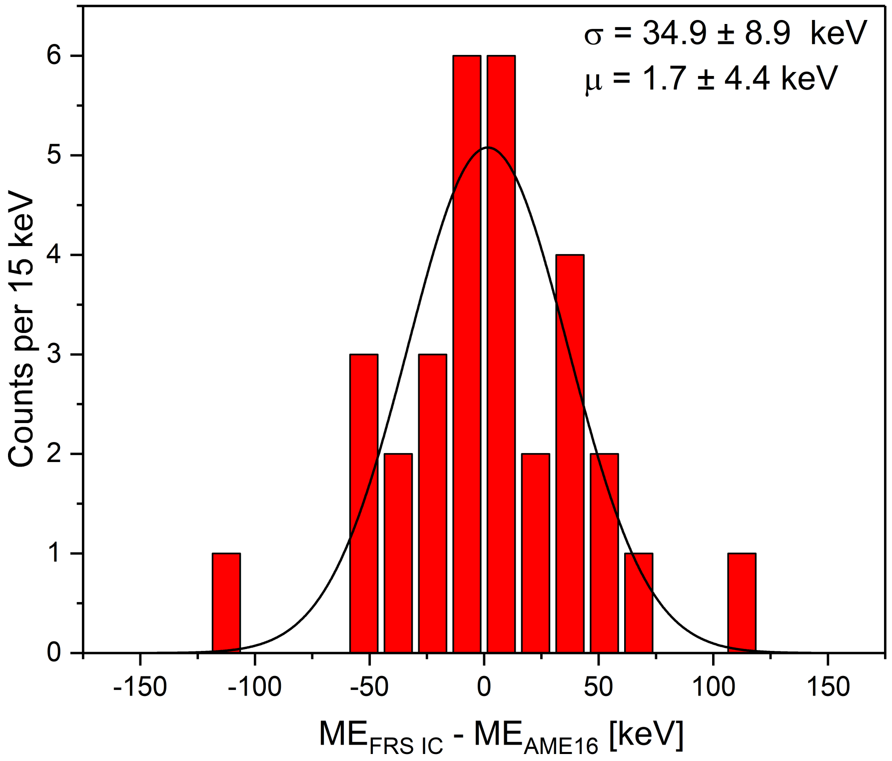

Figure 6.21.: Histogram with the differences of MR-TOF-MS ME values and the corresponding AME-2016 [Wang et al. (2017)] values. The fit with the Gaussian function was characterized by a mean value μ of 1.7(4.4) keV and a standard deviation σ of 34.9(8.9) keV. The experimental values of this work and of the thesis [Ayet San Andrés (2018)] are included.

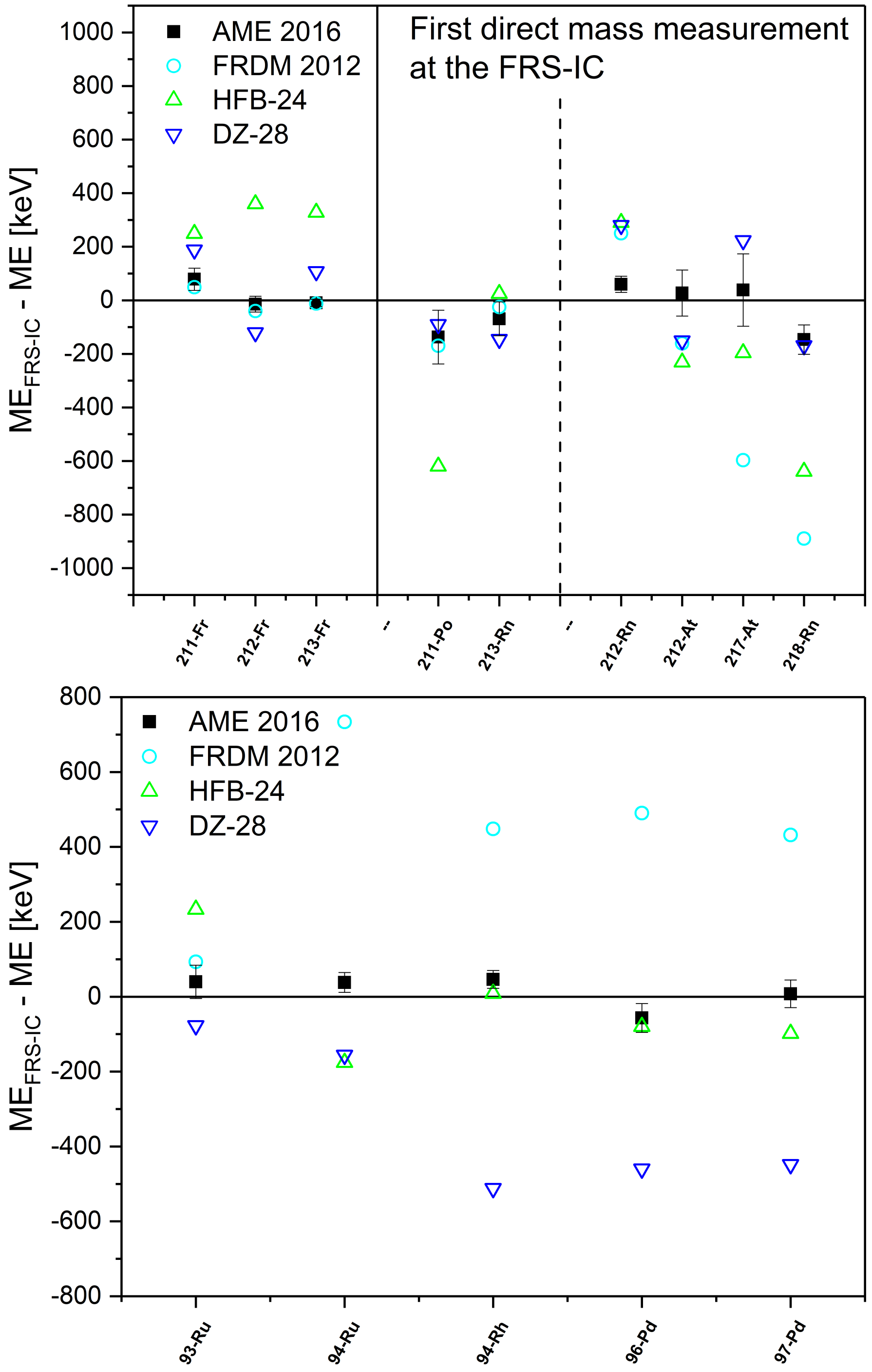

Figure 6.22.: Measured Mass Excess (*ME*) values determined with MR-TOF-MS at the FRS-IC compared to theoretical models. The upper panel shows the results uranium experiment, the results in lower panel are from the xenon experiment. For the theoretical and our ME values, the differences to the ME value of the AME 2016 [Wang et al. (2017)] are shown. The theoretical models are indicated in the comparison by: Microscopic-macroscopic finite-range droplet model (*FRDM 2012*) [Möller et al. (2016)], Hartree-Fock-Bogoliubov model (*HFB-24*) [Goriely et al. (2013)] and the Duflo-Zuker model (*DZ-28*) [Duflo and Zuker (1995)] are shown.

6.5. Isomer Studies via Mass Measurements

6.5.1. Excitation energy

The MR-TOF-MS is a perfect tool to access long-lived isomeric states with half-lives above a few millisecond. The excitation energy of the isomeric states can be derived from the difference in mass of the ground and isomeric state. If several isomeric states are measured simultaneously, their difference in excitation energy can be accessed directly as well. This opens the possibility to provide directly measured anchor points in the excitation scheme of the exotic nuclei. This is of special interest in the case of isomers, which are not accessible in common coincidence spectroscopy experiments due to their long half-life. An isomeric state with an unknown excitation energy can cause for one nucleus two uncorrelated level schemes, one is based on the ground state and one on the isomeric state. In such a case, a direct measurement of ground and isomeric state could provide a correlation of the full level scheme.

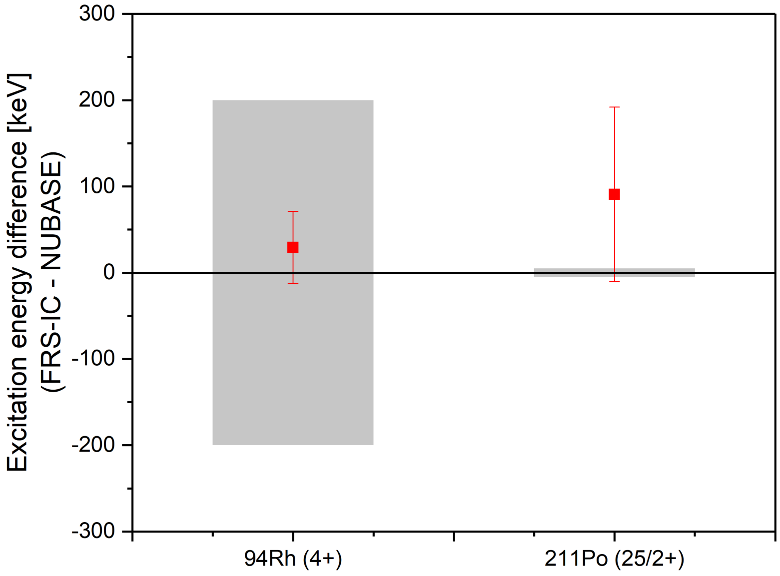

Figure 6.23.: Measured excitation energies of the isomeric states in ^{94}Rh and ^{211}Pb compared to values from the NUBASE 2016 [Audi et al. (2017)]. The values are given in Table 6.16. In the case of ^{94}Rh the value in the NUBASE 2016 is only estimated from systematics. Such systematics are based on properties of neighboring nuclei with the same Z and N parities. The error bars from the NUBASE 2016 are given by the grey band in the back.

The excitation energies of two isomeric states in ^{94}Rh and ^{211}Po nuclei were measured with the MR-TOF-MS. The $(25/2)^{+}$ state of ^{211}Po and the $(4)^{+}$ state of ^{94}Rh have been observed in the mass spectra. The actual measurements are discussed in more detail in Section 6.2.7 and in Section 6.3.4. The measured excitation energies in comparison to the NUBASE-2016 values [Audi et al. (2017)] are shown in Figure 6.23 and listed in Table 6.16. Both values agree with the previously known excitation energies. In the case of the $(4)^{+}$ isomeric state of ^{94}Rh, the stated value in the NUBASE-2016 has a big uncertainty due of the ambiguous assignment of previous measurements. The deviation from the NUBASE-2016 value for both excitation energies is less than 1 σ.

Isotope	E_{FRSIC} [keV]	E_{FRSIC} error [keV]	$E_{NUBASE2016}$ [keV]	$E_{NUBASE2016}$ error [keV]	Deviation [keV]
^{211}Po $(25/2)^+$	1553	101	1462	5	91
^{94}Rh $(4)^+$	329	42	300	200	29

Table 6.16.: Measured excitation energies of the isomeric states in ^{94}Rh and ^{211}Pb nuclei. The excitation energies of the isomeric are compared to the NUBASE-2016 values [Audi et al. (2017)].

6.5.2. First Spatial Separation of the Ground- and Isomeric State of ^{211}Po Nuclei

Pure isomeric beams can be of great interest for spectroscopy and reaction studies of exotic nuclei [Dracoulis et al. (2016); Eronen et al. (2008); Rodriguez Triguero et al. (2012); Rykaczewski et al. (1998); Stefanescu et al. (2007); Walker (2006); Watanabe et al. (2004)]. A new field can also be opened for fission studies of isomers [Metag et al. (1980)]. The storage of isomers can also be used for new applications of nuclear energy storage [Walker and Dracoulis (1999)].

There are several efforts to develop very specific experimental methods to separate the isomeric state from the ground state. However, high-resolution mass spectrometry represents a very unique and universal way to search for new isomers and separate the two states of a selected nucleus by the difference in their masses. The separation cannot only been achieved in the mass spectrum but also spatial separation is possible with the combination of technical methods.

The critical technical limitations are often given by the values of the half-lives and the excitation energy of the isomer. Pilot experiments towards the realization of spatial separation of a pure isomeric beam have been performed with Schottky Mass Spectrometry in the ESR storage ring [Geissel et al. (2007); Scheidenberger et al. (2006)]. In the ESR [Franzke (1987)] bare and few-electron exotic nuclei have been stored with a kinetic energy of about 400 MeV/u. The limitation for this method is the relatively long electron cooling time of the stored exotic nuclei which was a few seconds [Franzke et al. (2008)]. The present MR-TOF-MS is highly complementary to the experimental conditions in the ESR. The MR-TOF-MS can store and analyse mainly singly-charged ions at low kinetic energies of a few keV (1.3 keV in the present measurements). The maximum mass resolving power ($m/\Delta m = 600000$) of both devices are almost the same. However, the measuring period of a few ms with the MR-TOF-MS is much shorter. Therefore, also shorter-lived isomers can be analysed and converted to a pure isomeric beam.

The basic principle and the technical details of the MR-TOF-MS at the FRS-IC are discussed in Section 4.3 and is shown in Figure 4.3. This method was applied to the ground and isomeric state of ^{211}Po [Dickel et al. (2015a)]. The selected isotope is well suited for the demonstration of a spatially separated pure isomeric beam because both the ground and the isomeric states mainly decay via characteristic α-particle emission which gives the possibility to identify both states via their different α-decay branches.

The conversion from the time coordinates to the spatial coordinate at the MR-TOF-MS was performed with the Bradbury-Nielsen Gate (BNG) [Bradbury and Nielsen (1936)]. Based on the isomer-resolved mass spectrum of ^{211g,m}Po ions, the pulsing of the deflecting voltages on the BNG was adjusted.

The experimental procedure is schematically illustrated in Figure 4.3. The time-of-flight was measured with a SEV detector after multiple reflections between two electrostatic reflector. Without applying voltage to the BNG, all ions were transmitted to the Si decay detector behind the BNG. With proper timing of the voltages applied to the BNG, only the selected isomer ions were transmitted and their decay is measured.

In Figure 6.24 the α-decay energy spectra behind the BNG are shown without the deflecting voltages applied to the BNG (top) and with the deflecting voltages on the BNG pulsed to transmit only the isomeric state (bottom). With the applied deflecting voltages on the BNG, the ions are transmitted as a pure isomeric beam to the silicon detector. In this way, a beam consisting of only the isomeric state was achieved for the first time by using an MR-TOF-MS. Only two counts of ions in the ground state were transmitted and detected in this mode, caused by the overlap of the two mass-to-charge distributions of ^{211g,m}Po. This can be optimized in future by a higher resolving power and an improved peak-shape selection.

This pioneering experiment of spatial separation of isomers with an MR-TOF-MS in combination with a BNG opens new opportunities for experiments and for applications with pure isomeric beams [Dickel et al. (2015a)].

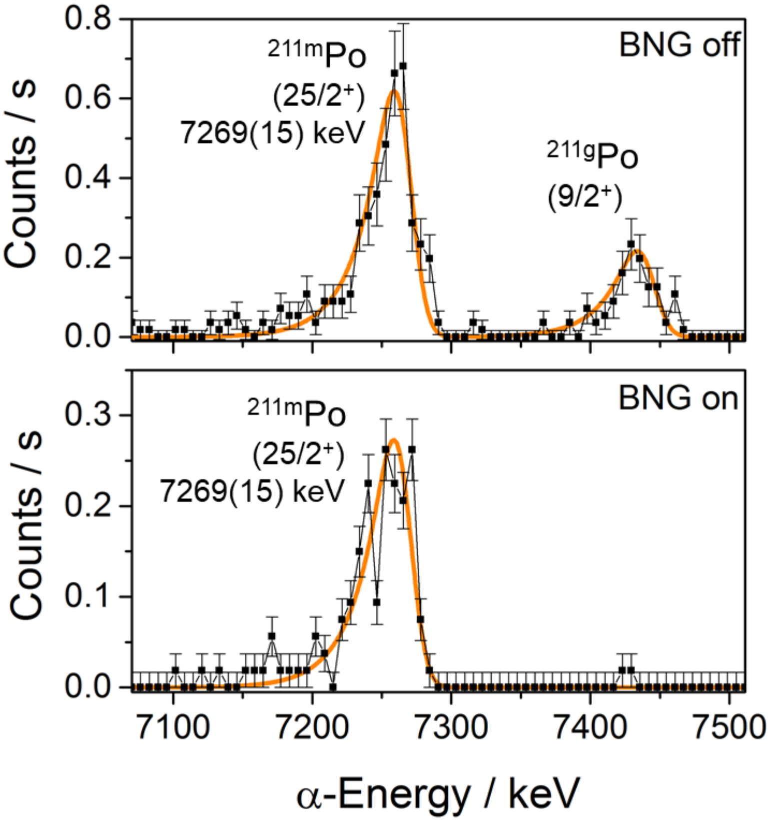

Figure 6.24.: Spatial separation of ground and isomeric state of ^{211}Po ions using the BNG. The different kinetic energy spectra of the α-particle from the ground and isomeric states were used as a signature of the achieved separation quality. The α-spectroscopy was done with a silicon surface barrier detector. Upper panel: The recorded α-spectrum without a deflecting voltage applied to the BNG. The result is that ions in the ground and isomeric states are transmitted Lower panel: A suitable deflecting voltages applied on the BNG which transmit a pure isomeric beam. (bottom).

6.6. Discovery of a New Isomer in ^{97}Ag Nuclei

In nuclear structure research much effort is made to measure and to understand the excitation levels of a nucleus close to regions of shell closures. A special milestone is the discovery of new isomeric states.

Driven by this motivation, the mass spectrum of ^{97}Ag ions were measured at the FRS-IC. A long-lived isomeric state was previously predicted for this nucleus from systematics.

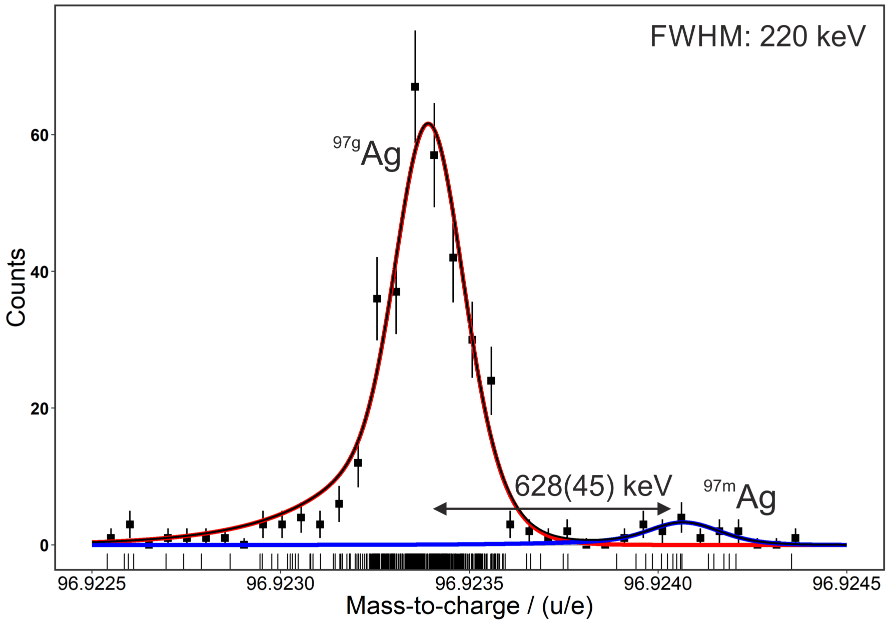

Figure 6.25.: Measured mass distribution of ^{97}Ag ions. Ground and isomeric states are clearly resolved and fitted by a double hyper-EMG (red line for ^{97g}Ag and blue line for ^{97m}Ag) with one exponential tail on both sides. The histogram of the measured spectrum is only drawn to guide the eye. The evaluation was based on measured unbinned data (rug graph) with the WMLE procedure.

The ^{97}Ag ions were measured with the MR-TOF-MS with 612 isochronous turns in the analyser. This corresponds to a mass resolving power of 500000. The measured mass spectrum clearly revealed a new isomeric state. The isotope was measured several times with different settings of the aluminium degrader (range selection) at the final focal plane of the FRS. In addition, a measurement with slightly different settings of the analyser of the MR-TOF-MS was performed, in which the ^{97}Ag ions were recorded with 613 isochronous turns. The measurements with a different number of isochronous turns served for further confirmation of the unambiguous identification of the ^{97g,m}Ag nuclei.

The sum of the accumulated mass distributions of the four mass measurements is shown in Figure 6.25. In the four measurements, calibrants from the electron impact ion source from C_3F_8 gas and krypton molecules with different turn numbers were used to determine the calibration constant c. The most abundant peak in the spectra corresponds to the molecule ($^{12}C_2\ ^{19}F_4$). It was used to perform the TRC. The peak shape parameters were determined from the peak of either ($^{12}C_2\ ^{16}O\ ^{19}F_3$) or ($^{12}C_2\ ^{19}F_4$) and scaled to the mass of ^{97}Ag.

The individual mass-to-charge ratios were evaluated independently for each of the four measurements and the ME values were determined. The mass and ME values of the different measurements of the ground and the isomeric state are listed in Table B.11 and Table B.12, respectively. The final mass for the singly charged ^{97}Ag $(9/2)^+$ ground state and the $(1/2)^-$ isomeric state were determined by averaging the single measurements weighted by their individual error bars (Equation 5.11). The excitation energy of 636(48) keV was determined from the mass difference of the ground and isomeric state.

Isotope	ME [keV]	Total Error [keV]	Mass [u]	Total Error [u]
^{97g}Ag	-70906	17	96.9238789	1.85E-5
^{97m}Ag	-70279	42	96.9245529	4.48E-5

Table 6.17.: Measured mass and ME values of ^{97g,m}Ag ions. The measured data of singly-charged ions are transformed to neutral atoms to be compatible with AME-2016. The given values correspond to the mean values determined from the results of the single measurements weighted by their errors (Equation 5.11).

In previous experiments [Alber et al. (1990)], the level scheme of ^{97}Ag was investigated in delayed γ-ray spectroscopy. This nucleus is of special interest because it is the three-neutron hole state of the doubly-magic ^{100}Sn isotope. The $(17/2)^{-}$ and the $(21/2)^{+}$ state in ^{97}Ag were identified in the γ-spectra. The experimental data were compared to a $\pi\left(p_{1/2}, g_{9/2}\right)^{-n}$ Shell Model calculation (*SM-PG*) and a $\pi\left(g_{9/2}\right)^{-n}$ approach (*SM-G*), see Figure 6.26. The same comparison was done for ^{95}Rh isotope, which has two neutrons less than the ^{97}Ag isotope and a similar level scheme. The $(1/2)^{-}$ and the $(17/2)^{-}$ states are only predicted in the SM-PG shell model calculation. Since both states are experimentally confirmed in ^{95}Rh and the $(17/2)^{-}$ state was seen in ^{97}Ag, the $(1/2)^{-}$ state should exist in ^{97}Ag as well.

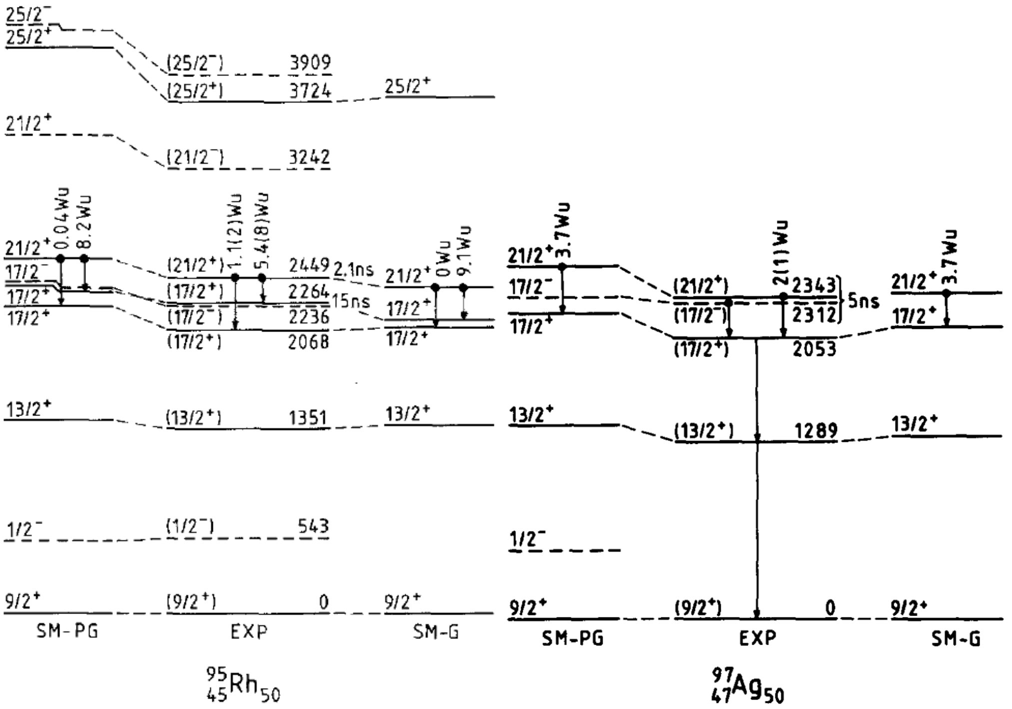

Figure 6.26.: Level scheme of ^{95}Rh and ^{97}Ag as derived from experiments in comparison to a $\pi\left(p_{1/2}, g_{9/2}\right)^{-n}$ Shell Model calculation (*SM-PG*) and a $\pi\left(g_{9/2}\right)^{-n}$ approach (*SM-G*) taken from [Alber et al. (1990)].

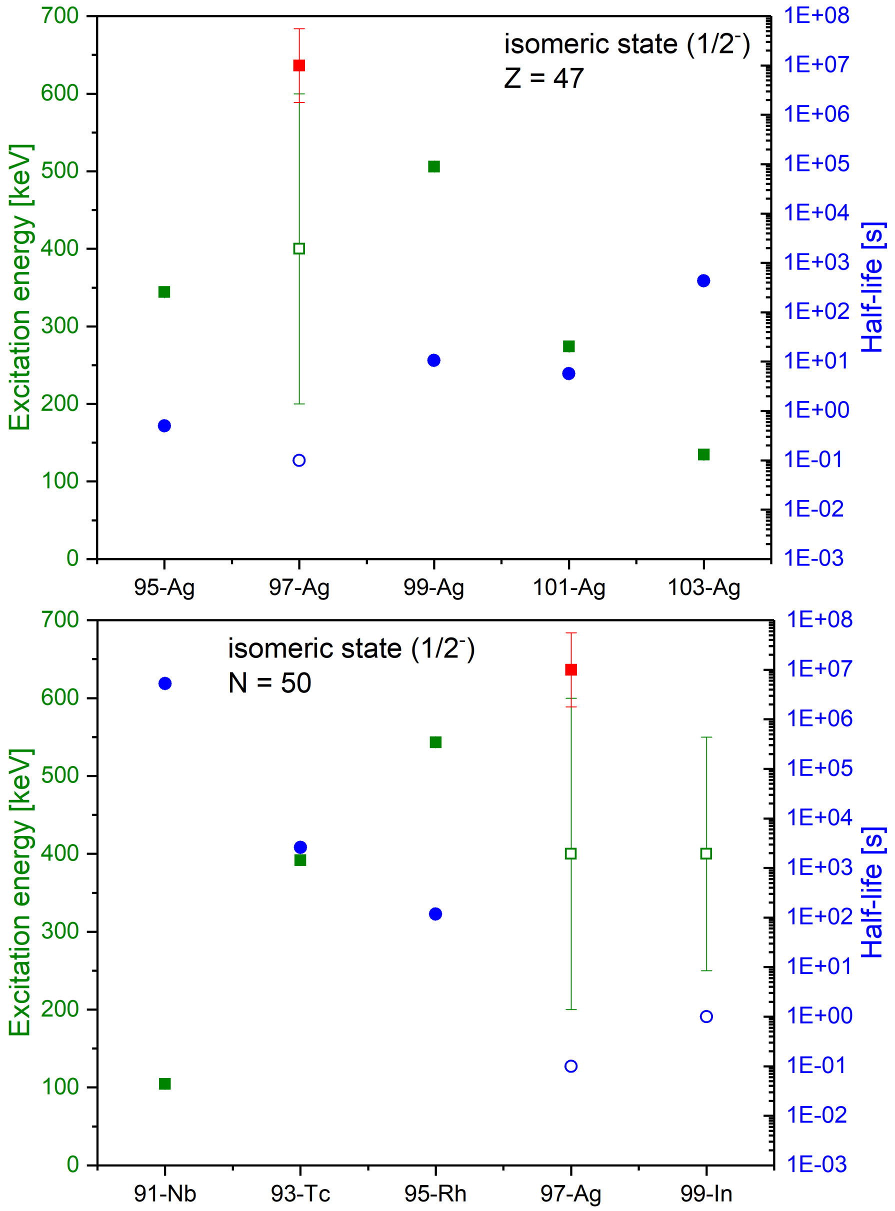

Figure 6.27.: Excitation energy (green squares) and half-life (blue circles) of the $(1/2)^-$ isomeric state in odd-even nuclei with Z=47 (upper panel) and N=50 (lower pannel) taken from the NUBASE 2016 [Audi et al. (2017)]. The measured excitation energy with the MR-TOF-MS at the FRS-IC is shown in red squares. The predicted values are indicated by open squares and circles.

Further investigations were done to explore the level scheme of ^{97}Ag, by $\gamma\gamma$-coincidence spectroscopy [Palacz et al. (2013)]. Their results were compared to different shell-model calculations. Among them a $\pi\left(p_{1/2}, g_{9/2}\right)$ shell model, based on a $^{88}_{38}Sr_{50}$ core, predicting an excitation energy of 618 keV for the $(1/2)^{-}$ state. The decay properties of ^{97}Ag were investigated in β-delayed γ-spectroscopy and similar shell model calculations were performed [Schmidt et al. (1997)]. It is stated that the decay properties and with this, the half-life of the $(1/2)^{-}$ state crucially depends on its excitation energy. Assuming an excitation energy of about 600 keV, a de-excitation would be only possible via a M4 transition to the ground state or a Gamow-Teller decay, leading to a predicted half-life up-to several hundred seconds.

The $(1/2)^{-}$ isomeric state was predicted from systematics. The excitation energies and half-lives of odd-even nuclei with Z=47 and N=50 from reference [Audi et al. (2017)] are shown in Figure 6.27. Both nuclear chains show that an $(1/2)^{-}$ isomeric state with an excitation energy of a few hundred keV is expected. This assumption is confirmed with the measured excitation energy of 628(45) keV in the present experiment. This is on the upper end of the error bar from the prediction in the NUBASE 2016. However, it is in agreement with the systematic behaviour in the odd-even nuclei with Z=47 and N=50. For the odd-even N=50 nuclei below ^{97}Ag the excitation energy is increasing with an increase in the proton number.

The $(9/2)^{+}$ ground state of ^{97}Ag was measured by γ-spectroscopy [Hu et al. (1999)]. The ratio between EC and β^{+}-decay was determined experimentally for two excitation energy windows in the β-spectrum. From those experimental results, the Q_{EC}-value was calculated to be 6980(110) keV. The measured mass value of the present experiment agrees with the value from the γ-spectroscopy experiment. A comparison with the literature values of the ground and isomeric states is shown in Figure 6.28.

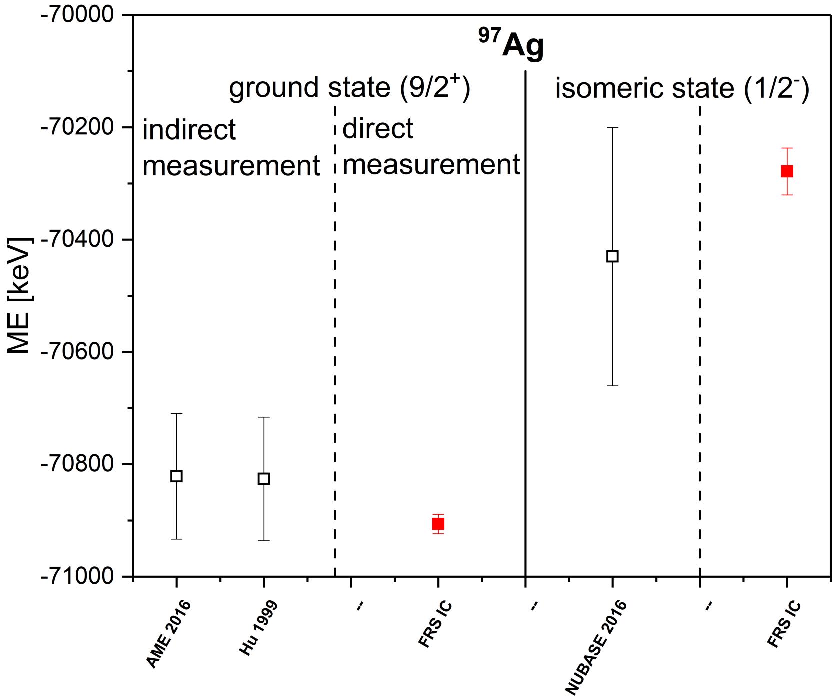

Figure 6.28.: The weighed mean values of the measured Mass Excess values of ^{97}Ag ions in the $(9/2)^{+}$ ground and $(1/2)^{-}$ isomeric states (full red squares) is compared to literature values (open black squares) obtained from γ-spectroscopy [Hu et al. (1999)]. Furthermore, they are also compared to the AME 2016 [Wang et al. (2017)] value and to the NUBASE 2016 [Audi et al. (2017)] prediction.

7. Summary and Outlook

The study of exotic nuclei far from the valley of stability provides basic information for a better understanding of nuclear structure and the synthesis of the elements in the universe. Nuclear structure and reaction experiments with exotic nuclei have top priorities in research at GSI-FAIR and other modern accelerator facilities.

The work of this thesis covered quite different fields of activity. For the present and future performance of the FRS Ion Catcher new experimental developments for the efficient transport and diagnosis of the ions between the Cryogenic Stopping Cell (*CSC*) and the Multiple-Reflection-Time-Of-Flight Mass Spectrometer (*MR-TOF-MS*) have been constructed and successfully commissioned. The new diagnosis unit consists of resistive RFQs, an RFQ switch yard, a calibration source and a dedicated RFQ mass filter. A versatile laser ablation calibration ion source has been constructed and commissioned. The laser provides polarized light with a wavelength of 532 nm and a pulse width of (5 to 10) ns and can be operated at repetition rates up to 100 Hz matched to the operating modes of the MR-TOF-MS. An x-y-movable target table can provide selected reference ions for calibration including carbon clusters and a constant movement. The laser-ablation source has been tuned such that long-term stable operation become possible. The dedicated RFQ mass filter can be used for pre-separation of the ions extracted from CSC.

A novel method of unambiguous isotope identification via atomic range and high-resolution mass measurement (*R-m method*) has been successfully applied with the combination of the FRS Ion Catcher and the in-flight separator FRS. The R-m method is fast, sensitive and universal and can also be favourably applied for exotic nuclei at low energies when multiple ionic charges states make an unambiguous application of the standard $\mathrm{B}\rho - \Delta \mathrm{E}^{*} - \mathrm{TOF}$ method difficult. The advantages of the R-m method have been demonstrated with ^{155}Yb ions. This novel, universal experimental method has a unique potential for the discovery and study of exotic nuclei produced at low kinetic energies. Of course, this statement holds not only for fragmentation products, but is valid for fusion and nucleon-transfer reactions as well. It is obvious that the R-m method is ideal for a combination with in-flight separators.

Another powerful experimental method, the spatial separation of pure isomeric and pure isobaric beams with an MR-TOF-MS, was pioneered in measurements with ^{211g,m}Po ions. The high mass resolving power of the MR-TOF-MS combined with the Bradbury-Nielsen Gate (*BNG*) were the key parts in this application. The conversion from the time coordinates to the spatial coordinates at the MR-TOF-MS was performed with BNG which let the ions of interest pass and deflects the other ions. Based on the isomer-resolved time-of-flight spectrum of ^{211g,m}Po ions, the pulsing of the deflecting voltages on the BNG was adjusted. Experiments with pure isomeric beams are since a long time the challenge in different laboratories but has been realized in combination with an MR-TOF-MS here for the first time.

In the present experiments, the MR-TOF-MS has reached a maximum accuracy of $6 \cdot 10^{-8}$ in the measurement with ^{213}Fr ions and a resolving power of $5{\cdot}10^{5}$, achieved with ^{97}Ag ions. The most short-lived nuclide in the present study was ^{213}Rn with a half-life of 19.5 ms. New data analysis methods have been refined and applied to obtain the achieved characteristics for mass spectrometry with an MR-TOF-MS. The MR-TOF-MS installed with the FRS Ion Catcher has presently in the performance a leading role worldwide.

Additional to these important experimental-technical developments performed in the frame work of this thesis, exotic nuclei, produced in high-energy fragmentation reactions with ^{124}Xe and ^{238}U projectiles at the entrance of the in-flight separator FRS, were investigated via mass spectrometry. The FRS was operated with different energy-degrader systems placed at the central and final focal planes. Energy bunching and thus a range compression is essential to have an high efficiency for stopping in the gas-filled CSC. The energy bunching is possible with a mono-energetic degrader and the high ion-optical resolving power of the FRS. The experiments gave access to exotic nuclei in the region above the doubly-magic ^{208}Pb nucleus and to neutron-deficient nuclei below the doubly-magic ^{100}Sn nucleus. The measured nuclei are at, or close to the neutron shells of N=50 and N=126.

The masses of 15 short-lived nuclei have been measured with MR-TOF-MS. For seven nuclides the ground-state masses were determined in the past only via decay spectroscopy. The analysis and evaluation of the measured masses are confirmed by a comparison with well-known masses from the literature. The distribution of the observed deviations are characterized by a Gaussian function with a mean value of 1.7±4.4 keV and a standard deviation of 34.9±8.9 keV. From these promising results, one can clearly conclude that the FRS Ion Catcher is now well suited to measure new masses over the full range of atomic elements in the coming experiments.

The accessible isomeric states were investigated via high-resolution, accurate mass spectrometry. The isomer-to-ground state ratios and the excitation energies have been measured. A new isomeric state has been observed in ^{97}Ag nuclei. The clear identification of the ground states and the isomeric states and the measured excitation energies substantially helps to understand the level schemes of nuclei.

The combination of the in-flight fragment separator FRS and the FRS Ion Catcher has opened new fields for the research with exotic nuclei. The new technical developments constructed and commissioned in the framework of this thesis will be applied in future FRS experiments planned for FAIR phase 0.

Zusammenfassung

Die Untersuchung exotischer Kerne, fernab des Tals der Stabilität lässt wichtige Rückschlüsse auf deren innere Struktur und die Element-Synthese im Universum zu. Experimente zum Studium der Kernstruktur und -reaktionen mit exotischen Nukliden stehen im Mittelpunkt der aktuellen Forschung bei GSI-FAIR und anderen Forschungseinrichtungen.

Im Rahmen dieser Arbeit wurden viele verschiedene Themenfelder bearbeitet. Experimentelle Entwicklungen am FRS Ion Catcher Experiment verbessern die aktuelle, sowie die zukünftige Performance. Eine Erweiterung für die bestehende RFQ basierende Strahlführung zwischen der kryogenen Stoppzelle (*CSC*) und dem Multireflexions-Flugzeitmassenspektrometer (*MR-TOF-MS*), bestehend aus resistiven RFQs, einer RFQ Strahlweiche, einer Laserablations-Kohlenstoffcluster-Ionenquelle und einem RFQ Massenfilter, wurde konstruiert und erfolgreich in Betrieb genommen. Der Laser liefert einen polarisierten Strahl mit einer Wellenlänge von 532 nm und einer Pulsbreite von (5 bis 10) ns und kann mit einer Repetitionsrate von bis zu 100 Hz betrieben werden. Diese Repetitionsrate ermöglicht einen synchronen Betrieb mit dem MR-TOF-MS. Ein zweidimensional-beweglicher Target-Tisch ermöglicht mehrere unterschiedliche Targets anzusteuern und diese in einer konstanten Bewegung zu scannen. Die Konstruktion der Laserablations-Ionenquelle wurde auf einen langzeit-stabilen Betrieb ausgelegt. Der RFQ welcher als Massenfilter fungiert, kann zur Vorseparation von Ionen aus der CSC eingesetzt werden.

Eine neue Methode zur eindeutigen Identifikation von Projektilfragmenten wurde erfolgreich an der Kombination aus FRS Ion Catcher und dem “in-flight” Separator FRS eingesetzt. Diese Methode basiert auf der Reichweite der Isotope in Materie kombiniert mit hochauflösender Massenspektrometrie (*R-m-Methode*). Die R-m-Methode ist schnell, sensitiv und universell. Diese Methode kann zur Identifikation von niederenergetischen exotischen Kernen verwendet werden. Dies ist auch möglich, wenn die niederenergetischen Kerne in mehreren Ladungszuständen vorliegen, was eine eindeutige Identifikation mit der Standard $\mathrm{B}\rho - \Delta\mathrm{E}^{*} - \mathrm{TOF}$ Methode erschwert. Die Vorzüge der neuen Methode wurden mit ^{155}Yb Ionen in der hier vorliegenden Arbeit demonstriert. Sie bietet ein einzigartiges Potential für die Entdeckung und Untersuchung von exotischen Kernen, welche bei niedrigen Energien produziert werden. Diese Aussage trifft nicht nur auf Fragmentationsprodukte zu, da die Methode auch bei Fusions- und Nukleonen-Transfer-Reaktionen eingesetzt werden kann. Die R-m-Methode ist entsprechend ideal für den Einsatz in Kombination mit einem “In-flight” Separator geeignet.

Eine weitere, wichtige und vielseitige experimentelle Methode ist die räumliche Separation von isobaren- und isomeren-reinen Strahlen mit einem MR-TOF-MS. Der Weg für diese Methode wurde mit Messungen von ^{211g,m}Po Ionen bereitet, welche in dieser Arbeit diskutiert wurden. Das hochauflösende MR-TOF-MS in Kombination mit einem schnell schaltenden Ionen Gatter (*BNG*) sind die Hauptteile, um diese Methode erfolgreich anwenden zu können. Der Übergang von einer Separation in Flugzeit zu einer Separation in räumlichen Koordinaten geschieht mit Hilfe des BNGs. Die Ionen von Interesse können dieses Gatter ungehindert passieren, während alle anderen abgelenkt werden. Basierend auf dem isomeren-aufgelösten Flugzeitspektrum wurde das Schalten des BNGs justiert. Experimente mit isomeren-reinen Strahlen sind seit geraumer Zeit eine Herausforderung für die Forschung. Im Rahmen dieser Arbeit konnte ein isomeren-reiner Strahl zum ersten Mal mit einem MR-TOF-MS erzeugt werden.

In den Experimenten, welche in dieser Arbeit vorgestellt wurden, konnte mit dem MR-TOF-MS eine Massengenauigkeit von $6 \cdot 10^{-8}$ mit ^{213}Fr Ionen und ein Massenauflösung von $5{\cdot}10^5$ mit ^{97}Ag Ionen erreicht werden. Mit einer Halbwertszeit von 19.5 ms war ^{213}Rn das kurzlebigste Isotop, dessen Masse in dieser Arbeit bestimmt wurde. Die speziell auf MR-TOF-MS Daten angepasste Datenauswertemethode wurde weiterentwickelt und verwendet, um die oben genannten Charakteristiken mit dem MR-TOF-MS zu erreichen. Das MR-TOF-MS des FRS Ion Catcher Experiments gehört mit seiner derzeitigen Performance zu den weltweit führenden Geräten.

Zusätzlich zu den experimentellen und technischen Entwicklungen im Rahmen dieser Arbeit wurden die Massen von exotischen Kernen bestimmt. Die Kerne wurden in Fragmentationsreaktionen bei (600 und 1000) A·MeV am Eingang des “in-flight” Separators FRS produziert. Der FRS wurde mit unterschiedlichen Degrader-Systemen in der zentralen und finalen Fokalebene betrieben. Dabei war das sogenannte “Energiebunchen”, wodurch eine Komprimierung der Reichweite erreicht wird, unabdingbar für ein effizientes Stoppen der Ionen in der gasgefüllten CSC. “Energiebunchen” ist mit einem monoenergetischen Degrader und dem hohen ionenoptischen Auflösungsvermögen des FRSs möglich. In den Experimenten wurden exotische Kerne in der Region oberhalb des doppelt-magischen Kerns ^{208}Pb und neutronenarme Kerne unterhalb des doppelt-magischen Kerns ^{100}Sn untersucht. Die gemessenen Kerne sind entweder auf oder in der Nähe der Neutronenschalen N=50 und N=126.

In der vorliegenden Arbeit wurden die Massen von 15 Kernen mit dem MR-TOF-MS bestimmt, darunter sieben deren Grundzustandsmassen bisher lediglich über ihre radioaktiven Zerfälle bestimmt waren. Durch einen Vergleich mit bekannten Massen, wie sie in der Literatur angegeben sind, wurden die gemessenen Massen und damit insbesondere die Datenauswertemethode bestätigt. Die Verteilung der Differenzen zu den Literaturwerten kann durch eine Gaußfunktion mit einem Mittelwert von 1.7 ± 4.4 keV und einer Standartabweichung von 34.9 ± 8.9 keV beschrieben werden. Mit diesen vielversprechenden Ergebnissen kann man eindeutig schlussfolgern, dass der FRS Ion Catcher für zukünftige Experimente zur Massenmessung von exotischen Kernen aller Elementen bestens geeignet ist.

Die Zugänglichkeit von Isomeren-Zuständen durch akkurate, hochauflösende Massenspektrometrie wurde ebenfalls untersucht. Isomer-zu-Grundzustands-Verhältnisse und Anregungsenergien konnten bestimmt werden. Ein neuer isomerer Zustand im Isotop ^{97}Ag wurde gemessen. Die eindeutige Zuordnung von Grund- und Isomeren-Kernzuständen und die Messung der Anregungsenergien können wesentlich zum Verständnis von Kern-Energie-Schemata beitragen.

Seit der Kombination des “in-flight” Fragment Separators mit dem FRS Ion Catcher Experiment hat sich ein neues Feld im Bereich der Forschung mit exotischen Kernen eröffnet. Die neuen technischen Entwicklungen, welche im Rahmen dieser Arbeit aufgebaut und in Betrieb genommen wurden, werden in den zukünftigen FRS Experimenten im Rahmen der FAIR Phase 0 zum Einsatz kommen.

Danksagung

An dieser Stelle möchte ich mich bei allen bedanken, die mich in den letzten Jahren unterstützt haben. Ohne die lieben Menschen in meinem Umfeld wäre diese Arbeit nicht möglich gewesen.

Ein ganz großer Dank gehört Prof. Dr. Dr. h.c. Hans Geissel. Er war während meiner gesamten Arbeit, seit meiner Bachelor-Arbeit, für mich immer ein Vorbild. Besonders in der Endphase meiner Arbeit war er mir eine große Unterstützung.

Bedanken möchte ich mich auch bei Prof. Dr. Christoph Scheidenberger für die Möglichkeit in der IONAS-Gruppe und an der GSI am FRS Ion Catcher Experiment zu promovieren sowie seinem Interesse an meiner Arbeit.

Besonders bedanken möchte ich mich auch bei Dr. Timo Dickel und Dr. Wolfgang R. Plaß. Bei allen anstehenden Problemen konnte man sich auf die Unterstützung beider für die Suche nach einer Lösung und hilfreichen Ideen zur Weiterentwicklung meiner Projekte verlassen. Zusätzlich möchte ich mich für die wissenschaftlichen Diskussionen und die daraus resultierenden Anregungen bedanken.

Ich möchte mich zudem bei all meinen aktuellen und ehemaligen Kollegen in Gießen bedanken. Ohne die tägliche Arbeit mit Dr. Marcel Diwisch, Dr. Jens Ebert, Dr. Chrsitian Jesch, Dr. Wayne Lippert, Dr. M. Pascal Reiter, Dr. Ann-Kathrin Rink, Daler Amanbayev, Samuel Ayet, Sönke Beck, Julian Bergmann, Florian Greiner, Lizzy Gröf, Daria Kostyleva und Ivan Misku wäre diese Promotion nicht möglich gewesen. Für die kontinuierliche gegenseitige Unterstützung, sei es durch eine helfende Hand oder eine anregende Diskussion, bin ich sehr dankbar.

Auch möchte ich mich bei meinen Kollegen an der GSI bedanken. Dr. Sivaji Purushothaman, Dr. Stephane Pietri, Dr. Emma K. Haettner und Dr. Ronja Knöbel standen mir bei all meinen Fragen mit einem offenen Ohr zur Seite.

Unserer Sekretärin Evelin Prinz gehört möchte ich mich ebenfalls bedanken. Sie ist die immer-helfende, gute Seele der Arbeitsgruppe und hat für jede bürokratische Hürde eine Lösung.

Ein besonderer Dank gilt auch Thomas Wasem, dem Team der feinmechanischen Werkstatt des Fachbereichs 07 in Gießen und den Technikern an der GSI für ihr Knowhow und ihre zuverlässige Arbeit.

Gerne denke ich an das gemeinsame Mittagessen sowie die Kaffeepausen im Theoretischen Institut, bei denen viele interessante Diskussionen über experimentelle und theoretische Physik zustande gekommen sind.

Zuletzt möchte ich mich noch bei meinen Freunden und meiner Familie, insbesondere bei meinen Eltern Elisabeth und Thomas, bedanken. Sie standen mir immer zur Seite und haben es immer verstanden, wenn sie mich für die Arbeit entbehren mussten. An dieser Stelle möchte ich mich auch bei meinem Freund Christian bedanken, der mich immer motiviert und bestärkt hat.

Bibliography

D. Abriola and A. A. Sonzogni. Nuclear Data Sheets for A = 94. *Nuclear Data Sheets*, 107(9): 2423–2578, 2006.

D. Alber, H. H. Bertschat, H. Grawe, H. Haas, B. Spellmeyer, and X. Sun. First in-beam observation of ^{97} Ag - The three-proton-hole spectrum in ^{100} Sn. *Zeitschrift für Physik A Atomic Nuclei*, 335(3):265–270, 1990.

Z. B. Alfassi, M. Bonardi, F. Groppi, and E. Menapace. A new alpha-emitter for nuclear medicine: 230 u. *Journal of radioanalytical and nuclear chemistry*, 270(2):483–487, 2006.

A. Aprahamian and Y. Sun. Nuclear physics - Long live isomer research. *NATURE PHYSICS*, 1(2):81–82, 2005.

F. Asaro and I. Perlman. Alpha-Particle and Gamma-Ray Spectra of the U-230 Decay Series. *Phys. Rev.*, 104(1):91–99, 1956.

F. W. Aston. Bakerian lecture. a new mass-spectrograph and the whole number rule. *Proceedings of the Royal Society of London. Series A, Containing Papers of a Mathematical and Physical Character*, 115(772):487–514, 1927.

G. Audi, A. H. Wapstra, and C. Thibault. The AME2003 atomic mass evaluation:(II). Tables, graphs and references. *Nuclear physics A*, 729(1):337–676, 2003.

G. Audi, F. G. Kondev, M. Wang, W. J. Huang, and S. Naimi. The nubase2016 evaluation of nuclear properties. *Chinese Physics C*, 41(3):030001, 2017.

T. Aumann. Prospects of nuclear structure at the future gsi accelerators. *Progress in Particle and Nuclear Physics*, 59(1):3–21, 2007.

W. E. Austin, A. E. Holme, and J. H. Leck. Chapter VI - The mass filter: design and performance. In P. H. Dawson, editor, *Quadrupole Mass Spectrometry and its Applications*, pages 121 – 152. Elsevier, 1976.

S. Ayet San Andrés. *Developments for Multiple-Reflection Time-of-Flight Mass Spectrometers and their Application to High Resolution Mass Measurements of Exotic Nuclei*. PhD thesis, Universität Gießen, 2018.

J. Äystö, J. Honkanen, W. Trzaska, K. Eskola, K. Vierinen, and S. Messelt. Features of the β-decay of ^{93m}Ru to proton emitting states in ^{93}Tc. *Nuclear Physics A*, 404(1):1–14, 1983.

L. Batist, M. Górska, H. Grawe, Z. Janas, M. Kavatsyuk, M. Karny, R. Kirchner, M. La Commara, I. Mukha, A. Plochocki, and E. Roeckl. Systematics of Gamow-Teller beta decay “Southeast” of ^{100}Sn. *The European Physical Journal A*, 46(1):45–53, 2010.

L. Batist, A. Blazhev, J. Doering, H. Grawe, M. Kavatsyuk, O. Kavatsyuk, R. Kirchner, M. La Commara, C. Mazzocchi, I. Mukha, C. Plettner, E. Roeckl, and M. Romoli. Beta decay of Pd-94 and of the 71 s isomer of Rh-94. *European Physical Journal A*, 29(2):175–182, 2006.

J. Bergmann. *Datenaufnahme und Systemsteuerung eines Flugzeitmassenspektrometers mit Anwendungen*. Master thesis, Universität Gießen, 2015.

J. Bergmann. *in preparation*. PhD thesis, Universität Gießen, 2019.

T.S. Bhatia, T.R. Canada, P.D. Barnes, R.A. Eisenstein, and C. Ellegaard. Levels of Po-209 and Po-211 Populated in One-Neutron Stripping and Pickup from Po-210. *Nuclear Physics A*, 314(1):101–114, 1979.

R. T. Birge. The calculation of errors by the method of least squares. *Physical Review*, 40(2): 207, 1932.

K. Blasche and B. Franczak. The heavy ion synchrotron sis. In *Proc. EPAC*, page 9, 1992.

K. Blaum. High-accuracy mass spectrometry with stored ions. *Physics Reports*, 425(1):1–78, 2006.

K. Blaum, G. Bollen, F. Herfurth, A. Kellerbauer, H.-J. Kluge, M. Kuckein, E. Sauvan, C. Scheidenberger, and L. Schweikhard. Carbon clusters for absolute mass measurements at ISOLTRAP. *Eur. Phys. J. A*, 15(1-2):245–248, 2002. 3rd International Conference on Exotic Nuclei and Atomic Masses, Hameenlinna, Finland, JUL 02-07, 2001.

K. Blaum, J. Dilling, and W. Nörtershäuser. Precision atomic physics techniques for nuclear physics with radioactive beams. *Physica Scripta*, 2013(T152):014017, 2013.

J. Blomqvist and L. Rydström. Shell-Model Description of the N = 50 Isotones Between Sr-88 and Sb-100. *Physica Scripta*, 31(1):31–36, 1985.

G. Bollen, R. B. Moore, G. Savard, and H. Stolzenberg. The accuracy of heavy ion mass measurements using time of flight ion cyclotron resonance in a penning trap. *Journal of Applied Physics*, 68(9):4355–4374, 1990.

G. Bollen, H.-J. Kluge, T. Otto, G. Savard, L. Schweikhard, H. Stolzenberg, G. Audi, R. B. Moore, and G. Rouleau. Maas determination of francium and radium isotopes by a Penning trap mass spectrometer. *Journal of Modern Optics*, 39(2):257–262, 1992.

J. D. Bowman, R. E. Eppley, and E. K. Hyde. Alpha-Spectroscopy of Nuclides Produced in the Interaction of 5 GeV Protons with Heavy Element Targets. *Phys. Rev. C*, 25(2):941–951, 1982.

M. Bowry, Zs. Podolyák, S. Pietri, J. Kurcewicz, M. Bunce, P. H. Regan, F. Farinon, H. Geissel, C. Nociforo, A. Prochazka, H. Weick, N. Al-Dahan, N. Alkhomashi, P. R. P. Allegro, J. Benlliure, G. Benzoni, P. Boutachkov, A. M. Bruce, A. M. Denis Bacelar, G. F. Farrelly, J. Gerl, M. Górska, A. Gottardo, J. Grębosz, N. Gregor, R. Janik, R. Knöbel, I. Kojouharov, T. Kubo, N. Kurz, Yu. A. Litvinov, E. Merchan, I. Mukha, F. Naqvi, B. Pfeiffer, M. Pfützner, W. Plaß, M. Pomorski, B. Riese, M. V. Ricciardi, K.-H. Schmidt, H. Schaffner, C. Scheidenberger, E. C. Simpson, B. Sitar, P. Spiller, J. Stadlmann, P. Strmen, B. Sun, I. Tanihata, S. Terashima, J. J. Valiente Dobón, J. S. Winfield, H.-J. Wollersheim, and P. J. Woods. Population of high-spin isomeric states following fragmentation of ^{238}U. *Physical Review C*, 88 (2):024611, 2013.

N. E. Bradbury and R. A. Nielsen. Absolute values of the electron mobility in hydrogen. *Physical Review*, 49:388–393, 1936.

M. Breitenfeldt, G. Audi, D. Beck, K. Blaum, S. George, F. Herfurth, A. Herlert, A. Kellerbauer, H. J. Kluge, M. Kowalska, D. Lunney, S. Naimi, D. Neidherr, H. Schatz, S. Schwarz, and L. Schweikhard. Penning trap mass measurements of $^{99-109}$Cd with the ISOLTRAP mass spectrometer, and implications for the rp process. *Physical Review C*, 80(3), 2009.

E. Browne. Nuclear Data Sheets for A = 212. *Nuclear Data Sheets*, 104(2):427–496, 2005.

W.M. Brubaker. An improved quadrupol mass analyser. *Adv. in Mass Spectrom.*, 4:293–299, 1968.

A. E. Cameron and D. F. Eggers Jr. An Ion “Velocitron”. *Review of Scientific Instruments*, 19 (9):605–607, 1948.

M. Chartier, G. Auger, W. Mittig, A. Lépine-Szily, L. K. Fifield, J. M. Casandjian, M. Chabert, J. Fermé, A. Gillibert, M. Lewitowicz, M. Mac Cormick, M. H. Moscatello, O. H. Odland, N. A. Orr, G. Politi, C. Spitaels, and A. C. C. Villari. Mass measurement of ^{100}Sn. *Physical Review Letters*, 77(12):2400, 1996.

A. Chaudhuri, M. Block, S. Eliseev, R. Ferrer, F. Herfurth, A. Martin, G. Marx, M. Mukherjee, C. Rauth, L. Schweikhard, and G. Vorobjev. Carbon-cluster mass calibration at SHIPTRAP. *Eur. Phys. J. D*, 45(1):47–53, OCT 2007. Workshop on the Atomic Properties of the Heaviest Elements, Chiemsee, Germany, SEP 25-27, 2006.

J. A. Clark, R. C. Barber, B. Blank, C. Boudreau, F. Buchinger, J. E. Crawford, J. P. Greene, S. Gulick, J. C. Hardy, A. A. Hecht, A. Heinz, J. K. P. Lee, A. F. Levand, B. F. Lundgren, R. B. Moore, G. Savard, N. D. Scielzo, D. Seweryniak, K. S. Sharma, G. D. Sprouse, W. Trimble, J. Vaz, J. C. Wang, Y. Wang, B. J. Zabransky, and Z. Zhou. Investigating the rp-process with the Canadian Penning trap mass spectrometer. *European Physical Journal A*, 25(1):629–632, 2005. 4th International Conference on Exotic Nuclei and Atomic Masses, Pine Mt, GA, SEP 12-16, 2004.

J. R. Cottle, Vandana Tripathi, B. A. Brown, B. Abromeit, J. M. Allmond, M. Anastasiou, L. T. Baby, J. S. Baron, P. D. Cottle, R. Dungan, T. C. Hensley, K. W. Kemper, R. S. Lubna, N. Rijal, E. Rubino, S. L. Tabor, P. L. Tai, K. Villafana, and I. Wiedenhoever. Complete spectroscopy of Po-211 below 2.0 MeV via the (alpha, n) reaction. *Physical Review C*, 95(6), 2017.

I. E. Dayton, F. C. Shoemaker, and R. F. Mozley. The measurement of two-dimensional fields. part ii: Study of a quadrupole magnet. *Review of Scientific Instruments*, 25(5):485–489, 1954.

M. de Jong, A. V. Ignatyuk, and K.-H. Schmidt. Angular momentum in peripheral fragmentation reactions. *Nuclear Physics A*, 613(4):435–444, 1997.

H. M. Devaraja, S. Heinz, O. Beliuskina, V. Comas, S. Hofmann, C. Hornung, G. Münzenberg, K. Nishio, D. Ackermann, Y. K. Gambhir, M. Gupta, R. A. Henderson, F. P. Heßberger, J. Khuyagbaatar, B. Kindler, B. Lommel, K. J. Moody, J. Maurer, R. Mann, A. G. Popeko, D. A. Shaughnessy, M. A. Stoyer, and A. V. Yeremin. Observation of new neutron-deficient isotopes with $z \geq 92$ in multinucleon transfer reactions. *Physics Letters B*, 748:199 – 203, 2015.

T. Dickel. *Design and Commissioning of an Ultra-High-Resolution Time-of-Flight Based Isobar Separator and Mass Spectrometer*. PhD thesis, Universität Gießen, 2010.

T. Dickel, M. I. Yavor, J. Lang, W. R. Plaß, W. Lippert, H. Geissel, and C. Scheidenberger. Dynamical time focus shift in multiple-reflection time-of-flight mass spectrometers. *International Journal of Mass Spectrometry*, 412:1–7, 2017.

T. Dickel, W. R. Plaß, S. Ayet San Andres, J. Ebert, H. Geissel, E. Haettner, C. Hornung, I. Miskun, S. Pietri, S. Purushothaman, M. P. Reiter, A. K. Rink, C. Scheidenberger, H. Weick, P. Dendooven, M. Diwisch, F. Greiner, F. Heisse, R. Knöbel, W. Lippert, I. D. Moore, I. Pohjalainen, A. Prochazka, M. Ranjan, M. Takechi, J. S. Winfield, and X. Xu. First spatial separation of a heavy ion isomeric beam with a multiple-reflection time-of-flight mass spectrometer. *Physics Letters B*, 744:137–141, 2015a.

T. Dickel, W. R. Plaß, A. Becker, U. Czok, H. Geissel, E. Haettner, C. Jesch, W. Kinsel, M. Petrick, C. Scheidenberger, A. Simon, and M. I. Yavor. A high-performance multiple-reflection time-of-flight mass spectrometer and isobar separator for the research with exotic nuclei. *Nuclear Instruments & Methods in Physics Reserach Section A*, 777:172–188, 2015b.

G. D. Dracoulis, P. M. Walker, and F. G. Kondev. Review of metastable states in heavy nuclei. *Reports on Progress in Physics*, 79:076301, 2016.

J. Duflo and A. P. Zuker. Microscopic mass formulas. *Physical Review C*, 52(1):R23, 1995.

J. Ebert. *Mass Measurements of 238-U-Projectile Fragments for the First Time with a Multiple-Reflection Time-Of-Flight Mass Spectrometer*. PhD thesis, Universität Gießen, 2016.

M. Eibach, G. Bollen, K. Gulyuz, C. Izzo, M. Redshaw, R. Ringle, R. Sandler, and A. A. Valverde. Double resonant enhancement in the neutrinoless double-electron capture of ^{190}Pt. *Phys. Rev. C*, 94:015502, 2016.

S. Eliseev, K. Blaum, M. Block, C. Droese, M. Goncharov, E. Minaya Ramirez, D. A. Nesterenko, Y. N. Novikov, and L. Schweikhard. Phase-imaging ion-cyclotron-resonance measurements for short-lived nuclides. *Physical Review Letters*, 110(8):082501, 2013.

V.-V. Elomaa, T. Eronen, U. Hager, A. Jokinen, T. Kessler, I.D. Moore, S. Rahaman, C. Weber, and J. Äystö. Development of a carbon-cluster ion source for JYFLTRAP. *Nuclear Instruments & Methods in Physics Reserach Section B*, 266(19-20):4425 – 4428, 2008.

V.-V. Elomaa, T. Eronen, U. Hager, J. Hakala, A. Jokinen, A. Kankainen, I. D. Moore, S. Rahaman, J. Rissanen, V. Rubchenya, C. Weber, and J. Äystö. Light-ion-induced reactions in mass measurements of neutron-deficient nuclides close to A=100. *European Physical Journal A*, 40(1):1–9, 2009a.

V.-V. Elomaa, G. K. Vorobjev, A. Kankainen, L. Batist, S. Eliseev, T. Eronen, J. Hakala, A. Jokinen, I. D. Moore, Yu. N. Novikov, H. Penttila, A. Popov, S. Rahaman, J. Rissanen, A. Saastamoinen, H. Schatz, D. M. Seliverstov, C. Weber, and J. Aysto. Quenching of the SnSbTe Cycle in the rp Process. *Physical Review Letters*, 102(25), 2009b.

J. Erler, N. Birge, M. Kortelainen, W. Nazarewicz, E. Olsen, A. M. Perhac, and M. Stoitsov. The limits of the nuclear landscape. *Nature*, 486(7404):509, 2012.

T. Eronen, V.-V. Elomaa, U. Hager, J. Hakala, A. Jokinen, A. Kankainen, S. Rahaman, J. Rissanen, C. Weber, and J. Äystö. Preparing isomerically pure beams of short-lived nuclei at JYFLTRAP. *Nuclear Instruments and Methods in Physics Research Section B*, 266(19-20): 4527–4531, 2008.

T. Faestermann, M. Gorska, and H. Grawe. The structure of Sn-100 and neighbouring nuclei. *Progress in Particle and Nuclear Physics*, 69:85–130, 2013.

J. Fallis, J. A. Clark, K. S. Sharma, G. Savard, F. Buchinger, S. Caldwell, A. Chaudhuri, J. E. Crawford, C. M. Deibel, S. Gulick, A. A. Hecht, D. Lascar, J. K. P. Lee, A. F. Levand, G. Li, B. F. Lundgren, A. Parikh, S. Russell, M. Scholte-van de Vorst, N. D. Scielzo, R. E. Segel, H. Sharma, S. Sinha, M. G. Sternberg, T. Sun, I. Tanihata, J. Van Schelt, J. C. Wang, Y. Wang, C. Wrede, and Z. Zhou. Mass measurements of isotopes of Nb, Mo, Tc, Ru, and Rh along the nu p- and r p-process paths using the Canadian Penning trap mass spectrometer. *Physical Review C*, 84(4), 2011.

F. Farinon. *Unambiguous identification and investigation of uranium projectile fragments & discovery of 63 new neutron-rich isotopes in the element range 61 less-than or equal to Z less-than or equal to 78 at the FRS*. PhD thesis, Universitätsbibliothek Giessen, 2011.

K. Fransson, M. af Ugglas, P. Carle, and T. Erikson. On the high multipole alpha-decays of the 18+ state in 212 po and the 1-and 9-states in 212 at. Technical Report 76-09, Stockholm Univ.(Sweden). Fysiska Institutionen, 1976.

B. Franzke. The heavy ion storage and cooler ring project esr at gsi. *Nuclear Instruments and Methods in Physics Research Section B*, 24:18–25, 1987.

B. Franzke, H. Geissel, and G. Münzenberg. Mass and lifetime measurements of exotic nuclei in storage rings. *Mass Spectrometry Reviews*, 27(5):428–469, 2008.

D. Freedman and P. Diaconis. On the histogram as a density estimator: L2 theory. *Zeitschrift für Wahrscheinlichkeitstheorie und verwandte Gebiete*, 57(4):453–476, 1981.

L. P. Gaffney, P. A. Butler, M. Scheck, A. B. Hayes, F. Wenander, M. Albers, B. Bastin, C. Bauer, A. Blazhev, S. Bönig, N. Bree, J. Cederkäll, T. Chupp, D. Cline, T. E. Cocolios, T. Davinson, H. De Witte, J. Diriken, T. Grahn, A. Herzan, M. Huyse, D. G. Jenkins, D. T. Joss, N. Kesteloot, J. Konki, M. Kowalczyk, Th. Kröll, E. Kwan, R. Lutter, K. Moschner, P. Napiorkowski, J. Pakarinen, M. Pfeiffer, D. Radeck, P. Reiter, K. Reynders, S. V. Rigby, L. M. Robledo, M. Rudigier, S. Sambi, M. Seidlitz, B. Siebeck, T. Stora, P. Thoele, P. Van Duppen, M. J. Vermeulen, M. von Schmid, D. Voulot, N. Warr, K. Wimmer, K. Wrzosek-Lipska, C. Y. Wu, and M. Zielinska. Studies of pear-shaped nuclei using accelerated radioactive beams. *Nature*, 497(7448):199, 2013.

J.-J. Gaimard and K.-H Schmidt. A Reexamination of the Abrasion-Ablation Model for the Description of the Nuclear Fragmentation Reaction. *Nuclear Physics A*, 531(3-4):709–745, 1991.

N. D. Gamage, G. Bollen, M. Eibach, K. Gulyuz, C. Izzo, R. M. E. B. Kandegedara, M. Redshaw, R. Ringle, R. Sandler, and A. A. Valverde. Precise determination of the Cd-113 fourth-forbidden non-unique beta-decay Q value. *Physical Review C*, 94(2), 2016.

F. Garcia, R. Turpeinen, J. Äystö, T. Grahn, S. Rinta-Antila, A. Jokinen, B. Voss, J. Kunkel, V. Kleipa, H. Risch, C. Caesar, C. Simons, A. Prochazka, C. J. Schmidt, J. Hoffmann, Rusanov I., and Kurz N.and Heggen H. Twin gem-tpc prototype (hgb4) beam test at gsi - a tracking detector for the super-frs. *GSI Scientific Report 2016*, 2017.

L. R. Gasques, M. Dasgupta, D. J. Hinde, T. Peatey, A. Diaz-Torres, and J. O. Newton. Isomer ratio measurements as a probe of the dynamics of breakup and incomplete fusion. *Physical Review C*, 74(6), 2006.

H. Geissel, T. Schwab, P. Armbruster, J. P. Dufour, E. Hanelt, K.-H. Schmidt, B. Sherrill, and G. Münzenberg. Ions penetrating through ion-optical systems and matter—non-liouvillian phase-space modelling. *Nuclear Instruments and Methods in Physics Research Section A*, 282(1):247–260, 1989.

H. Geissel, P. Armbruster, K.H. Behr, A. Brünle, K. Burkard, M. Chen, H. Folger, B. Franczak, H. Keller, O. Klepper, B. Langenbeck, F. Nickel, E. Pfeng, M. Pfützner, E. Roeckl, K. Rykaczewski, I. Schall, D. Schardt, C. Scheidenberger, K.-H. Schmidt, A. Schröter, T. Schwab, K. Sümmerer, M. Weber, G. Münzenberg, T. Brohm, H.-G. Clerc, M. Fauerbach, J.-J. Gaimard, A. Grewe, E. Hanelt, B. Knödler, M. Steiner, B. Voss, J. Weckenmann, C. Ziegler, A. Magel, H. Wollnik, J.P. Dufour, Y. Fujita, D.J. Vieira, and B. Sherrill. The GSI projectile fragment separator (FRS): a versatile magnetic system for relativistic heavy ions. *Nuclear Instruments and Methods in Physics Research Section B*, 70(1-4):286 – 297, 1992.

H. Geissel, G. Münzenberg, and K. Riisager. Secondary exotic nuclear beams. *Annual Review of Nuclear and Particle Science*, 45(1):163–203, 1995.

H. Geissel, H. Weick, M. Winkler, G. Münzenberg, V. Chichkine, M. Yavor, T. Aumann, K.-H. Behr, M. Böhmer, A. Brünle, K. Burkard, J. Benlliure, D. Cortina-Gil, L. Chulkov, A. Dael, J.-E. Ducret, H. Emling, B. Franczak, J. Friese, B. Gastineau, J. Gerl, R. Gernhäuser, M. Hellström, B. Jonson, J. Kojouharova, R. Kulessa, B. Kindler, N. Kurz, B. Lommel, W. Mittig, G. Moritz, C. Mühle, J. A. Nolen, G. Nyman, P. Roussell-Chomaz, C. Scheidenberger, K.-H. Schmidt, G. Schrieder, B. M. Sherrill, H. Simon, K. Sümmerer, N.A. Tahir, V. Vysotsky, H. Wollnik, and A.F. Zeller. The super-frs project at gsi. *Nuclear Instruments and Methods in Physics Research Section B*, 204:71–85, 2003.

H. Geissel, J. S. Winfield, G. P. A. Berg, B. Franczak, N. Iwasa, G. Münzenberg, C. Nociforo, W. R. Plaß, C. Scheidenberger, H. Weick, M. Winkler, and M. Yavor. Dispersion-matched spectrometer in the low-energy branch of the super-frs for high-resolution measurements with large-emittance relativistic fragment beams. *Nuclear Instruments and Methods in Physics Research Section B: Beam Interactions with Materials and Atoms*, 317:277–283, 2013.

H. Geissel, Yu.A. Litvinov, K. Beckert, P. Beller, F. Bosch, D. Boutin, C. Brandau, L. Chen, M. Hausmann, O. Klepper, R. Knoebel, C. Kozhuharov, J. Kurcewicz, S.A. Litvinov, M. Mazzocco, G. Münzenberg, C. Nociforo, F. Nolden, Z. Patyk, M. Pfutzner, W. Plass, C. Scheidenberger, M. Steck, B. Sun, K. Takahashi, H. Weick, N. Winckler, and M. Winkler. Present and future experiments with stored exotic nuclei at the FRS-ESR facility. *European Physical Journal-Special Topics*, 150:109–115, 2007. 7th International Conference on Radioactive Nuclear Beams, Cortina, ITALY, JUL 02-07, 2006.

J.R. Gibson and S. Taylor. Numerical investigation of the effect of electrode size on the behaviour of quadrupole mass filters. *Rapid Communications in Mass Spectrometry*, 15(20): 1960–1964, 2001.

K. A. Gladnishki, Z. Podolyak, P. H. Regan, J. Gerl, M. Hellstrom, Y. Kopatch, S. Mandal, M. Gorska, R. D. Page, H. J. Wollersheim, A. Banu, G. Benzoni, H. Boardman, M. La Commara, J. Ekman, C. Fahlander, H. Geissel, H. Grawe, E. Kaza, A. Korgul, M. Matos, M. N. Mineva, C. J. Pearson, C. Plettner, D. Rudolph, C. Scheidenberger, K.-H. Schmidt, V. Shishkin, D. Sohler, K. Summerer, J. J. Valiente-Dobon, P. M. Walker, H. Weick, M. Winkler, and O. Yordanov. Angular momentum population in the projectile fragmentation of U-238 at 750 MeV/nucleon. *Physical Review C*, 69(2), 2004.

H. Göktürk, N. K. Aras, P. Fettweis, P. Del Marmol, J. Vanhorenbeeck, and K. Cornelis. The Decay of Pd-97. *Nuclear Physics A*, 344(1):1–14, 1980.

A. S. Goldhaber. Statistical-Models of Fragmentation Processes. *Physics Letters B*, B 53(4): 306–308, 1974.

N. A. Golovkov, Sh. Guetkh, B. S. Dzhelepov, Yu V. Norseev, V. A. Khalkin, and V. G. Chumin. Fine structure of the alpha-particle spectra of 209at, 210at, 211at and 211po. *Izv. Akad. Nauk SSSR, Ser. Fiz.*, 33:1622, 1969.

N. A. Golovkov, R. B. Ivanov, A. Kolachkovski, Yu. V. Norseev, and V. G. Chumin. α decay of neutron-deficient radon isotopes. Technical report, Joint Inst. for Nuclear Research, Dubna (USSR). Lab. of Nuclear Problems, 1971.

S. Goriely, N. Chamel, and J. M. Pearson. Further explorations of skyrme-hartree-fock-bogoliubov mass formulas. xiii. the 2012 atomic mass evaluation and the symmetry coefficient. *Physical Review C*, 88(2):024308, 2013.

H. Grawe, K. Langanke, and G. Martínez-Pinedo. Nuclear structure and astrophysics. *Reports on Progress in Physics*, 70(9):1525, 2007.

F. Greiner. *Construction and Commissioning of a RFQ switchyard*. Bachelor thesis, Universität Gießen, 2013.

F. Greiner. *Collision-induced Dissociation - An effective Method for Removing Molecular Contaminants in Beams of short-lived Nuclei*. Master thesis, Universität Gießen, 2017.

L. Gröf. *Inbetriebnahme und erste Experimente mit einer Kalibrations-Ionenquelle für die Flugzeitmassenspektrometrie*. Bachelor thesis, Universität Gießen, 2017.

E. Haettner. *A novel radio frequency qudrupol system for SHIPTRAP and New mass measurements of rp nuclides*. PhD thesis, Universität Gießen, 2011.

E. Haettner, D. Ackermann, G. Audi, K. Blaum, M. Block, S. Eliseev, T. Fleckenstein, F. Herfurth, F. P. Heßberger, S. Hofmann, J. Ketelaer, J. Ketter, H.-J. Kluge, G. Marx, M. Mazzocco, Yu. N. Novikov, W. R. Plaß, S. Rahaman, T. Rauscher, D. Rodriguez, H. Schatz, C. Scheidenberger, L. Schweikhard, B. Sun, P. G. Thirolf, G. Vorobjev, M. Wang, and C. Weber. Mass Measurements of Very Neutron-Deficient Mo and Tc Isotopes and Their Impact on rp Process Nucleosynthesis. *Physical Review Letters*, 106(12), 2011.

O. Hahn. Über eine neue radioaktive substanz im uran. *Berichte d. D. Chem. Gesellschaft*, 6: 1131, 1921.

R. L. Hahn, M. F. Roche, and K. S. Toth. Alpha Decay of U-227. *Physical Review*, 182(4):1329, 1969.

H. Herndl and B. A. Brown. Shell-model calculations for the properties of nuclei with A = 86-100 near the proton drip line. *Nuclear Physics A*, 627(1):35–52, 1997.

F. P. Heßberger, S. Hofmann, D. Ackermann, V. Ninov, M. Leino, S. Saro, A. Andreyev, A. Lavrentev, A. G. Popeko, and A. V. Yeremin. Decay properties of neutron-deficient nuclei in the region Z=86-92. *European Physical Journal A*, 8(4):521–535, AUG 2000.

C. B. Hinke, M. Böhmer, P. Boutachkov, T. Faestermann, H. Geissel, J. Gerl, R. Gernhäuser, M. Gorska, A. Gottardo, H. Grawe, J. L. Grebosz, R. Kruecken, N. Kurz, Z. Liu, L. Maier, F. Nowacki, S. Pietri, Zs Podolyak, K. Sieja, K. Steiger, K. Straub, H. Weick, H. J. Wollersheim, P. J. Woods, N. Al-Dahan, N. Alkhomashi, A. Atac, A. Blazhev, N. F. Braun, I. T. Celikovic, T. Davinson, I. Dillmann, C. Domingo-Pardo, P. C. Doornenbal, G. de France, G. F. Farrelly, F. Farinon, N. Goel, T. C. Habermann, R. Hoischen, R. Janik, M. Karny, A. Kaskas, I. M. Kojouharov, Th Kroell, Y. Litvinov, S. Myalski, F. Nebel, S. Nishimura, C. Nociforo, J. Nyberg, A. R. Parikh, A. Prochazka, P. H. Regan, C. Rigollet, H. Schaffner, C. Scheidenberger, S. Schwertel, P.-A. Soederstroem, S. J. Steer, A. Stolz, and P. Strmen. Superallowed gamow-teller decay of the doubly magic nucleus ^{100}sn. *Nature*, 486(7403):341, 2012.

P. Hornshoj, P .G. Hansen, and B. Jonson. Alpha-Decay Widths of Neutron-Deficient Francium and Astatine Isotopes. *Nuclear Physics A*, A230(3):380–392, 1974.

C. Hornung. *A Laser Ablation Carbon Cluster Ion Source for a Multiple-Reflection Time-Of-Flight Mass Spectrometer*. Master thesis, Universität Gießen, 2013a.

C. Hornung. *Simulation of the LACCI Switch-Yard for the FRS Ion-Catcher*. Spezialisierungsmodul-bericht, Universität Gießen, 2013b.

Z. Hu, L. Batist, J. Agramunt, A. Algora, B. A. Brown, D. Cano-Ott, R. Collatz, A. Gadea, M. Gierlik, M. Górska, H. Grawe, M. Hellström, Z. Janas, M. Karny, R. Kirchner, F. Moroz, A. Płochocki, M. Rejmund, E. Roeckl, B. Rubio, M. Shibata, J. Szerypo, J. L. Tain, and V. Wittmann. β decay of ^{97}ag: Evidence for the gamow-teller resonance near ^{100}sn. *Physical Review C*, 60:024315, 1999.

N. Iwasa, H. Geissel, G. Münzenberg, C. Scheidenberger, T. Schwab, and H. Wollnik. MOCADI, a universal Monte Carlo code for the transport of heavy ions through matter within ion-optical systems. *Nuclear Instruments and Methods in Physics Research Section B*, 126 (1-4):284–289, 1997.

C. Izzo, G. Bonen, S. Bustabad, M. Eibach, K. Gulyuz, D. J. Morrissey, M. Redshaw, R. Ringle, R. Sandler, S. Schwarz, and A. A. Valverde. A laser ablation source for offline ion production at LEBIT. *Nuclear Instruments and Methods in Physics Research Section B*, 376:60–63, 2016. 17th International Conference on Electromagnetic Isotope Separators and Related Topics (EMIS2015), Michigan State Univ, Grand Rapids, MI, MAY 11-15, 2015.

A. K. Jain, B. Maheshwari, S. Garg, M. Patial, and B. Singh. Atlas of nuclear isomers. *Nuclear Data Sheets*, 128:1–130, 2015.

W. Jentschke, A. C. Juveland, and G. H. Kinsey. Alpha-Emitting Isomer Polonium 211. *Physical Review*, 96(1):231, 1954.

C. Jesch. *The Multiple-Reection Time-of-Flight Isobar Separator for TITAN and Direct Mass Measurements at the FRS Ion Catcher*. PhD thesis, Universität Gießen, 2016.

Valli K. and E. K. Hyde. New Isotopes od Thorium Studied with an Improved Helium-Jet Recoil Transport Apparatus. *Physical Review*, 176(4):1377–&, 1968.

J. Ketelaer, G. Audi, T. Beyer, K. Blaum, M. Block, R. B. Cakirli, R. F. Casten, C. Droese, M. Dworschak, K. Eberhardt, M. Eibach, F. Herfurth, E. Minaya Ramirez, Sz. Nagy, D. Neidherr, W. Nörtershäuser, C. Smorra, and M. Wang. Mass measurements on stable nuclides in the rare-earth region with the penning-trap mass spectrometer triga-trap. *Physical Review C*, 84:014311, 2011.

S. Kimura, Y. Ito, D. Kaji, P. Schury, M. Wada, H. Haba, T. Hashimoto, Y. Hirayama, M. MacCormick, H. Miyatake, J.Y. Moon, K. Morimoto, M. Mukai, I. Murray, A. Ozawa, M. Rosenbusch, H. Schatz, A. Takamine, T. Tanaka, Y.X. Watanabe, and H. Wollnik. Atomic masses of intermediate-mass neutron-deficient nuclei with relative uncertainty down to 35-ppb via multireflection time-of-flight mass spectrograph. *International Journal of Mass Spectrometry*, 2018. ISSN 1387-3806.

R. Knöbel, M. Diwisch, H. Geissel, Yu. A. Litvinov, Z. Patyk, W. R. Plaß, C. Scheidenberger, B. Sun, H. Weick, F. Bosch, D. Boutin, L. Chen, C. Dimopoulou, A. Dolinskii, B. Franczak, B. Franzke, M. Hausmann, C. Kozhuharov, J. Kurcewicz, S. A. Litvinov, M. Matoš, M. Mazzocco, G. Münzenberg, S. Nakajima, C. Nociforo, F. Nolden, T. Ohtsubo, A. Ozawa, J. Stadlmann, M. Steck, T. Suzuki, P. M. Walker, M. Winkler, and T. Yamaguchi. New results from isochronous mass measurements of neutron-rich uranium fission fragments with the frs-esr-facility at gsi. *European Physical Journal A*, 52(5):138, 2016.

M. König, G. Bollen, H.-J. Kluge, T. Otto, and J. Szerypo. Quadrupole excitation of stored ion motion at the true cyclotron frequency. *International Journal of Mass Spectrometry and Ion Processes*, 142(1-2):95–116, 1995.

M. Kowalska, S. Naimi, J. Agramunt, A. Algora, G. Audi, D. Beck, B. Blank, K. Blaum, Ch. Boehm, M. Breitenfeldt, E. Estevez, L. M. Fraile, S. George, F. Herfurth, A. Herlert, A. Kellerbauer, D. Lunney, E. Minaya-Ramirez, D. Neidherr, B. Olaizola, K. Riisager, M. Rosenbusch, B. Rubio, S. Schwarz, L. Schweikhard, and U. Warring. Preparing a journey to the east of Pb-208 with ISOLTRAP: Isobaric purification at A=209 and new masses for Fr211-213 and Ra-211. *European Physical Journal A*, 42(3):351–359, DEC 2009. 5th International Conference on Exotic Nuclei and Atomic Masses (ENAM'08), Ryn, POLAND, SEP 07-13, 2008.

T. Kubo. In-flight ri beam separator bigrips at riken and elsewhere in japan. *Nuclear Instruments and Methods in Physics Research Section B*, 204:97–113, 2003.

H. Kudo, T. Nomura, K. Sueki, M. Magara, and N. Yoshlda. Isomeric transitions of 211mpo and 212mpo and e4 effective charge. *Nuclear Physics A*, 494(2):203–213, 1989.

J. Kurcewicz, W. Czarnacki, M. Karny, M. Kasztelan, M. Kisielinski, A. Korgul, W. Kurcewicz, J. Kurpeta, S. Lewandowski, P. Majorkiewicz, H. Penttila, A. Plochocki, B. Roussiere, O. Steczkiewicz, and A. Wojtasiewicz. Identification of an alpha-decaying (9(-)) isomer in (216)Fr. *Physical Review C*, 76(5), 2007.

W. Kurcewicz, E. F. Zganjar, R. Kirchner, O. Klepper, E. Roeckl, P. Komninos, E. Nolte, D. Schardt, and P. Tidemand-Petersson. Investugations of Very Neutron-Deficient Isotopes Below Sn-100 in Ca-40-Induced Reactions. *Zeitschrift für Physik A - Hadrons and Nuclei*, 308(1):21–31, 1982.

P Kuusiniemi, JFC Cocks, K Eskola, PT Greenless, K Helariutta, P Jones, R Julin, S Juutinen, H Kankaanpaa, A Keenan, H Kittunen, M Leino, M Muikku, P Nieminen, P Rahkila, and J Uusitalo. Studies of U-225,U-226 alpha decay chains. *Acta Physica Polonica B*, 32(3): 1009–1013, MAR 2001. XXXVth Zakopane School of Physics on Trends in Nuclear Physics, Zakopane, Poland, SEP 05-13, 2000.

P. Kuusiniemi, F. P. Heßberger, D. Ackermann, S. Hofmann, and I. Kojouharov. Decay studies of Fr210-214 using alpha-gamma-coincidences. *European Physical Journal A*, 23(3):417–428, 2005.

R. M. Lambrecht and S. Mirzadeh. Cyclotron isotopes and radiopharmaceuticals—xxxv astatine-211. *The International journal of applied radiation and isotopes*, 36(6):443–450, 1985.

G.E. Lee-Whiting and L. Yamazaki. Semi-analytical calculations for circular quadrupoles. *Nuclear Instruments and Methods*, 94(2):319 – 332, 1971.

E. Leistenschneider, M. P. Reiter, S. Ayet San Andrés, B. Kootte, J. D. Holt, P. Navrátil, C. Babcock, C. Barbieri, B. R. Barquest, J. Bergmann, J. Bollig, T. Brunner, E. Dunling, A. Finlay, H. Geissel, L. Graham, F. Greiner, H. Hergert, C. Hornung, C. Jesch, R. Klawitter, Y. Lan, D. Lascar, K. G. Leach, W. Lippert, J. E. McKay, S. F. Paul, A. Schwenk, D. Short, J. Simonis, V. Somà, R. Steinbrügge, S. R. Stroberg, R. Thompson, M. E. Wieser, C. Will, M. Yavor, C. Andreoiu, T. Dickel, I. Dillmann, G. Gwinner, W. R. Plaß, C. Scheidenberger, A. A. Kwiatkowski, and J. Dilling. Dawning of the $n = 32$ shell closure seen through precision mass measurements of neutron-rich titanium isotopes. *Physical Review Letters*, 120(6):062503, 2018.

W. B. Lewis and Bowden B.V. An analysis of the fine structure of the α-particle groups from thorium c and of the long range groups from thorium c'. *Proc. Roy. Soc. (London)*, 145:235, 1934.

C.F. Liang, P. Paris, R.K. Sheline, P. Alexa, and A. Gizon. Alpha Decay of Fr-216 and At-212. *Physical Review C*, 54(5):2304–2309, 1996.

Yu.A. Litvinov, H. Geissel, Yu.N. Novikov, Z. Patyk, T. Radon, C. Scheidenberger, F. Attallah, K. Beckert, F. Bosch, M. Falch, B. Franzke, M. Hausmann, Th. Kerscher, O. Klepper, H.-J. Kluge, C. Kozhuharov, K.E.G. Löbner, G. Münzenberg, F. Nolden, M. Steck, and H. Wollnik. Precision experiments with time-resolved schottky mass spectrometry. *Nuclear Physics A*, 734:473–476, 2004.

Z. Liu, J. Kurcewicz, P.J. Woods, C. Mazzocchi, F. Attallah, E. Badura, C.N. Davids, T. Davinson, J. Döring, H. Geissel, M. Górska, R. Grzywacz, M. Hellström, Z. Janas, M. Karny, A. Korgul, I. Mukha, M. Pfützner, C. Plettner, A. Robinson, E. Roeckl, K. Rykaczewski, K. Schmidt, D. Seweryniak, and H. Weick. Decay spectroscopy of suburanium isotopes following projectile fragmentation of ^{238}u at 1gev/u. *Nuclear Instruments and Methods in Physics Research Section A: Accelerators, Spectrometers, Detectors and Associated Equipment*, 543 (2):591 – 601, 2005.

J. Lommen. *Reference Masses for Precision Mass Spectrometry: Design and Implementation of a Pierce Geometry to the Cluster Ion Source at ISOLTRAP*. Bachelor thesis, University of Heidelberg, 2011.

D. Lunney, J. M. Pearson, and C. Thibault. Recent trends in the determination of nuclear masses. *Reviews of Modern Physics*, 75(3):1021, 2003.

R. Mackintosh, Jim Al-Khalili, Bjorn Jonson, and Teresa Pena. *Nucleus: a trip into the heart of the matter*. Canopus Publishing Limited, United Kingdom, November 2001.

A. G. Marshall, C. L. Hendrickson, and G. S. Jackson. Fourier transform ion cyclotron resonance mass spectrometry: A primer. *Mass Spectrometry Reviews*, 17(1):1–35, 1998.

T. Mayer-Kuckuk. *Kernphysik: Eine Einführung*. Teubner-Studienbücher : Physik. Teubner, 5 edition, 1992.

W. W. Meinke, A. Ghiorso, and G. T. Seaborg. Further work on heavy collateral radioactive chains. *Physical Review*, 85(3):429, 1952.

V. Metag, D. Habs, and H. J. Specht. Spectroscopic properties of fission isomers. *Physics Reports*, 65(1):1–41, 1980.

I. Miskun. *Commissioning, performance and possible applications of RFQ mass-filter in the diagnostic unit of the FRS Ion Catcher facility*. Diploma thesis, Tomsk Polytechnic University, 2015.

I. Miskun. *in preparation*. PhD thesis, Universität Gießen, 2019.

P. Möller, A. J. Sierk, T. Ichikawa, and H. Sagawa. Nuclear ground-state masses and deformations: Frdm (2012). *Atomic Data and Nuclear Data Tables*, 109:1–204, 2016.

P. Möller, J. R. Nix, W. D. Myers, and W. J. Swiatecki. Nuclear ground-state masses and deformations. *Atomic Data and Nuclear Data Tables*, 59(2):185–381, 1995.

F. F. Momyer, F. Asaro, and E. K. Hyde. Exact Alpha-Particle Energies for the Isotopes Em-211, Em-210, Em-209, Em-208, and Fr-212. *Journal of Inorganic & Nuclear Chemistry*, 1(4-5): 267–273, 1955.

J. J Moré. The levenberg-marquardt algorithm: implementation and theory. In *Numerical analysis*, pages 105–116. Springer, 1978.

K. Oxorn, B. Singh, and S. K. Mark. The Decay of 26-s Rh-94 and 71-s Rh-94 Isomers. *Zeitschrift für Physik A*, 294(4):389–394, 1980.

S. Pal and R. Palit. Angular momentum population in fragmentation reactions. *Physics Letters B*, 665(4):164–167, 2008.

M. Palacz, J. Nyberg, H. Grawe, K. Sieja, G. de Angelis, P. Bednarczyk, A. Blazhev, D. Curien, Z. Dombradi, O. Dorvaux, J. Ekman, J. Galkowski, M. Górska, J. Iwanicki, G. Jaworski, J. Kownacki, J. Ljungvall, M. Moszyński, F. Nowacki, D. Rudolph, D. Sohler, D. Wolski, and M. Zięblinski. Odd-Parity ^{100}Sn Core Excitations. *Acta Physica Polonica B*, 44(3), 2013.

I. Perlman, F. Asaro, A. Ghiorso, A. Larsh, and R. Latimer. Isomeric state of po 212. *Physical Review*, 127(3):917, 1962.

M. Pfützner, M. Karny, L. V. Grigorenko, and K. Riisager. Radioactive decays at limits of nuclear stability. *Reviews of Modern Physics*, 84(2):567, 2012.

M. Pfützner, P. H. Regan, P. M. Walker, M. Caamano, J. Gerl, M. Hellström, P. Mayet, K.-H. Schmidt, Z. Podolyak, M. N. Mineva, A. Aprahamian, J. Benlliure, A. M. Bruce, P. A. Butler, D. C. Gil, D. M. Cullen, J. Döring, T. Enquist, C. Fox, J. Garces Narro, H. Geissel, W. Gelletly, J. Giovinazzo, M. Gorska, H. Grawe, R. Grzywacz, A. Kleinböhl, W. Korten, M. Lewitowicz, R. Lucas, H. Mach, C. D. O'Leary, F. De Oliveira, C. J. Pearson, F. Rejmund, M. Rejmund, M Sawicka., H. Schaffner, C. Schlegel, K. Schmidt, C. Theisen, F. Vives, D. D. Warner, C. Wheldon, H.-J. Wollersheim, and S. Wooding. Angular momentum population in the fragmentation of Pb-208 at 1 GeV/nucleon. *Physical Review C*, 65(6), 2002.

A. Pikhtelev. Original version of MAc software. private communication, 2014.

W. R. Plaß, T. Dickel, S. Ayet San Andres, J. Ebert, F. Greiner, C. Hornung, C. Jesch, J. Lang, W. Lippert, T. Majoros, D. Short, H. Geissel, E. Haettner, M. P. Reiter, A.-K. Rink, C. Scheidenberger, and M. I. Yavor. High-performance multiple-reflection time-of-flight mass spectrometers for research with exotic nuclei and for analytical mass spectrometry. *Physica Scripta*, T166, 2015. 9th International Conference on Nuclear Physics at Storage Rings (STORI), Sankt Goar, GERMANY, SEP 29-OCT 03, 2014.

W.R. Plaß, T. Dickel, U. Czok, H. Geissel, M. Petrick, K. Reinheimer, C. Scheidenberger, and M.I. Yavor. Isobar separation by time-of-flight mass spectrometry for low-energy radioactive ion beam facilities. *Nuclear Instruments and Methods in Physics Research Section B*, 266(19-20):4560–4564, 2008. 15th International Conference on Electromagnetic Isotope Separators and Techniques Related to their Applications, Deauville, France, JUN 24-29, 2007.

W.R. Plaß, T. Dickel, S. Purushothaman, P. Dendooven, H. Geissel, J. Ebert, E. Haettner, C. Jesch, M. Ranjan, M.P. Reiter, H. Weick, F. Amjad, S. Ayet, M. Diwisch, A. Estrade, F. Farinon, F. Greiner, N. Kalantar-Nayestanaki, R. Knöbel, J. Kurcewicz, J. Lang, I. Moore, I. Mukha, C. Nociforo, M. Petrick, M. Pfützner, S. Pietri, A. Prochazka, A.-K. Rink, S. Rinta-Antila, D. Schäfer, C. Scheidenberger, M. Takechi, Y.K. Tanaka, J. S. Winfield, and M. I. Yavor. The FRS Ion Catcher - A facility for high-precision experiments with stopped projectile and fission fragments. *Nuclear Instruments and Methods in Physics Research Section B*, 2013a.

W.R. Plaß, T. Dickel, and C. Scheidenberger. Multiple-reflection time-of-flight mass spectrometry. *International Journal of Mass Spectrometry*, 349-350:134 – 144, 2013b. 100 years of Mass Spectrometry.

Z. Podolyák, J. Gerl, M. Hellström, F. Becker, K.A. Gladnishki, M. Górska, A. Kelić, Y. Kopatch, S. Mandal, P.H. Regan, K.-H. Schmidt, P.M. Walker, H.J. Wollersheim, A. Banu, G. Benzoni, H. Boardman, E. Casarejos, J. Ekman, H. Geissel, H. Grawe, D. Hohn, I. Kojouharov, J. Leske, R. Lozeva, M.N. Mineva, G. Neyens, R.D. Page, C.J. Pearson, M. Portillo, D. Rudolph, N. Saito, H. Schaffner, D. Sohler, K. Sümmerer, J.J. Valiente-Dobón, C. Wheldon, H. Weick, and M. Winkler. High angular momentum states populated in fragmentation reactions. *Physics Letters B*, 632(2-3):203–206, 2006.

S. Purushothaman, M. P. Reiter, E. Haettner, P. Dendooven, T. Dickel, H. Geissel, J. Ebert, C. Jesch, W. R. Plaß, M. Ranjan, H. Weick, F. Amjad, S. Ayet, M. Diwisch, A. Estrade, F. Farinon, F. Greiner, N. Kalantar-Nayestanaki, R. Knöbel, J. Kurcewicz, J. Lang, I. D. Moore, I. Mukha, C. Nociforo, M. Petrick, M. Pfützner, S. Pietri, A. Prochazka, A.-K. Rink, S. Rinta-Antila, C. Scheidenberger, M. Takechi, Y. K. Tanaka, J. S. Winfield, and M. I. Yavor. First experimental results of a cryogenic stopping cell with short-lived, heavy uranium fragments produced at 1000 mev/u. *EPL (Europhysics Letters)*, 104(4):42001, 2013.

S. Purushothaman, T. Dickel, S. Ayet, S. Bagchi, K.-H. Behr, J. Bergmann, T. Blatz, P. Constantin, J. Ebert, A. Finley, H. Geissel, F. Greiner, E. Haettner, C. Hornung, S. Kaur, W. Lippert, B. Lommel, I. Mardor, B. Mai, I. Miskun, I. Moore, J.-H. Otto, S. Pietri, A. Pikhtelev, W. R. Plaß, I. Pohjalainen, A. Prochazka, M. P. Reiter, A.-K. Rink, C. Scheidenberger, B. Szczepanczyk, Y. Tanaka, H. Weick, and J. S. Winfield. A gas degrader for the low-energy branch of the super-frs at fair. *GSI Scientific Report 2016*, 2017.

S. Purushothaman, S. Ayet San Andres, J. Bergmann, T. Dickel, J. Ebert, H. Geissel, C. Hornung, W. R. Plaß, C. Rappold, C. Scheidenberger, Y. K. Tanaka, and M. I. Yavor. Hyper-EMG: A new probability distribution function composed of Exponentially Modified Gaussian distributions to analyze asymmetric peak shapes in high-resolution time-of-flight mass spectrometry. *International Journal of Mass Spectrometry*, 421:245–254, 2017.

R Core Team. *R: A Language and Environment for Statistical Computing*. R Foundation for Statistical Computing, Vienna, Austria, 2018. URL `http://www.R-project.org/`.

T. Radon, Th. Kerscher, B. Schlitt, K. Beckert, T. Beha, F. Bosch, H. Eickhoff, B. Franzke, Y. Fujita, H. Geissel, M. Hausmann, H. Irnich, H. C. Jung, O. Klepper, H.-J. Kluge, C. Kozhuharov, G. Kraus, K. E. G. Löbner, G. Münzenberg, Yu. Novikov, F. Nickel, F. Nolden, Z. Patyk, H. Reich, C. Scheidenberger, W. Schwab, M. Steck, K. Sümmerer, and H. Wollnik. Schottky mass measurements of cooled proton-rich nuclei at the gsi experimental storage ring. *Physical Review Letters*, 78(25):4701, 1997.

M. Ranjan, S. Purushothaman, T. Dickel, H. Geissel, W. R. Plaß, D. Schäfer, C. Scheidenberger, J. Van de Walle, H. Weick, and P. Dendooven. New stopping cell capabilities: RF carpet performance at high gas density and cryogenic operation. *EPL (Europhysics Letters)*, 96(5): 52001, 2011.

P. L. Reeder. Alpha Spectroscopy of At-212g and At-212m. *Physical Review C*, 1(2):721–&, 1970.

M. P. Reiter. *Simulation of the cryogenic stopping cell of the FRS Ion Catcher experiment and construction of a novel RFQ beam line system.* Master thesis, Universität Gießen, 2011.

M. P. Reiter. *Pilot Experiments with Relativistic Uranium Projectile and Fission Fragments Thermalized in a Cryogenic Gas-filled Stopping Cell.* PhD thesis, Universität Gießen, 2015.

A .J. Reuben, G. B. Smith, P. Moses, A. V. Vagov, M. D. Woods, D. B. Gordon, and R. W. Munn. Ion trajectories in exactly determined quadrupole fields. *International Journal of Mass Spectrometry and Ion Processes*, 154(1):43 – 59, 1996.

A.-K. Rink. *Mass and Life-time Measurement of the 1.7 ms 215-Po Isotope - A Crucial Test of the Novel Concept of the Cryogenic Ion Catcher for the Super-FRS at GSI-FAIR.* PhD thesis, Universität Gießen, 2017.

C. Rodriguez Triguero, A. M. Bruce, T. Eronen, I. D. Moore, M. Bowry, A. M. Denis Bacelar, A. Y. Deo, V.-V. Elomaa, D. Gorelov, J. Hakala, A. Jokinen, A. Kankainen, P. Karvonen, V. S. Kolhinen, J. Kurpeta, T. Malkiewicz, P. J. R. Mason, H. Penttilä, M. Reponen, S. Rinta-Antila, J. Rissanen, A. Saastamoinen, G. S. Simpson, and J. Äystö. Trap-assisted separation of nuclear states for gamma-ray spectroscopy: the example of 100nb. *Journal of Physics G*, 39(1):015101, 2012.

M. Rosenbusch, Y. Ito, P. Schury, M. Wada, D. Kaji, K. Morimoto, H. Haba, S. Kimura, H. Koura, M. MacCormick, H. Miyatake, J. Y. Moon, K. Morita, I. Murray, T. Niwase, A. Ozawa, M. Reponen, A. Takamine, T. Tanaka, and H. Wollnik. New mass anchor points for neutron-deficient heavy nuclei from direct mass measurements of radium and actinium isotopes. *arXiv preprint arXiv:1801.02823*, 2018.

K. Rykaczewski, R. Grzywacz, M. Lewitowicz, and M. Pfützner. New μs-isomers and isomeric beams. *Nuclear Physics A*, 630(1-2):307–315, 1998.

K. Rykaczewski, I. S. Grant, R. Kirchner, O. Klepper, V. T. Koslowsky, P. O. Larsson, E. Nolte, G. Nyman, E. Roeckl, D. Schardt, L. Spanier, P. Tidemand-Petersson, E. F. Zganjar, and J. Zylicz. The Gamow-Teller Transitions in the Pd-96->Rh-96 Decay. *Zeitschrift für Physik A*, 322(2):263–270, 1985.

C. Scheidenberger. The contribution of precision mass measurements to nuclear physics. *Nuclear Physics A*, 751:209–225, 2005.

C. Scheidenberger, G. Bollen, F. Herfurth, A. Kellerbauer, H.-J. Kluge, M. Koizumi, S. Schwarz, and L. Schweikhard. Production and trapping of carbon clusters for absolute mass measurements at ISOLTRAP. *Nuclear Physics A*, 701:574C–578C, 2002. 5th International Conference on Radioactive Nuclear Beams, Divonne, France, MAR 27-APR 01, 2000.

C. Scheidenberger, K. Beckert, P. Beller, F. Bosch, C. Brandau, D. Boutin, L. Chen, B. Franzke, H. Geissel, R. Knöbel, C. Kozhuharov, J. Kurcewicz, S. A. Litvinov, Y. A. Litvinov, M. Mazzocco, G. Münzenberg, F. Nolden, W.R. Plaß, M. Steck, B. Sun, H. Weick, and M. Winkler. Isobar separation at FRS-ESR - a development towards pure isomeric stored beams. *Hyperfine Interactions*, 173(1-3):61–66, 2006.

K. Schmidt, P. C. Divari, T. W. Elze, R. Grzywacz, Z. Janas, I. P. Johnstone, M. Karny, H. Keller, R. Kirchner, O. Klepper, A. Plochocki, E. Roeckl, K. Rykaczewski, L. D. Skouras, J. Szerypo, and J. Zylicz. Decay properties of very neutron-deficient isotopes of silver and cadmium. *Nuclear Physics A*, 624(2):185–209, 1997.

R. Schneider, J. Friese, J. Reinhold, K. Zeitelhack, T. Faestermann, R. Gernhäuser, H. Gilg, F. Heine, J. Homolka, P. Kienle, H. J. Körner, H. Geissel, G. Münzenberg, and K. Sümmerer. Production and identification of ^{100} sn. *Zeitschrift für Physik A*, 348(4):241–242, 1994.

P. Schury, M. Wada, Y. Ito, F. Arai, S. Naimi, T. Sonoda, H. Wollnik, V. A. Shchepunov, C. Smorra, and C. Yuan. A high-resolution multi-reflection time-of-flight mass spectrograph for precision mass measurements at RIKEN/SLOWRI. *Nuclear Instruments and Methods in Physics Research Section B*, 335:39–53, 2014.

G. T. Seaborg and I. Perlman. Table of isotopes. *Reviews of Modern Physics*, 20(4):585, 1948.

B. Singh, D. Abriola, C. Baglin, V. Demetriou, T. Johnson, E. McCutchan, G. Mukherjee, S. Singh, A. Sonzogni, and J. Tuli. Nuclear Data Sheets for A= 211. *Nuclear Data Sheets*, 114(6-7):661–749, 2013.

C. Smorra, K. Blaum, K. Eberhardt, M. Eibach, J. Ketelaer, J. Ketter, K. Knuth, and Sz Nagy. A carbon-cluster laser ion source for TRIGA-TRAP. *Journal of Physics B*, 42(15):154028, 2009.

C. Smorra, T. Beyer, K. Blaum, M. Block, Ch. E. Düllmann, K. Eberhardt, M. Eibach, S. Eliseev, Sz. Nagy, W. Nörtershäuser, and D. Renisch. Direct mass measurements of cadmium and palladium isotopes and their double-β transition q values. *Physical Review C*, 85:027601, 2012.

F. Soddy. The complexity of the chemical elements. *Nature*, 99:433, 1917.

O. Sorlin and M.-G. Porquet. Nuclear magic numbers: New features far from stability. *Progress in Particle and Nuclear Physics*, 61(2):602–673, 2008.

A. Spataru. *Extension of the particle identification at the GSI Fragment Separator by high resolution mass spectrometry*. Master thesis, Universty of Bucharest, 2017.

I. Stefanescu, G. Georgiev, F. Ames, J. Äystö, D. L. Balabanski, G. Bollen, P. A. Butler, J. Cederkäll, N. Champault, T. Davinson, A. De Maesschalck, P. Delahaye, J. Eberth, D. Fedorov, V. N. Fedosseev, L. M. Fraile, S. Franchoo, K. Gladnishki, D. Habs, K. Heyde, M. Huyse, O. Ivanov, J. Iwanicki, J. Jolie, B. Jonson, Th. Kröll, R. Krücken, O. Kester, U. Köster, A. Lagoyannis, L. Liljeby, G. Lo Bianco, B. A. Marsh, O. Niedermaier, T. Nilsson, M. Oinonen, G. Pascovici, P. Reiter, A. Saltarelli, H. Scheit, D. Schwalm, T. Sieber, N. Smirnova, J. Van De Walle, P. Van Duppen, S. Zemlyanoi, N. Warr, D. Weisshaar, and F. Wenander. Coulomb excitation of Cu-68,Cu-70: First use of postaccelerated isomeric beams. *Physical Review Letters*, 98(12), 2007.

G. Suliman, S. Pommé, M. Marouli, R. Van Ammel, V. Jobbágy, J. Paepen, H. Stroh, C. Apostolidis, K. Abbas, and A. Morgenstern. Measurements of the half-life of 214po and 218rn using digital electronics. *Applied Radiation and Isotopes*, 70(9):1907–1912, 2012.

O. B. Tarasov and D. Bazin. Lise++: Radioactive beam production with in-flight separators. *Nuclear Instruments and Methods in Physics Research Section B*, 266(19-20):4657–4664, 2008.

M. Thoennessen. Current status and future potential of nuclide discoveries. *Reports on Progress in Physics*, 76(5):056301, 2013.

W. Trzaska, J. Äystö, and J. Kantele. Semiconductor telescope spectrometer for beta-ray spectra. *Nuclear Instruments and Methods in Physics Research*, 212(1):221 – 225, 1983.

K. Valli. An experimental investigation of the alpha fine structure in ac-225, er-221, at-217, and po-213. Technical report, Univ. of Helsinki, 1964.

K. Valli, E.K. Hyde, and W. Treytl. Alpha decay of neutron-deficient francium isotopes. *Journal of Inorganic and Nuclear Chemistry*, 29(10):2503 – 2514, 1967.

K. Valli, E. K. Hyde, and J. Borggreen. Production and decay properties of thorium isotopes of mass 221-224 formed in heavy-ion reactions. *Physical Review C*, 1:2115–2132, 1970.

A. A. Vorob'ev, A. P. Komar, and V. A. Korolev. Measurement of the energy of α-particles from some emitters. *Zhur. Eksptl'. i Teoret. Fiz.*, 39, 1960.

T. Vylov, N. A. Golovkov, B. S. Dzhelepov, R. B. Ivanov, M. A. Mikhailova, Yu V. Norseev, and V. G. Chumin. The decay of 221rn. *Izv. Akad. Nauk SSSR, Ser. Fiz.*, 41:1635, 1977.

R. J. Walen. Spectrographic α due radium 224 et de ses dèrives. *Comptes rendus de l'Acad émie des sciences*, 255:1604, 1962.

R. J. Walen, V. Nedovessov, and G. Bastin-Scoffier. Spectrographie α de 223ra (acx) et de ses dérivés. *Nuclear Physics*, 35:232–252, 1962.

P. Walker. High-spin isomers: structure and applications. *Nuclear Physics A*, 834(1-4):22c–27c, 2010. 10th International Conference on Nucleus-Nucleus Collisions (NN2009), Beijing, PEOPLES R CHINA, AUG 16-21, 2009.

P. Walker and G. Dracoulis. Energy traps in atomic nuclei. *Nature*, 399(6731):35–40, 1999.

P. M. Walker. Isomer beams. *International Journal of Modern Physics E*, 15(07):1637–1644, 2006.

M. Wang, G. Audi, F. G. Kondev, W. J. Huang, S. Naimi, and Xing Xu. The AME2016 atomic mass evaluation (II). Tables, graphs and references. *Chinese Physics C*, 41(3), 2017.

Z. Wang. *Aufbau und Charakterisierung einer Laserablationsionenquelle mit Kohlenstoffclustern als Referenz für Flugzeitmassenspektrometrie von exotischen Kernen*. PhD thesis, Universität Gießen, 2006.

H. Watanabe, K. Asahi, T. Kishida, H. Ueno, W. Sato, A. Yoshimi, Y. Kobayashi, M. Ishihara, D. Kameda, H. Miyoshi, T. Fukuchi, Y. Wakabayashi, T. Sasaki, M. Kibe, N. Hokoiwa, A. Odahara, B. Cederwall, K. Lagergren, Z. Podolyak, M. Ishihara, and Y. Gono. Application of the high-spin isomer beams to secondary fusion reaction and measurement of g-factor. In *A New Era Of Nuclear Structure Physics*, pages 99–103. World Scientific, 2004.

C. Weber, V.-V. Elomaa, R. Ferrer, C. Fröhlich, D. Ackermann, J. Äystö, G. Audi, L. Batist, K. Blaum, M. Block, A. Chaudhuri, M. Dworschak, S. Eliseev, T. Eronen, U. Hager, J. Hakala, F. Herfurth, F. P. Heßberger, S. Hofmann, A. Jokinen, A. Kankainen, H. J. Kluge, K. Langanke, A. Martin, G. Martinez-Pinedo, M. Mazzocco, I. D. Moore, J. B. Neumayr, Yu. N. Novikov, H. Penttilä, W. R. Plaß, A. V. Popov, S. Rahaman, T. Rauscher, C. Rauth, J. Rissanen, D. Rodriguez, A. Saastamoinen, C. Scheidenberger, L. Schweikhard, D. M. Seliverstov, T. Sonoda, F. K. Thielemann, P. G. Thirolf, and G. K. Vorobjev. Mass measurements in the vicinity of the r p-process and the nu p-process paths with the Penning trap facilities JYFLTRAP and SHIPTRAP. *Physical Review C*, 78(5), 2008. ISSN 2469-9985.

H. Weick, H. Geissel, N. Iwasa, C. Scheidenberger, J. L. Rodriguez Sanchez, A. Prochazka, Purushotaman S., and the Super-FRS experiment collaboration. Improved accuracy of the code ATIMA for energy loss of heavy ions in matter. *GSI Scientific Report 2017*, 2018.

L. v. d. Wense, B. Seiferle, M. Laatiaoui, and P. G. Thirolf. The extraction of ^{229}th^{3+} from a buffer-gas stopping cell. *Nuclear Instruments and Methods in Physics Research Section B*, 376:260–264, 2016.

J. Winfield, H. Geissel, J. Gerl, G. Münzenberg, C. Nociforo, W. R. Plaß, C. Scheidenberger, H. Weick, M. Winkler, and M. I. Yavor. A versatile high-resolution magnetic spectrometer for energy compression, reaction studies and nuclear spectroscopy. *Nuclear Instruments and Methods in Physics Research Section A*, 704:76 – 83, 2013.

A. Wojtasiewicz, W. Czarnacki, M. Kasztelan, M. Kisielinski, A. Korgul, J. Kurcewicz, W. Kurcewicz, S. Lewandowski, S. Mianowski, A. Plochocki, B. Roussiere, and O. Steczkiewicz. Search for α-decaying isomers in trans-lead isotopes using the igisol device. Technical Report B-10, University of Warsaw Heavy Ion Laboratory, 2009. Annual Report 2008.

H. Wollnik and M. Przewloka. Time-of-Flight Mass Spectrometers with Multiply Reflected Ion Trajectories. *Int. J. Mass Spectrom. Ion Processes*, 96(3):267 – 274, 1990.

M.I. Yavor, W.R. Plaß, T. Dickel, H. Geissel, and Scheidenberger C. Ion-optical design of a high-performance multiple-reflection time-of-flight mass spectrometer and isobar separator. *International Journal of Mass Spectrometry*, 381 - 382:1–9, 2015.

B.M. Young, D. Bazin, W. Benenson, J.H. Kelley, D.J. Morrissey, N.A. Orr, R. Ronningen, B.M. Sherrill, M. Steiner, M. Thoennessen, J.A. Winger, S.J. Yennello, I. Tanihata, X.X. Bai, N. Inabe, T. Kubo, C.-B. Moon, S. Shimoura, T. Suzuki, R.N. Boyd, and K. Subotic. Strong isomer production in fragmentation reactions. *Physics Letters B*, 311(1-4):22–26, 1993.

List of Abbreviations

AME	Atomic Mass Evaluation
BNG	Bradbury-Nielson ion Gate
CID	Collision-Induced Dissociation
CSC	Cryogenic Stopping Cell
EC	Electron Capture
DAQ	Data AcQuisition
DU1	first Diagnostic Unit
DU2	second Diagnostic Unit
EMG	Exponentially Modified Gaussian
FRS	FRagment Separator
FRS-IC	FRS Ion Catcher
FT-ICR MS	Fourier Transform Ion-Cyclotron-Resonance Mass Spectrometry
hyper-EMG	hyper-Exponentially Modified Gaussian
IOI	Ion Of Interest
IMS	Isochronous Mass Spectrometry
ITAG	Isomer TAGging detector
LACCI	Laser Ablation Carbon Cluster Ion source
LS	Least-Square
NIE	Non-Ideal Ejection
MAc	data Mass Acquisition software
MCP	Micro-Channel Plate
ME	Mass Excess
MR-TOF-MS	Multiple-Reflection Time-Of-Flight Mass-Spectrometer
MRS	Mass Range Selector
MUSIC	MUltiple Sampling Ionisation Chamber
NS-EMG	Negative Skewed EMG
PAR	Post-Analyser Reflector
PDF	Probability Distribution Function
PID	Particle IDentification
PS-EMG	Positive Skewed EMG
RFQ	Radio-Frequency Quadrupole
RMS	Root Mean Squared
RU	Recapturing Unit
SCI	SCIntillator
SEETRAM	SEcondary Electron TRAnsmission Monitor
SEV	Secondary Electron Multiplier
SMS	Schottky Mass Spectrometry

SM-G	$\pi\left(g_{9/2}\right)^{-n}$ Shell Model
SM-PG	$\pi\left(p_{1/2}, g_{9/2}\right)^{-n}$ Shell Model
SY	Switch Yard
TDC	Time-to-Digital Converter
TFS	Time-Focus-Shift
TOF	Time-Of-Flight
TOF-ICR	Time-Of-Flight Ion-Cyclotron-Resonance
TOF-MS	Time-Of-Flight Mass Spectrometer
TPC	Time-Projection Chamber
TRC	Time Resolved Calibration
WMLE	Weighted Maximum Likelihood Estimation

A. Appendix

A.1. Mass Resolving Power

The mass resolving power of a TOF-system is defined in Equation 3.7. The total TOF in an MR-TOF-MS is given by

$$t = t_{TFS} + N_{IT} t_{IT} \ , \tag{A.1}$$

depending on the TOF in TFS mode t_{TFS} and the TOF, while undergoing N_{IT} isochronous turns with a TOF of t_{IT} each. The peak width Δt in an MR-TOF-MS measurement can be approximated by the turn-around time Δt_{ta} and ion optical effects. These effects can be divided into a turn number N_{IT} independent part $\Delta t_{TFS,ab}$ and a turn number dependent part. The turn number depended part is described by maximum resolving power of the system $R_{m,N\to\infty}$ considering the limit for the turn number to infinity. All these effects can be assumed in a first estimation to be independent, caused by this they can be added quadratically, resulting in

$$\Delta t = \sqrt{(q_{Cal}/q) \cdot (\Delta t_{ta})^2 + (\Delta t_{TFS,ab})^2 + (N_{IT} t_{IT} / R_{m,N\to\infty})^2} \ . \tag{A.2}$$

With Equation A.1 and Equation A.2 the mass resolving power of an MR-TOF-MS can be written as

$$R_m(q,N) = \frac{t_{TFS} + N_{IT} t_{IT}}{2 \cdot \sqrt{(q_{Cal}/q) \cdot (\Delta t_{ta})^2 + (\Delta t_{TFS,ab})^2 + (N_{IT} t_{IT} / R_{m,N\to\infty})^2}} \ . \tag{A.3}$$

The used turn-around time Δt_{ta} is given by the kinetic Energy $E_{kin,ex}$ in direction of the extraction and the extraction field strength [Dickel (2010)]. It can be written as the fraction $\lambda_{\Delta,ta}$ of the TOF of an isochronous turn t_{IT}, which is a mass-to-charge independent parameter, by:

$$\Delta t_{ta}\left((m/q), \lambda_{\Delta,ta}\right) = \lambda_{\Delta,ta} t_{IT} = \lambda_{\Delta,ta} A \sqrt{(m/q)}, \tag{A.4}$$

The aberrations in the TFS turn $\Delta t_{TFS,ab}$ can be described in a similar way by a mass-to-charge independent parameter $\lambda_{\Delta,TFS,ab}$:

$$\Delta t_{TFS,ab}\left((m/q), \lambda_{\Delta,TFS,ab}\right) = \lambda_{\Delta,TFS,ab} t_{IT} = \lambda_{\Delta,TFS,ab} A \sqrt{(m/q)}, \tag{A.5}$$

Considering the introduced parameters one can derive for the mass resolving power R_m the mass but not charge independent expression

$$R_m(q,N) = \frac{\lambda_{TFS} + N_{IT}}{2 \cdot \sqrt{(q_{Cal}/q) \cdot (\lambda_{\Delta,ta})^2 + (\lambda_{\Delta,TFS,ab})^2 + (N_{IT} / R_{m,N\to\infty})^2}} \ . \tag{A.6}$$

The mass resolving power of an MR-TOF-MS is a charge dependent value, caused by the linear dependency of the turn-around time on the charge. For a large number of isochronous turns, the contributions from the turn-around time and the turn number independent ion optical aberration can be neglected and the resolving power converges to $R_{m,N\to\infty}$. Since the mass resolving power relates its mass-to-charge ratio to its peak width, it is used in the data evaluation to scale the mass-to-charge dependent peak shape parameters of the hyper-EMG (Section 5.2).

A.2. Mass window of an MR-TOF-MS

The size of the mass window in an MR-TOF-MS measurement depends on the number of isochronous turns N_{IT} of the ions in the analyser. One has to consider the TOF corresponding to the point where lighter ions with N_{IT} turns and heavier ions with $N_{IT} - 1$ turns are at the same position in the exit reflector, while it is pulsed to a lower potential for ejection. This is shown schematically in fig. A.1. In order derive a mathematical description for the mass range, one has to spilt up the TOF in several sections. The TOF from the ejection from the injection trap until the exit reflector t_{inj} can be described as the fraction λ_{inj} of the TOF of an isochronous turn t_{IT} (Equation 3.8), which is a mass-to-charge independent parameter, by

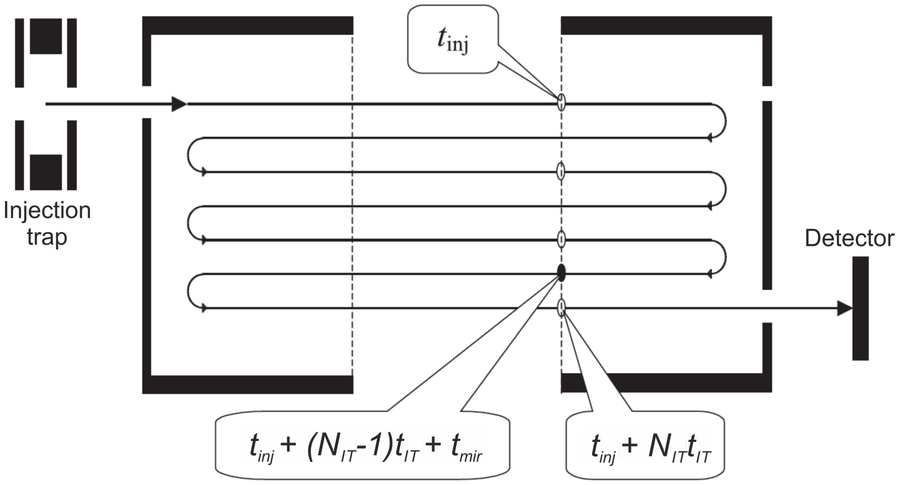

Figure A.1.: Schematic illustration of the different flight path in a MR-TOF-MS, giving the TOF at certain positions in the analyser, taken from [Yavor et al. (2015)]. The TOF from the ejection from the injection trap until the exit reflector is t_{inj}. The TOF inside one mirror of the analyser is t_{mir}. N_{IT} is the number of isochronous turn, corresponding to a TOF t_{IT} for each turn. The mass window in an MR-TOF-MS can be derived from the point where lighter ions with N_{IT} turns and heavier ions with $N_{IT} - 1$ turns are at the same position in the exit reflector, while it is pulsed to a lower potential for ejection.

$$t_{inj}\left(m/q\right) = \lambda_{inj} t_{IT}\left(m/q\right) = \lambda_{inj} A \sqrt{(m/q)}\ . \tag{A.7}$$

The TOF inside one mirror of the analyser t_{mir} can be described similarly as a fraction λ_{mir} of the TOF of an isochronous turn by

$$t_{mir}\left(m/q\right) = \lambda_{mir} t_{IT}\left(m/q\right) = \lambda_{mir} A \sqrt{(m/q)}\ . \tag{A.8}$$

This will lead to the following equation for the TOF corresponding to the point where ions with N_{IT} turns and ions with $N_{IT} - 1$ turns are at the same position in the exit reflector, considering the minimum mass-to-charge $(m/q)_{min}$ undergoing N_{IT} turns and the maximum mass-to-charge $(m/q)_{max}$ undergoing $(N_{IT} - 1)$ turns

$$\begin{aligned} t\left((m/q)_{min}, N_{IT}\right) =& t\left((m/q)_{max}, (N_{IT}-1)\right)\ , \\ t_{inj}\left((m/q)_{min}\right) + N_{IT} t_{IT}\left((m/q)_{min}\right) =& t_{inj}\left((m/q)_{max}\right) + (N_{IT}-1)\, t_{IT}\left((m/q)_{max}\right) + t_{mir}\left((m/q)_{max}\right)\ , \\ (\lambda_{inj} + N_{IT}) \cdot A\sqrt{(m/q)_{min}} =& (\lambda_{inj} + (N_{IT}-1) + \lambda_{mir}) \cdot A\sqrt{(m/q)_{max}}\ . \end{aligned} \tag{A.9}$$

With the difference in the mass-to-charge ratio, between the maximum and minimum,

$$\Delta(m/q) = (m/q)_{max} - (m/q)_{min} \ , \tag{A.10}$$

the relative mass-to-charge window $\frac{\Delta(m/q)}{(m/q)}$ can be described with by

$$\frac{\Delta(m/q)}{(m/q)} = \left(\frac{N_{IT} + \lambda_{inj}}{N_{IT} + \lambda_{inj} - (1 - \lambda_{mir})}\right)^2 - 1 \ . \tag{A.11}$$

A similar description of the relative mass-to-charge window was derived by [Schury et al. (2014)], given by

$$\frac{\Delta(m/q)}{(m/q)} = \frac{2\left(N_{IT} + \lambda_{inj}\right) + 1}{\left(N_{IT} + \lambda_{inj}\right)^2} \ . \tag{A.12}$$

A.3. Known Unresolved Isobars and Isomers

In the case that two or more mass lines are overlapping it is necessary to relate the mostly unknown underlying structure to the measured value, which is a mixture of the underlying masses m_i and to determine the uncertainty σ. This can be done using a probability theory, recommended in the AME 2016 [Wang et al. (2017)]. The measured mass-to-charge ratio is assumed to be the mean value $\overline{(m/q)}$ of the distribution. One considers that each mass-to-charge ratio value (m/q) is distributed following certain underlying normalised probability distribution $P((m/q))$. In this case the mean value $\overline{(m/q)}$ is given by the first moment of the probability distribution,

$$\overline{(m/q)} = \int_{-\infty}^{\infty} P((m/q))\, m \, d(m/q) \ . \tag{A.13}$$

The second moment of the probability distribution reflects the variance of the distribution, which is the square of their uncertainty σ, given by

$$\sigma^2 = \int_{-\infty}^{\infty} P((m/q)) \left((m/q) - \overline{(m/q)}\right)^2 d(m/q) \ . \tag{A.14}$$

In the case of two overlapping isobars or nuclear states $(m/q)_0$ and $(m/q)_1$ with an unknown distribution one can follow the approach above. Consequently the measured mass-to-charge ratios are equally distributed. This leads to a the following normalised probability distribution

$$P((m/q)) = \begin{cases} \frac{1}{(m/q)_1 - (m/q)t_0} & \text{if } (m/q)_0 \leq (m/q) \leq (m/q)_1 \\ 0 & \text{elsewhere} \ . \end{cases} \tag{A.15}$$

This normalised probability distribution leads to a mean value of

$$\overline{(m/q)} = \frac{1}{2}\left((m/q)_0 + (m/q)_1\right) \ , \tag{A.16}$$

and to an error Δm_{Iso} of

$$\Delta m_{Iso} = \frac{\sqrt{3}}{6}\left((m/q)_1 - (m/q)_0\right) \ . \tag{A.17}$$

In the case that $(m/q)_0$ is the ground state and $(m/q)_1$ is an isomeric state with the excitation energy E_{Iso} their values and the additional error contribution for the unresolved isomeric state Δm_{Iso} can be rewritten as

$$\begin{aligned} (m/q)_0 &= \overline{(m/q)} - \frac{1}{2}E_{Iso} \ , \\ (m/q)_1 &= \overline{(m/q)} + \frac{1}{2}E_{Iso} \ , \\ \Delta m_{Iso} &= \frac{\sqrt{3}}{6}E_{Iso} \ . \end{aligned} \tag{A.18}$$

B. Tables of Measured Masses

B.1. Masses of 1 GeV/u Uranium Fragments

ME [keV]	Total Error [keV]	Mass [u]	Total Error [u]	S4 Degrader Thickness [mg/cm2]	Counts
-4242	57	210.9954461	6.14E-05	2992	75
-4139	115	210.9955563	1.23E-04	2992	11
-3951	149	210.9957584	1.60E-04	2944	9
-3949	113	210.9957605	1.21E-04	2960	9
-3901	125	210.9958121	1.34E-04	2976	7
-3897	153	210.9958163	1.64E-04	2992	7
-3931	219	210.9957800	2.35E-04	2992	5
-4239	189	210.9954496	2.02E-04	2992	3
-4061	40	210.9956399	4.25E-05		

Table B.1.: Measured mass and the Mass Excess (*ME*) values of ^{211}Fr. ^{211}Fr was measured several times with different degrader thicknesses at the final focal plane of the FRS with different number of ions. The given mean value (bottom line) of the ME value is determined from the results of the single measurements weighted by their errors (Equation 5.11).

ME [keV]	Total Error [keV]	Mass [u]	Total Error [u]	S4 Degrader Thickness [mg/cm2]	Counts
-3568	57	211.9961696	6.08E-05	2992	97
-3374	230	211.9963783	2.47E-04	2976	8
-3513	110	211.9962292	1.18E-04	2992	21
-3582	148	211.9961545	1.59E-04	2992	12
-3499	128	211.9962441	1.38E-04	3008	17
-3675	120	211.9960549	1.28E-04	3024	27
-3525	76	211.9962152	8.18E-05	3040	66
-3505	52	211.9962370	5.55E-05	3056	131
-3672	127	211.9960581	1.37E-04	3016	24
-3428	126	211.9963203	1.35E-04	2992	25
-3456	92	211.9962902	9.83E-05	2992	17
-3530	28	211.9962099	3.01E-05		

Table B.2.: Measured mass and the Mass Excess (*ME*) values of ^{212}Fr. ^{212}Fr was measured several times with different degrader thicknesses at the final focal plane of the FRS with different number of ions. The given mean value (bottom line) of the ME value is determined from the results of the single measurements weighted by their errors (Equation 5.11).

ME [keV]	Total Error [keV]	Mass [u]	Total Error [u]	S4 Degrader Thickness [mg/cm2]	Counts
-3573	17	212.9961646	1.83E-05	2992	1536
-3571	34	212.9961668	3.60E-05	2992	260
-3667	441	212.9960635	4.73E-04	2944	3
-3670	185	212.9960605	1.99E-04	2960	7
-3655	78	212.9960766	8.38E-05	2976	39
-3539	35	212.9962009	3.79E-05	2992	257
-3539	35	212.9962009	3.79E-05	3008	508
-3559	27	212.9961790	2.88E-05	3024	744
-3569	33	212.9961680	3.51E-05	3040	450
-3527	56	212.9962135	6.00E-05	3056	105
-3545	26	212.9961942	2.83E-05	3016	787
-3574	31	212.9961628	3.34E-05	2992	688
-3513	37	212.9962284	3.93E-05	2992	638
-3562	12.3	212.9961756	1.32E-05		

Table B.3.: Measured mass and the Mass Excess (*ME*) values of ^{213}Fr. ^{213}Fr was measured several times with different degrader thicknesses at the final focal plane of the FRS with different number of ions. The given mean value (bottom line) of the ME value is determined from the results of the single measurements weighted by their errors (Equation 5.11).

ME [keV]	Total Error [keV]	Mass [u]	Total Error [u]	S4 Degrader Thickness [mg/cm2]	Counts
-8724	61	211.9906347	6.52E-05	2992	107
-8546	133	211.9908259	1.43E-04	2992	17
-8751	280	211.9906060	3.01E-04	2976	5
-8566	128	211.9908044	1.38E-04	2992	17
-8663	108	211.9906998	1.16E-04	3008	28
-8590	106	211.9907780	1.14E-04	3024	30
-8611	185	211.9907562	1.99E-04	3040	9
-8535	153	211.9908376	1.64E-04	3056	13
-8559	111	211.9908116	1.20E-04	3016	31
-8581	54	211.9907884	5.75E-05	3253	208
-8483	105	211.9908933	1.13E-04	2992	34
-8562	85	211.9908078	9.16E-05	2992	15
-8600	30	211.9907673	3.21E-05		

Table B.4.: Measured mass and the Mass Excess (*ME*) values of ^{212}Rn. ^{212}Rn was measured several times with different degrader thicknesses at the final focal plane of the FRS with different number of ions. The given mean value (bottom line) of the ME value is determined from the results of the single measurements weighted by their errors (Equation 5.11).

ME [keV]	Total Error [keV]	Mass [u]	Total Error [u]	S4 Degrader Thickness [mg/cm2]	Counts
5154	101	218.0055332	1.09E-04	3504	50
5063	72	218.0054351	7.69E-05	3496	92
4656	336	218.0049984	3.60E-04	3528	4
5151	156	218.0055301	1.67E-04	3480	16
5071	54	218.0054436	5.85E-05		

Table B.5.: Measured mass and the Mass Excess (*ME*) values of ^{218}Rn. ^{218}Rn was measured several times with different degrader thicknesses at the final focal plane of the FRS with different number of ions. The given mean value (bottom line) of the ME value is determined from the results of the single measurements weighted by their errors (Equation 5.11).

B.2. Masses of 600 MeV/u Xenon Fragments

ME [keV]	Total Error [keV]	Mass [u]	Total Error [u]	S4 Degrader Thickness [mg/cm2]	Counts
-76303	85	95.9180858	9.08E-05	4492.60	9
-76243	47	95.9181497	5.06E-05	4516.60	124
-76177	105	95.9182201	1.12E-04	4516.60	91
-76240	38	95.9181533	4.12E-05		

Table B.6.: Measured mass and the Mass Excess (*ME*) values of ^{96}Pd. ^{96}Pd was measured several times with different degrader thicknesses at the final focal plane of the FRS with different number of ions. The given mean value (bottom line) of the ME value is determined from the results of the single measurements weighted by their errors (Equation 5.11).

ME [keV]	Total Error [keV]	Mass [u]	Total Error [u]	S4 Degrader Thickness [mg/cm2]	Counts
-77742	77	96.9165405	8.25E-05	4492.6	18
-77793	44	96.9164853	4.68E-05	4492.6	12
-77919	143	96.9163501	1.54E-04	4516.6	5
-77798	37	96.9164801	3.94E-05		

Table B.7.: Measured mass and the Mass Excess (*ME*) values of ^{97}Pd. ^{97}Pd was measured several times with different degrader thicknesses at the final focal plane of the FRS with different number of ions. The given mean value (bottom line) of the ME value is determined from the results of the single measurements weighted by their errors (Equation 5.11).

ME [keV]	Total Error [keV]	Mass [u]	Total Error [u]	S4 Degrader Thickness [mg/cm2]	Counts
-82546	29	93.9113832	3.11E-05	4635.0	64
-82540	59	93.9113897	6.37E-05	4635.0	24
-82546	26	93.9113833	2.81E-05		

Table B.8.: Measured mass and the Mass Excess (*ME*) values of ^{94}Ru. ^{94}Ru was measured several times with different degrader thicknesses at the final focal plane of the FRS with different number of ions. The given mean value (bottom line) of the ME value is determined from the results of the single measurements weighted by their errors (Equation 5.11).

ME [keV]	Total Error [keV]	Mass [u]	Total Error [u]	S4 Degrader Thickness [mg/cm2]	Counts
-72941	106	93.9216946	1.13E-04	4635.0	4
-72845	24	93.9217973	2.61E-05	4695.8	334
-72862	24	93.9217796	2.55E-05		

Table B.9.: Measured mass and the Mass Excess (*ME*) values of ^{94g}Rh. ^{94g}Rh was measured several times with different degrader thicknesses at the final focal plane of the FRS with different number of ions. The given mean value (bottom line) of the ME value is determined from the results of the single measurements weighted by their errors (Equation 5.11).

ME [keV]	Total Error [keV]	Mass [u]	Total Error [u]	S4 Degrader Thickness [mg/cm2]	Counts
-72367	146	93.9223112	1.57E-04	4635.0	2
-72573	36	93.9220896	3.81E-05	4695.8	62
-72533	35	93.9221329	3.71E-05		

Table B.10.: Measured mass and the Mass Excess (*ME*) values of ^{94m}Rh. ^{94m}Rh was measured several times with different degrader thicknesses at the final focal plane of the FRS with different number of ions. The given mean value (bottom line) of the ME value is determined from the results of the single measurements weighted by their errors (Equation 5.11).

ME [keV]	Total Error [keV]	Mass [u]	Total Error [u]	S4 Degrader Thickness [mg/cm2]	Counts
-70878	22	96.9239093	2.38E-05	4492.6	181
-70924	32	96.9238603	3.44E-05	4492.6	115
-70955	57	96.9238266	6.14E-05	4516.6	18
-70902	88	96.9238841	9.44E-05	4516.6	26
-70906	17	96.9238789	1.86E-05		

Table B.11.: Measured mass and the Mass Excess (*ME*) values of ^{97g}Ag. ^{97g}Ag was measured several times with different degrader thicknesses at the final focal plane of the FRS with different number of ions. The given mean value (bottom line) of the ME value is determined from the results of the single measurements weighted by their errors (Equation 5.11).

ME [keV]	Total Error [keV]	Mass [u]	Total Error [u]	S4 Degrader Thickness [mg/cm2]	Counts
-70175	209	96.9246635	2.24E-04	4492.6	5
-70299	43	96.9245304	4.57E-05	4492.6	9
-70279	42	96.9245529	4.48E-05		

Table B.12.: Measured mass and the Mass Excess (*ME*) values of ^{97m}Ag. ^{97m}Ag was measured several times with different degrader thicknesses at the final focal plane of the FRS with different number of ions. The given mean value (bottom line) of the ME value is determined from the results of the single measurements weighted by their errors (Equation 5.11).

Erklärung

Ich habe die vorgelegte Dissertation selbstständig und ohne unerlaubte fremde Hilfe und nur mit den Hilfen angefertigt, die ich in der Dissertation angegeben habe. Alle Textstellen, die wörtlich oder sinngemäß aus veröffentlichten Schriften entnommen sind, und alle Angaben, die auf mündlichen Auskünften beruhen, sind als solche kenntlich gemacht. Ich stimme einer evtl. Überprüfung meiner Dissertation durch eine Antiplagiat-Software zu. Bei den von mir durchgeführten und in der Dissertation erwähnten Untersuchungen habe ich die Grundsätze guter wissenschaftlicher Praxis, wie sie in der Satzung der Justus-Liebig-Universität Gießen zur Sicherung guter wissenschaftlicher Praxis niedergelegt sind, eingehalten.

Gießen, den 28. Mai 2018

Christine Hornung